THE APPLICATION OF TWO- AND THREE-DIMENSIONAL STRESS ANALYSIS TECHNIQUES TO THE DESIGN OF ROCK STRUCTURES, WITH PARTICULAR REFERENCE TO UNDERGROUND PILLARS

by

MICHAEL KARMIS, BSc(Hons.)MinEng

Thesis presented to the University of Strathclyde
for the Degree of
Doctor of Philosophy in Engineering

Department of Mining Engineering

SEPTEMBER 1974

GLASGOW

CONTENTS

REFERENCES

ACKNOWLEDGEMENTS

The author is indebted to Professor J Dewi Jenkins, MSc, CEng, FIMinE, for giving him the opportunity to undertake this investigation.

To Mr D O Davies, BSc, DipMetMin, CEng, MIME, FGS, whose direction and advice was generous, throughout this work, the author is sincerely thankful.

The assistance of Dr B Smart, BSc, PhD, during the first underground project and his general interest, is greatly appreciated.

The author is indebted to Mr P Waddell, MSc, CEng, MIMechE, for introducing him to the image de-rotation techniques and for much stimulating discussion in the field of experimental stress analysis.

The generous co-operation of the National Coal Board, and in particular of the management of Killoch and Cairnhill Collieries, is greatly acknowledged.

To Mr A Chattell, Chief Technician, at the Mining Engineering Department, University of Strathclyde, whose skill and craftsmanship was invaluable during this work, the author is greatful.

Finally, the author wishes to express his appreciation to the National Coal Board and the University of Strathclyde, for financing this investigation.

SUMMARY

An attempt was made in the course of this investigation, to introduce some modern laboratory and 'in-situ' techniques of Experimental Stress Analysis to mining configurations, and in particular, to the design of underground pillars.

Chapters I and II are both introductory ones. In the former, the basic problems associated with the design of structures in rock are briefly outlined whereas in the latter, a detailed and up to date discussion is given, on the behaviour of underground pillars and their design considerations.

In Chapters III and IV two modern and sophisticated photo-elastic techniques are described, with particular reference to their application to mining. The Scattered Light technique of three-dimensional photo-elasticity, and the special polariscope on which this method can be executed, are described in Chapter III. In Chapter IV, an Image De-rotation technique has been specially adapted, to enable gravity loading simulation in 'real time'.

The application of the Scattered Light technique to the field of Rock Mechanics, is given in Chapter V, where two cases of underground pillars are examined photo-elastically, in three dimensions.

In order to examine the underground behaviour of pillars as well as establishing the degree of reliance of the photo-

elastic results, two 'in-situ' investigations were carried out, and are described in detail in Chapter VI.

Finally, the important problem of developing improved methods of 'in-situ' measurements was not ignored. The design and laboratory testing of two instruments capable of triaxial measurements at a point 'in-situ', from a single borehole, is discussed in Chapter VII.

LIST OF ILLUSTRATIONS

CHAPTER I

SOME BASIC PROBLEMS ASSOCIATED WITH THE DESIGN IN ROCK

CHAPTER I

SOME BASIC PROBLEMS ASSOCIATED WITH THE DESIGN IN ROCK

1.1 INTRODUCTION

Although rock has been used as a structural material since the beginning of civilization, its structural competency has always been accepted for granted, and it is only recently, that a more scientific examination of rock behaviour was felt necessary. As a result, unlike the long history of rock in engineering practice, rock mechanics has a relatively short history, of about three decades.

The scope of the science of rock mechanics was clearly defined by the Committee on Rock Mechanics of the Geological Society of America[1], as follows:

> 'Rock Mechanics is the Theoretical and Applied Science of the mechanical behaviour of rock; it is that branch of mechanics concerned with the response of rock to the force fields of its physical environment'.

In order to investigate a rock mechanics problem, therefore, three basic concepts must be determined, in accordance with the definition above. Firstly, the nature and magnitude of the applied forces must be known. Secondly, the properties of the rock, on an engineering basis, must be determined. Thirdly, a theory of rock behaviour must be

adopted, capable of explaining its response to the applied stress field.

It is on rare occasions that all these principles can be accurately defined. In most problems, for a realistic solution, the scientific approach must be accompanied by empirical knowledge of the problem. However, such knowledge should only strengthen and not substitute the scientific analysis.

In this Chapter, therefore, some preliminary considerations towards establishing design criteria, from a scientific basis, are briefly discussed.

1.2 THE MECHANICAL PROPERTIES OF ROCK

Unlike other engineering disciplines, rock mechanics offers no choice, with respect to the structural material. Furthermore, the mechanical properties of rock in general will be highly directional and their magnitude will considerably vary in accordance with the testing procedure.

There are two groups of properties necessary for any investigation. Firstly, the strength of rock under various loading conditions and secondly, the stress-strain-time relationships. The former will determine the structural competency of the rock, whereas the latter will define the best suited theory of rock behaviour.

These properties can be evaluated by either large scale

'in-situ' tests, or small scale laboratory testing. 'In-situ' rock tests[2,3,4,5] are, obviously more representative of the actual underground conditions; however, due to large scale can be expensive in time and money and have often proved inaccurate. Small scale laboratory tests, on the other hand, offer a faster and cheaper alternative, with good control of the various parameters involved[6,7]. However, there is the problem of how accurately a rock mass can be represented by small samples, as well as the difficulty in reproducing the 'in-situ' state of stress in the laboratory.

Engineering properties of rock, apart from being affected by environmental factors, such as water or temperature, will be greatly influenced by the presence of geological structural features. No earth material is perfectly homogeneous or isotropic, and as a result, most properties will be highly directional. An experimental determination of rock properties on a megascopic scale, therefore, must be extremely systematic if it is to be representative, so that the influence of the above factors can be ascertained[8].

The treatment of rock, on a microscopic scale, has also been attempted. By dividing rock in representative volumes, each containing a large number of elements, and assuming a suitable statistical distribution, the effect of anisotropy and non-homogeneity is then included in the analysis. Such

methods have been used to evaluate the compressive strength of coal[9]. Petrographic studies have also been used, to establish indirect methods of strength evaluation and to examine modes of failure[10]. However, microscopic investigations have not, as yet, been fully explored.

Since a knowledge of the engineering properties of rock is invaluable to the designer, many investigators have attempted to classify rocks, on an engineering basis, in order to guide his judgement. However, as in any other classification system, a definite criterion is required, something extremely difficult to establish when dealing with rock. As a result various criteria have been adopted by investigators; Terzaghi[11] classified rocks, in a broad sense, in order to determine the type and amount of tunnel support. A similar classification[12] was also attempted, the criterion being the competency of rock, which includes some information of the relative rock strength. Coates[13,14] tried to evolve a more comprehensive classification system assuming three basic rock characteristics, strength, deformation and rock structure. However, these classifications can only give a rough indication at their best, of the engineering properties, and therefore are of limited practical importance.

1.3 THE 'IN-SITU' STATE OF STRESS

Underground structures are acted upon two types of stresses. The pre-mining or 'primitive' stresses and the post-mining or 'induced' stresses.

If a level strata is assumed, in homogeneous isotropic rock, then the primitive stresses will be the result of gravity. If 'σ_y' is the vertical stress component and 'σ_x, σ_z' the two lateral ones then

$$\sigma_y = \gamma h$$

$$\sigma_x = \sigma_z \qquad (1.3.1)$$

where 'h' is the depth from the surface and 'γ' is the specific weight of the rock (22.5kN/m^2 for every metre of depth, for British coal measure strata). If, in addition, perfect elasticity is assumed under lateral restraints (plane strain condition), then

$$\sigma_y = \gamma h$$

$$\sigma_x = \sigma_y = \frac{\nu}{1 - \nu} \sigma_y \qquad (1.3.2)$$

where 'ν' is the Poisson's ratio.

The oldest theory of primitive stresses was developed by Heim[1], in 1878. He suggested that the state of stress in the earth's crust is hydrostatic. Heim postulated that due to prolonged periods of loading, slow adjustments due to creep will occur, tending to relieve the stress differences,

and resulting in a hydrostatic state of stress, i.e.

$$\sigma_y = \sigma_x = \sigma_z = \gamma h \qquad (1.3.3)$$

Apart from the plane strain and hydrostatic theories, Seager[15] considered other possibilities, covering the case of no creep, with perfect elasticity up to a certain stress level. By assuming that yielding initiates at a stress value 'S', then plastic deformation will take place when the difference of the principal stresses '$(\sigma_1 - \sigma_2)$'is

$$(\sigma_1 - \sigma_2) = S \qquad (1.3.4)$$

and equation (1.3.4) will be satisfied in the plastic zone. These results are illustrated in Figure 1.3.1. Figure 1.3.2 shows the effect of brittle fracture on the stress system.

The 'in-situ' determination of stress has been attempted by many investigators[1,16,17,18,19,20] using various methods. It was found in general, that the vertical stress, σ_y, was higher than predicted by the overburden stress. The values of the lateral stresses, however, showed extreme inconsistency, ranging from 0.6 to 8 times the vertical stress. The most extreme case was that reported by Hooker et al[21], where lateral stresses between $3.5MN/m^2$ - $21MN/m^2$ were measured in an outcrop, at depth of a few metres. The presence of such high lateral stresses can only be explained by assuming additional stresses, to the ones induced by gravity. These

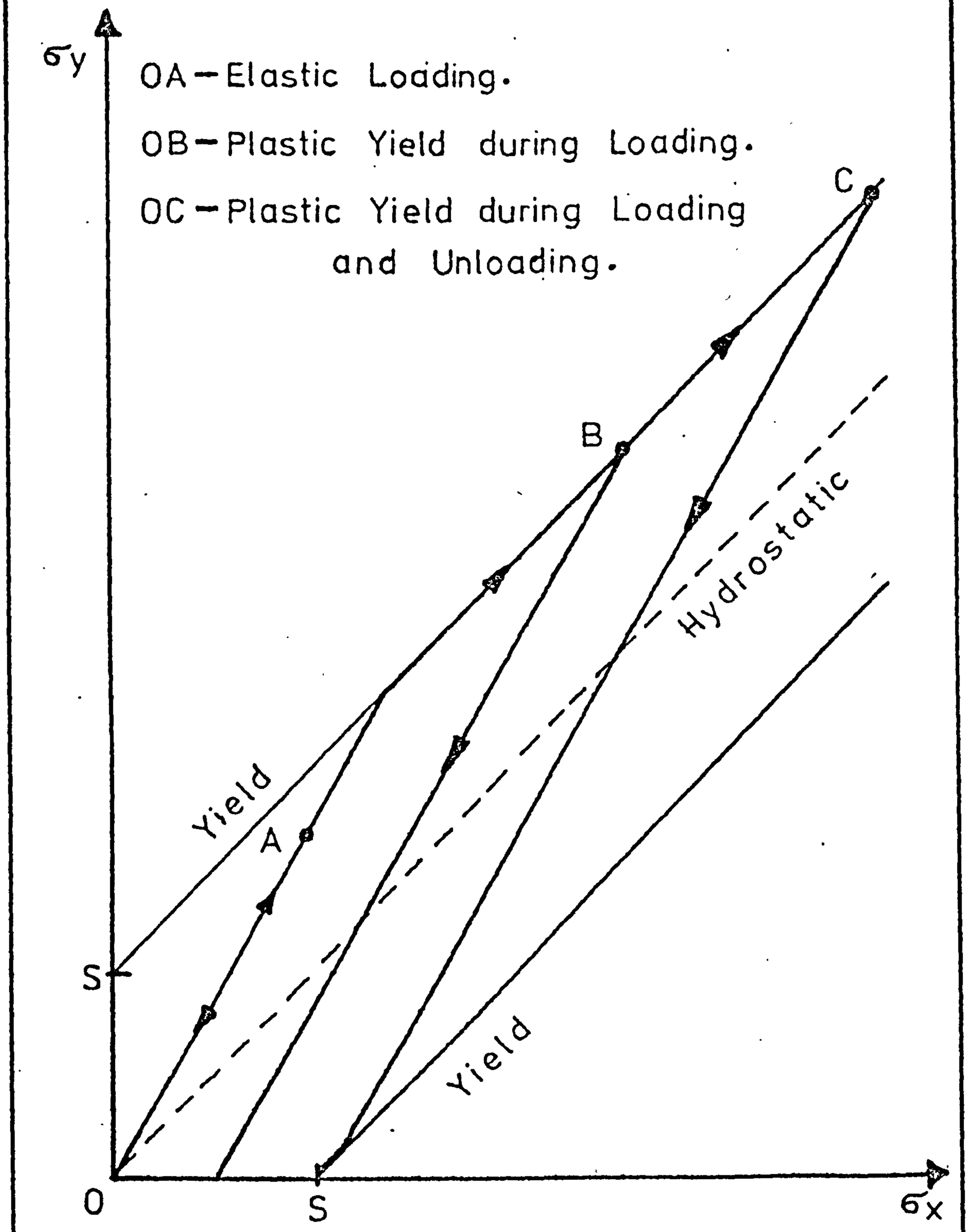

FIG. 1.3.1 SOME RELATIONSHIPS OF THE PRIMITIVE STRESSES IN THE EARTH'S CRUST.

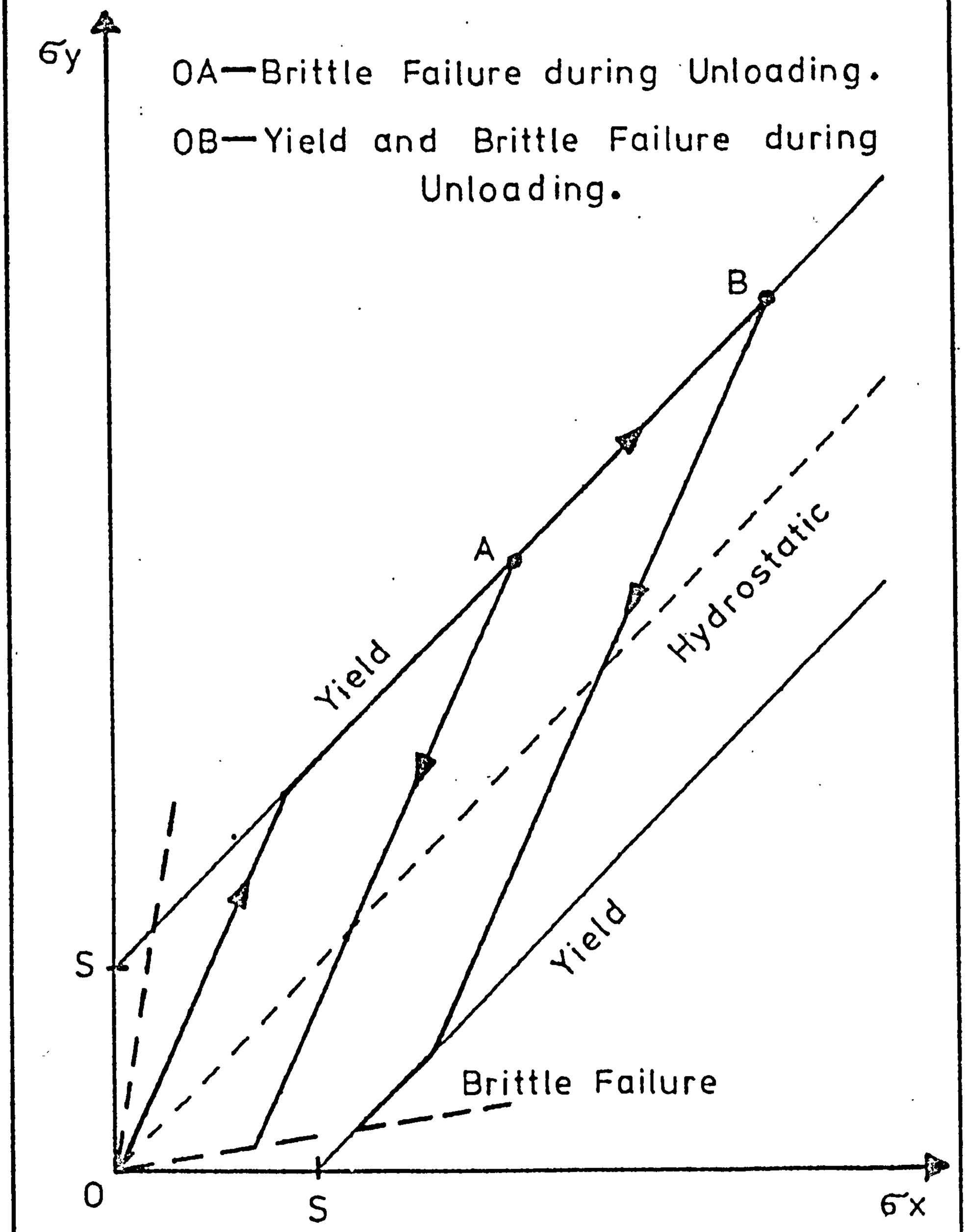

FIG. 1.3.2 THE EFFECT OF BRITTLE FAILURE ON THE PRIMITIVE STRESSES.

can be either due to local deformations in the earth's crust, 'tectonic' stresses, or 'locked-in' stresses associated with previous rock history, 'residual' stresses. Evidence of such stresses are overwhelming, and some typical examples have been given by Coates[22].

It appears, therefore, that although vertical and lateral stresses both increase with depth, their relationship can not be determined, accurately, and values predicted by the plain strain theory of equations (1.3.2) are on the conservative side. Since for most rocks, the Poisson's ratio is about 0.25, equations suggest that the horizontal stresses will be about one third of the vertical. In most probability, however, the lateral stresses will be unequal, ranging between 0.6 - 0.8 the vertical stress, which in turn will be higher than predicted by the gravity stress.

Heim's hydrostatic theory, however, is still widely accepted; Everling[23] suggested that such conditions exist in the Carboniferous Sediments of Central Europe. He pointed out that equations (1.3.2) do not apply in the case of strained rocks, under temporarily tectonic stresses.

When an excavation is made underground, the equilibrium of the primitive stresses is disturbed, and induced stresses will result, due to the stress redistribution. Induced stresses will depend on a number of factors, such as the

mechanical behaviour of the strata, the type of excavation and the primitive stress system.

This subsequent state of stress is three-dimensional and highly directional, producing compressive and tensile stress concentrations (abutments), at various localities. The magnitude of these concentrations could be several times that of the primitive stress, previously acting. It is essential, therefore, to determine the magnitude and position of such concentrations, by analysing the distribution of the induced stresses. However, in order to accomplish this, a theory of rock behaviour must be assumed which is capable of explaining the response of the rock, under certain loading conditions.

1.4 THE MECHANICAL BEHAVIOUR OF ROCK

Whatever theory of ground behaviour is adopted to study an underground situation, some basic assumptions have to be made. These assumptions will reduce the actual problem to an idealized prototype, which can then be treated accurately by theory or experiment[24,25].

The majority of analyses of stress distribution problems in rock, are based on the theory of 'perfect' elasticity. The main advantage of the theory is simplicity and in addition, solutions can be deduced by several well established theoretical or experimental methods.

If the response of the rock, under a certain stress field is to be within the bounds of the theory of perfect elasticity, four main rock characteristics must be assumed: Linearity (Linear stress-strain relationship), Perfect Elasticity (full strain recovery upon removal of stress), Homogeneity (continuous distribution of matter), and Isotropy (no-directional variance of the elastic properties). The two former assumptions refer to the mechanical behaviour of the rock under stress, whereas the latter ones, to its geological structure.

Although these assumptions can only be rough approximations, leading to an ideal prototype situation, for quasi- or semi-elastic rocks (Linear or curvi-linear stress-strain relationships) such behaviour can be assumed within reason. The design of simple structures in such rocks, as openings of various shapes, has been realized, therefore, with success, by employing well-known principles of elasticity, as the theory of plates and beams[A.8].

Investigations into more complicated lay-outs, however, present a much more difficult problem, due to the nature and number of the parameters involved. The design of such structures has been, traditionally, based on empirical knowledge and on information derived from rather qualitative theories of ground behaviour such as the pressure arch theory[25,A.10].

Nevertheless, attempts have been made to expand the theory of elasticity, so that the response of the rock, around such excavations, can be explained. Salamon[26] presented a method of elastic analysis of displacements and stresses, induced by the mining of seam or reef deposits. The theory was in good agreement with underground measurements in the vicinity of Longwall excavations in a South African gold mine[27]; it was concluded therefore, that the design of such excavations in this case can be carried out by utilizing the displacements and stresses predicted by the elastic theory. However, it must be emphasized, that the rocks in the vicinity of the South African, deep gold mines, present the best approximation of the four assumptions of the theory of elasticity. Quartzite, for example, shows less than 5% hysteresis in the stress-strain relationship with no evidence of anisotropic behaviour. Also due to the depth of mining, the condition of an infinite elastic mass is applied. This can explain why other elastic treatments are of less quantitative value, when applied, for example to the design of Longwall coal faces in Britain[28,29], where the mechanical and geological properties of rock are less favourable.

For most rocks, even when they exhibit a reasonable degree of elasticity, the assumptions of homogeneity and isotropy are, rarely, realistic. Anisotropy, for example,

could have a pronounced impact in the stress distribution. Habib[2] suggested that the Young's Modulus 'in-situ' could be as much as five times less than the value determined by laboratory testing, in anisotropic strata. He attributed this to the localised stress concentration areas, produced by the anisotropy, which can add large amounts of strain, and as a result, the measured strain values 'in-situ', are by far in excess of the ones due to the theoretical vertical stress. Clutterbuck[30], also carried out an extensive theoretical and experimental study to determine the effect of the elastic constants on the stress distribution. She concluded that variations of the Young's modulus can greatly influence the stress system, whereas the effect of the Poisson's ratio is less significant. As a result a system of rock layers, with different elastic properties, will produce a non-symmetrical stress distribution.

The theoretical elastic treatment of ground behaviour mentioned before, can be adopted to include the case of transverse isotropy[26,31,32]. However, such an analysis can be extremely complex and this problem is best suited for the modern 'Finite Element'[A.11] method of stress analysis, or for experimental treatment.

There are, however, some rocks for which the assumption of elasticity is no longer acceptable. Such rocks, loosely

termed here as 'inelastic', can only show some degree of linearity at very low stress levels, under particularly short loading periods. However, beyond this point inelastic behaviour will commence which can be described by a residual strain upon stress removal (plastic behaviour), or by a variable strain under constant applied stress (viscous behaviour), or by a combination of the two.

The result of inelastic behaviour could be the deflection of the stress concentration zone deeper inside the rock, with the stress peak decreasing in magnitude, but spreading over a larger region. Such behaviour is most important when designing underground openings and pillars[33,34,35].

The inelastic response under a stress field can be examined by various theories which, in general, are more complex and less flexible than the theory of elasticity. Although such theories are basically evolved for materials other than rock, nevertheless, they have been used in the field of rock mechanics. However, the usual procedure is to treat an inelastic problem, as the first approximation, by the theory of elasticity. The departure of the elastic solution can then be analysed, by assuming the appropriate inelastic theory. In this respect, therefore, the elastic and inelastic theories of rock behaviour will supplement, and not contradict each other.

It was stated before, that short loading periods can restrict rock behaviour within elasticity, whereas, longer periods have a tendency to encourage inelastic response. It is obvious, therefore, that both loading rate and duration of loading, will have a marked impact on the manner which the ground behaves. This can be clearly demonstrated from the results of small scale laboratory static and dynamic tests[6,7]. The overall stress field underground will include not only static, but dynamic components also. Dynamic stresses will certainly result, for example, from blasting rock bursts and even microseismic activity within certain rocks (especially coarse, inhomogeneous, anisotropic), under high stresses[36]. These factors usually ignored by the traditional theoretical treatment, must also be considered by the designer, since their influence on stress distribution of certain excavations can not longer be ignored[37].

Finally, most mathematical and experimental methods of stress analysis are restricted to two-dimensions. Mining configurations, however, represent a three-dimensional stress problem, and ideally should be treated as such. Three-dimensional stress analysis, by theory or experiment, is an extremely complex procedure, and as a result, has only been applied to a limited number of problems, and in particular, to underground cavities[16].

Two-dimensional analyses of mining problems are often considered sufficient by some investigators since the solutions are expected to be on the conservative side. However, this approach could never accurately determine the stress distribution, particularly when the three-dimensional problem is greatly affected by the elastic constants, which are of little significance in two-dimensions, where the stress distribution is the same for all isotropic materials. This is clearly demonstrated by comparing, for example, the elastic solutions for a circular and spherical underground opening[B.10]. Also, when the design is based on such conservative solutions, there is always the danger of over-design, a rather expensive practice. It is important, therefore, wherever possible, to try to analyse mining problems with respect to the three axes. Such an attempt was made by the author, and is presented in later chapters.

1.5 METHODS OF ANALYSIS

The complete study of a rock mechanics problem can be carried out by considering a number of stages, in accordance to the assumptions made. Each stage can then be treated individually by an appropriate stress analysis technique, in order to retrieve maximum information. Design criteria, therefore, can thus be established by viewing all the available information collectively. This procedure is illustrated

schematically, in the flow chart of Figure 1.5.1.

Information derived from the actual problem is generally due to observation. By making no assumptions regarding the stress field or the behaviour of the rock, only simple 'in-situ' methods can be employed, mainly restricted to linear measurements (e.g. roof to floor convergency recordings, or surface measurements of subsidence).

A detailed 'in-situ' investigation can be carried out, therefore, by making a number of basic assumptions, leading to a realistic prototype situation. Such assumptions will describe, for example, the state of stress underground, the degree of elasticity of the rock under investigation, the ability of rock to bond with a foreign inclusion, and as a result, 'in-situ' techniques based on such considerations can be undertaken.

Exploration by 'in-situ' methods is expensive in time and money, and has often proved inconclusive. On the other hand, a complete, accurate and inexpensive analysis is possible, by the well established techniques of theoretical and experimental stress analysis. However, the adoption of the latter methods necessitates further assumptions to be made, leading to the case of an ideal prototype. These assumptions are required to define additional parameters to the previous ones, as geology of strata, loading conditions,

geometry of excavation, the behaviour of wastes and others.

The idealised problem can be subsequently treated by theoretical or experimental methods, the choice depending on the actual complexity of the problem. Theoretical methods, mathematical or analytical, are mainly adopted for simple problems, and have been discussed in the previous section. On the other hand, experimental analysis can be employed by using large or small scale simulated models, which is capable of dealing with more complex configurations. With today's advancement of experimental stress analysis, the range of materials and techniques available is quite extensive, and an excellent account of these is given in reference 38.

It is easily seen from this procedure, that as one advances from one stage to the next, the amount of information and the accuracy of the results obtained from each analysis, greatly increase. On the contrary, however, the degree of realism exhibited by each model is progressively deteriorating. It is concluded, therefore, that the information retrieved, in both qualitative and quantitative terms, is inversely proportional to the reality of the situation.

Finally, some questions arise regarding the sequence of analysis. Should one follow each step as shown in the Figure 1.5.1, or consider the opposite order? And, are all these stages necessary for a solution or some of them can be

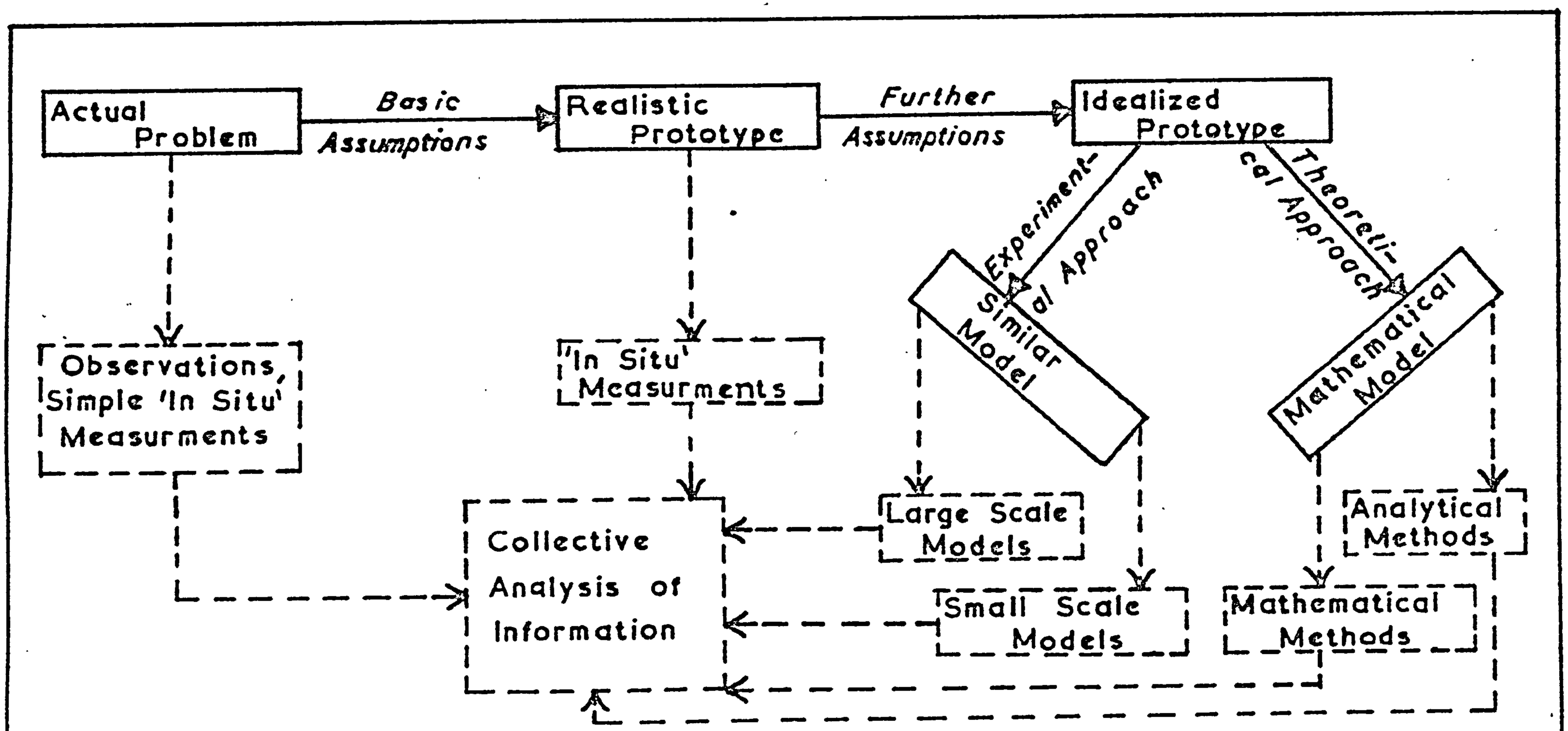

FIG. 1.5.1 FLOW CHART OF A ROCK MECHANICS PROBLEM ANALYSIS.

by-passed? In most cases, the initial step is to build a theory and check its validity by small scale models, assuming an ideal prototype. Thereafter, observations and 'in-situ' measurements are carried out, and an attempt is made to explain the latter in terms of the evolved theory. In other problems, however, observations and 'in-situ' measurements are the initial data. The object in this case, therefore, is to try to establish a theory, capable of explaining these conditions. Having approximated such theory, a further refinement is possible, by assuming the idealised prototype.

It appears that the deciding factor of the sequence of an analysis, is the nature of the problem itself. In the South African gold fields, for example, where mining conditions are perfectly suited for elastic treatment, the design is primarily based on the theoretical approach. Since initial 'in-situ' measurements have been found to be in agreement with the theoretical solutions[27], it was concluded that except for certain circumstances, such measurements are no longer necessary for the design of subsequent problems[39]. In coal mining, however, where the mining conditions can not be accurately simulated by mathematical or experimental models, it is preferable to base the analysis on 'in-situ' information and large scale model studies. The development of a theory can then be attempted, peripheral to these results[40,41,42,43,44].

Nevertheless, different approaches for the same problem are often adopted by investigators. At the Public Inquiry concerning the extraction of potash in Yorkshire, for example, Bryan[45] wrote: "Whereas some of the experts 'relied on extensive laboratory and 'in-situ' investigations to produce a behavioural theory applicable to a specific set of conditions' others presented 'a theoretical approach, backed by laboratory and 'in-situ' testing".

1.6 THE SCIENTIFIC AND INTUITIVE PHASES OF ROCK DESIGN

It was stated in the introduction that although rock has centuries of history as a structural material, the science of rock mechanics is only a few decades old. A basic question, therefore, arises; is the scientific analysis really necessary when engineers survived without it for generations?

The prolonged success of rock design by a non-scientific approach must, without doubt, be attributed to the ingenuity, adaptability and observation power of the man 'on the spot', the practical engineer. These qualities led to an accumulative emperical knowledge of a particular problem, which, in turn, often developed to an intuitive design philosophy. It was this intuition that, in most cases, would dictate which was a recommended or avoidable engineering practice.

A scientific examination of a rock mechanics problem is

possible nowadays, by employing various stress analysis techniques. However, their common feature is the number of assumptions necessary for a complete analysis. Such assumptions, therefore, can not be expected to discribe the behaviour of the rock accurately and as a result, design considerations, thus established, are not always successful when applied to the actual problem. It is of no surprise, therefore, to find that many structures, even today, are basically designed on emperical considerations.

In today's large scale mechanised engineering operations, economic factors are commonly the primary design considerations. Empirical design, therefore, is in general an inferior engineering practice, due to its expensive tendency of overdesign. Further, empirical knowledge of a particular problem, has often been misused and even abused. Empirical formulae have in many instances taken for granted, without realizing that they are only applicable for identical problems, under identical conditions. The author, therefore, feels that the greatest disadvantage of empirical design is that the solutions thus obtained, do not necessarily imply a complete understanding of the problem.

The answer to the question posed at the beginning of this section, therefore, is evidently a positive one. Scientific methodology, however idealistic may be, will always enable

the investigator to appreciate fully, the problem under consideration. Empirical knowledge and intuition, in this case therefore, are not the singular design criteria, but important aids towards consolidating the scientific findings.

1.7. CONCLUSIONS

(i) When undertaking an underground examination, a knowledge of the mechanical properties of rocks is essential. Such knowledge must be extended to include details of geological structural features, and their influence on the mechanical properties.

(ii) The mechanical properties of rocks can be estimated by small scale laboratory or large scale 'in-situ' tests. In general, laboratory tests are more accurate, inexpensive and flexible than 'in-situ' tests. The accuracy of the results will greatly depend on the testing procedure and various authorities have suggested that it is within 25%.

(iii) The primitive state of stress underground can be calculated by either assuming plane strain or hydrostatic conditions, although other solutions have occasionally been used. Underground measurements of primitive stresses suggest that the vertical stress is rather greater than predicted by the overburden pressure, whereas the lateral stresses are, in all probability, unequal

ranging from 0.6-0.8 the vertical stress. However, the results of such tests are often inconsistent or inconclusive.

(iv) The presence of other stresses than those due to gravity, has been demonstrated in many cases. The additional stresses can be of either tectonic or residual origin, and will greatly influence the 'in-situ' state of stress. Lateral stresses more than eight times the vertical stress can result from these conditions.

(v) When an excavation is made, the stress equilibrium is disturbed and induced stresses will result. The subsequent state of stress is three-dimensional and highly directional, producing stress concentrations at various localities. It is essential, therefore, to determine the magnitude and position of these concentrations when designing underground excavations.

(vi) Although at shallow depths there is a small degree of elasticity, and at great depth, stress concentrations can load the rocks beyond their elastic limit, it is customary to treat rocks by the theory of elasticity. Methods of solution, theoretical or experimental, can be extended to include anisotropy, but little work has been done to establish three-dimensional solutions. The latter can have a large influence on the stress distribution due to their dependency on the elastic constants. Dynamic stress

components usually ignored by the analyses, must also be considered in the design of some excavation.

(vii) When a rock is characterised by inelastic behaviour, the elastic solution can only serve as a first approximation. Such solution is, in general, on the conservative side, becoming even more conservative when two-dimensional. Its deviation, however, can be estimated by adopting an appropriate inelastic theory. When designing on such rocks, therefore, the most important factor is the expected life of the excavation.

(viii) The complete analysis of a rock-mechanics problem can be approached in stages in accordance with the assumptions made. These stages will range from the actual problem, via a realistic prototype, to an idealised prototype. By advancing through these stages, better methods of analysis can be employed, yielding maximum information, but unfortunately, the degree of realism of the situation becomes progressively worse.

(ix) The sequence and necessity of each individual stage must be dictated by the nature of the problem, under investigation. However, often investigators follow different approaches for the same problem.

(x) Although intuitive design, based on empirical knowledge, has been used with success for the design of many

structures, it can be inefficient and expensive and is often accompanied by a lack of understanding the problem under investigation. Scientific analysis, on the other hand, however idealistic, will allow a thorough examination, considering all the parameters involved, and if not else, will at least enable the designer to appreciate the problem fully. Therefore, only by properly blending scientific and empirical knowledge so that they supplement and not contradict each other, accurate design criteria can be established.

CHAPTER II

A REVIEW OF THE CURRENT KNOWLEDGE ON PILLAR BEHAVIOUR AND DESIGN CONSIDERATIONS

CHAPTER II

A REVIEW OF THE CURRENT KNOWLEDGE ON PILLAR BEHAVIOUR AND DESIGN CONSIDERATIONS

2.1 INTRODUCTION

Pillars are blocks of unmined rock left between two or more underground openings, and consitute the oldest and most common means of natural support of a mine section. Their size and shape will vary, therefore, in accordance with the adopted method of working and the purpose they are called upon to fulfil.

A pillar is characterised by its three dimensions, height, length and width, the two latter ones being the longest and shortest plan dimensions, respectively. If economic and safety objectives are to be met successfully, therefore, when designing a mine layout, the smallest effective width of pillar must be used.

The determination of such width in most cases is an extremely difficult task, due to the number and nature of the parameters involved. As a result, pillar width is rather approximated from empirical knowledge, than calculated from a scientific analysis.

This Chapter, therefore, presents a review of the current knowledge on the behaviour of pillars, with particular reference to the design considerations usually adopted. The author's investigation on pillars by 'in-situ' and laboratory

experimental stress analysis techniques, will be given in later chapters.

2.2 STRESS DISTRIBUTION OF PILLARS

The stress distribution in pillars is discussed by broadly dividing pillars into two categories:

(a) small pillars typical to the room-pillar method of mining, and

(b) large pillars such as the ones encountered in longwall mining.

(a) The Stress Distribution in Small Pillars

The first analytical expression for predicting pillar loading was suggested by Duvall[46], and is known as the 'Tributary Area Theory'. This is a simple theory, assuming that the entire weight of the ground overlying the tributary area (A_t), is supported by the pillar. Therefore, the average pillar stress, '$\bar{\sigma}_p$' can be expressed in two-dimensions, as follows:

$$\bar{\sigma}_p = \sigma_y \frac{A_t}{A_p} = \frac{\sigma_y}{1-R} = \frac{\gamma h}{1-R} \qquad (2.2.1)$$

where σ_y = Vertical stress

A_p = Pillar area

A_t = Tributary area

$R = \frac{A_t - A_p}{A_t}$ = Extraction ratio

γ = Specific weight of the strata

h = Depth of mining

The theory is as shown in Figure 2.2.1.

This simple approach ignores, among other factors, the variation of the mechanical properties of roof-floor-pillar materials, geological structural features, and perhaps most important of all, the height of the pillars. However, even allowing for such omissions, the basic assumptions of the theory that the pillar supports an area half the room, and that the stress is uniformly distributed over the area of the pillar, are unrealistic and incorrect.

In an attempt to obtain more information about pillar loading, Duvall carried out extensive photo-elastic studies[46,47]. His results demonstrated that:

(i) The pillar is not loaded uniformly as the theory suggests , but maximum stresses are present, at the edge of the pillar as well as at the corners between pillar and roof or floor. The magnitude of the stress concentrations or abutments will depend upon the type of the stress field, and the geometrical shape of the opening.

(ii) Openings can be treated as single if they are at least one diameter apart.

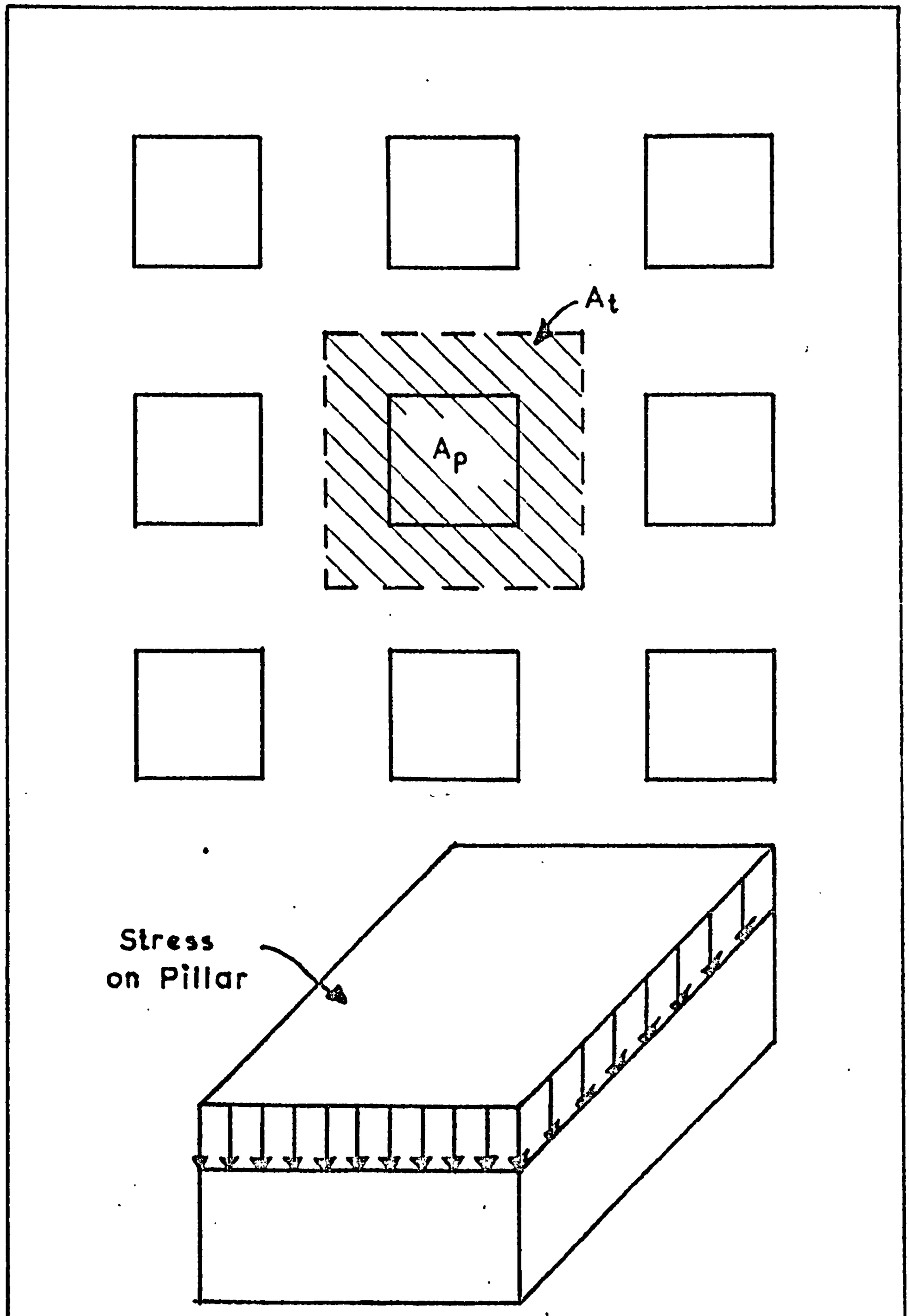

FIG. 2.2.1 THE TRIBUTARY AREA THEORY.

(iii) For multiple openings, as the opening to pillar width increases, the maximum stress concentration tends towards the average stress concentration.

(iv) For equal height pillars, the centre pillar should be under more stress than the peripheral ones.

In conclusion, Duvall suggested that the maximum stress concentration can be approximated by an empirical formula, which is a function of the shape of opening and percentage recovery:

$$K = S + 0.09 \left[\left(\frac{100}{100-R} \right)^2 - 1 \right] \qquad (2.2.2)$$

where

K = Maximum stress concentration of the pillar, and

S = Maximum stress concentration of the single opening.

However, the above results were derived for ideally elastic bodies. In practice differential loading is most probable, due to localised yielding which could relieve a portion of a pillar, thus increasing the stress on another. Additionally, the opening will be surrounded by a fractured zone of rock, which in conjunction with localised yielding tendencies, will move the maximum stress concentration from the boundary

to some point in the interior of the pillar. Holland[48], for example, suggested that for coal pillars having a fractured zone of 1-3 times the seam thickness, the stress concentration peak can be expected at a distance 1-8 times the seam thickness inside the boundary. Hobbs[41], also carried out an extensive investigation of broken rock under triaxial compression. Some of his results are shown in Figure 2.2.2., and clearly demonstrate that fracture stress, yield stress, fracture strain, yield strain and Young's modulus are dependent upon the magnitude of the applied confining pressure. As an example, for a circural roadway of 1.83m radius, driven in either broken Hucknall shale or Bilsthorpe mudstone and subjected to applied pressures of 13.8 and 27.6MN/m^2, the maximum stress concentrations are 5.9m to 8.0m for the mudstone and 3.5m to 4.5m for the shale. The same roadway when driven in solid rock will show maximum concentrations at 4.4m for the mudstone and 1.8 for the shale, at 13.8MN/m^2, rising to 7.5m and 2.4m respectively, at a stress level of 27.6MN/m^2.

Streart[49] visualised a conical stress distribution on a developed area, circular in plan. The maximum stress concentration, therefore,will be acting on the centre pillars. Further, he suggested that the maximum stress

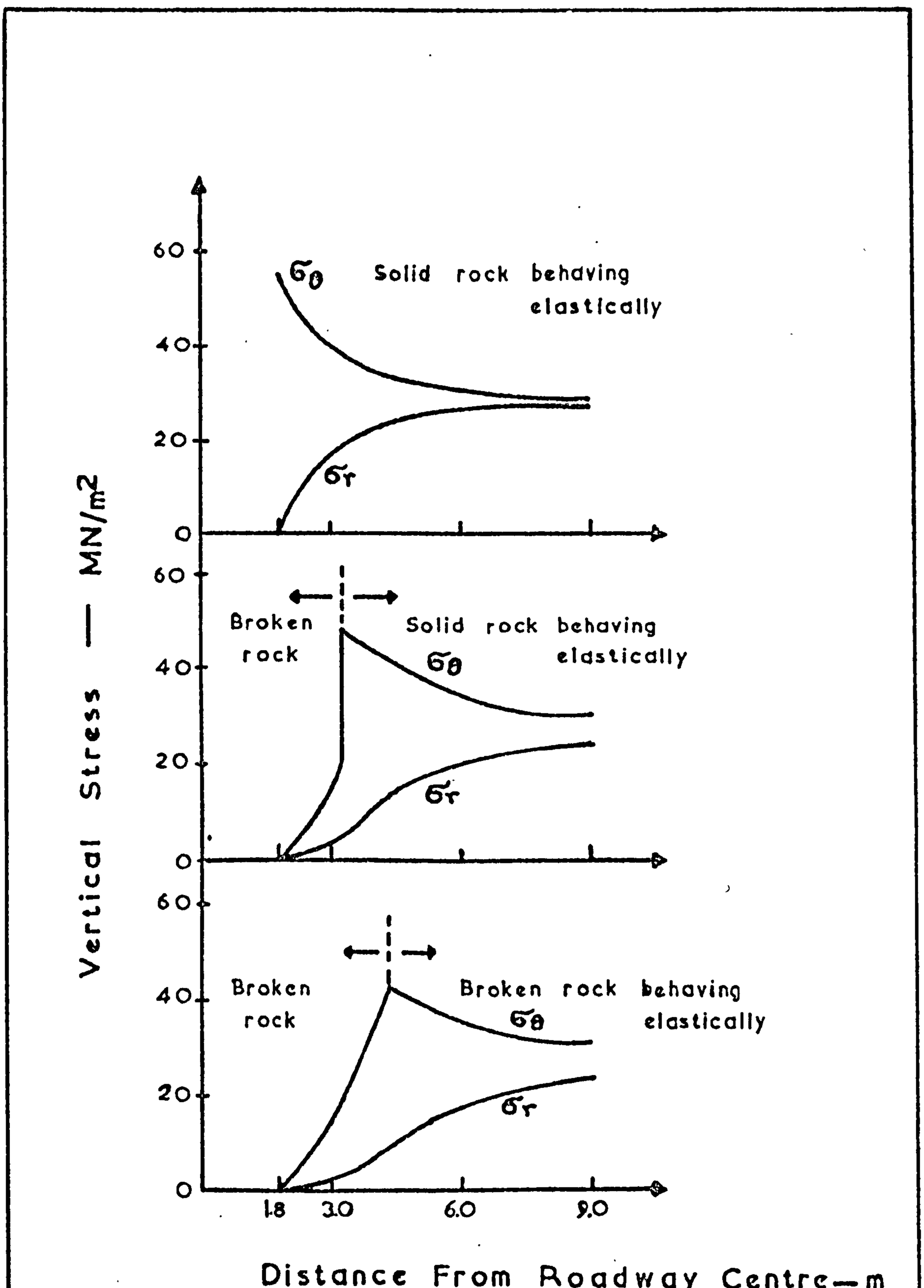

FIG. 2.2.2 STRESS DISTRIBUTION ON A HYPOTHETICAL ROADWAY.

will be attained when the radius of the stoping area was equal to the working depth, divided by the ratio of the mining area to that of the pillars. Although these results were not substantiated by any theoretical or experimental investigation, and were only due to observation, nevertheless, they did not contradict Duvall's theories.

Coates[50,51], attempted a more comprehensive analysis of pillar loading, by solving the statically indeterminant net deflection of the walls, resulting due to mining. He suggested that the net pillar deflection will be the algebraic sum of the following:

(i) The deflection of the potential pillar rock, due to the applied stress field (D_i).

(ii) The reverse deflection of the wall due to the increased stress on the pillar (D_2).

(iii) The deflection created by the release of confinement on the pillar, due to mining (D_3).

(iv) The local penetration of the pillars, resulting from the stress concentration on the walls.

These deflections are schematically shown, in the stated order, in Figure 2.2.3.

Since the net deflection is a measure of the increase in pillar stress, due to mining by establishing expressions

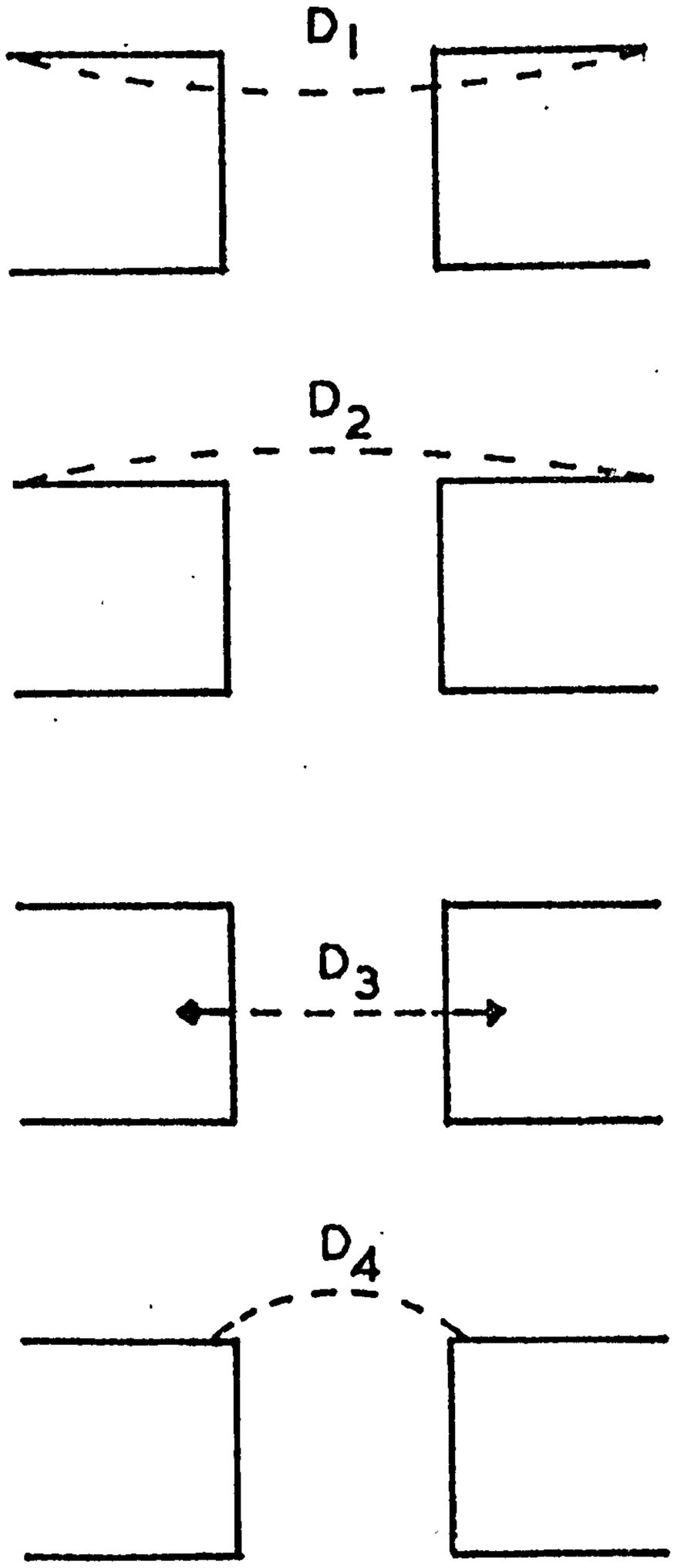

FIG. 2.2.3 COMPONENTS OF WALL DEFLE-CTION DUE TO MINING.

for the deflections, Coates was able to produce formulae covering the cases of long, deep mining zones as well as shallow ones, in an infinite elastic medium, under conditions of plane stress or plane strain. The hypothesis was, thereafter, thoroughly tested by an extensive experimental program[51], and subsequently modified, to increase its accuracy. The relationship, therefore, in plane strain, after the empirical adjustment, was given as follows:

$$\frac{\Delta\sigma_p}{S_o} = \frac{2R(1 - x/5 + h) - Kn(1 - w + w_p n)}{hn + 1.8(1-R)(1+1/N)(1+h/(1-x/5)) + 2Rb(1-w)/\pi} \qquad (2.2.3)$$

where $\Delta\sigma_p$ = Increase in pillar stress due to mining

R = Extraction ratio

S_o = Vertical applied stress

S_t = Lateral applied stress

$K = S_t/S_o$

H = Pillar height

l = Span of the mining zone

h = H/l

E,ν = Mechanical properties of wall rock

E_p, ν_p = Mechanical properties of pillar rock

x' = Linear co-ordinate in the x-direction

x = x'/l

N = Number of pillars

B = Width of the pillar

$b = B/l$

$w = \nu/(1-\nu)$

$w_p = \nu_p(1-\nu_p)$

$M = E/(1-\nu^2)$

$M_p = E/(1-\nu_p^2)$

$n = M/M_p$

The assumption of the pillars being long, simply enables the analysis to be carried out in plane strain.

From a number of field tests, Coates suggested that better predictions of pillar loading are possible by this approach, than by the tributary area theory[52]. He also demonstrated that the theory can be adopted to deal with the problem of inclined workings[53]. However, pillar loading is a three-dimensional problem, and these principles were further extended, with the aid of an electrical analogue simulation technique to describe such loading, with considerable success[54,55].

Coates' semi-analytical solution includes a number of parameters, previously ignored by the tributary area theory, as geometrical and mechanical properties of strata, and nature of the applied stress field. Nevertheless, it is worth noting that when $K = o$, $x = o$, and $h \longrightarrow o$, $b \longrightarrow o$, equation 2.2.3 is reduced to an expression

similar to the one suggested by the tributary area theory. Salamon et al[56], also treated the problem of small pillars by a mathematical analysis. It was assumed, in this case, that the change of vertical stress over the pillar area is proportional to the compression of the pillar with the horizontal constraining stresses being neglected. Two cases were examined, the isotropic and transversely isotropic elastic medium. From a number of underground measurements, it was concluded that the mathematical treatment offered a good description of the observed dispacements.

Recently, Stacey[57] suggested a somewhat different approach to the problem by using the finite element method of stress analysis. The method is based on representing a continuous medium by a network of elements, usually of triangular shape, jointed together at their vertices, the nodal points. As a result, if a body is subdivided to an extremely large number of elements, a large digital computer is required and the computing operation can become expensive. In general, therefore the method is limited to two-dimensions. Stacey, however, demonstrated that a three-dimensional stress analysis on small pillars is feasible by the finite element technique. For such investigation, a solution can be obtained by superimposing the results of, at least, two orthogonal plane strain

solutions or, alternatively, by choosing a three-dimensional element. The latter method was adopted in this case, the element being hexahedral.

Figure 2.2.4 shows the stress distribution across a pillar, as predicted by various theories, as well as the results of underground measurements made by Van Heerden[58]. The results were derived for a South African Colliery with room width of 6.4m and pillar width to height ratio of 6.4/2.7. Details of the mechanical properties of the pillar and surrounding rock are given elsewhere[57]. Some important figures are given in the table below:

MAXIMUM STRESS CONS.	AVERAGE STRESS CONS.	METHOD
4.3	3.6	3-D finite element[57]
6.0	3.6	Theoretical analysis, Salamon et al[56]
3.1	3.0	Coates' Hypothesis, equation (2.2.3)
4.0	4.0	Tributary theory, equation (2.2.1)
5.3	-	Duvall's formula, equation (2.2.2)
10.0	4.0	'In-situ' tests, after Van Heerden[58]

From these results the following remarks can be made:

(i) Although Salamon's theoretical analysis and the finite element investigation are in close agreement, for distances more than 1m inside the pillar, some

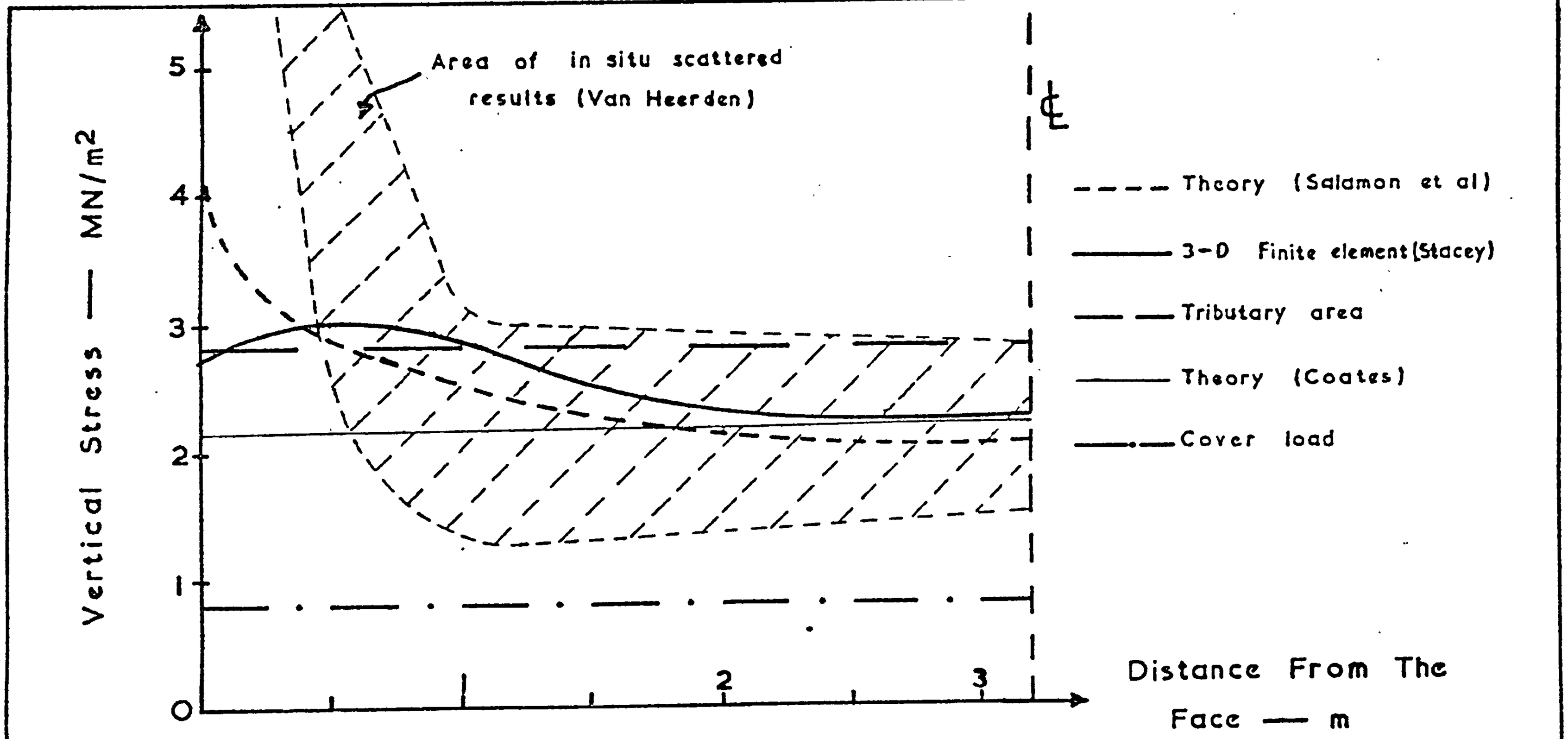

FIG. 2.2.4 VERTICAL STRESS DISTRIBUTION ALONG PILLAR CENTRE-LINE.

deviation exists at the near boundary region. Higher concentrations are predicted by the theory, the maximum acting at the boundary, whereas, concentrations from the finite element analysis are lower, the maximum acting at some point in the pillar's interior (0.5m). It is claimed that the latter distribution has been substantiated by photo-elastic results[59]. However, it is worth noting, that the average stress concentration predicted by both methods is nearly identical (3.6)

(ii) Since conditions of uniaxial loading were assumed, Coates' hypothesis delineated to a nearly straight line, as previously discussed, predicting smaller stresses than the tributary area theory. However, the average stress concentration found by the earlier methods is nearly straddling the one reduced by Coates' theory.

(iii) The maximum stress concentration calculated from Duvall's empirical formula, is near the value given by Salamon's analysis. In general, however, if one considers the diverse evolution of all these methods, and the parameters involved in each individual analysis, the range of the maximum stress concentrations is, surprisingly, good.

(iv) Although the underground results show a degree of scatter, they are in agreement with the theoretical solutions, except near the pillar edge, where concentrations of

about ten were found. However, it is interesting to note that the average stress concentration, although a crude practice in this case due to the scatter of the results, is identical to the one predicted by the tributary area theory. This therefore, demonstrates clearly that regardless of its simplicity, the tributary area theory is an excellent indication of the average pillar stress.

(b) <u>The stress distribution in large pillars</u>

The loading theories discussed so far can only describe the behaviour of small pillars left inside a rather simple mining geometry, as in the case of the room and pillar method of mining. The distribution of the induced stress in larger pillars, as the ones met in the longwall system of mining, however, can not be approximated by such theories, due to the relative complexity of the mining layout.

The distribution of the stresses in the vicinity of a long wall face, is, qualitatively shown in Figure 2.2.5. A pressure arch exists in the longitudinal direction, the front abutment of which is acting just ahead of the face line. This distance has been measured by many investigators and was found to range between 1-18m, depending on the properties of the strata and seam

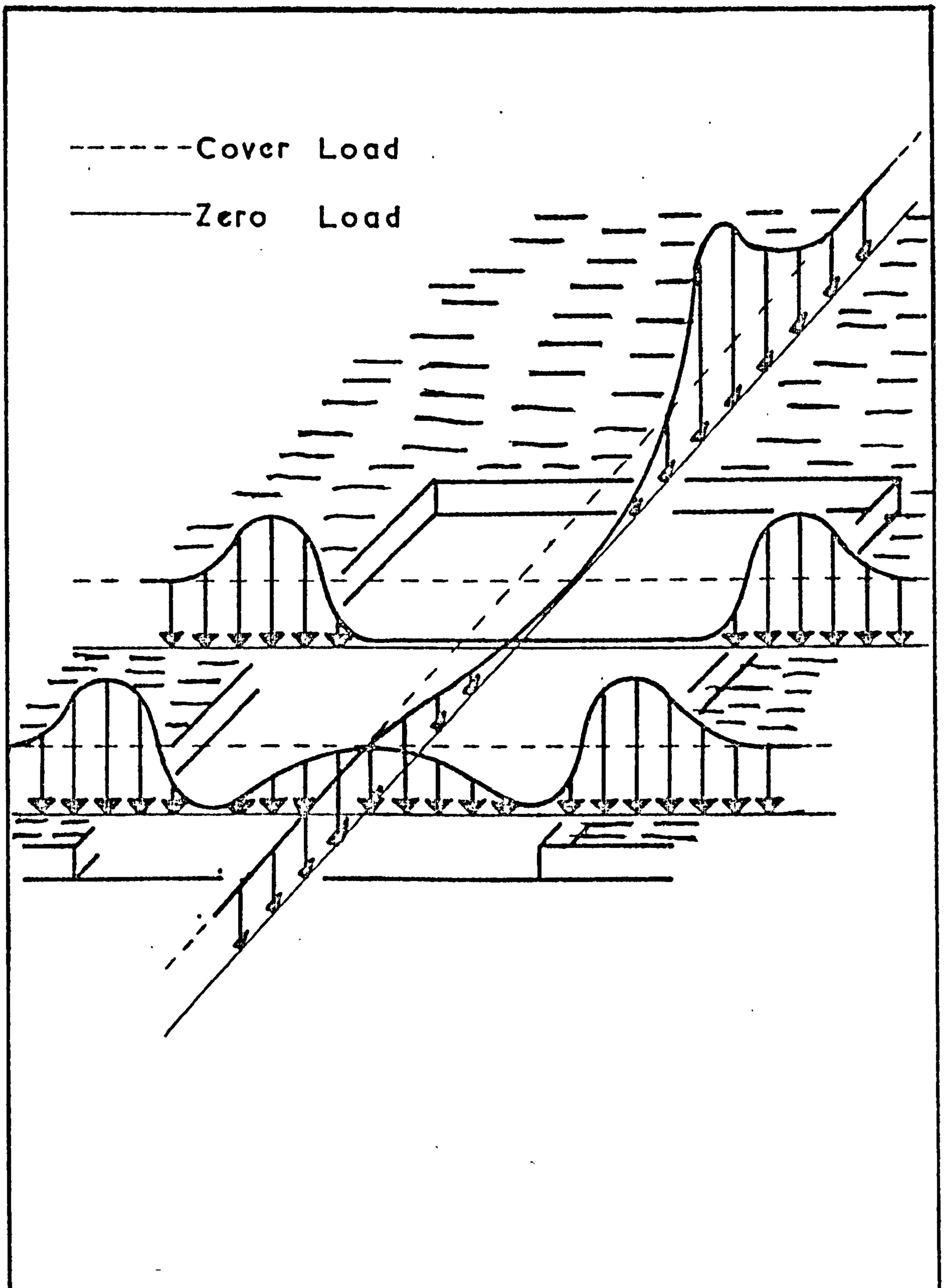

FIG. 2.2.5 STRESS DISTRIBUTION IN THE VICINITY OF A LONGWALL FACE.

thickness[60,61,62,63]. In general, however, it is expected to be about 1-3m ahead of the face. The value of this abutment was calculated theoretically by Van Iterson[64] and was found to be 1.7 times the cover load. 'In-situ' measurements, however, point towards a much higher value, several times that of the cover load[61,62]. The zone of influence of the induced stresses will extend to a considerable distance ahead of the face and activity at 100m from the face line is possible[60].

The existence of the back abutment of the pressure arch, acting on the waste, is a matter of dispute. Evans et al[65] found this abutment to be 3.4 times the cover load. They suggested that for depths of 66-99m the abutment will be located at 46.5-59.5m behind the face line. Depth is of prime importance in this case due to the time factor of subsidence. No such abutment was detected, however, from measurements of other investigators[61,66]. Extensive measurements in Germany over a period of several years, for example, showed a maximum back pressure of about 92% of the cover load[61]. The Working Party reporting on the design of mine layouts with reference to geological and geometrical factors[67], concluded that 'no evidence has been found of a rear abutment in the waste, and the damage caused to roadways about 100m back from the face, is

considered to be the result of the completion of compaction of the packs, which can cause damage to roof and floor'.

British investigators have suggested that the width of the maximum pressure arch (i.e. the distance between abutments), is a function of the depth of the workings[68,69].

Results of underground measurements have shown a nearly linear relationship, approximated by the following expression:

$$D = 18.3 + 0.15h \qquad (2.2.4)$$

where D, h are the width of the maximum pressure arch and depth, respectively, in metres. However, such a relationship is not substantiated from measurements in German collieries.

Phillips[70] suggested the presence of a transverse pressure arch, with abutments acting on the solid ribside and the waste. The location of the transverse rear abutment can be considered to be at a distance equal to the width of the maximum pressure arch, at that depth. The transverse arch is shown, for two sections, in Figure 2.2.5. At some distance behind the face where the critical dimensions have been reached, the cover load is re-established due to the full compaction of the waste. Whereas the longitudinal pressure arch is advancing with the face, the transverse

arch, at this stage is static, and represents the final state of stress.

When a large pillar is left behind the face, an abutment zone is created between the pillar and the face. Oram[71], fron an underground investigation on such pillar, found the abutment to be maximum at a face advance of 86.4m. The abutment was located at 6.1m from the pillar edge and its magnitude varied in accordance with the assumed stress field. However, it is probable that the horizontal stress increases from less than half the vertical, near the boundary, to hydrostatic stress, at the pillar's interior, and for such conditions, the maximum abutment will be over five times the cover load. The stress distribution, in this case was as shown in Figure 2.2.6. Jenkins[72] suggested that since surface subsidence observations are the best documented rock mechanics phenomena of a longwall configuration, it is possible, based on such information, to predict the distribution of stress underground. Assuming that the primitive stresses are re-established when full subsidence has been reached, then from subsidence information, such distance can be taken as 0.6 times the depth of working. Additionally, by assuming that the increase of loading is felt as far as 0.7 times the depth, from the ribside, then the overall simplified stress profile, neglecting the sharp stress

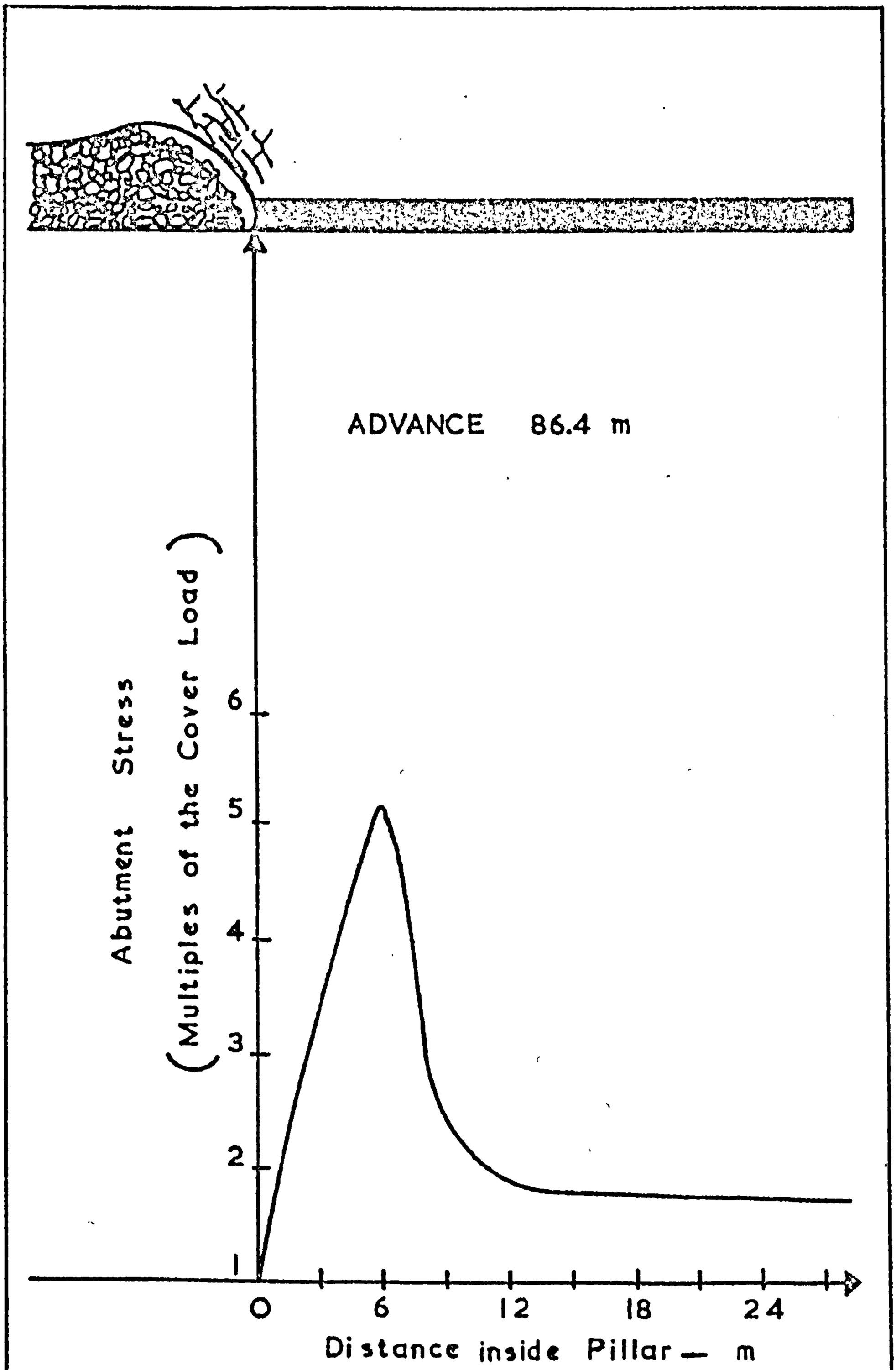

FIG. 2.2.6 STRESS DISTRIBUTION ON PILLAR.

fall at the edge, might be as shown in Figure 2.2.7. If a pillar, therefore, is considered, with extensive wastes on both sides, then, by superposition, the average pillar stress will be

$$\overline{\sigma}_p = \gamma h \left(1 + \frac{0.6h}{W}\right) \qquad (2.2.5)$$

where

γ = Specific weight of the strata

h = Depth of working

W = Width of pillar

King et al[73], also, estimated pillar loading from subsidence information, on a generalised basis, by considering the angle of draw, as shown in Figure 2.2.8. The average pillar load in this case is given by

$$\overline{\sigma}_p = \gamma\left(h + \frac{hl}{W} - \frac{l^2}{4W} \cot a\right) \qquad (2.2.6)$$

where

a = Angle of draw

l = Width of the panel.

Equation (2.2.6) is a more general equation and can be reduced to equation (2..2.5) by assuming a panel width of 1.2h and an angle of draw of 31^o.

Wilson[43], postulated a hypothesis regarding pillar loading by considering two distinct zones; a central inner core subjected to triaxial stress conditions, and a

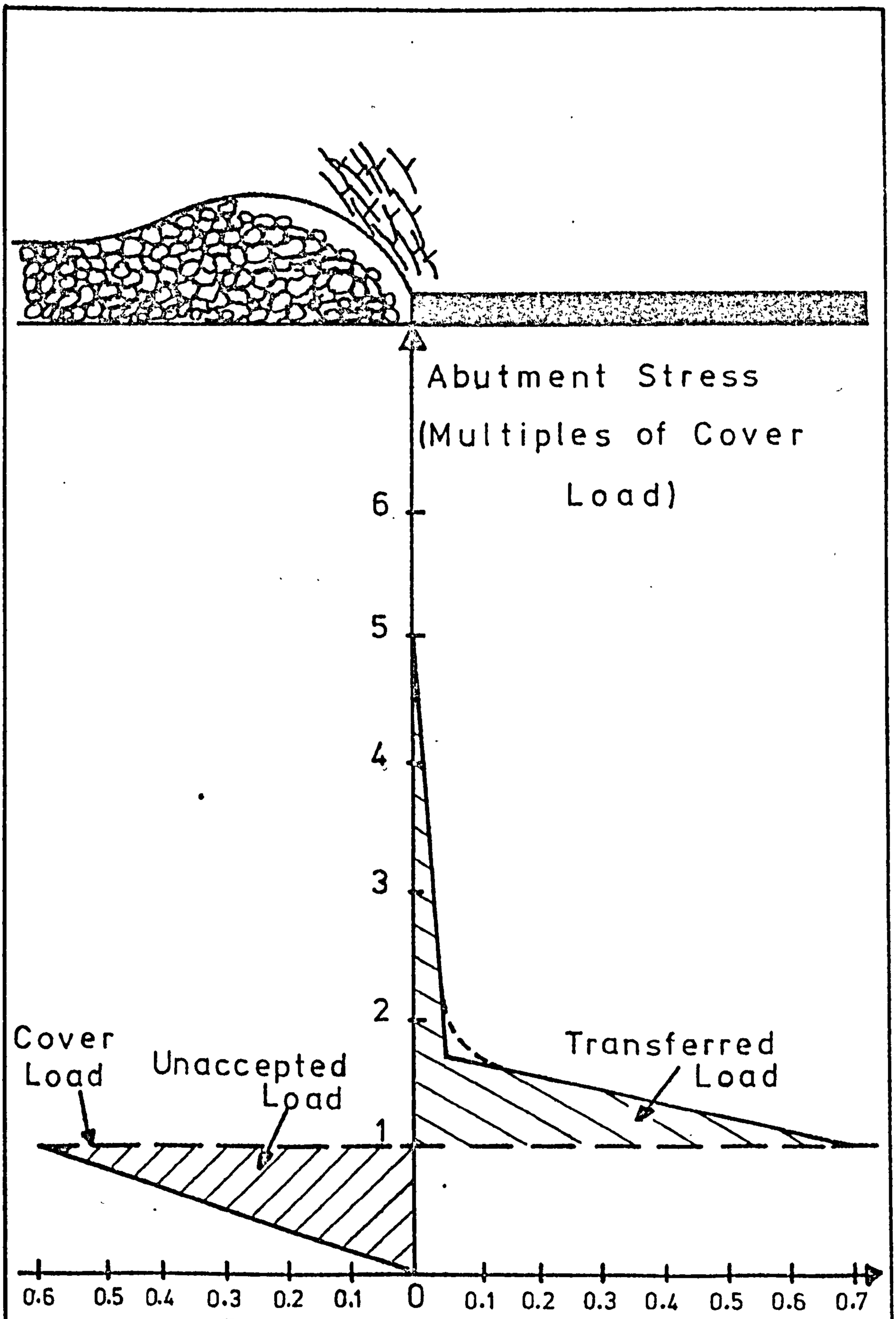

FIG. 2.2.7 STRESS DISTRIBUTION OVER A RIBSIDE AND ADJACENT WASTE.

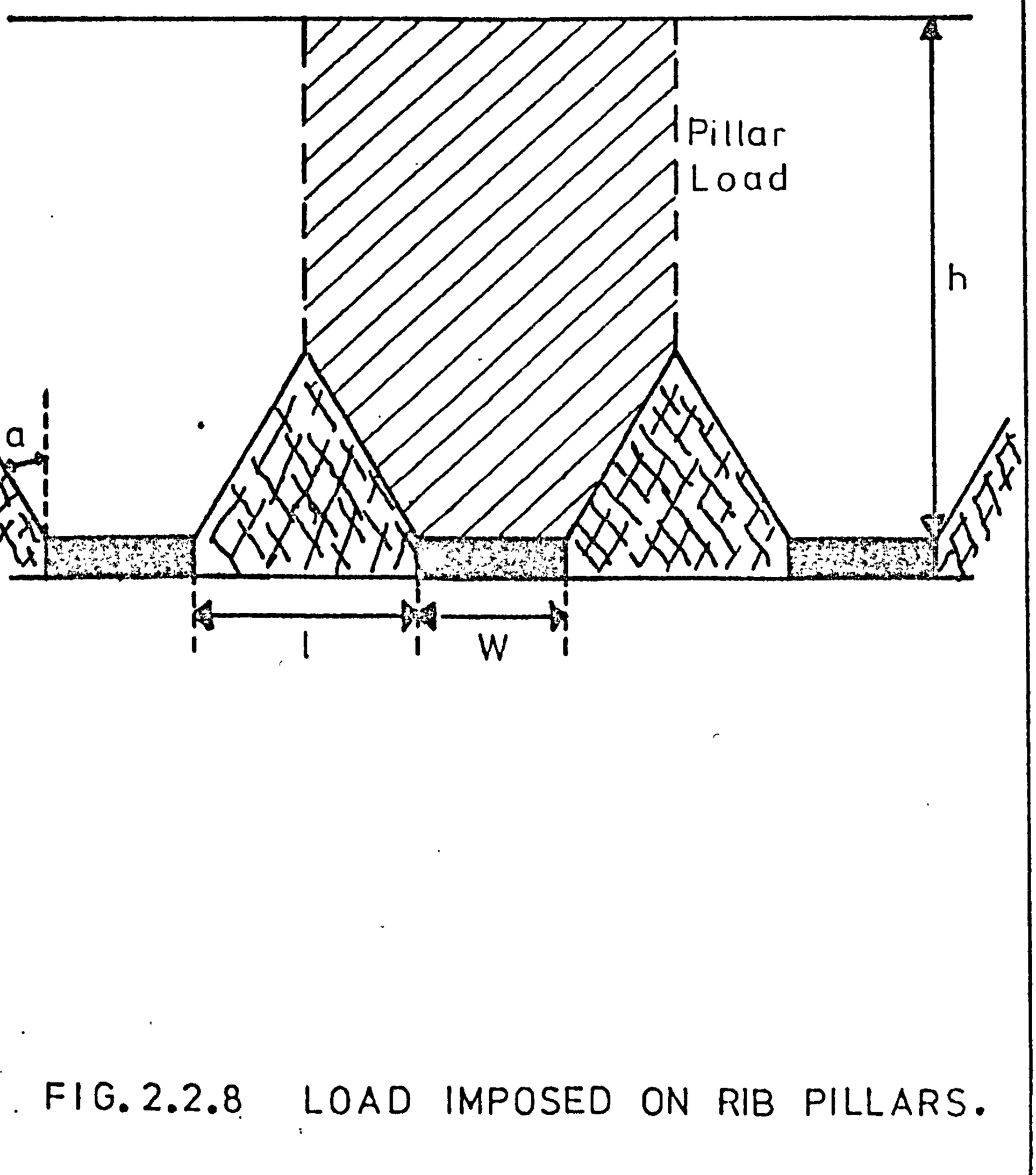

FIG. 2.2.8 LOAD IMPOSED ON RIB PILLARS.

surrounding yielding zone which constrains the inner core. The stress distribution for such a system is shown in Figure 2.2.9. Using results based on the strength of British coal measure rocks under triaxial conditions[42], he estimated that the maximum abutment load is about four times the cover load, occuring at a distance 'y' from the pillar's edge, given by the expression

$$y = 0.0049th \qquad (2.2.7)$$

where

t = Roadway height (m)

h = Depth of the seam (m)

As opposed to the previous assumption, Wilson considered that the full load is accepted by the waste at a distance of 0.3h, from the edge of the pillar. The average pillar stress, therefore, for a pillar with extensive wastes on either side, assuming critical dimensions, will be identical to the one suggested by equation (2.2.5), apart from the 0.6 factor, i.e.

$$\bar{\sigma}_p = \gamma h \left(1 + \frac{0.3h}{W}\right) \qquad (2.2.8)$$

From an underground investigation on two barrier pillars, at Lea Hall Colliery, Ashwin[44] revealed a wavelike distribution. Except for the two ribside abutments, predicted by Wilson's hypothesis, a larger median abutment was detected, unexpectedly, near the pillar's

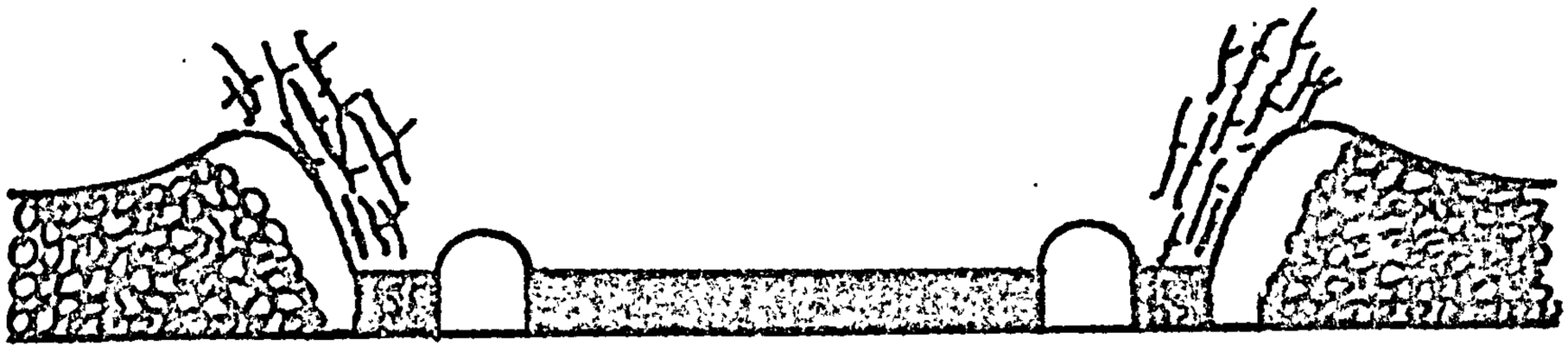

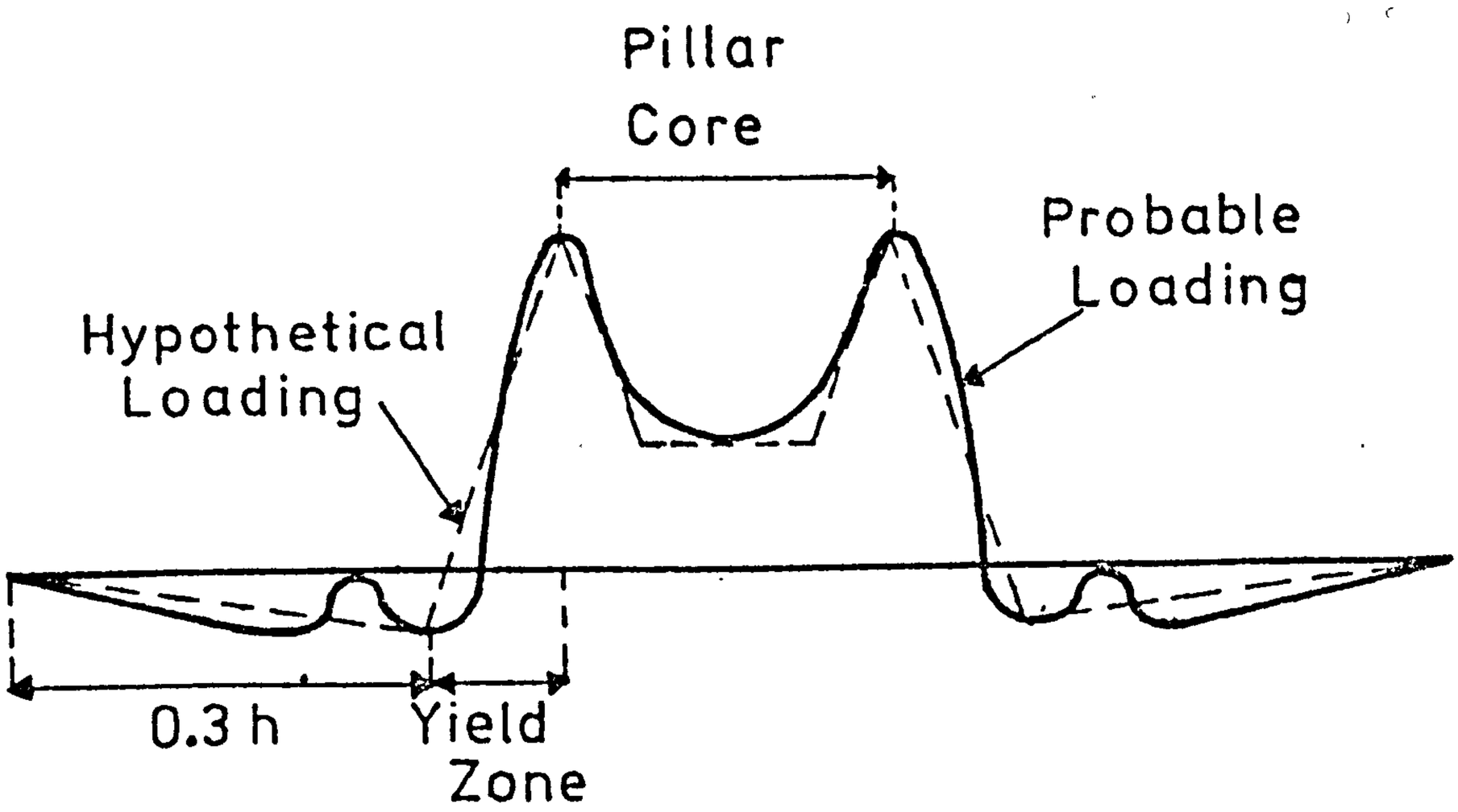

FIG. 2.2.9 THE PILLAR CORE PRINCIPLE.

centre. The investigation also demonstrated that the ribside abutments occured at distances from the ribside in agreement with the hypothesis, although their nominal value was rather less than predicted.

2.3 SOME BASIC PARAMETERS INFLUENCING PILLAR DESIGN

Due to the number and character of the factors influencing the design of pillars, there is no standard designing procedure, capable of withstanding the varying nature of underground conditions. However, some basic parameters can be singled out, as common factors, providing a degree of guidance to the designer. The author believes that the following factors belong to the latter category:

(a) The pillar's function within the mining layout.

It is of the utmost importance to define initially, the purpose that a pillar has to fulfil; the pillar's function, therefore, will dictate to a great extent, its size and location. Pillars, for example, may be intended to protect roadways underground or the surface above, and may be required to remain stable or yield under stress. As a result, a pillar may be large enough to remain stable, but not sufficient to protect a roadway.

(b) The primitive stress field

An approximation of the nature and magnitude of the

primitive stresses is essential. Although, in most cases, the vertical stress component can be estimated, reasonably accurate, from the overburden stress due to gravity, the magnitude of the lateral components is a matter of some conjecture. The latter stress, however, will clearly influence the abutment stresses. Oram[71], for example, found the maximum stress concentration, on the pillar's edge, to range from about 8.5 to 14 as the stress field varied from horizontal stress half the vertical, to hydrostatic conditions.

Further, if the working area is in the proximinty of faults or other geological disturbances, as so often is the case in British coal mines, then the approximation of the primitive stress field becomes even more complex, due to the possible presence of tectonic or residual stresses.

This topic, however, was discussed, in greater detail in section 1.3.

(c) <u>The strength of coal pillars</u>

It has been attempted by many investigators, employing different approaches, to express the strength of pillars in terms of its representative dimensions. From laboratory testing on small specimens, Steart[49] suggested for South African coals, the empirical expression

$$S = K\, W^{0.5}\, H^{-1.0} \qquad (2.3.1)$$

where

S = Pillar strength

K = Constant

W = Pillar width

H = Pillar height

Tests on Pittsburgh coals by Holland[48] revealed a similar expression, as shown below

$$S = C\, W^{0.5}\, H^{-0.5} \qquad (2.3.2)$$

where

C = Constant equal to the unit strength of a cubical specimen with edge dimension equal to height

Further, it was shown, that C is greatly influenced by the coefficient of friction at the interface of the pillar with roof and floor 'in-situ' or by the degree of friction between specimen and platens, during testing.

Evans et al[9], tested cubical and irregularly shaped specimens and suggested that for Barnsley Hards coals

$$S = L\, W^{-0.17\pm0.02} \qquad (2.3.3)$$

$$S' = M\, V^{-0.04\pm0.02}$$

where

W = Cube dimension

V = Mean volume of irregular specimen

S' = Crushing load divided by the mean contact area

L,M = Constants

In the case of Deep Duffryn coals the equivalent expressions are

$$S = N\ W^{-0.32\pm0.02} \qquad (2.3.4)$$

$$S' = Q\ V^{-0.09\pm0.03} \qquad (2.3.5)$$

From a number of 'in-situ' large tests, on Pittsburgh coals, Greenwald[74] found that

$$S = C\ W^{0.5}\ H^{-0.83} \qquad (2.3.6)$$

which compares favourably with equation (2.3.2), derived from laboratory testing of the same coal.

However, Bieniawski[5], carried the most extensive 'in-situ' testing on the South African coals, employing cubical specimens ranging in size from about 7.62cm to 2m. From his results, shown in Figure 2.3.1, it is clear that the strength (and the scatter of results), is decreasing with increasing specimen size, until an asymptotic value is approached for a size of 1.5m. As a result, he concluded that 'in-situ' tests on specimens over 1.5m are directly applicable to full scale prototype pillars, since, as the graph suggests, no significant decrease of strength for increasing size is expected, beyond this value. His

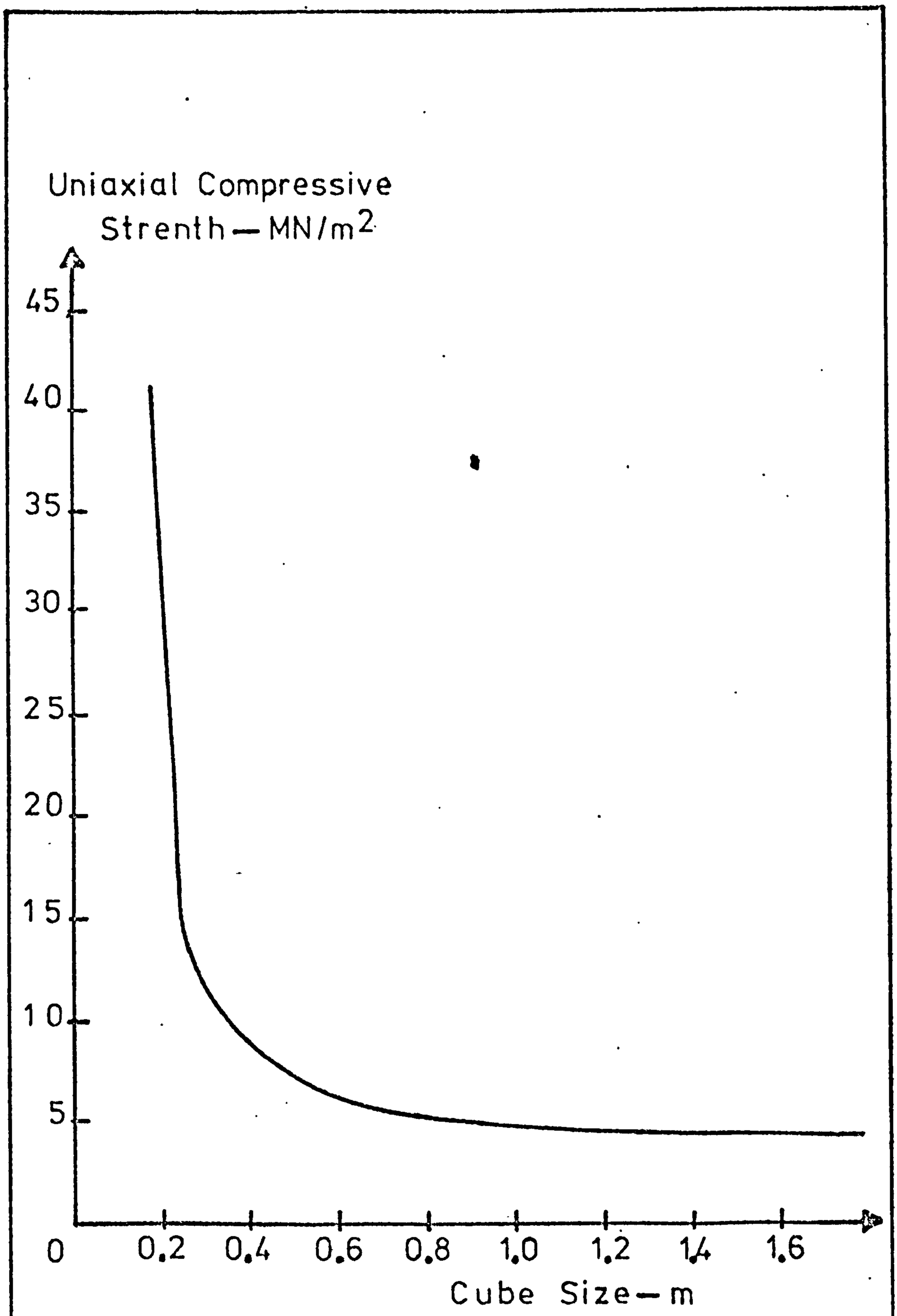

FIG. 2.3.1 THE EFFECT OF SPECIMEN SIZE ON STRENTH.
G

results can be summarised by the following expression in MN/m^2

$$S = 2.76 + 1.52W/H \qquad (2.3.7)$$

where

$$W \geqslant 1.5m$$

and $$W/H \geqslant 1$$

Bieniawski results clearly demonstrate, that the larger the specimen, the greater the number of weakness planes or structural defects present, and as a result, the lower the strength. This led some investigators to the notion that better results can be obtained by examining the micro-structure of the material rather than the specimen size. As mentioned in section 1.2, such examination can negotiate with the anisotropic effects and the presence of cracks or other discontinuities.

Basically, such methods are assuming a statistical distribution of 'weak places' or 'links', either in form of cracks or dislocations, in the atomic grid. Such planes of weakness cause cracks to propagate under stress, leading eventually to megascopic rapture. In essense, therefore, it is assumed that a material is only as strong as its volume element containing the worst flaw. With reference to rock failure, the work of Evans et al[9] and Grobbelaar[75] is noticeable in this field.

However, statistical theories of strength have often suggested unrealistic results, and in general, are of limited practical importance. Salamon et al[76], on the other hand, employed statistical principles, only to formulate, in this case, data, collected from pillar failure history. They considered 125 known collapse cases, and they suggested the following empirical formula, for the South Africal coals

$$S = 14.9W^{0.46}\ H^{-0.66} \qquad (2.3.8)$$

where S is in MN/m^2.

It is seen, that the W and H exponents suggested by the last equation compare favourably with the ones found by Steart and Bieniawski (equations (2.3.1) and (2.3.7)), for the same coal strata.

Some attempts have also been made to evaluate pillar strength from theoretical considerations. Bryan et al[77] suggested that the strength can be expressed as

$$S = C\ W^a H^b + B\ \exp\left(\frac{FW'}{H}\right) \qquad (2.3.9)$$

where

t = Thickness of fractured zone

W'= W-2t

a,b,C,B,F= Constants

Therefore, for small pillars, the last term of the

equation (2.3.9) can be neglected, and the expression reduces to the familiar shape, discussed previously. On the other hand, from triaxial laboratory testing, the strength of coal can be obtained from Mohr's envelope, in terms of the confining pressure (S_1), i.e.

$$S = S_o + \tan b\ S_1 \qquad (2.3.10)$$

where

S = Confining strength

S_o = Unconfined strength

tanb = Slope of envelope

The last term has been found to be nearly 4, and as a result, the equation can be reduced to[43]

$$S = S_o + 4S_1 \qquad (2.3.11)$$

Finally, apart from the obvious relationship between strength and size or shape, other factors also, as the mechanical properties of coal, the nature of the environment and mode of loading, will largely influence the pillar strength.

(d) <u>The mechanical properties of the strata</u>

The stress distribution will greatly depend on the mechanical properties of pillar, roof and floor rock. In the case of the heavily creeping evaporite rocks, usually extracted by the room and pillar method of mining, pillar stability is primarily dictated by the

time-dependent behaviour and the expected pillar life. Such behaviour is also inherent in some coals[78], and should not be disregarded when designing pillars of long term stability.

However, in addition to the mechanical behaviour of the pillar rock, the properties of the roof and floor rock, providing the lateral restraint to the pillar, should also be considered. Since the roof-pillar-floor system, comprises of elastically dissimilar rocks, the stress distribution at the interface planes, is an important problem. The stress system on such plane is as shown in the two elements of Figure 2.3.2. In general two conditions must be satisfied, i.e.

$$(\tau_{xy})h = (\tau_{xy})s$$

$$(\sigma_y)h = (\sigma_y)s \qquad (2.3.12)$$

Smart[79] carried out an extensive laboratory investigation employing photo-elastic and moire techniques of stress analysis; although the first condition was reasonably approximated, by his results, the second one was not substantiated at all. Since the investigation was executed under plane strain conditions, he concluded that the discrepancies could be due to friction between the model and the containing rig. Frictional forces, therefore, will oppose the displacement and thus increase the

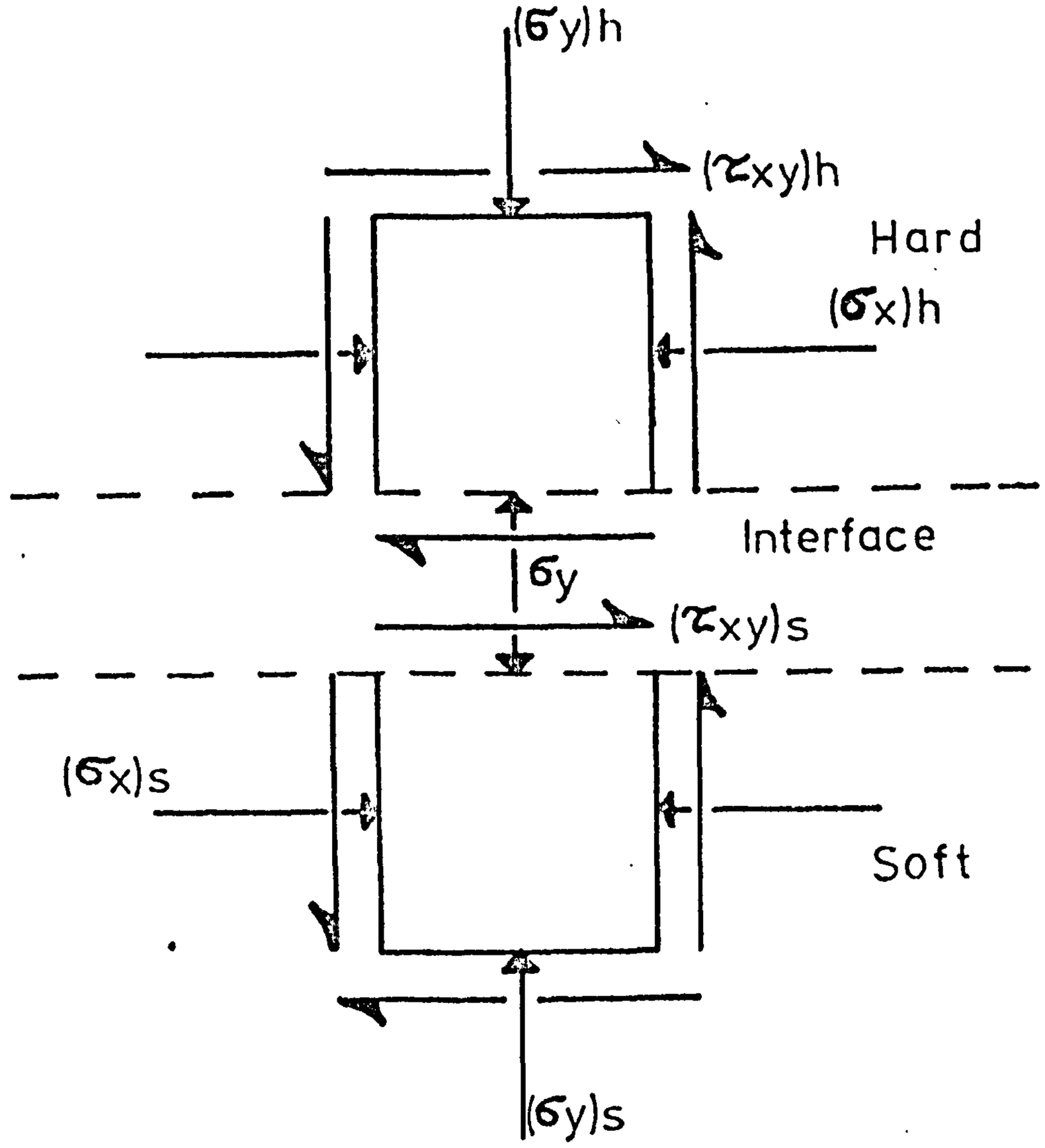

FIG. 2.3.2 EQUILIBRIUM CONDITIONS ACROSS AN INTERFACE.

stiffness of the layer.

Jenkins[72], also investigated this problem by testing two cylinders of elastically dissimilar materials in compression while taking steps to ensure no slip at the interface. Some of his results are shown in Figure 2.3.3. He suggested that the high modulus medium has a constraining effect on the low one, whereas, the latter tends to produce tensile stresses in the high modulus material. The value of this tensile stress can be expressed as following

$$\sigma_x = \frac{\nu}{1-\nu}\,\sigma\left(\sqrt{\frac{E_1}{E_2}} - 1\right) \qquad (2.3.13.)$$

where σ = Applied stress

ν = Poisson's ratio

$E_1 > E_2$

Although this tensile stress is relatively low, it is rather significant due to the low tensile strength of rocks. Jenkins suggested, therefore, that in the case of coal pillars with soft fireclay floor, roadway closure may be exaggerated by any disintegration of the coal produced by such tensile stresses.

(e) Load transference

It is important when designing pillars, to estimate the amount of load transferred on to the pillar and the

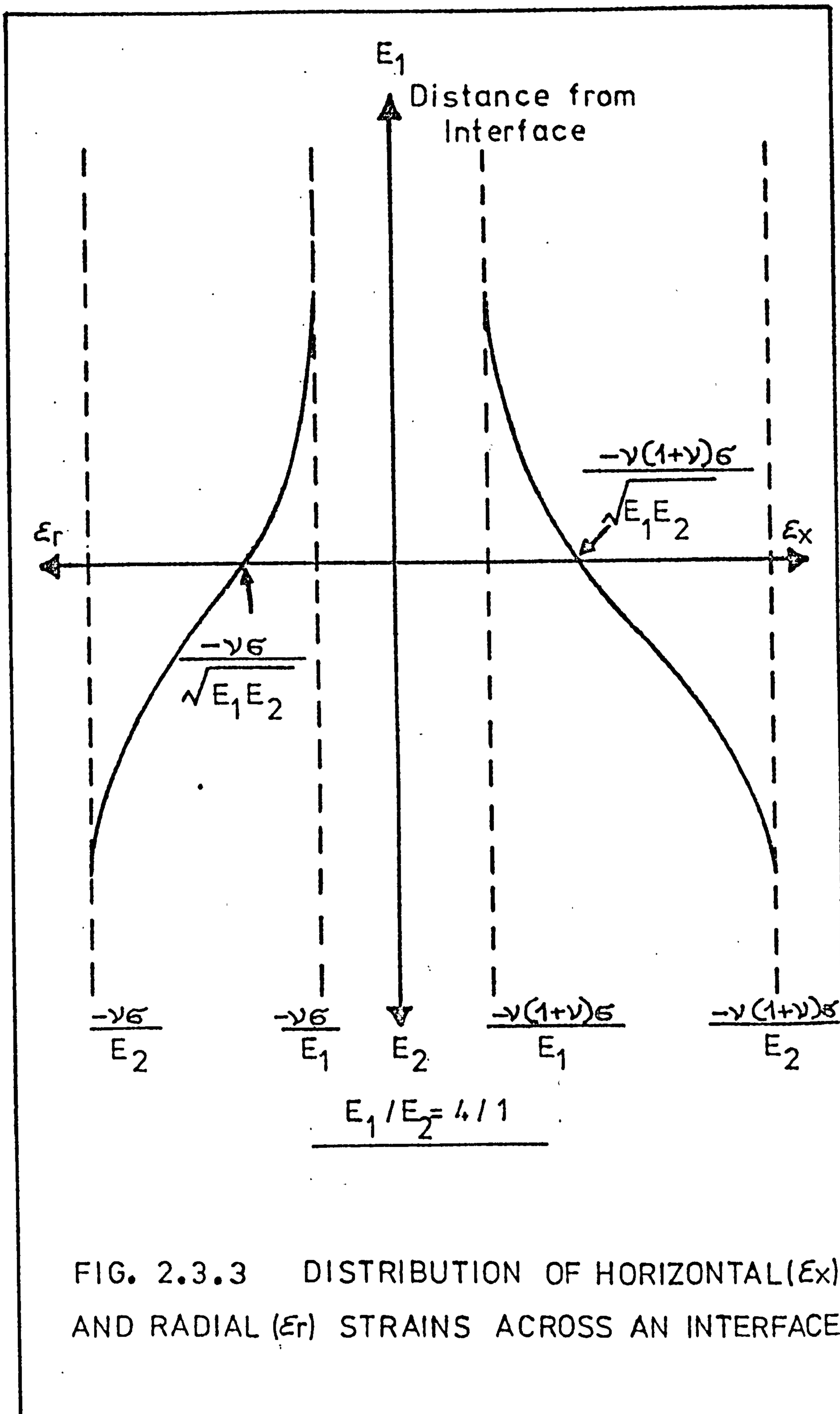

FIG. 2.3.3 DISTRIBUTION OF HORIZONTAL (εx) AND RADIAL (εr) STRAINS ACROSS AN INTERFACE.

position and magnitude of the abutment stresses. As mentioned earlier, these factors will greatly depend on subsidence, depth and extent of the excavation and the mechanical properties of the strata.

Jenkins suggested[72], that whereas the transferred load, calculated from the principles developed in section 2.2, has been proved realistic, the abutment stresses can not be estimated to the same accuracy and, as a result, are rather approximated. Model studies, therefore, are in this case invaluable and can greatly increase the confidence of the designer, when predicting pillar widths. Oram[71], from an extensive photo-elastic study, using multi-layered models, showed a considerable increase of the abutment stresses with decreasing pillar width. Their relationship was approximated by the following equation

$$C = 0.43 + \frac{63}{W} - \frac{181}{W^2} \qquad (2.3.14)$$

where

C = Average shear stress concentration

W = Pillar width in meters

He concluded, therefore, that for pillar widths less than 30m, a great increase of the stress concentration must be expected.

(f) Interaction of pillars

When a pillar is left underground, stress concentrations will develop, which will not be limited to the pillar rock itself, but extend to the strata above and below the pillar. As a result, any present or future workings within the pillar's zone of influence will be subjected to interacting stresses and such practice should, in general, be avoided.

In order to establish the zone of influence, King et al[73], carried out a theoretical investigation based on the Boussinesq's solution of a line load, on a semi-infinite elastic medium. The contours of the stress concentrations thus found, are shown in Figure 2.3.4, together with the high pressure zone underneath the pillar.

In a similar investigation, Jenkins[72] examined the effect of the pillar width on the zone of influence. He concluded that irrespective of pillar width, this zone (with stress concentrations of at least 1.5) would extend for one-third of the depth above and below the pillar. He also pointed out that the wider the pillar, the wider the zone of influence will be, which should be kept in mind when designing pillars.

From another theoretical investigation based on Berry's[32] solution for transversely isotropic ground, Whittaker[80]

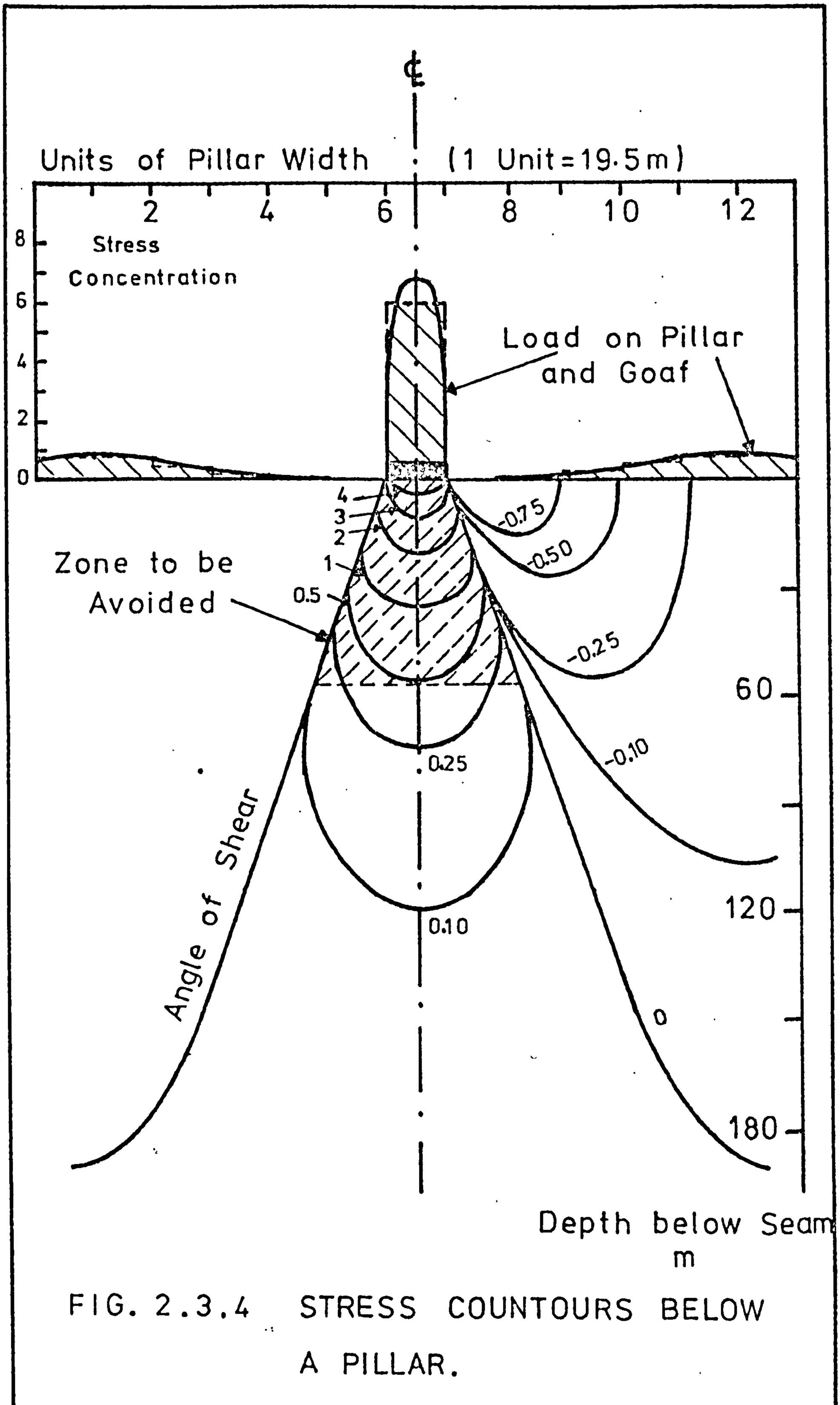

FIG. 2.3.4 STRESS COUNTOURS BELOW A PILLAR.

constructed a nomogram of the stress concentrations above a rib-side. He concluded that abutment stresses spread over a wider area, at increasing distances above the pillar, although their magnitude is substantially reduced beyond 36m. The location of these abutments will be displaced by approximately 11° to the vertical at distances above the pillar. The effect of interaction, however, will be noticeable even at 90m above the pillar, as shown in Figure 2.3.5.

From underground measurements, British investigators[68] have suggested that the zone of influence can be approximated in terms of the maximum pressure arch, at a particular depth (equation (2.2.4)). By assuming that the relaxed zone is ellipsoidal in shape, then its extent can be taken as twice that of the maximum pressure arch, at that depth, i.e.

$$2D = 36.6 + 0.3h \qquad (2.3.15)$$

where

2D = Twice the maximum pressure arch

h = Depth

The last equation, although on the conservative side, it is in agreement with the theoretical investigations described before, which postulate a zone of influence of at least 0.3h.

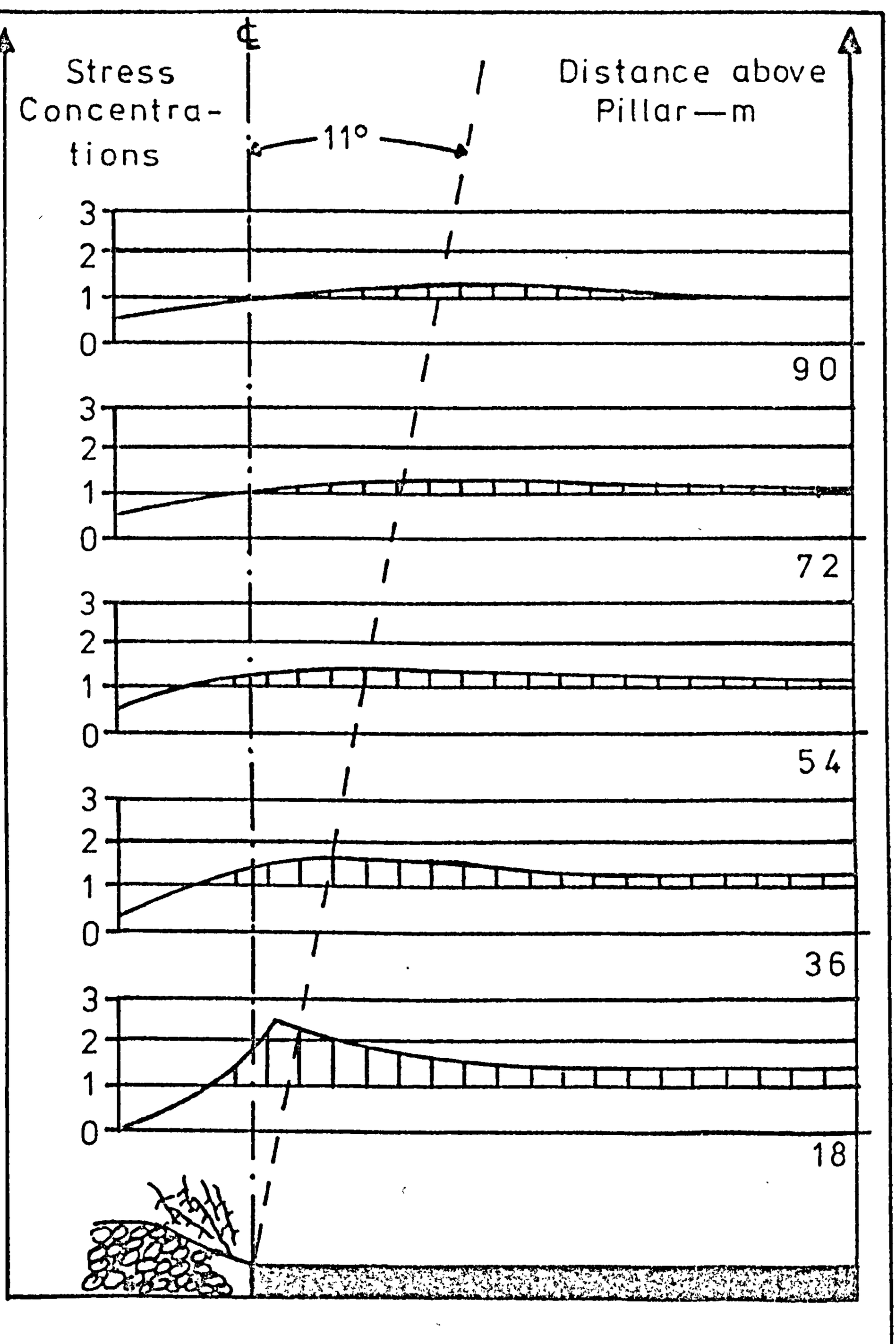

FIG. 2.3.5 STRATA LOADING ABOVE A PILLAR.

Jacobi[81], from underground convergence measurements in a gate road, 42m below a coal pillar, found that the maximum peak of the additional pressure does not occur below the pillar edge but at a distance 13m from the edge. Excessive convergence recordings were shown at distances 2m ahead of the pillar edge, extending to 10m beyond the maximum as shown in Figure 2.3.6. Similar results were also found by other investigators[82].

If, therefore, the severe stresses around pillar edges often the cause of roof falls, are to be contained, then the order of extraction of successive seams must be considered, in deciding pillar width. King et al[73] suggested, therefore, that if rib pillars are to be capable of withstanding possible stress interactions in multi-level workings, their layout should be as shown in Figure 2.3.7, in accordance with the extraction order.

2.4 THE DESIGN OF PILLARS

Having carefully studied the major factors influencing the behaviour of pillars, one must then proceed to design a pillar which is capable of fulfilling all the objectives.

With reference to room and pillar method of mining, it was shown that the average pillar stress, as predicted by the tributary area theory (equation (2.2.1)), is reasonably realistic. As a result, the problem reduces to one of

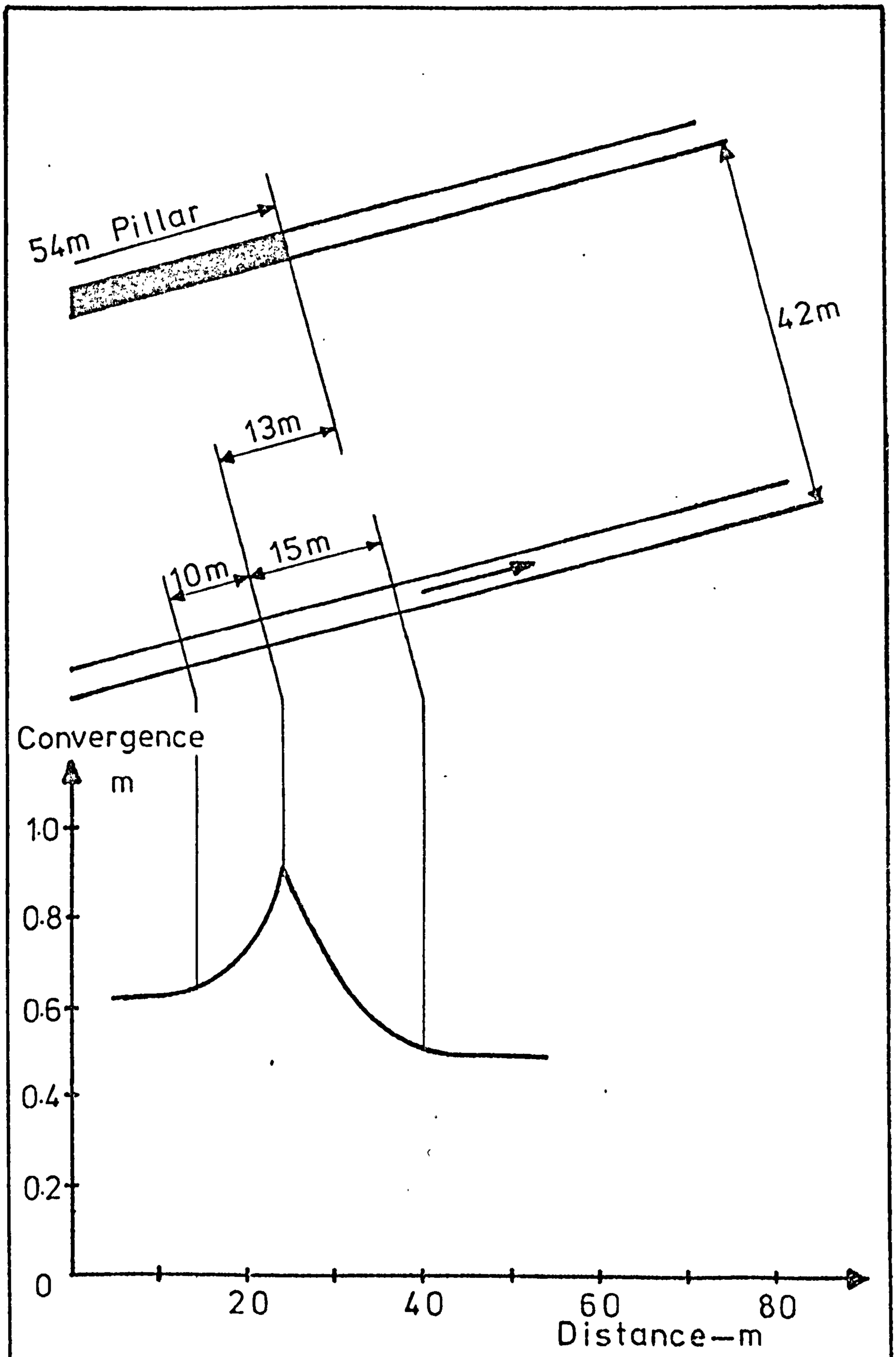

FIG. 2.3.6 THE INFLUENCE OF THE PILLAR EDGE ON A PANEL BELOW.

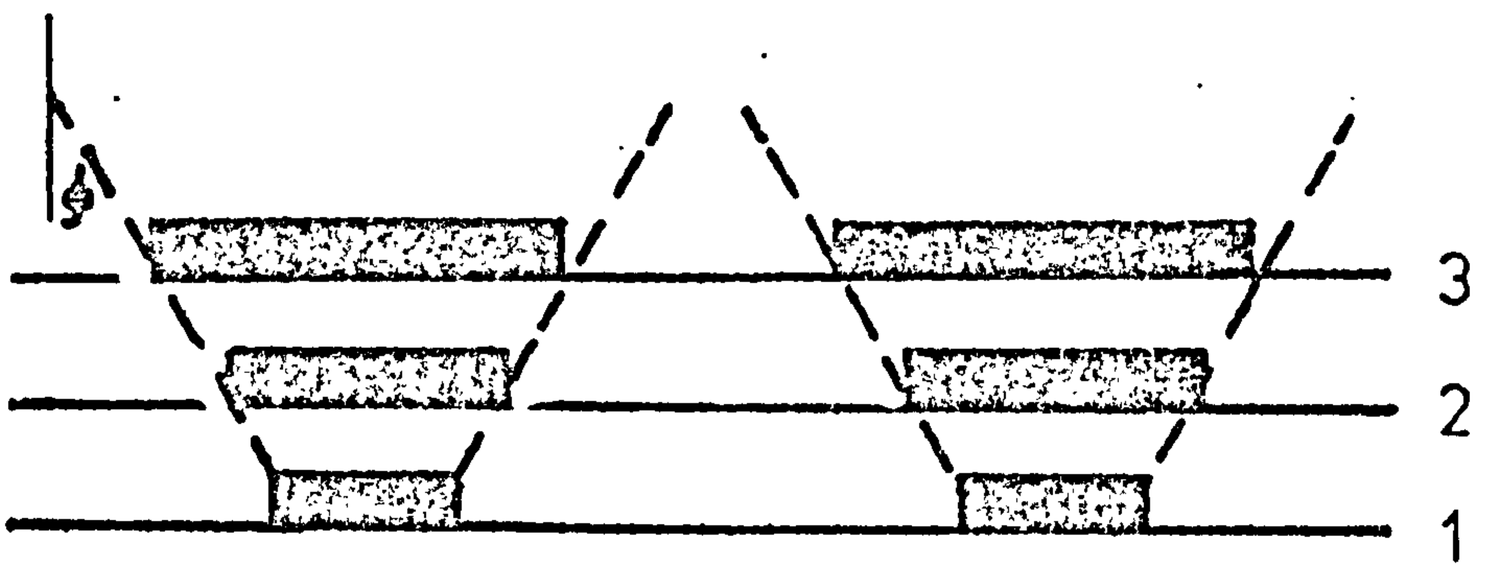

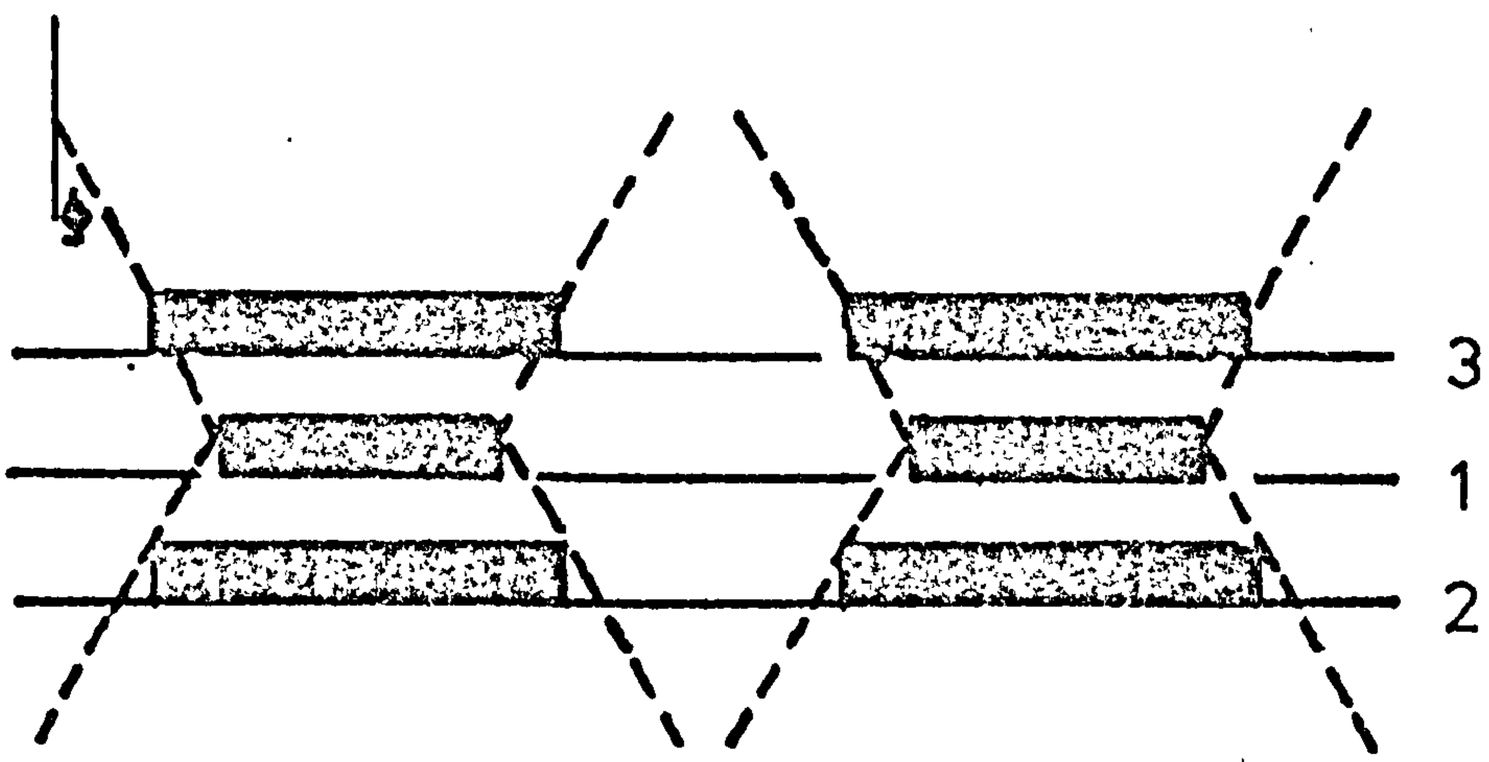

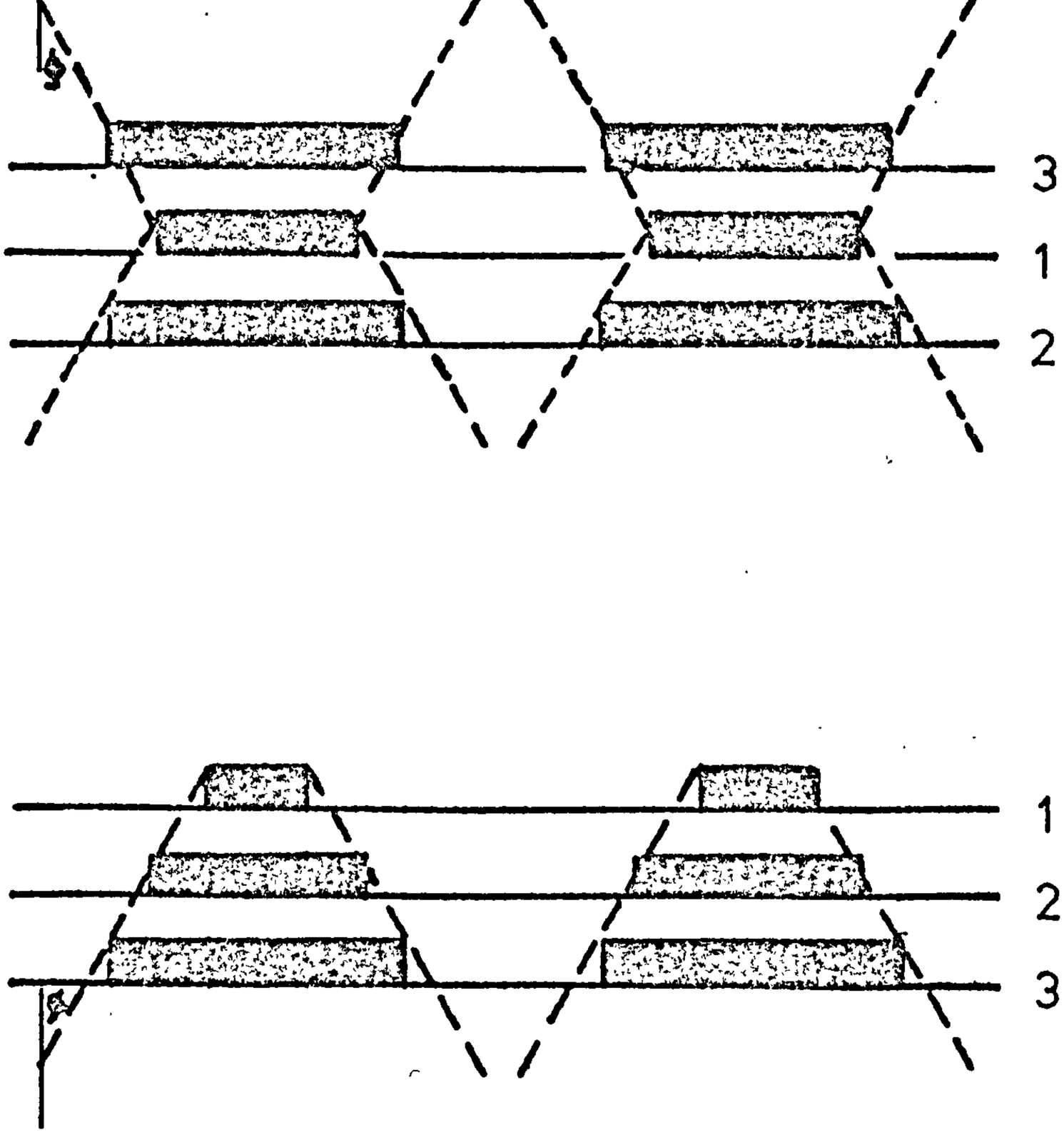

ϕ — Angle of Shear

1,2,3 — Order of Extraction

FIG. 2.3.7 LAYOUT OF PILLARS FOR MULTI-SEAM EXTRACTION.

deciding an appropriate Safety Factor (S.F.), where

$$S.F. = \frac{S}{\bar{\sigma}_p} \qquad (2.4.1)$$

where

S = Strength of pillar

$\bar{\sigma}_p$ = Pillar stress (equation(2.2.1.))

The pillar strength as previously explained, can be expressed in terms of pillar height and width, as follows

$$S = K\, W^a\, H^b \qquad (2.4.2)$$

where the constants K, a, b, vary in accordance with the method employed, and the nature of the rock.

It was found, for example, that the strength of the South African coals is best described by the statistically derived equation (2.3.8), where $K = 14.9(MN/m^2)$, $a = 0.46$ and $b = 0.66$. Therefore,

$$S.F. = \frac{14.9W^{0.46}}{\gamma h(1-R)H^{0.66}} \qquad (2.4.3)$$

Salamon suggested[76] that a safety factor between 1.3 - 1.9 is adequate for most cases and as a result, the width of pillars can be calculated from equation (2.4.3).

Pillar design has also been attempted in South Africa by adopting Bieniawski's relationship for strength, derived from large 'in-situ' tests (equation (2.3.7)). The equivalent equation, in this case, is

$$S.F. = \frac{2.76 + 1.52W/H}{\gamma h(1-R)} \qquad (2.4.4)$$

The safety factor using the last equation, is within the same range as before.

It is apparent, therefore, that the safety factor will depend on the same parameters as the ones influencing the strength of pillars. Denkhaus[83] suggested that the usual range is between 2-7, the upper values adopted for, particularly, small pillar widths.

As the depth of mining increases, the confining stresses acting upon the pillar become greater and, as a result, its strength will be in considerable excess of the value predicted by unconfined, uniaxial, compressive testing. Lower safety factors, therefore, are required, with increasing depth.

Singh[84] reported that the design of pillars, in the Indian coalfields, is based on a formula suggested by Shevyakov which is as follows

$$W = \frac{B}{\left(\frac{S}{S.F.\gamma h} - \frac{\gamma' H}{\gamma h}\right)^{0.5} - 1} \qquad (2.4.5)$$

where

W = Width of square pillar

B = Width of room

S = Strength of pillar rock

S.F. = Safety factor

H = Pillar height

h = Depth

γ = Specific weight of the overburden

γ' = Specific weight of the pillar rock

The relationship of the safety factor usually adopted with depth, is shown in Figure 2.4.1, for typical strengths of the Indian coals.

These, relatively simple, designing concepts can not, however, be employed in the design of larger pillars, encountered in a longwall complex. In this case, the parameters listed in section 2.3 should be carefully evaluated before deciding pillar sizes. Jenkins[72] suggested that equation (2.2.5) can be used to estimate the load transference on to the pillar, with the abutment stresses reasonably adjusted to suit the particular underground conditions.

Wilson[43] suggested that a pillar can not be assumed stable unless it possesses a core, i.e.

$$W \geqslant 0.0098th \qquad (2.4.6)$$

(see equation (2.2.7)).

If there is a pillar core, then the abutment stress will be four times the cover load, located at a distance given by equation (2.2.7). The load that the pillar will take can then be evaluated if the length of the panel is known, with respect to depth. If, for example, critical dimensions are assumed, i.e. panel length 0.6h according to Wilson's hypothesis, then

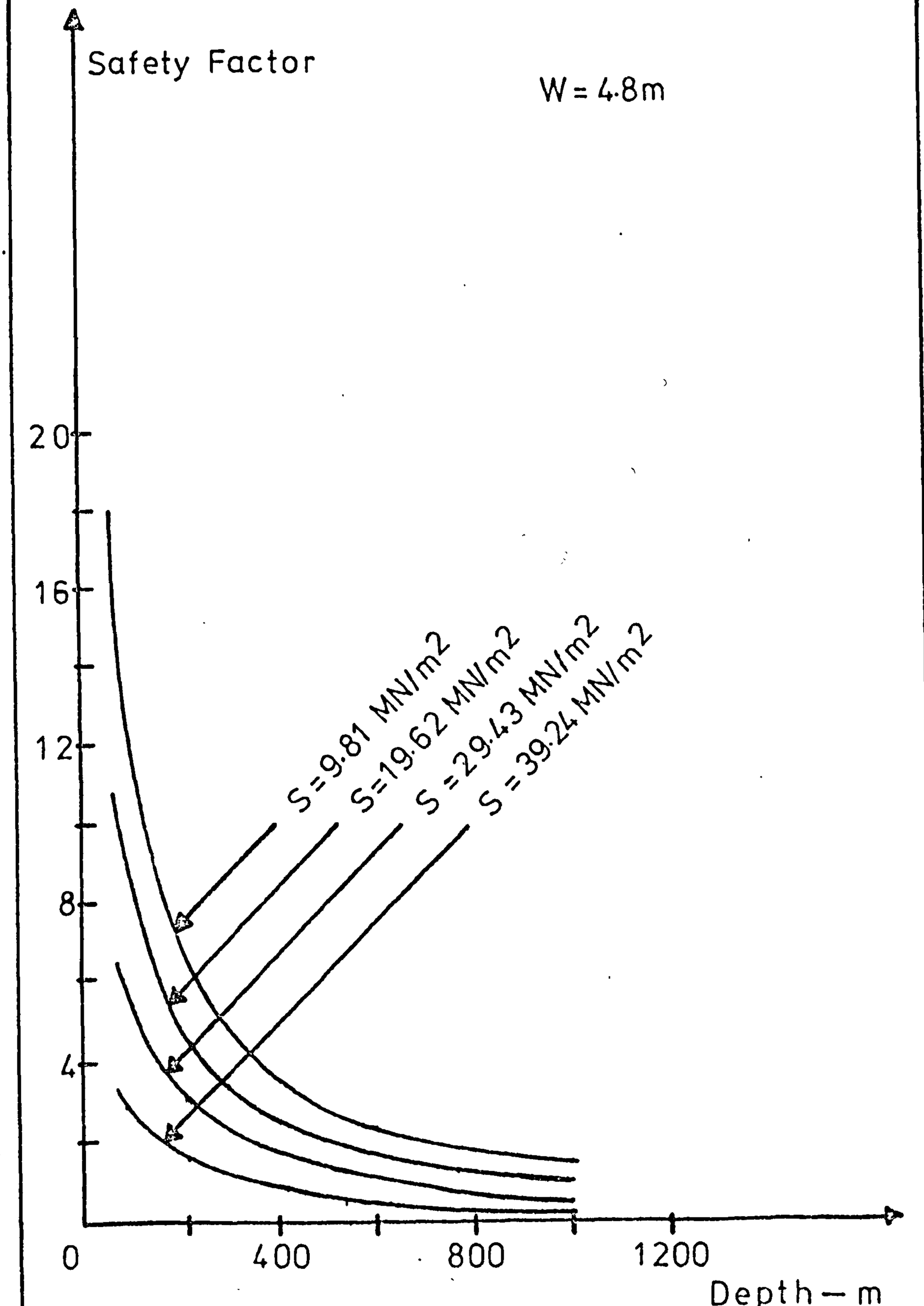

FIG. 2.4.1 THE RELATIONSHIP OF THE SAFETY FACTOR WITH DEPTH.

the load taken by the pillar, from Figure 2.2.9, is

$$\sigma_{max} = 4\gamma h \left(1 - \frac{0.0049th}{W}\right) \qquad (2.4.7)$$

where

σ_{max} = Maximum pillar load

γ = Specific weight of strata

h = Depth

W = Pillar width

t = Roadway height

By equating equation (2.4.7) with equation (2.2.8), expressing the load imposed on the pillar, and assuming a typical roadway height of 3m, then the maximum required pillar width is given by

$$W = 0.12h \qquad (2.4.8)$$

A similar expression can also be obtained in the case of wastes with less than 0.6h length. It is worth noting, however, that since it is most unlikely that the pillar will attain its maximum load (equation (2.4.7)), a safety factor of 1 was considered adequate in this analysis.

King et al[73], assuming that the load imposed on the pillar is given by equation (2.2.6), suggested that Bieniawski's relationship (equation (2.3.7)), can be used to approximate the maximum load that a pillar will take, if the strength of a rectangular pillar, with W width, is not greatly in excess of a square pillar, with side W. If the two expressions are

then equated the following quadratic equation will result

$$1520 \frac{W^2}{H} + (2760-\gamma h)W + l\gamma(\frac{1}{4} \cot a - h) = 0 \qquad (2.4.9)$$

where

W = Pillar width

H = Pillar height

h = Depth

l = Length of panel

a = Angle of draw

γ = Specific weight

and the constants are in KN/m^2.

However, some fundamental questions arise in this analysis with regard to the application of Bieniawski's formula. Firstly, it was evolved on an emperical basis, for the South African coals and its validity, when applied to the British coal measures, can be disputed. Secondly, the formula was established by testing only cubical specimens. With reference to the first point, however, Bieniawski found that the deviation of his formula, derived from tests on a particular seam, was within $\pm$ 12.5% when compared with the strength of other South African coals of different nature. It is not unreasonable, therefore, to assume that equation (2.3.7) may describe the strength of pillars in the British Coalfields.

However, the second point made above, is also of extreme importance. Investigators have often accepted that the

strength of rectangular pillars is nearly the same as that of square pillars, having a side equal to the minimum dimension (width) of the rectangle. If this is so, then Bieniawski's equation, derived for cubical specimens, can also be used for long rectangular pillars, having a width equal to a corresponding cube size.

In the course of his investigation, however, Bieniawski found evidence contradicting this assumption. A specimen of 5 x 4 x 9cm, for example, was over 22% stronger than a 5cm cube. This, in effect, means that if long rectangular pillars are designed using equation (2.3.7), it is possible that their strength is much higher than predicted. Although this can be taken, to some extent, as a safety factor, it can also lead, when the difference is excessive, to an over-estimate in pillar size, and as a result, economic objectives may not be met.

It is also worth noticing that if Wilson's hypothesis is applied to small rectangular pillars, having no core, then an expression similar to Bieniawski's equation is obtained, i.e.

$$S = 3.4^{W}/H \qquad (2.4.10)$$

where S in MN/m^2.

If the W/H ratio, for example, is 5/1, then the strength of the pillar, from equation (2.3.7) is given as $10.36MN/m^2$ and from equation (2.4.10) as $17MN/m^2$. If the ratio is only 2/1 then the corresponding values are 5.80 and $6.80MN/m^2$, respectively. Wilson, therefore, suggested that the true

strength to W/H ratio relationship will be somewhere between the straight lines suggested by these two equations.

Having so far discussed the various approaches to pillar design, based on a scientific analysis, it is of interest to compare them with the practical solutions to the problem, based entirely on observation, and without any theoretical foundations. The application of empirical design to pillars can be traced back to the last century. The eminent mining engineer, Mathias Dunn[85] said, as early as 1846, that the size of coal pillars may be approximated by the following empirical rule: 'At 180 feet deep (54.9m) a width of five yards (4.57m), to be increased by one yard (0.91m) for each additional 60 feet (18.3m) of depth'.

Since the design of pillars is influenced by a large number of often complex parameters, the effect of which can not, always, be estimated, it is of no surprise that large pillars even today, are designed to a large extent from empirical rules. In Britain the following rule has been adopted with remarkable success

$$W = 0.1h + 13.71 \qquad (2.4.11)$$

where W in metres.

The last equation shows that the pillar width predicted from the rule of thumb, although without any scientific background is nearly identical to the one reduced from Wilson's

hypothesis, equation (2.4.8). The accuracy of the empirical solution was also demonstrated by Oram's investigation[71]. From extensive photo-elastic and 'in-situ' measurements, he suggested a minimum width of 61m for a pillar left behind a longwall face, whereas the width suggested by the empirical rule was 64m, for the particular conditions.

Finally, as an example, if a long pillar is to be designed at depth of 500m(h), the height of the pillar being 2m(H), i.e. the seam thickness, where the specific weight is 22.6KN/m^2/m(γ), and critical extraction is assumed, then from the theories listed in this section, the following results can be deduced: From King's et al[73] approach (equation (2.4.9)), pillar width is given as 75.5m, with an average stress concentration (equation (2.2.5)) of about five times the cover load; from Wilson's[43] hypothesis (equation (2.4.8)), the width is given as 60m, the average stress concentration being 3.5 times the cover load (equation (2.2.8)), and the maximum abutment nearly four times the cover load, at a distance of 7m from the pillar's edge (equation (2.2.7)); from the empirical rule (equation (2.4.11)), the width predicted is 64m, the average stress concentration being about 5.7 or 3.3 times the cover load, depending on the critical dimensions assumed (equation (2.2.5) or (2.2.8) respectively).

2.5 CONCLUSIONS

(i) The loading of small pillars, as in the room and pillar method of mining, can be estimated reasonably accurate by various analytical theories. However, it is evident that the tributary area theory, regardless its simplicity, is an excellent indication of the average pillar stress (equation (2.2.1)).

(ii) The position of the maximum abutment, in these pillars will not occur at the edge, as predicted by theory, but due to localised yielding and fracture zones, near the boundary, will be shifted to some point inside the pillar. The magnitude of the abutment stress will depend upon the nature of the primitive stresses and and shape of openings and its location will be determined amongst other factors, by the depth, seam thickness and friability of pillar rock, but in general, should be expected within 8m from the pillar's edge.

(iii) The stress distribution, in the vicinity of a long wall face, can be visualised in terms of two pressure arches. The longitudinal arch shows a front abutment, just ahead of the face line (1-3m), with its zone of influence extending as much as 100m ahead of the face. The magnitude of this abutment can be taken, in general, as 3-5 times the cover load. The existence of the back

abutment, acting on the waste, is often disputed, and it is generally assumed that the maximum back stress will tend to approach the cover stress value. Although British investigators have suggested a nearly linear relationship between maximum pressure arch width and depth (equation (2.2.4)), German authorities found no evidence of such relationship. The transverse pressure arch, acting on the solid ribside and the waste, can be assumed at a distance equal to the width of the maximum pressure arch at that depth. While the longitudinal arch is following the advancing face, the transverse arch, when critical extraction has been reached and the cover load is re-established, will represent the final state of stress.

(iv) The load transferred on to a pillar, adjacent to extensive wastes, can be approximated from subsidence information for various panel lengths (equations (2.2.5) and (2.2.6). Wilson, in addition, suggested that the maximum abutment will be four times the cover load at a distance given by equation (2.2.7). As a result, it is unlikely that a pillar will remain stable, unless possesses an inner core.

(v) When designing pillars, some basic parameters should be carefully evaluated. Initially, the precise function of the pillar should be determined. The type of stress

field must then be approximated since it will greatly influence the nominal value of the abutment stress. The strength of pillar is usually expressed in terms of its height and width. Such expressions can be deduced from small or large scale testing, statistical, theoretical strength theories, and from data of pillar failure history. However, due to the large size of the prototype, large 'in-situ' tests offer the best estimate (equation (2.3.7)). Apart from the obvious importance of the mechanical properties of the pillar rock, the interface problem is also important. Tensile stresses transmitted from a low to a high modulus material when compressed together, can not be ignored in the case of a pillar with soft floor and are capable of exaggerating roadway closure.

The effect of leaving a pillar, will be the creation of interacting stresses above and below it, and such disturbed areas should be avoided in future operations. The zone of influence is at least 0.3h and is worth noting that the wider the pillar, the more stable it is, but the width of the zone of influence will also increase.

(vi) Since the loading of small pillars can be reasonably approximated, their design will be based on the safety

factor. Its usual range is between 2-7 and in the case where strength prediction are considered accurate, can be reduced to less than two (equations (2.4.3) and (2.4.4)). In general, therefore, higher values of safety factor are needed for small pillar widths, decreasing, however, as mining gets deeper.

(vii) The width of long pillars can be estimated, according to Wilson's hypothesis, by equating the load taken by the pillar to the load imposed on the pillar (equations (2.2.8) and (2.4.7)). For a roadway height of about 3m, the expression suggests a pillar width of 0.12h, which is nearly identical to the empirical rule, derived from practical observations (equation (2.4.11)).

Pillar width can also be estimated by assuming Bieniawski's equation applicable to British coals, (equation (2.3.7)). However, in the first approach, it is unlikely that the pillar will reach its maximum load, whereas in the second, the strength of long pillars could be in considerable excess of square ones, as suggested by equation (2.3.7). Although this can be taken as an additional safety factor, there is a possibility of over-designing, when using the above methods which is an expensive engineering practice.

(viii) In concluding Chapter II, some reference must be made to the role of model studies and 'in-situ' measurements in this problem. The design of pillars capable of remaining stable for a length of time and at the same time permitting high percentage of extraction, is a difficult task, due to the parameters involved. Whereas, it is impossible to evaluate the precise influence of these parameters from theoretical considerations, their effect, however, can be better understood from small scale model studies. Photo-elastic models, in particular, have a lot to offer, since they are capable of accurately simulating most mining configurations. Such investigations, therefore, can clearly define the influence of individual parameters on the behaviour of pillars, thus yielding a quick and economic solution.

Although it can be argued that such model studies possess an inherent defect, with regard to the degree of realism exhibited by the model, such analysis, even on a rather idealised model, will enable the designer to fully appreciate his problem. However, before such results are interpreted in terms of designing criteria, they must be substantiated from 'in-situ' measurements. It appears to be a great deal of lack of 'in-situ'

measurements in pillars, and this could explain why pillars are often designed from empirical rather than scientific criteria. If, therefore, a more sound designing basis is to be established, a great deal more measurements must be taken underground on pillars. Model studies and 'in-situ' measurements on pillars, therefore, comprise a necessary and not just a desirable part of the investigation; although is not postulated that both together are sufficient to produce a singular designing criterion, they can, however, greatly increase the confidence of the designer and its understanding of the problem. Such knowledge, therefore, when coupled with theoretical and empirical considerations, should lead the designer to a proper pillar size, and as a result the purpose of leaving such support will be fully realized.

CHAPTER III

THE THEORY OF THE SCATTERED LIGHT PHOTO-ELASTIC TECHNIQUE AND ITS APPLICATION TO THREE-DIMENSIONAL STRESS PROBLEMS

CHAPTER III

THE THEORY OF THE SCATTERED LIGHT PHOTO-ELASTIC TECHNIQUE AND ITS APPLICATION TO THREE-DIMENSIONAL STRESS PROBLEMS

3.1 INTRODUCTION

Stress analysis problems are conventionally approached by either mathematical or experimental methods, the latter being, mainly, strain gauge or photo-elastic exploration.

Although when choosing the most suitable method of analysis, the prime consideration must be the particular nature of the problem under investigation, it can be said, however, that in general mathematical methods have often produced insufficient or unrealistic results, whereas the main problem of a strain gauge analysis is the expense in time and money.

Photo-elasticity, however, in numerous instances, has supplied the designer with accurate solutions, obtained quickly as well as economically, and as a result, has established itself as one of the most important tools in the science of Rock Mechanics.

3.2 BASIC DEFINITIONS

Some basic concepts are briefly defined; for further information the reader is directed to bibliography, section B.

Photo-elastic Effect: Certain materials optically isotropic when unstrained, become anisotropic when subjected to stress, and behave like a natural uniaxial crystal. A plane polarised

light wave, entering such materials, will be split into two components, plane polarised in the direction of the principal stresses at the point of entry, travelling with different velocities. On emerging from the plate one of the components is retarded behind the other by a certain length, knwon as the Relative Retardation.

Stress-Optic Law: The relative retardation is directly proportional to the difference of the principal stresses and the thickness of the plate, the constant of proportionality being the Stress-Optical Coefficient. This coefficient determines the stress-optical sensitivity of the material, which is nearly constant for the different wavelengths of light. It can also be taken as the relative retardation produced for unit difference in the two principal stresses at a point per unit thickness of the material.

Fringe: A black band of constant relative retardation. The maximum shear stress, and therefore, the difference between the principal stresses, in the plane normal to the direction of light, is constant at points along the fringe. Fringes are seen when stressed birefringent models are placed in a polariscope. Fringe order, is the number of fringes counting from zero order fringe; Is a number of wavelengths (or fractions of a wavelength) of interference, arising from the relative retardation produced in a model.

Compensator: A device producing a measurable change in the relative retardation.

Principal Stresses: The maximum, intermediate and minimum normal stress values, that a body attains in three mutually perpendicular directions. Principal stresses act in a direction normal to their respective Principal Planes of stress. There is zero shear stress acting on these planes, but a Maximum Shear stress equal to half the difference of the principal stresses, on the three Principal Shear Planes at 45^{o} to the principal planes of stress.

Secondary Principal Stresses: Are defined, for a given direction 'i' as the principal stresses resulting from the stress components which lie in a plane normal to the axis 'i'. The planes on which these stresses act are the Secondary Principal Planes. Such planes are free of shear stress in the direction at right angles to 'i', but shear stress may exist along the direction 'i'. Whereas, there is only one set of principal stresses, there is an infinite number of secondary principal stresses, one and only one set of which corresponds to the given direction 'i'.

3.3 HISTORY AND DEVELOPMENT OF THE PHOTO-ELASTIC METHOD FOR TWO- AND THREE-DIMENSIONAL STRESS ANALYSIS

The science of photo-elasticity begun in 1816 when Brewster[86] discovered the basic phenomenon of double refraction. In 1841 Neumann formulated the stress-optic law

in terms of strain, and in 1853, Maxwell[87] reformulated the stress-optic law in terms of stress. However, the first engineering application of the method, appeared 50 years later when the French engineer Mesnager carried out complete two-dimensional investigations on simplified geometrical models, made of glass. But the science of photo-elasticity as a stress analysis method, was firmly established and presented to the world in 1931, when Coker and Filon[88] published the results of many years' work in their Treatise on Photo-elasticity.

Numerous investigators adopted this method of analysis (bibliography section B), and many developments, since 1931, led to its perfection, so that the subject today, over 150 years old, is a standard technique of stress exploration in every laboratory.

Whereas the photo-elastic method, in two-dimensional stress analysis, can be applied to most engineering problems, there are many cases, where the simplification of a two-dimensional geometrical model can not be realistic. Such cases should be treated by three-dimensional analysis, and fortunately, photo-elasticity can also be employed in association with some other physical property of the model material, to achieve such analysis.

The most widely used method of three-dimensional photo-

elastic explorations is the Freezing Method. It is based on the diphasic physical property of the plastics, i.e. these materials consist of an elastic and viscous phase. When such a material is heated under loading conditions, above its critical temperature, the entire load is supported by the elastic phase, which will start to deform, whereas during cooling the solidification of the viscous phase will prevent any load recovery of the deformed elastic phase. As a result, this deformation will not vanish, even when the applied load is removed. Furthermore, any slicing of the model will not alter the deformation.

The first frozen stress experiments were carried out, accidentally by Maxwell[87] in 1853, and Filon and Harris[89] in 1923. However, it was Oppel[90] who, in 1936, suggested a technique whereby complete three-dimensional investigations were possible. He postulated that fringes can be locked or frozen into a model as a result of heat treatment; thereafter the two-dimensional photo-elastic theory can be expanded to three-dimensions, by slicing the model so that certain of its planes can be isolated and examined individually. Oppel and later Hetenyi[91], investigated in detail the characteristics of the frozen stress effects and suggested many techniques to overcome some problems associated with this method, especially the problem of avoiding the creation of thermal stresses during the heating-cooling cycle. Today the freezing method is an

established technique of experimental stress analysis and has been successfully employed in many three-dimensional problems, especially in the field of Mechanical Engineering.

The other three-dimensional photo-elastic method is the Scattered Light technique. This is a modern and sophisticated approach based on the light scattering ability of some photo-elastic materials.

Observations of the phenomenon of light scattering date back to 1802, when Richter[92] observed the path of a light beam through a sol of celloidal gold. Tyndall[93] re-investigated this in detail and obtained an artificial blue sky by passing light through a tube containing mixed vapours. He showed that if the incident light was polarised, the scattering was only visible in one plane. Rayleigh[94] used the Tyndall effect in 1881 to study the light from the sky. He suggested that the blue light of the sky can be explained by the inverse dependence of the scattered light on the fourth power of the wavelength; the shorter wavelengths of the blue range are the most easily and intensely scattered.

The problems, theoretical and practical, of scattered light, have been persued steadily ever since. The phenomenon has been greatly used for critical point scattering studies from gases and liquids, as a means of measuring Avogardo's number for kinetic studies of micromolecules created from

changes in their shape and size and in numerous other problems of physical chemistry[95].

Photo-elasticians realised the potentialities of light scattering much later. It was Weller[96] who firstly observed in 1939 that when a beam of polarised light enters certain photo-elastic materials, the scattering light component, normal to the entering one, is crossed by interference fringes. Jessop[97] in 1951, and later Frocht and Srinath[98,99], made an extensive study of the method and perfected the techniques involved. The main difficulty was the separation of the stresses, however, this was overcome when Frocht and Guernsey[100] developed the Shear Difference method in 1952, which made possible complete three-dimensional solutions. Research during the last decade brought further advances to this technique; the application of a Laser beam[101] as the light component, for example, was a great step towards accuracy and efficiency.

The scattered light method was employed for experimental work, during this investigation. It was executed on a special polariscope built by Davies[102], with the author's assistance, at the Department of Mining Engineering, University of Strathclyde. The development of the instrument is discussed in reference 102. Its basic characteristics, however, together with the associated techniques are outlined in the following sections.

3.4 SCATTERED LIGHT CHARACTERISTICS

Scattered light possesses the following important characteristics:

(i) Polarisation: When an unpolarised light wave enters a scattering medium, then the scattered wave, viewed at right angles to the entering one, is completely polarised in the plane defined by the direction of the two waves. Polarisation will decrease, as the two axes approach each other, and will diminish when they coincide.

(ii) Light Ellipse: Assume a beam of plane polarised light entering a stressed medium. If 'p' and 'q' are the secondary principal axes, then the beam will be resolved into two components, 'u' and 'v' along these axes. At any point O, the u and v vibrations can be represented by

$$u = a\cos wt$$

$$v = b\cos(wt + f) \qquad (3.4.1)$$

where 'a', 'b' are the amplitudes of the two components and 'f' is their relative phase difference.

Solving the above equations by eliminating the term wt, and re-arrange

$$\frac{u^2}{a^2} + \frac{v^2}{b^2} - \frac{2}{ab}\,uv\cos f = \sin^2 f \qquad (3.4.2)$$

Equation 3.4.2 describes an ellipse, the axes of which are inclined at an angle 'x', with respect to the u axis, as shown in Figure 3.4.1. This inclination x, therefore, is given by

$$\tan 2x = \frac{2ab}{a^2-b^2}\cos f \qquad (3.4.3)$$

Examining the above equations, the following cases can be considered:

(a) Light circularly polarised, i.e. a = b.

Then equation 3.4.2 becomes

$$u^2 + v^2 - 2uv\cos f = a^2\sin^2 f \qquad (3.4.4)$$

and depending on the function f, two cases are possible

(1) $f = (2m + 1)\pi$, where m = 0,1,2,3.....,

and equation 3.4.4 becomes

$$u = -v \qquad (3.4.5)$$

which shows that the light motion describes a straight line.

(2) $f = (2m + 1)\pi/2$, in which case equation 3.4.4. is

$$u^2 + v^2 = a^2 \qquad (3.4.6)$$

The light, therefore, describes this time, a circular orbit of radius a.

(b) Non-circularly polarised light, i.e. $a \neq b$.

The light motion is given by equation 3.4.2, and as

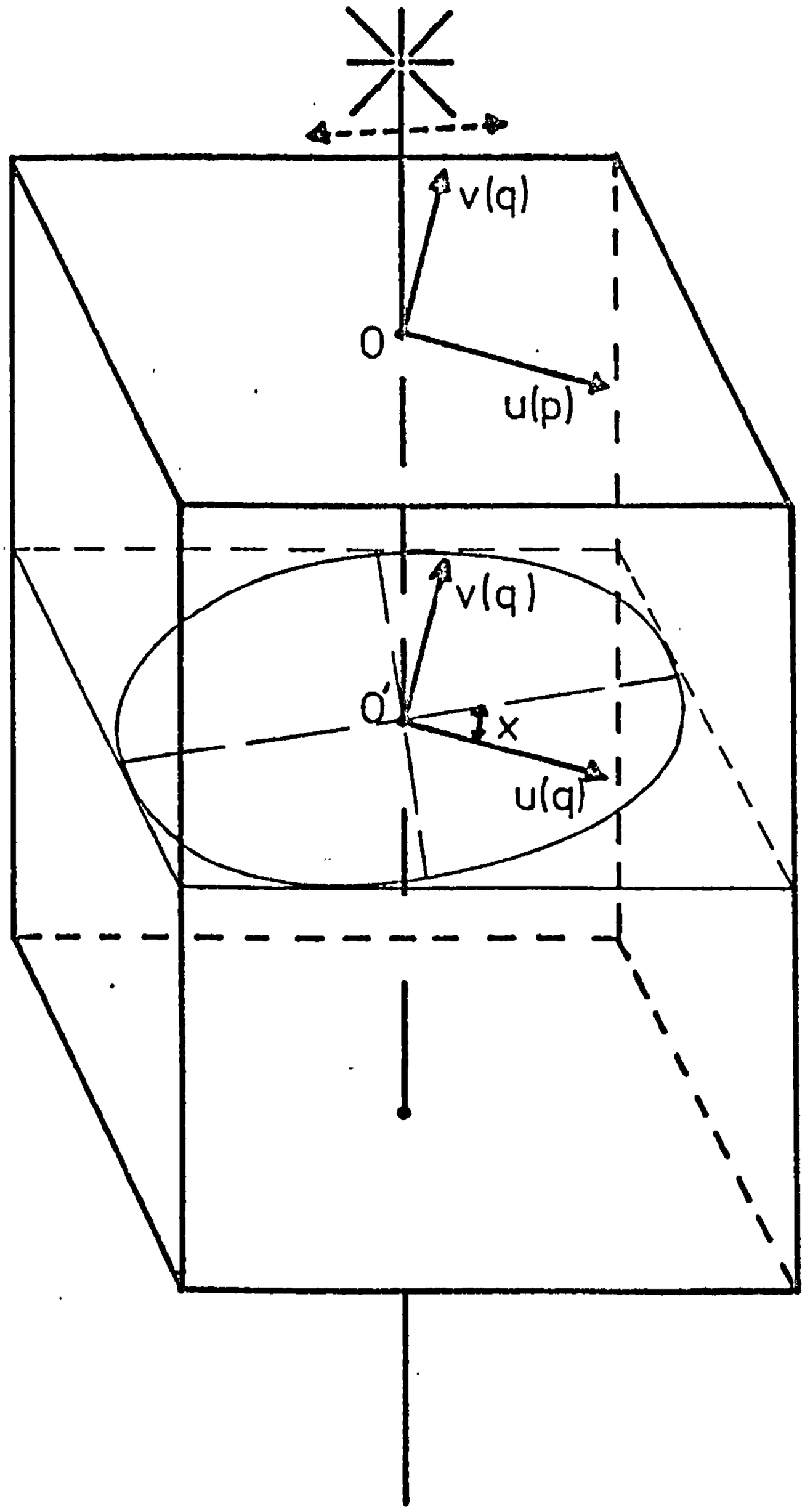

FIG. 3.4.1 THE LIGHT ELLIPSE.

before, depending on the function f, two cases are possible

(1) $\underline{f = (2m + 1)\pi}$, whereby the ellipse light equation is reduced to

$$v = \pm \frac{b}{a} u \qquad (3.4.7)$$

The above equation suggests that the light ellipse has degenerated into two straight lines, at an angle 'x_1' from the u axis, where

$$\tan x_1 = \pm \frac{b}{a} \qquad (3.4.8)$$

(2) $\underline{f = (2m + 1)\pi/2}$, in which case equation 3.4.2 becomes

$$\frac{u^2}{a^2} + \frac{v^2}{b^2} = 1 \qquad (3.4.9)$$

The last equation indicates that the light describes an elliptical path. However, whereas in the initial equation the axes of the ellipse are inclined at an angle x, from the u axis (equation (3.4.3)), in the latter case, the ellipse axes coincide with those of the secondary principal stresses.

(iii) Intensity: The intensity of illumination 'I' of a light wave having an amplitude 'a' is

$$I = 2a^2 \qquad (3.4.10)$$

If two waves have separate intensities, 'Ia' and 'Ib', with corresponding amplitudes 'a' and 'b', then the combined

intensity 'I' is

$$I = Ia + Ib = 2(a^2 + b^2) \qquad (3.4.11)$$

Consider now the secondary axes, p and q, and a direction of observation OM, at an angle 'y' from the p axis, as shown in Figure 3.4.2. The two motions can be represented as follows

$$u_1 = a\cos wt\sin y$$
$$v_1 = b\cos(wt + f)\cos y \qquad (3.4.12)$$

The total algebraic displacement at any instant t, therefore, is

$$v_1 - u_1 = b\cos(wt + f)\cos y - a\cos wt\sin y$$
$$= R\cos(Q + wt) \qquad (3.4.13)$$

where

$$b\cos f\cos y - a\sin y = R\cos Q$$
$$b\sin f\cos y = R\sin Q \qquad (3.4.14)$$

Equation (3.4.13) shows that the resultant motion is simple harmonic, with amplitude 'R' and with the same period, as each of the two impressed motions. Furthermore, by elminating Q in equation (3.4.14), the resultant amplitude R is

$$R^2 = a^2\sin^2 y + b^2\cos^2 y - 2ab\sin y\cos y\cos f \qquad (3.4.15)$$

Therefore the light intensity from equation (3.4.11), is

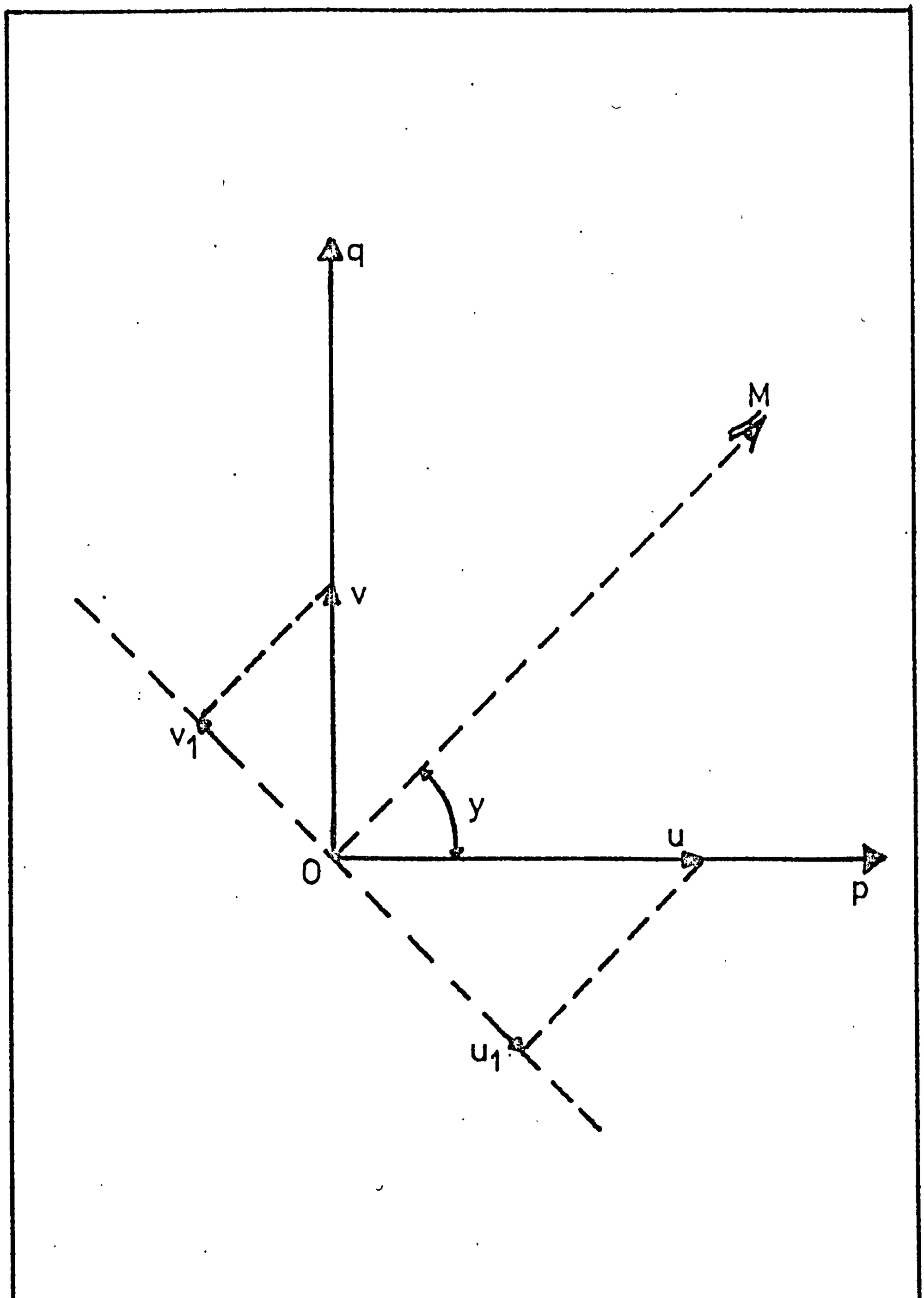

FIG. 3.4.2 RESULTANT OF TWO VARIATIONS.

$$I = 2R^2$$

and for scattered light

$$I = KR^2$$

$$= K(a^2\sin^2 y + b^2\cos^2 y - 2ab\sin y\cos y\cos f) \qquad 3.4.16)$$

where 'K' is a constant, depending on the scattering properties of the material.

The scattering intensity is proportional to the incident intensity, and is an inverse function of the wavelength. In fact, it is proportional to $1/\lambda^4$, and since red light, for example, has a wavelength (7200Å), 1.8 times greater than, say, violet light (4000Å), this law predicts $(1.8)^4$ or ten times greater scattering intensity for violet light.

For circularly polarised light, the intensity equation is reduced to

$$I = Ka^2(1 - \sin 2y\cos f) \qquad (3.4.17)$$

Also, the directions of observations, for maximum and minimum intensity, are given by

$$\frac{dI}{dy} = K(\sin 2y\ (a^2 - b^2) - 2ab\cos 2y\cos f) = 0$$

or

$$\tan 2y = \frac{2ab}{a^2 - b^2}\cos f \qquad (3.4.18)$$

Examination of the last equation and equation (3.4.3) reveals that the light intensity is a maximum (minimum)

when the direction of observation is along the minor (major) ellipse axis.

(iv) Birefringence: Assume a beam of plane polarised light entering a light scattering model. The beam is optically conditioned so that its cross-section is a rectangle of the minimum possible width. On entering the model, such a beam will illuminate and isolate one plane parallel to its direction. This imaginary slicing of the model can be executed on any plane, by moving the model with respect to the beam, as necessary.

Every particle in the model will become a source of scattering and when the observation direction is at right angles to the entering beam, the scattered light is also polarised. When, therefore, the observer looks at point M_1, as shown in Figure 3.4.3, then the accumulated photo-elastic effect from BM_1 is seen. Similarly, when analysing at point M_2, the accumulated photo-elastic effect from BM_2 is considered. Finally, the M_1M_2 layer will be the difference of the M_1, M_2 readings.

The accumulated photo-elastic effect is of the same nature as in conventional photo-elasticity, the analyser in this case being the scattering effect itself.

The pattern of the scattered light fringes can be easily explained by closely examining the intensity

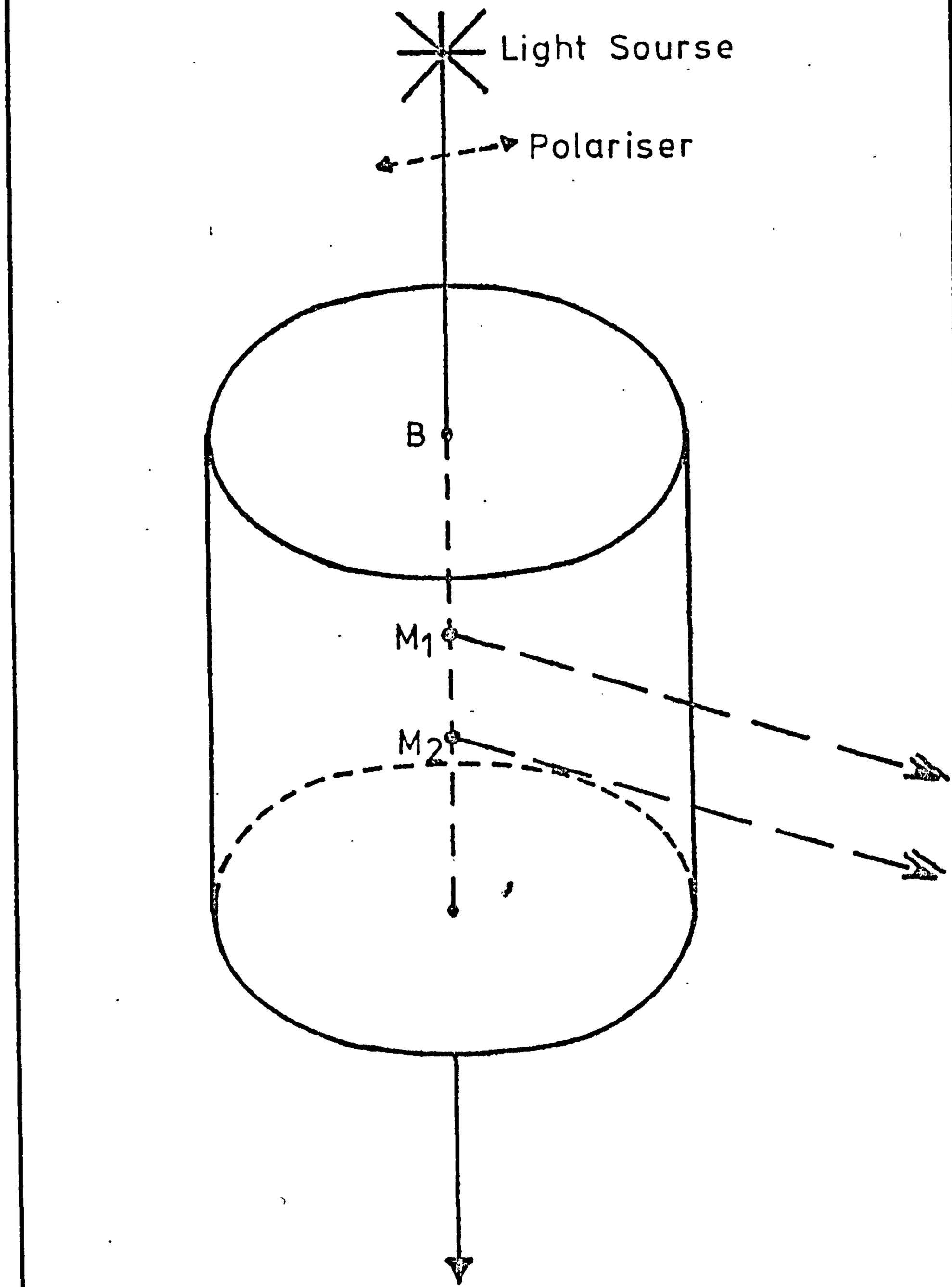

FIG. 3.4.3 BIREFRINGENCE OF SCATTERED LIGHT.

equation (equation (3.4.16)). The intensity is a function of the observation angle y, and the phase difference f. Assuming y is less than 90^{o} then

I is minimum for $f = 2m\pi$

I is maximum for $f = (2m + 1)\pi$

Therefore, the entrance point (f = 0) will be a dark field. Subsequent dark fringes represent even number of wavelengths, whereas light fringes are odd multiples of wavelengths. If y is more than 90^{o}, then the opposite conditions will exist.

Therefore, as f varies from zero to a number of wavelengths, along the points of the propagation axis, the conditions of minimum and maximum intensity will be assumed, and a fringe pattern will result.

3.5 THE STRESS-OPTIC LAW

The stress-optic law, in this case, is similar to that of the conventional photo-elasticity, and can be expressed as

$$dn = Cds\ (p - q) \qquad (3.5.1)$$

where 'dn' is the relative retardation,(C) is the stress-optical coefficient, 'ds' the interval between the points under investigation, along the light axis, and '(p - q)' the difference of the secondary principal stresses with respect to the propagation axis. The equation can be re-written as

$$(p - q) = \frac{1}{C} \frac{dn}{ds} \qquad (3.5.2)$$

where dn/ds is the slope of the retardation against distance curve at a point. This is similar to the conventional law, except that the stress difference in this case is proportional to the birefringence gradient rather than to the total birefrigence.

The above two equations are limited to the case where the secondary principal stresses maintain constant directions along the axis of light propagation. Nevertheless, a small degree of rotation of the secondary axes is always present and its effect can have a considerable impact on the results.

Assume as before the two vibrations u and v (equation (3.4.1)), at a point 's'.

$$u = a\cos wt$$

$$v = b\cos(wt + f)$$

where f is, as before, the phase difference at point s. At point 's + ds' along the propagation axis the two components are

$$u = a\cos wt \qquad (3.5.3)$$

$$v = b\cos(wt + f + df)$$

where 'df' is the phase difference caused by the secondary principal stress difference in travelling distance ds. If at this point (s + ds) the secondary stress axes have rotated by an angle 'dl', as shown in Figure 3.5.1, then the equivalent

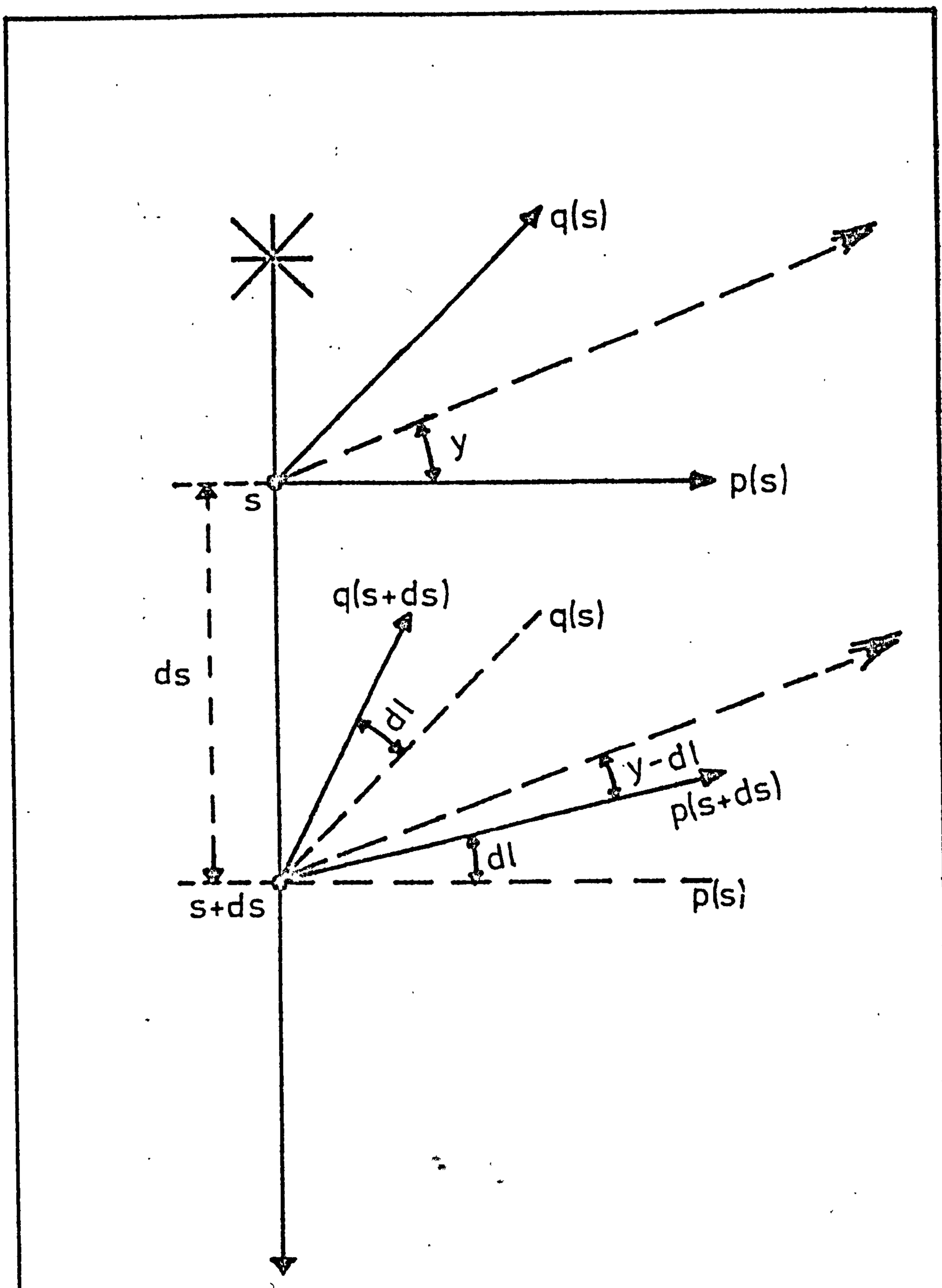

FIG. 3.5.1 ROTATION OF THE SECONDARY PRINCIPAL AXES.

stress-optic law is given by Neumann's equation[88] as

$$df = dn + \left(\frac{a}{b} - \frac{b}{a}\right) \sin f dl \qquad (3.5.4)$$

The last equation shows that the total relative retardation, df, acquired over a distance ds, is partly made of the retardation dn, caused by the stresses alone, and partly by the rotation dl of the secondary axes over the distance ds; a and b are the amplitudes of the light vectors, and f the retardation at point s. Substituting the dn value from equation (3.5.1), the last equation becomes

$$df = C\,(p - q)\,ds + \left(\frac{a}{b} - \frac{b}{a}\right) \sin f dl \qquad (3.5.5)$$

The amplitudes a,b do not, in general, remain constant and their variation can be expressed as follows[88]

$$\frac{da}{ds} = b \cos f \frac{dl}{ds}$$

$$\frac{db}{ds} = -a \cos f \frac{dl}{ds} \qquad (3.5.6)$$

From these equations it is easily seen that the rotational effect will vanish when a = b, dl = 0, or f = 2mπ.

3.6 THE INFLUENCE OF THE ROTATION ON THE LIGHT PARAMETERS

It is reasonable to assume that the light waves, u and v, will follow the secondary axes as they rotate; then, by using the same procedure as in section 3.4, equation (3.4.13), it follows

$$R = usin(y - dl) - vcos(y - dl)$$

$$= acoswtsin(y - dl) - bcos(wt + f+df)cos(y-dl)$$

$$= Tcos(Q - wt) \qquad (3.6.1)$$

and

$$TsinQ = bcos(y - dl)sin(f + df)$$

$$TcosQ = asin(y - dl)-bcos(f + df)cos(y - dl) \qquad (3.6.2)$$

where 'R' is the resultant displacement and 'T' is the amplitude of the scattered resultant.

The intensity, from equation (3.4.11), will be

$$I = KT^2$$

$$= K(a^2sin^2(y - dl) + b^2cos^2(y - dl) -$$

$$-2abcos(f + df)cos(y - dl)sin(y - dl) \qquad (3.6.3)$$

Similarly the light ellipse equation is

$$\left(\frac{u}{a}\right)^2 + \left(\frac{v}{b}\right)^2 - \frac{2cos(f + df)}{ab} uv = sin^2(f + df) \qquad (3.6.4)$$

with its axes inclined with respect to the u axis, at an angle given by

$$tan2x = \frac{2ab}{a^2-b^2} cos(f + df) \qquad (3.6.5)$$

As for the non-rotation condition, it is easily deduced again, that the intensity extremities occur for observations coincidental to the ellipse's axes.

3.7 BIREFRINGENCE MEASUREMENTS

In the case where the rotation of the secondary axes can be ignored, measurements of the relative retardation, with respect to distance along the propagation axis are sufficient. The secondary principal stress difference can then be found by differentiating this relationship. Such measurements can be accurately obtained from photographic negatives of the fringe pattern, with the aid of a travelling microscope, or directly from the model, using optical density recordings, by means of a scanning photometer.

Alternatively, the same relationship can be established using a compensator, with its axes parallel to the secondary axes at the point of entrance. Assuming that any retardation due to the compensator is equally transmitted throughout the model (i.e. the birefrigence curve has been shifted parallel to itself by an amount equal to the additional retardation introduced by the compensator), then

$$(p - q) = \frac{1}{C} \frac{Dn_1 - Dn_2}{Ds} \qquad (3.7.1)$$

where

n_1, n_2 = Retardation of two points Ds apart

Dn_1, Dn_2 = Retardation added by the compensator to raise n_1 and n_2 to the next whole fringe N.

(p-q) = Secondary principal stress difference at a point middling Ds.

When the secondary axes rotate, the previous assumption, that the compensator increases the birefringence by the same amount at every point, is not longer true, as shown by equation (3.5.5). Such birefrigence measurements are only significant when a = b, $dl/ds \rightarrow 0$, or $f = 2m\pi$, in which case, the second term of the equation (3.5.5) is zero, and the rotation effect vanishes. However, it is worth noticing, that if the above assumption was valid, under rotating conditions, then the rotation effect, however large, can be easily eliminated by making the retardation full or half wavelength i.e. $f = 2m\pi$.

Other methods, for determining the birefrigence, can also be employed as for example, by using intensity measurements. However, one has to deal with actual magnitudes of light intensity which, in general, is rather undesirable.

3.8 LOCATION OF THE SECONDARY AXES

The directions of the secondary principal stresses can be accurately determined by various methods based, in general, on the properties of the scattered light intensity[98]. Equation (3.4.16) shows that for observations along the secondary axes, i.e. $y = 0$, the intensity equation becomes

$$I = Kb^2 \tag{3.8.1}$$

and is totally independent of the retardation f.

By rotating the model, therefore, and altering the retardation at every position, using a compensator, an angle

can be detected by the photometer where no intensity variation occurs. At this point the line of vision (photometer) coincides with the secondary axes.

When rotation is present, the change in retardation can introduce amplitude changes as shown in equation (3.5.6). As a result, this could influence the intensity measurements.

The secondary axes can also be located by adjusting the compensator so that the minimum and maximum intensity is reached at a point, i.e. $f = 2m\pi$ or $(2m - 1)\pi$ from equation (3.4.16). In both cases the light ellipse has degenerated into a straight line, inclined at an angle x_1 from the u-axis given by equation (3.4.8). For observations along these lines ($y = \pm x_1$), the intensity will be zero. The location of these lines, therefore, will automatically determine the secondary axes, since the latter are equally inclined with respect to the ellipse axes.

If, however, the amplitudes of the vibrations do not remain constant, while the retardation is varying, then the ellipse will 'nearly' become a line ellipse, and for observations along the major axis the light intensity will be a minimum and not absolutely zero.

If the rotational effect can be neglected, for circularly polarised light, the secondary axes can be easily determined from the ellipse axes as shown in equation (3.4.17), since are at 45^{o} to each other.

3.9 STRESS SEPARATION IN THREE-DIMENSIONS

The separation of stresses in a three-dimensional, non-destructive system became possible, only after Frocht and Guernsey[100] developed the Shear Difference Method. This technique is primarily based on the equilibrium equations of the general space coordinates, for zero body stresses, i.e.

$$\frac{\partial \sigma x}{\partial x} + \frac{\partial \tau xy}{\partial y} + \frac{\partial \tau zx}{\partial z} = 0 \qquad (3.9.1)$$

By integrating, from B to 0, the above equation

$$(\sigma_x)_B = (\sigma_x)_0 - \int_0^B \frac{\partial \tau xy}{\partial y}\, dx - \int_0^B \frac{\partial \tau zx}{\partial z}\, dx \qquad (3.9.2)$$

If $\tau_{xy} \equiv F(Y)$ and $\tau_{zx} \equiv F(Z)$, then the quantities $(\partial \tau_{xy}/\partial_y)$ and $(\partial \tau_{zx}/\partial_z)$ represent the slope of the τ_{xy} and τ_{zx} curves, at any point, with respect to Y- and Z-axes, respectively. These slopes are best approximated from the shear stress difference between two points, equidistant above and below the point under investigation, i.e.

$$\left(\frac{\partial \tau xy}{\partial_y}\right)_p \doteq \frac{(\tau_{xy})_Q - (\tau_{xy})_B}{\Delta_y} \qquad (3.9.3)$$

where

$$PQ = PR = \frac{\Delta y}{2}$$

Substituting these values into equation (3.9.2) then

$$(\sigma_x)_B = (\sigma_x)_0 - \int_0^B \frac{\tau xy}{\Delta_y}\Delta_x - \int_0^B \frac{\tau zx}{\Delta_z}\Delta_x \qquad (3.9.4)$$

or by expressing the last equation in terms of summations

$$(\sigma_x)_B = (\sigma_x)_0 - \sum_0^B \frac{\Delta\tau_{xy}}{\Delta_y}\Delta_x \sum_0^B \frac{\Delta\tau_{zx}}{\Delta_z}\Delta_x \qquad (3.9.5)$$

If, therefore, the shear stress values are known on four auxiliary lines, parallel to the line under investigation, each pair being Δ_y and Δ_z apart, then the normal stress σ_x can be determined, at any point on the line OB, if an initial (boundary) value $(\sigma_x)_0$ is known. This procedure is, diagramatically, shown in Figure 3.9.1.

3.10 THE COMPLETE STRESS SOLUTION IN THREE-DIMENSIONS

Assume that the stress system shown in Figure 3.10.1 is a positive one. If the entering light is parallel to the Y-axis, then the scattered light observations are contained in the ZX plane. The difference of the secondary principal stresses for this plane, $(p - q)_{zx}$, can be directly determined from the fringe pattern. Similarly, when the entering light is parallel to the Z-or X-axis, obsevations are on the XY or YZ plane, respectively, and again $(p - q)_{xy}$, $(p - q)_{yz}$ can be found.

The directions of the secondary axes can be determined from the scattered light intensity measurements as previously explained. If h_{xy}, h_{yz} and h_{zx} are angles, positively counter-clockwise from the positive X-, Y- and Z-axis, to the algebraically maximum secondary principal stress, p, and in

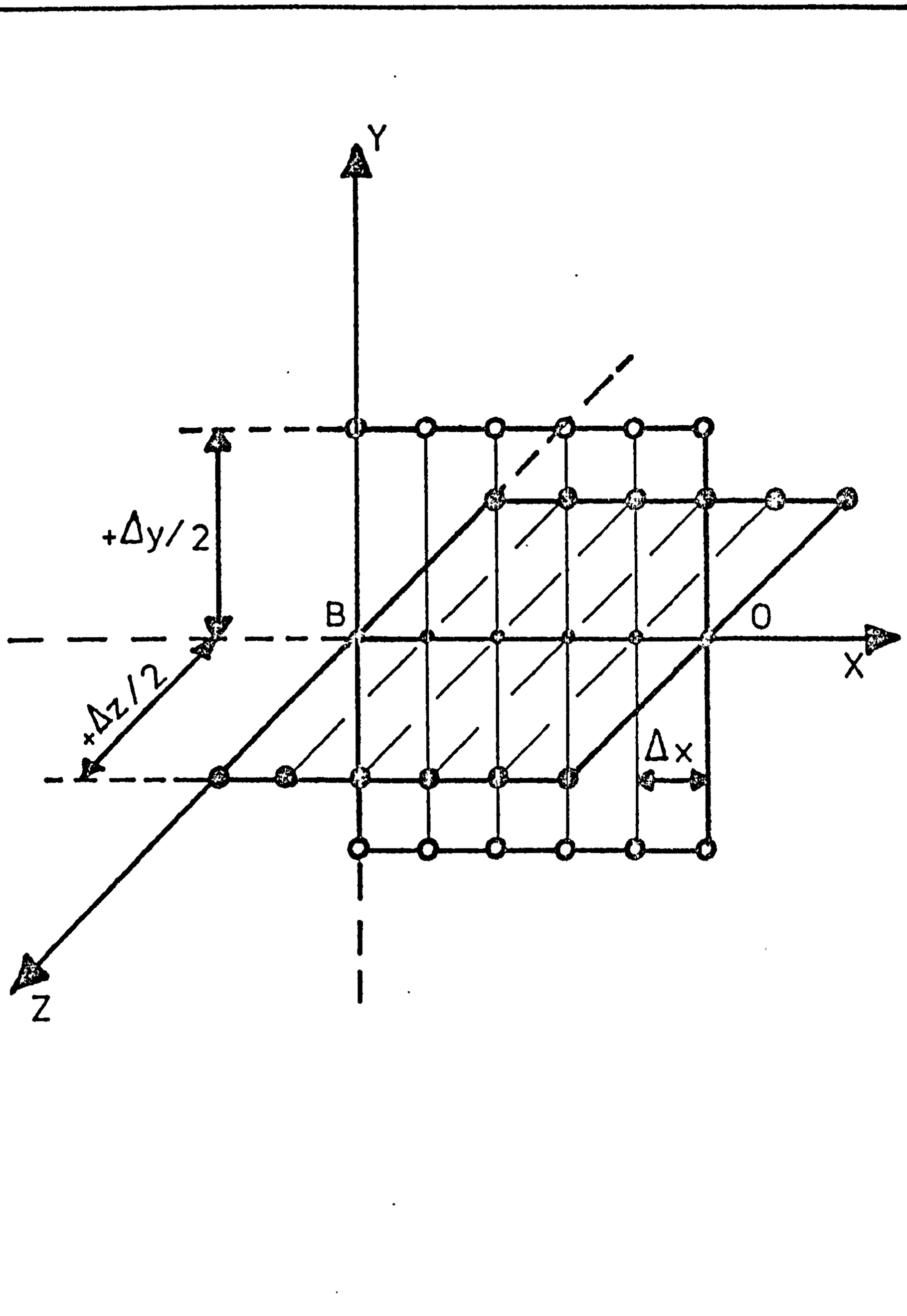

FIG. 3.9.1 THE SHEAR DIFFERENCE METHOD.

the XY, YZ, ZX planes respectively, then

$$\tau_{xy} = \frac{1}{2}(p - q)_{xy}\sin 2h_{xy}$$

$$\tau_{yz} = \frac{1}{2}(p - q)_{yz}\sin 2h_{yz} \qquad (3.10.1)$$

$$\tau_{zx} = \frac{1}{2}(p - q)_{zx}\sin 2h_{zx}$$

and

$$(\sigma_x - \sigma_y) = (p - q)_{xy}\cos 2h_{xy}$$

$$(\sigma_y - \sigma_z) = (p - q)_{yz}\cos 2h_{yz} \qquad (3.10.2)$$

$$(\sigma_z - \sigma_x) = (p - q)_{zx}\cos 2h_{zx}$$

This notation, Figure 3.10.1, will assign the correct shear stress sign, in accordance with the positive stress system.

The individual normal stresses can then be found from the shear difference method, equation (3.9.5), if the normal stress at one point, such as a boundary point, is known. Care should be taken, however, in using this equation that the correct sign is given to all quantities.

3.11 THE SCATTERED LIGHT TECHNIQUE IN TWO-DIMENSIONS

Assume conditions of plane stress so that the stress components parallel to the Z-axis are zero. If the entering light is along the X-axis, then

$$(p - q)_{yz} = \frac{1}{C}\frac{dn}{dx} \qquad (3.11.1)$$

Since conditions of plane stress have been assumed, the σ_z

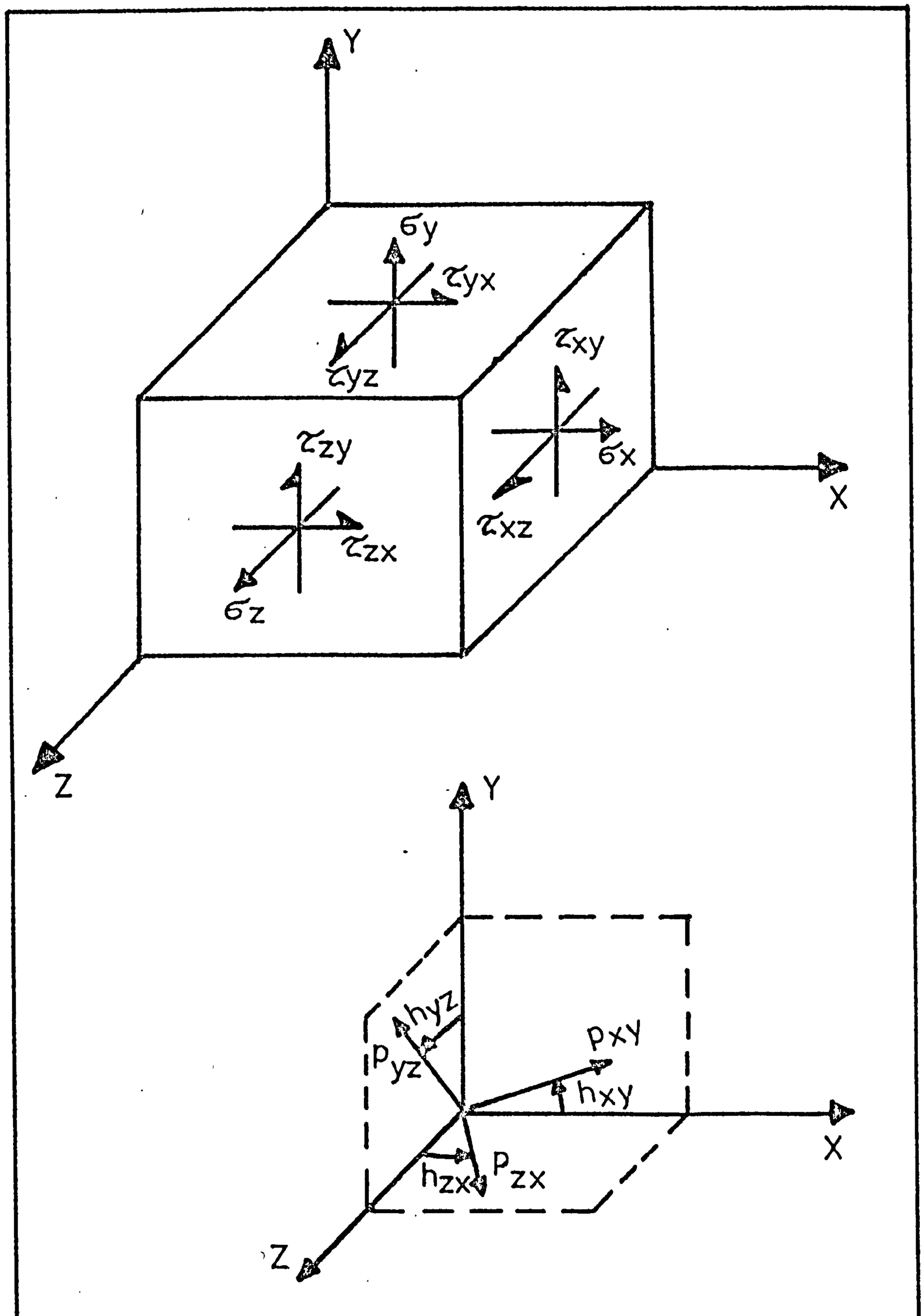

FIG. 3.10.1 POSITIVE STRESS SYSTEM.

component does not contribute towards the fringe pattern, and because the observations are on scattered light entering parallel to the X-axis, the σ_x component will do likewise. The only effective stress, therefore, is the σ_y component. It then follows, from the above equation that

$$\sigma_y = \frac{1}{C} \frac{dn}{dx} \qquad (3.11.2)$$

Similarly, if the light enters parallel to the Y-axis, then

$$(p - q)_{zx} = \frac{1}{C} \frac{dn}{dy} = \sigma_x \qquad (3.11.3)$$

The scattered light technique, therefore, can be used for direct determination of the normal stresses, when conditions of plane stress are assumed. In addition, from the properties of the stress invariants

$$(\sigma_x + \sigma_y) = (p + q)_{xy} = \frac{1}{C} (\frac{dn}{dx} + \frac{dn}{dy}) \qquad (3.11.4)$$

If, therefore, the $(p - q)_{xy}$ values are determined from conventional photo-elastic methods, the scattered light can be used as a means of separating the principal stresses, in two dimensions.

3.12 THE SCATTERED LIGHT POLARISCOPE

When examining models, using the scattered light photo-elastic technique, the incident light should possess the following characteristics:

(a) Intense beam

(b) Monochromatic light

(c) Polarised beam

(d) Highly collimated beam

(e) Conditioned cross-section of the beam, so that it is a sheet of light as thin as possible

The work of many investigators[97,98,102], as well as the author's early experiences on this subject[103], revealed that it was nearly impossible to fulfill accurately, the above requirements by employing optical systems based on conventional light sources. As a result, therefore, the potentiality of alternative light systems had to be examined and in particular, that of the laser beams.

The application of lasers, in scattered light photo-elasticity, was firstly attempted by Taylor et al[101] with very encouraging results. The laser beam, due to its structural principles, fully satisfies the requirements set at the beginning. Is an intense, monochromatic, polarised and highly collimated beam, and due to its small width (about 2mm) can be used directly as a line of light without necessitating transformation to a rectangular sheet of light. This means that the laser itself is sufficient to fulfill all the characteristics of the light system, without requiring the

addition of other optical components into the system, with the possible exception of a quarter-wave plate when circularly polarised light is desired.

After a careful examination of the various types of lasers available, it was decided to use a continuous emission Helium-Neon gas laser, of 2mW power, before polarisation. The latter was achieved by an internally introduced magnetic field. This laser, although small, was found sufficient for scattered light investigations and in addition, was, relatively, inexpensive. However, there is an inherent disadvantage in these lasers, concerning the wavelength of the output light. The Helium-Neon emission has a wavelength of about 6328Å (red band), and it was mentioned previously, that in the atmosphere the scattering intensity is inversely proportional to the fourth power of the wavelength. Greater intensity and more fringes for the same stress level (better sensitivity), can be obtained, therefore, by using a laser with a shorter output wavelength. The Argon lasers, for example, are capable of output wavelengths within the range of 4800Å (blue band) to 5200Å (green band). However, when compared with the Helium-Neon type, Argon lasers are excessively costly and rather uneconomical for this type of instrument.

The models were stressed by using a simplified loading frame consisting of two 13 x 13cm perspex plates, of sufficient

thickness, 1.27cm, to avoid any bending tendencies during loading. These plates were held in position by four screws, O.B.A. size, running through four holes at their corners. One of the plates was rigidly fixed, while the other was able to slide through the screws so that the required compression could be imposed on the model and subsequently maintained by means of four brass bolts. The loading device was adequate when simulating uniform compressive loading, however, if the approximate nominal value of the applied stress was required then the model had to be loaded through a specially designed rig, shown in Figure 3.12.1.

If a model is to be fully investigated using the scattered light method, then it must be capable of the following:

(a) Rotation about the vertical (light) axis

(b) Vertical movement (raised or lowered)

(c) Transverse and radial movement in the horizontal plane.

This is accomplished on a special accommodating assembly shown in Figure 3.12.2. The whole system is held into position by the two vertical shafts of the frame, which are running through two holes drilled on a rotating stage. This stage, R, has a 5cm central hole to enable light passage into the model. The latter, stressed inside the loading frame, L, is screwed on to a bracket, B, so that all three axes of the

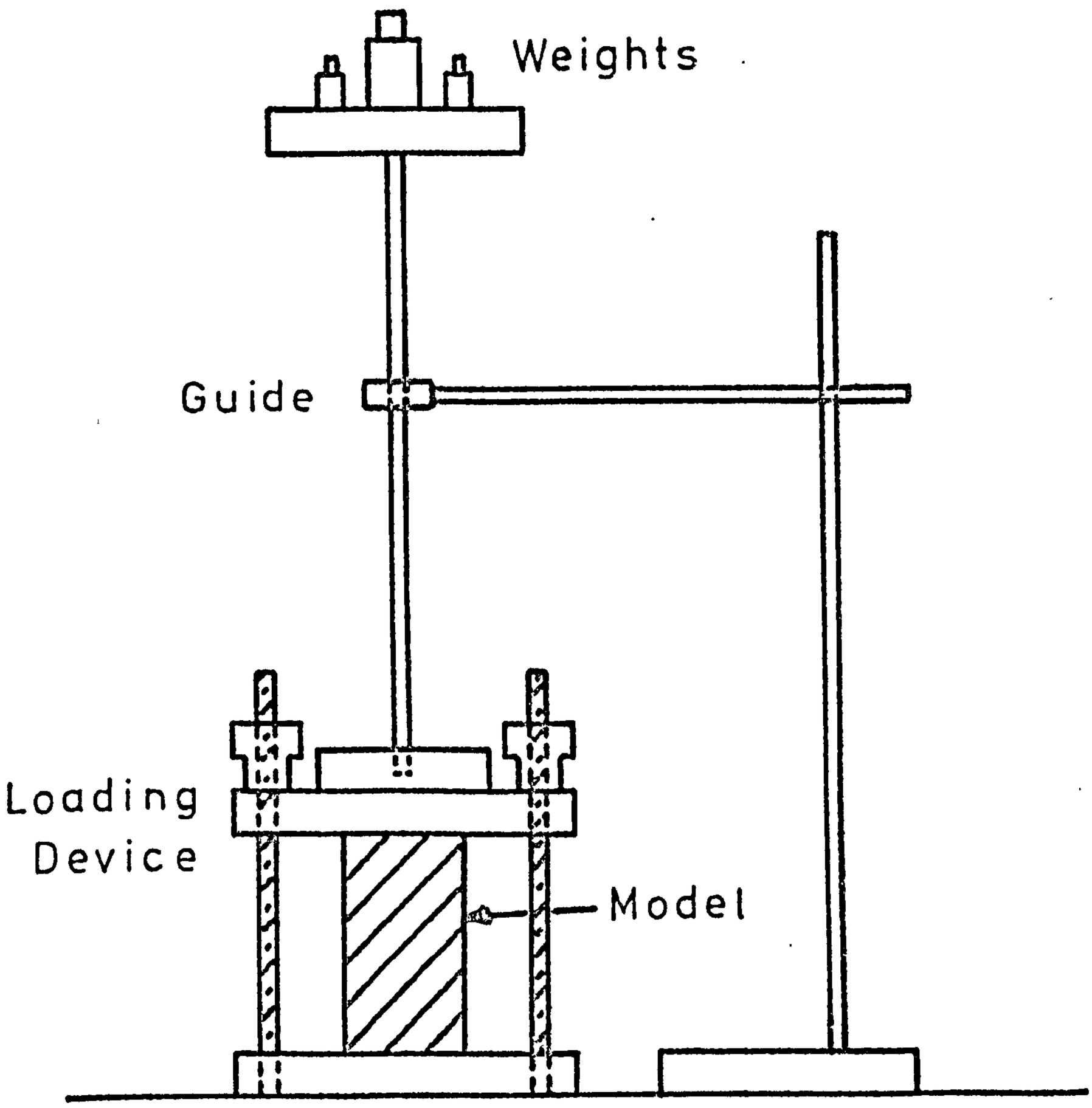

FIG. 3.12.1 LOADING RIG.

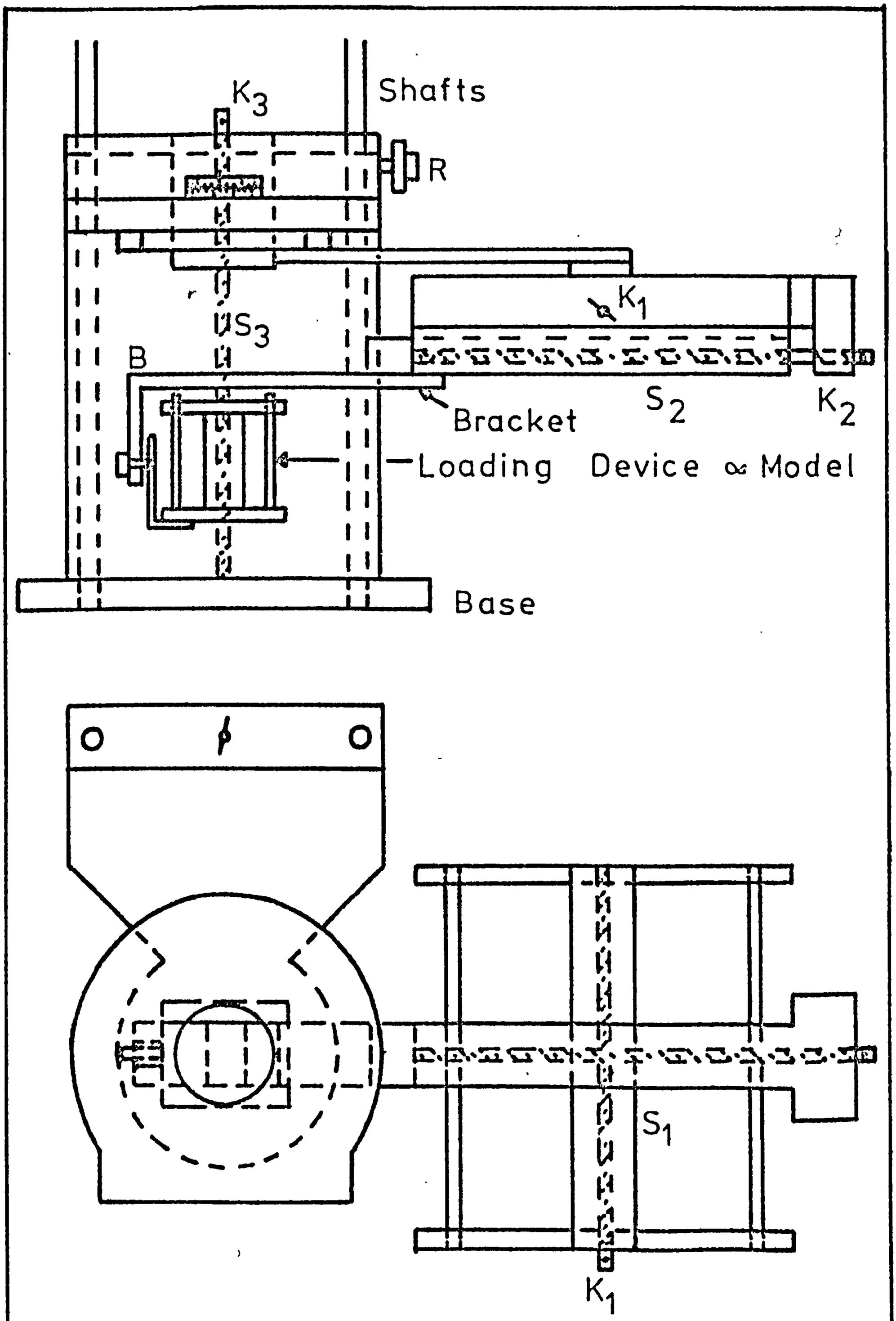

FIG. 3.12.2 MODEL'S ACCOMMODATING ASSEMBLY.

model can be made, in turn, vertical, and thus parallel to the entering light. When the stage is rotating, therefore, about the vertical axis, the whole assembly, including the model, is following the motion and the angle of turn can be read on a horizontal Vernier plate with respect to a reference axis. Two screws, S_1 and S_2, supply the horizontal movement (radial or transverse) to the bracket and consequently to the model. This movement is accurately read by the two knobs, K_1 and K_2, graduated into 25 divisions each representing a movement of 0.024mm. A third screw, S_3, vertical between the two shafts, can be used to raise or lower the fixture, the movement read, in this case, by a similar knob, K_3. This arrangement, therefore, enabled the model to undertake the three basic movements, previously mentioned, and as a result, every point of the model could be examined.

In order to eliminate undesirable refractions, the model was immersed inside a 30 x 17 x 19cm perspex tank, filled with a liquid of the same refractive index as the model.

When compensation was used, the compensator was firmly supported on top of the rotating stage, so that it could follow the model's rotation.

The horizontal arm of the polariscope determines the observation plane, and comprises the data reduction station. The following operations are possible at this station:

(a) Visual observations of the stress pattern

(b) Photographic recordings of the stress pattern

(c) Direct determination of the birefringence, at any point or line

(d) Direct determination of the isoclinic parameters at any point.

These operations can be carried out by employing a special photo-metric system, consisting of the following components:

(i) Technical Camera: The fringe pattern was focused on to the back screeen of a Micro Technical Camera, through a high resolution lens. Photographs were taken using a Kodak Tri-X film, with exposures ranging from 1-3 minutes.

(ii) Scanning Device: Is a brass plate, 15 x 15cm in cross-section and 0.5cm thick. The plate has a central slot, 12cm long and 0.7cm wide in front of which a strip of high quality glass screen is attached. A very accurately cut screw, O.B.E. size, is positioned adjacent and parallel to the slot, with its end coupled to a small synchronous, reversible, electric motor. A specially designed carrier is passing through this screw accurately threaded, so that it is capable of running up or down the rotating screw, with constant speed. The carrier is 4.7 x 1.5cm

in cross-section and 1.2cm thick, and has a 0.6cm hole at one end which always remains co-centric with the slot, as the carrier moves. The motor is operating at 250rpm and since a slow speed for the carrier is required, a 5/1 reduction gear is used; this gives to the carrier a linear speed of about 1/15cm/sec.

The plate was rigidly fixed on the bottom of the camera which had its back screen removed. In this way, the fringe pattern was focused as near to the slot as possible. Extreme care was taken so that the slot was perfectly co-axial with the laser line, passing through the model; as a result the carrier's hole was precisely tracing this line as it moved up or down. The system is shown in detail in Figure 3.12.3.

(iii) Fibre Optics Element: It consists of numerous glass fibres, arranged together to form an element, and is capable of transmitting light or images by a process of total internal reflection. The element can be either coherent or non-coherent; in the former the relative positions of the fibres are the same at both ends and, therefore, the image is transmitted unaltered, whereas in the latter, the fibres are randomly placed, so that only light can be transmitted.

The fibre optics used here was a 3mm in diameter non-

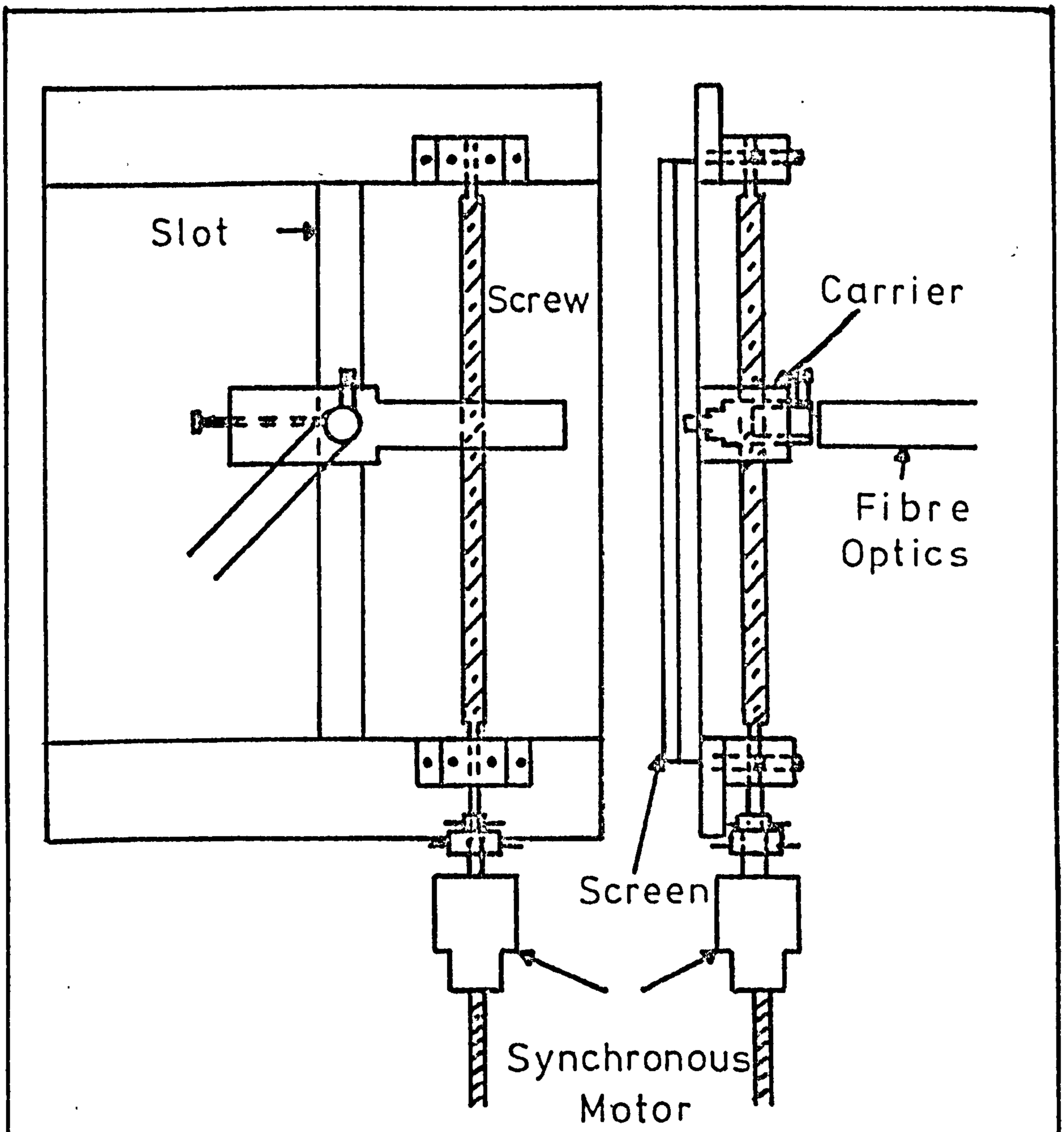

FIG. 3.12.3 THE SCANNING DEVICE.

-coherent element. One end of the element was locked inside a small brass tube, which, in turn, was placed inside the carriers hole, whereas the other was fixed on to a photo-multiplying tube, using a light proof seal. To ensure that fringes were picked singularly by the element, and no interaction was taken place, the tube inside the carrier's hole, had a very small observation hole, of rectangular shape, about 0.5mm long, depending on the fringe spacing.

As the fibre optics was tracing the pattern inside the travelling carrier, therefore, any changes of light intensity were accurately transmitted to the photo-multiplying tube (dark or light fringes). Similarly, with the carrier stationary, any intensity changes at a particular point, due to model rotation, were also detected.

(iv) Photo-multiplying Tube: The scattered light transmitted from the model to the tube, via the fibre optics element, falls on the tube's photo-cathode. Each photon has a probability of causing the emission of photo-electrons from the photo-cathode. This probability will depend upon the material of the cathode, and the wavelength of the incident light. Only a fraction of the emitted electrons, therefore, will reach the tube's first dynode,

and produce secondary pulses of electrons, which are multiplied as they travel along the stages of the tube. Ideally, all the pulses resulting from single photo-electrons should be of the same height. However, in reality, they show a spectrum of heights since the secondary emission is a statistical process.

In addition to the pulses due to the incident light, the tube also exhibits 'dark' pulses, regardless of whether the cathode is illuminated. During this experimental procedure, however, it was assumed that the average dark pulses were much weaker than the average signal pulses.

(v) Power Supply: A high voltage system is required to operate the photo-multiplying tube. Basically, it consists of a special transformer coupled to a solid state regulator, so that the transformer's output voltage automatically adjusts itself to the needs of the regulator.

(vi) Pico-ammeter: The photo-multiplying tube's output is fed into a pico-ammeter. This is extremely sensitive instrument, capable of measuring over 17 ranges, from 10^{-2} to 10^{-10} amperes, full scale. Its accuracy is claimed to be, by the manufacturers, between $\pm$ 2-4%, so that any variation of the light intensity, however small,

can be easily detected and read by this instrument.

(vii) Recorder: The data required for complete analysis, birefringence and isoclinic parameters, depend on the intensity variations rather than actual intensity readings. The output of the pico-ammeter, therefore, was fed into a potentiometric pen recorder. All the points of light variation, i.e. maximum, minimum or constant intensity, could, therefore, be detected from the chart.

Since the recorder has a range of running speed, all different to that of the fibre optics, the former had to be calibrated in terms of actual distance inside the model.

A schematic diagram, together with a photograph, of the scattered light polariscope are given in Figures 3.12.4 and 5. For safety reasons, the laser was fixed horizontally, and was vertically reflected by a right angle prism. Figures 3.12.6 to 3.12.9 show photographs of two fringe patterns and corresponding chart traces. Figures 3.12.10 and 11 show the fringe order against distance curves, and the birefringence curves, for these patterns, resulting from a graphical differentiation procedure. Such procedure yields better averaging results than the conventional slope of the tangent method.

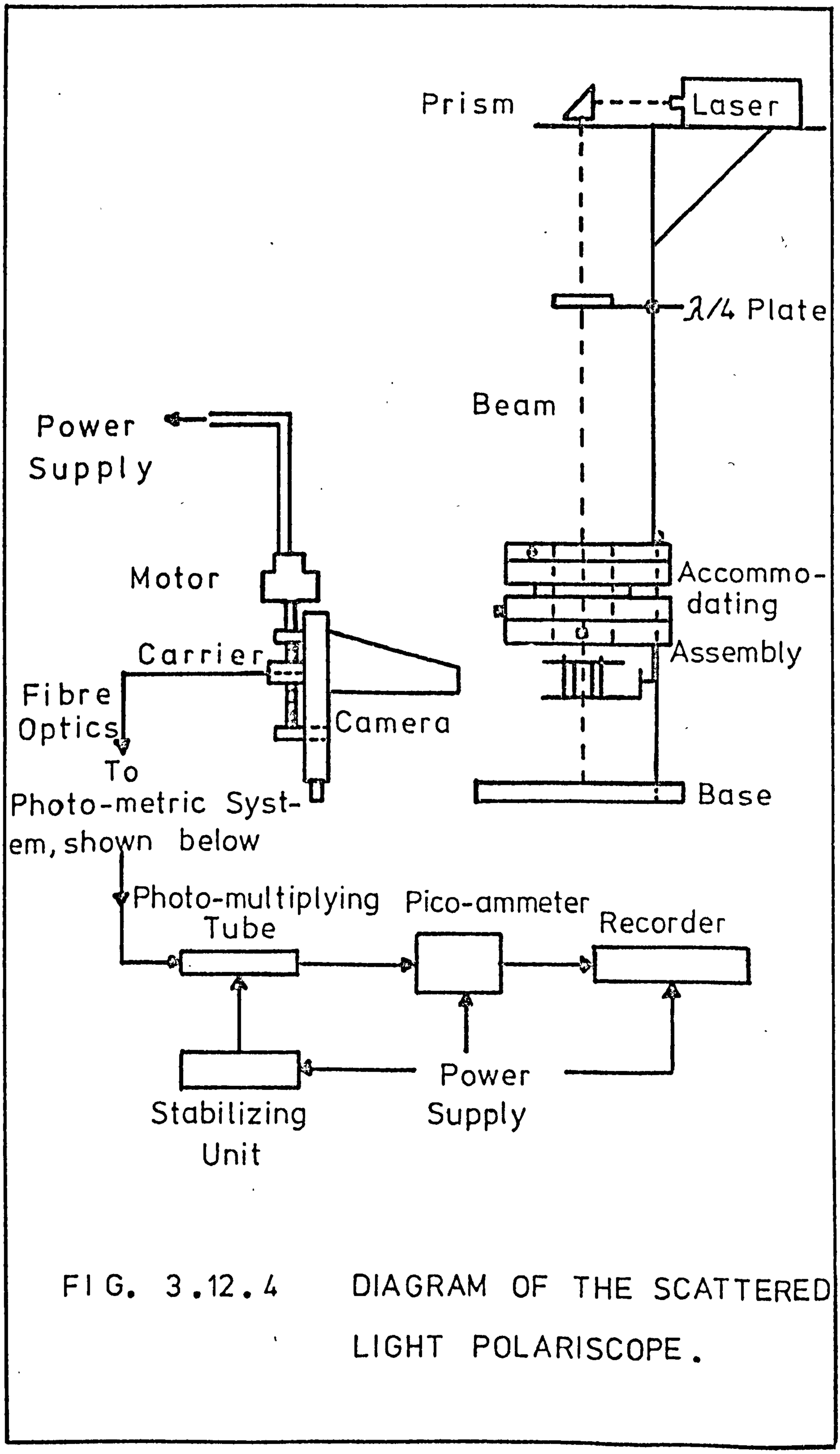

FIG. 3.12.4 DIAGRAM OF THE SCATTERED LIGHT POLARISCOPE.

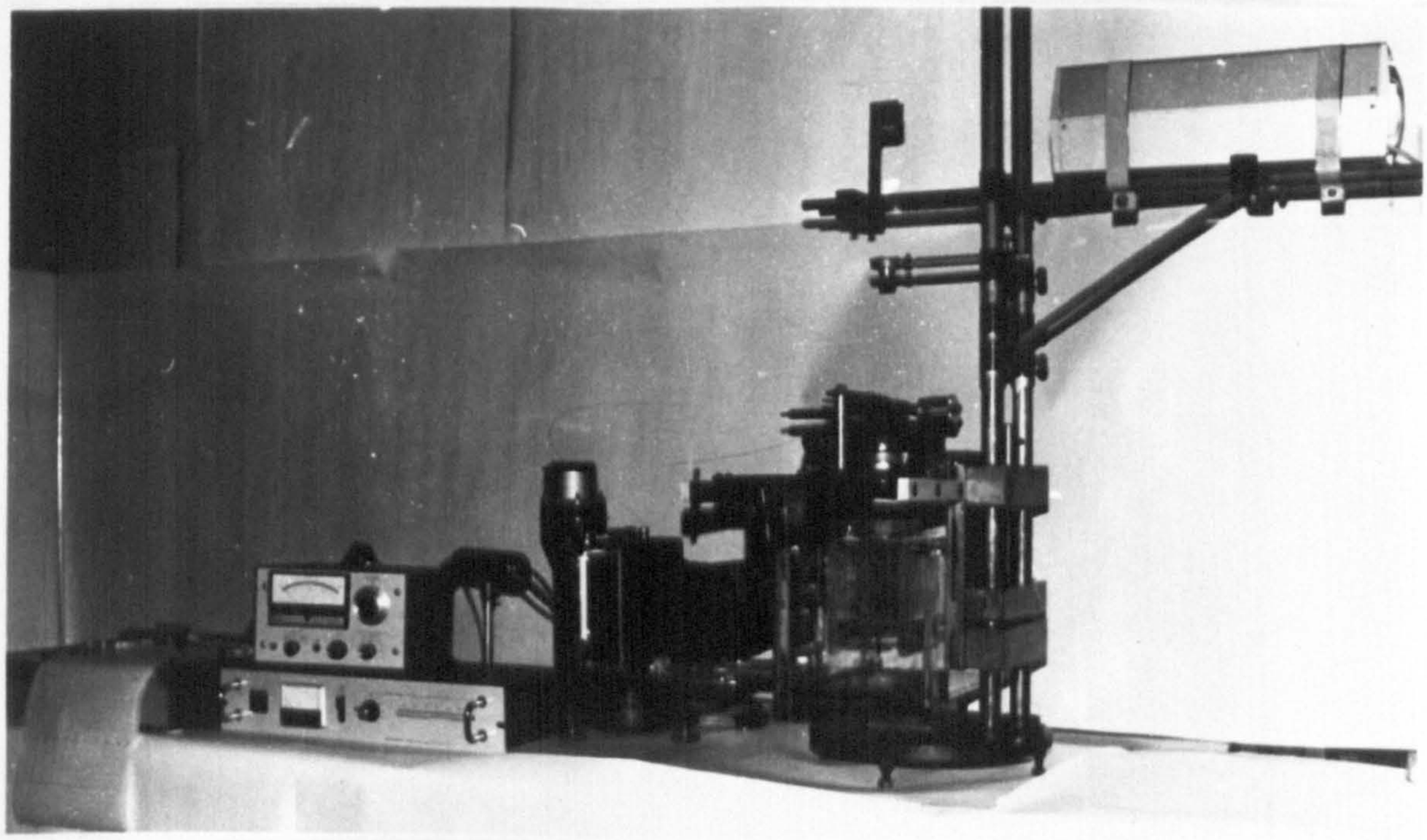

FIG. 3.12.5 THE SCATTERED LIGHT POLARISCOPE.

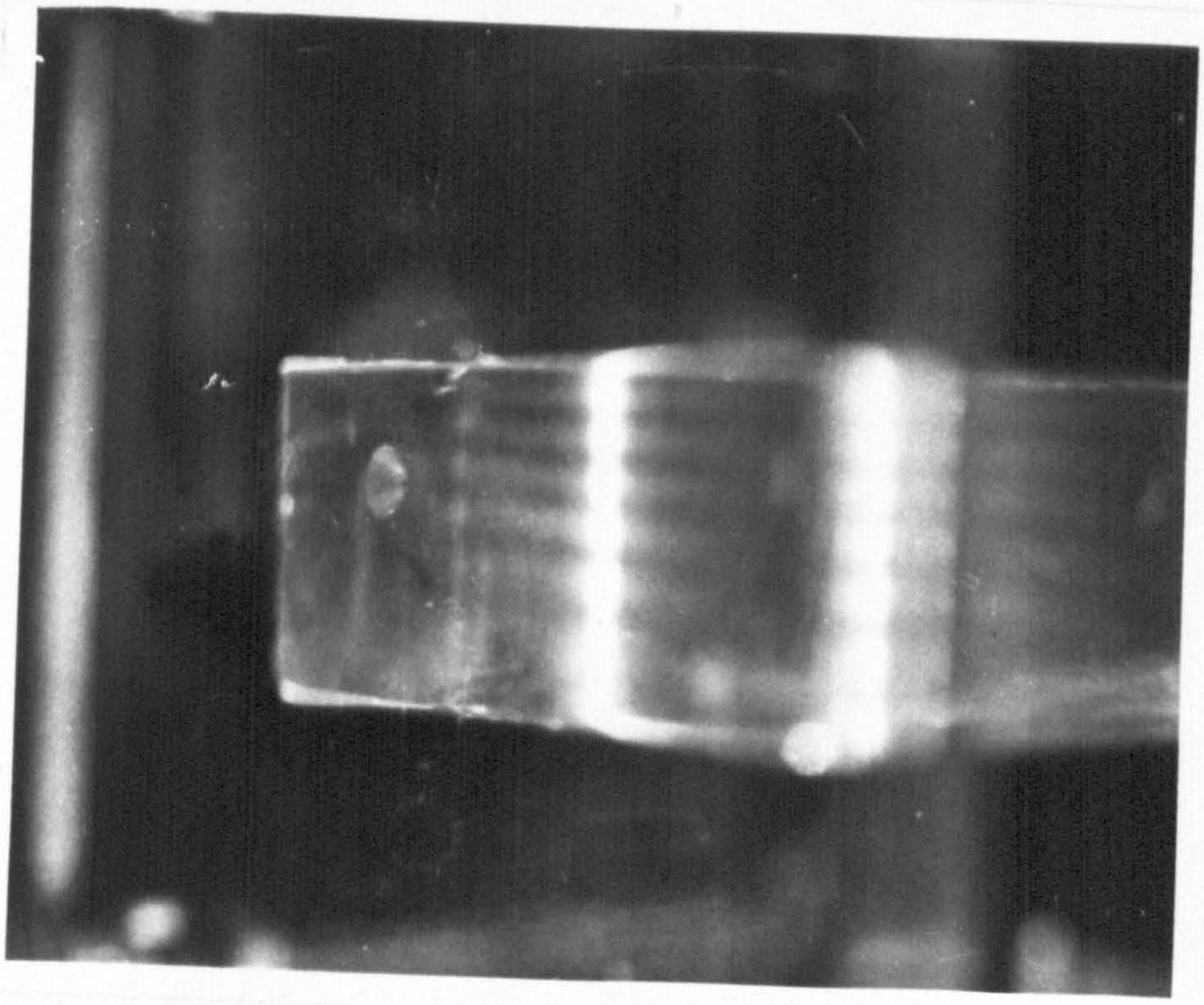

FIG. 3.12.6 FRINGE PATTERN OF MODEL A.

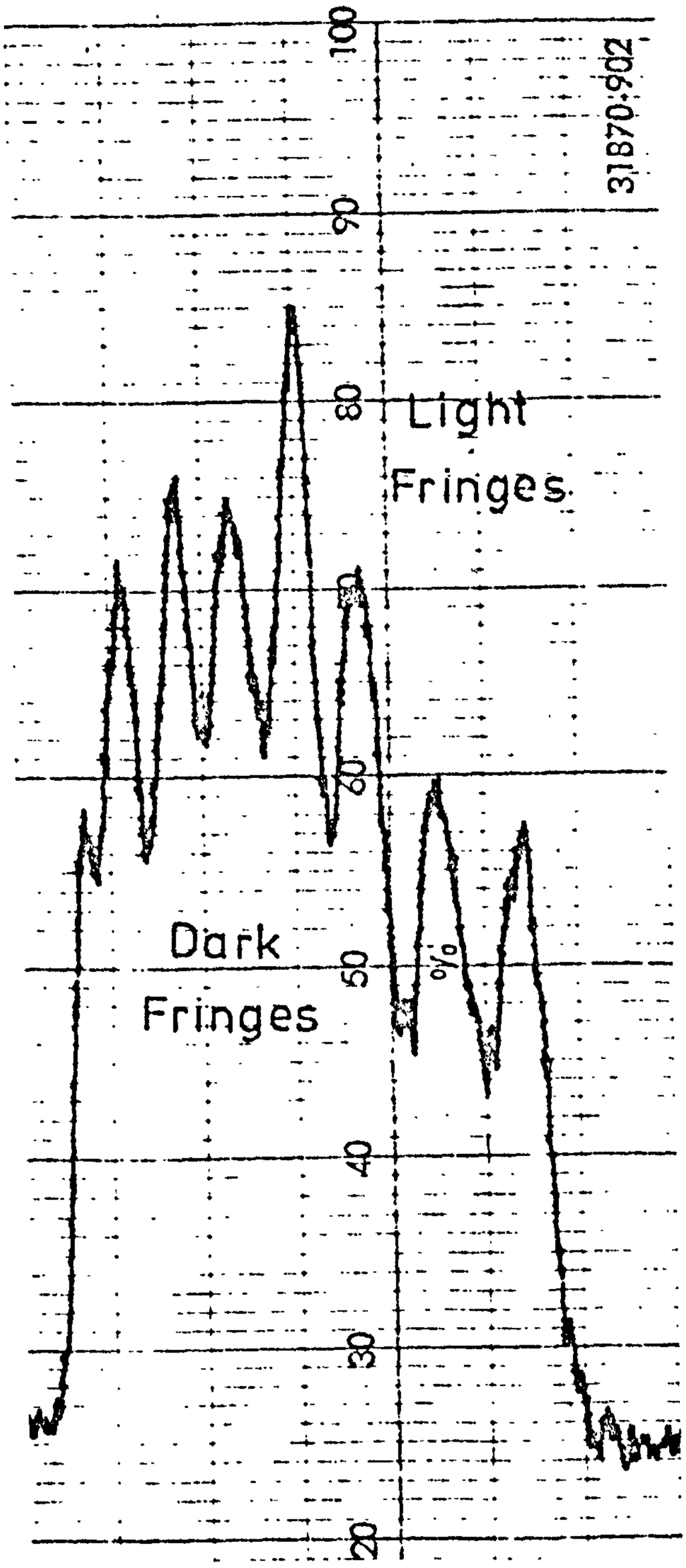

FIG. 3.12.7 FRINGE TRACING OF MODEL A.

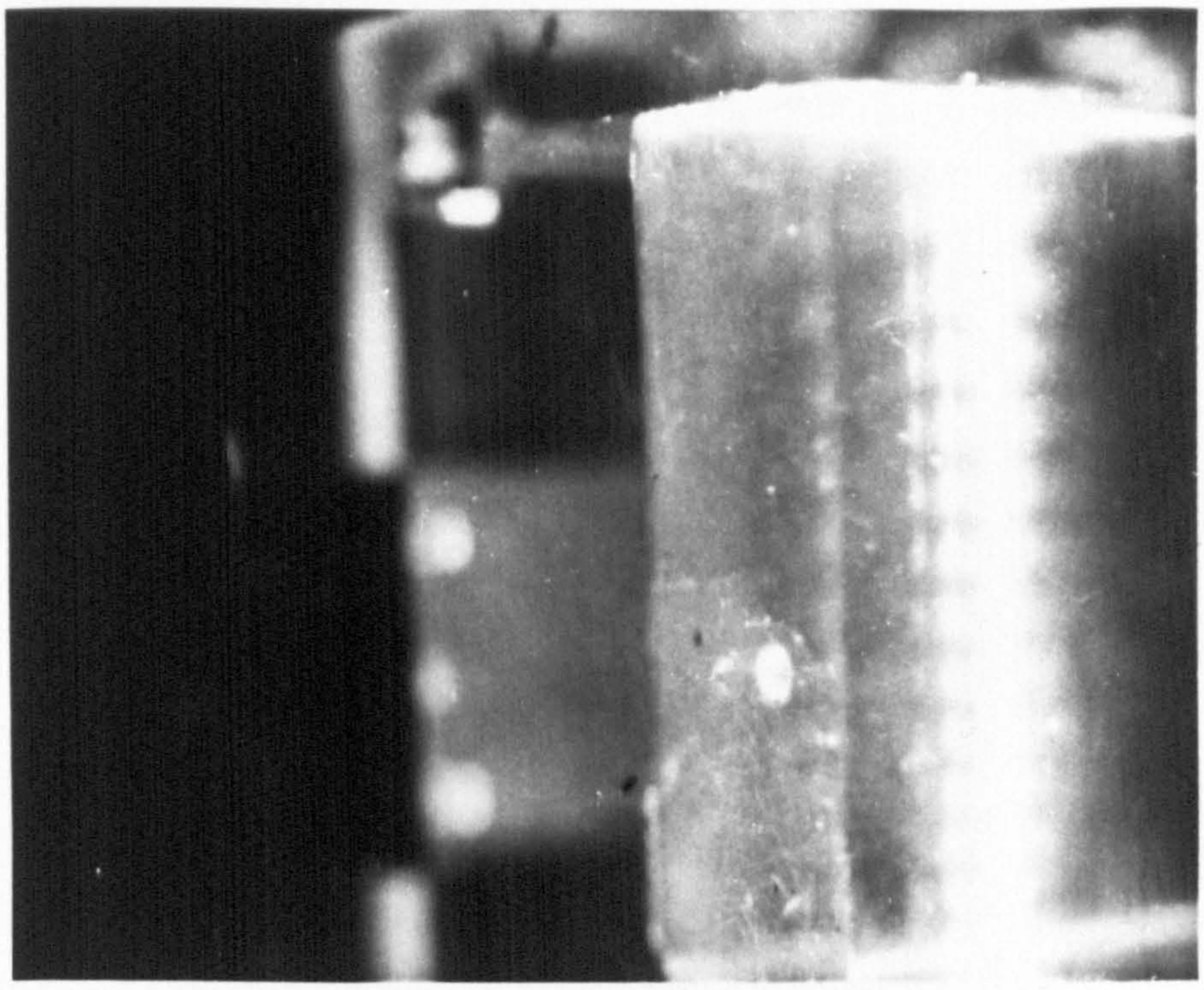

FIG. 3.12.8 FRINGE PATTERN OF MODEL B.

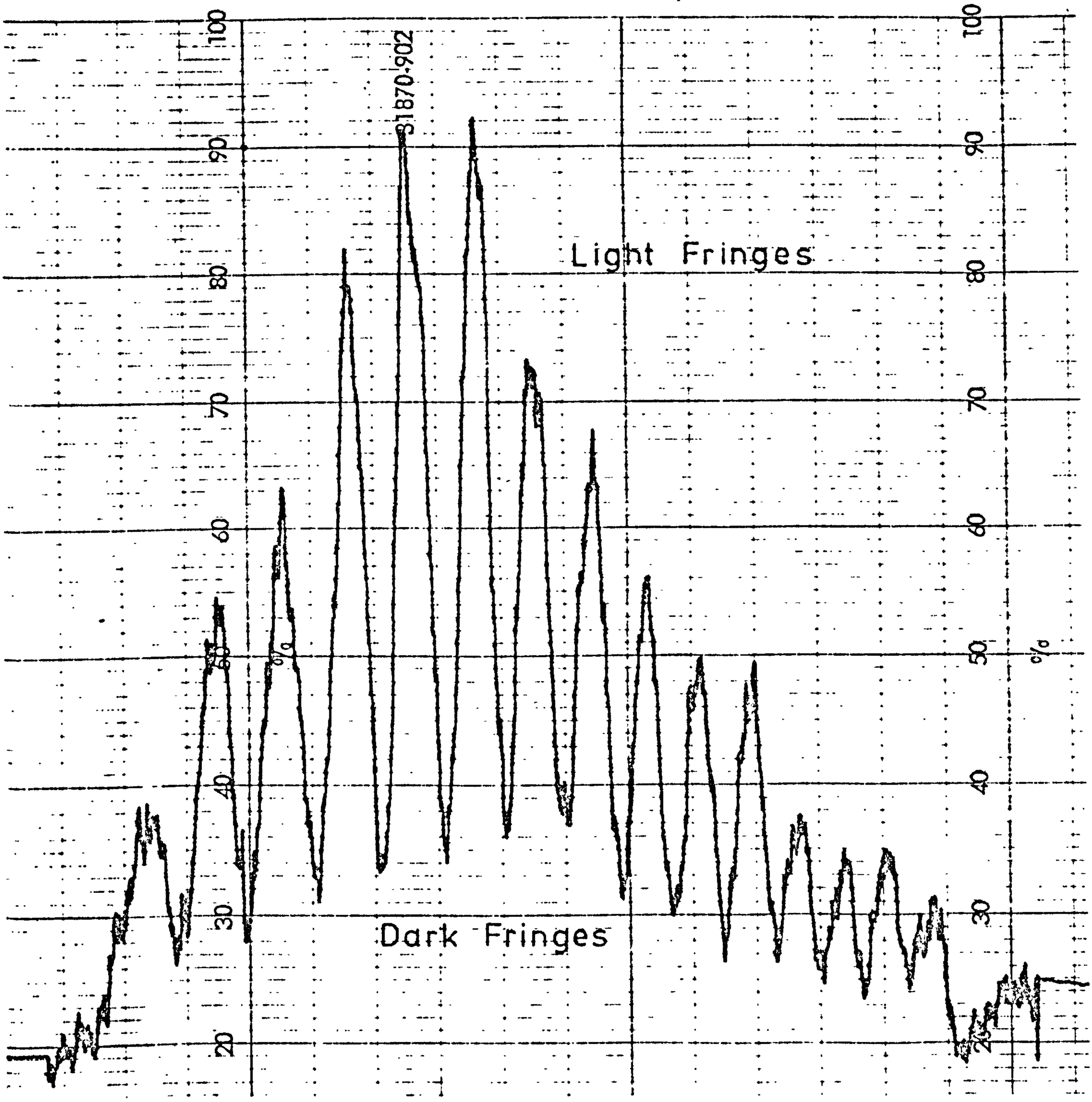

FIG. 3.12.9 FRINGE TRACING OF MODEL B.

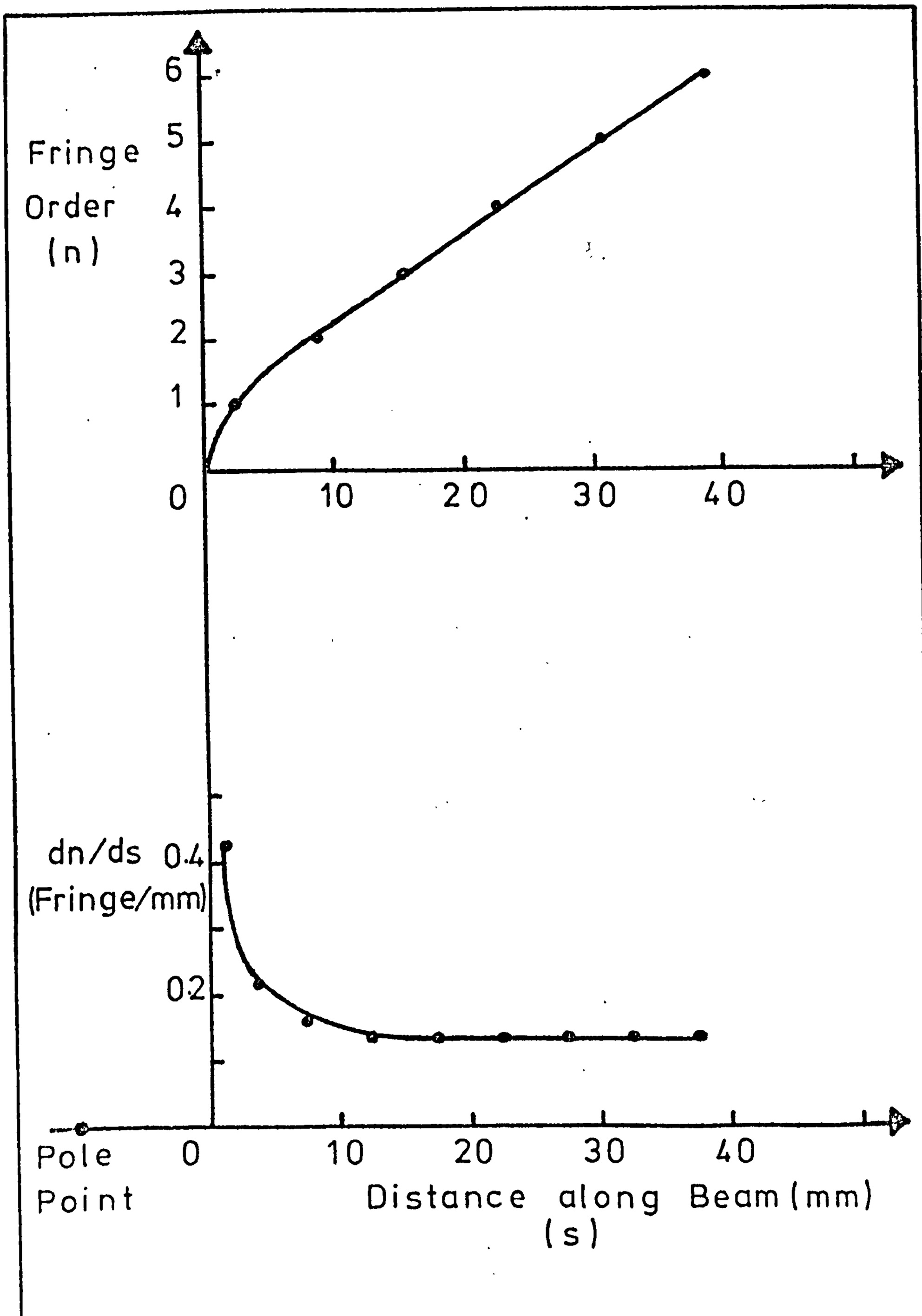

FIG. 3.12.10 BIREFRINGENCE CURVE OF MODEL A.

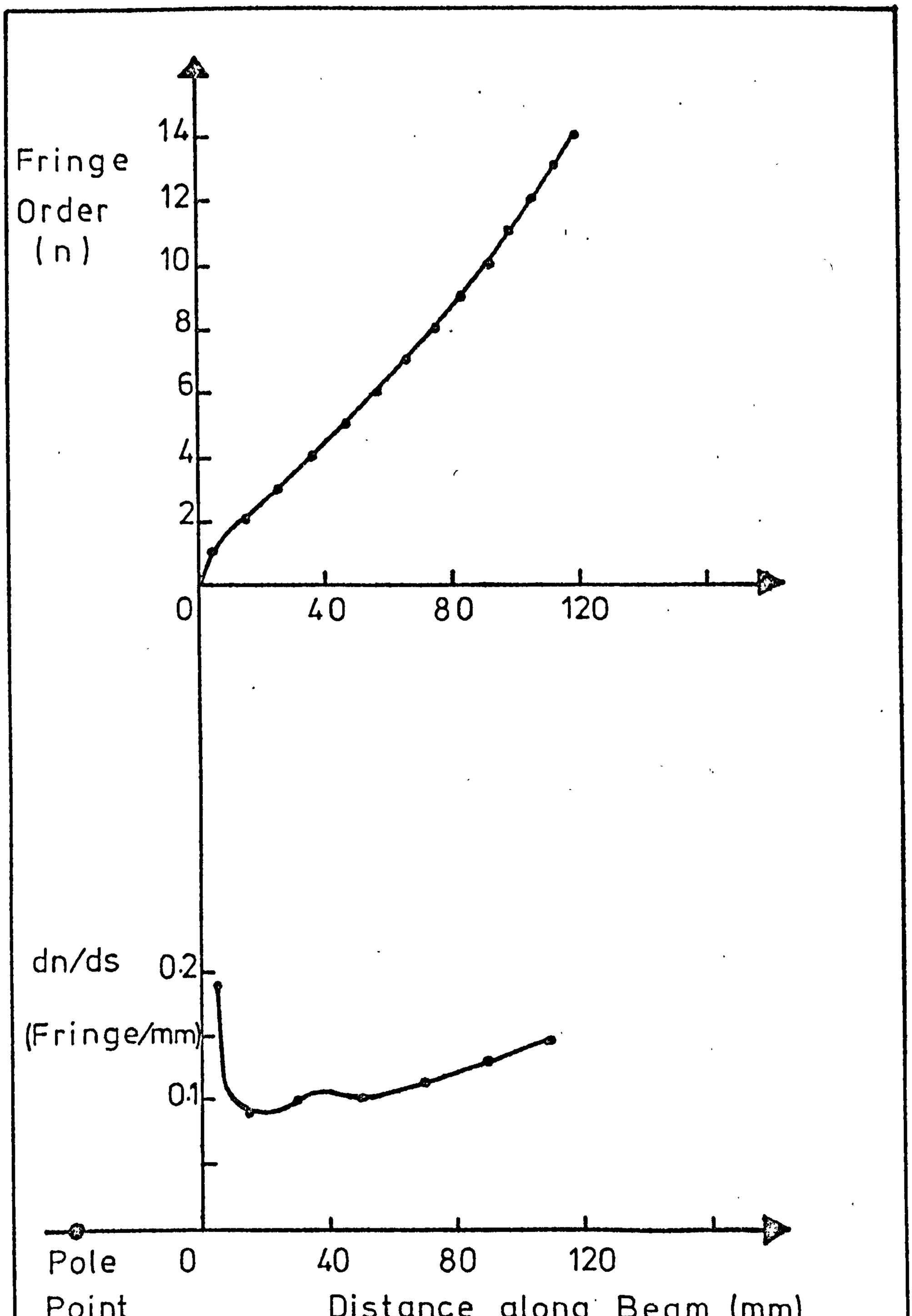

FIG. 3.12.11 BIREFRINGENCE CURVE OF MODEL B.

3.13 MODEL MATERIALS IN SCATTERED LIGHT PHOTO-ELASTICITY

Early investigators were faced with a big task when they tried to establish models capable of light scattering, which could give a complete stress analysis under live loading conditions. This, in general, was due to the lack of information regarding scattering properties of photo-elastic materials.

The problem was partly overcome by resorting to the previously mentioned freezing method. It was known that certain diphasic materials exhibit a small degree of scattering as well as being capable of stress freezing. It follows, therefore, that after the freezing cycle, these models could be non-destructively examined in scattered light[97,98].

Such examinations were not, strictly speaking, scattered light, neither freezing investigations, but a combination of the two. They are best described as stress freezing analyses, in which the scattered light executed an imaginary slicing, instead the actual physical slicing required in the conventional freezing method.

In order to achieve investigations under live loading conditions, two materials were considered. At the beginning Gelatin was used, a material of remarkable optical sensitivity (nearly 400 times greater than the epoxies), with excellent 'natural' scattering properties, and capable of stress freezing,

in the literary sense. This material is well known in two-dimensional photo-elasticity, and in particular, in problems of gravity loaded structures. However, although gelatin exhibits a number of attractive features, nevertheless, it had to be abandoned in the end, due to its high susceptibility to optical, mechanical and biological creep.

After a careful examination into the possibilities of other available photo-elastic materials, it was decided that Polyurethane Rubber could provide the alternative material. Polyurethane consists of two parts, a prepolymem (Solithane 113) and a catalyst (Solithane 300). It has excellent mechanical and optical properties, is practically elastic, at room temperature over a great range of strain, and is free from time-edge stresses. In addition, by controlling the amounts of prepolymer and catalyst in the mixture, modular ratios up to 40/1 can be achieved thus rendering the material ideal for multilayer model studies. However, unlike gelatin, this material does not exhibit any natural scattering properties, and if it is to be used in scattered light photo-elasticity, the scattering effect must, in this case, be induced.

Induction of scattering or exaggeration of weak scattering ability (as in epoxies), was firstly suggested by Jessop[97]. This can be achieved by adding to the material extremely small particles (less than the wavelength of the incident light), of scattering media, as silica or alumina. Preliminary

investigations, using silica, were not successful mainly because the majority of the commercially available silicas was not of sufficiently fine grade. This problem, however, was overcome when a silica with trade name Aerosil 200 was traced, having an average particle size of about 12 x 10^{-9}m, as compared to 632.8 x 10^{-9}m of the wavelength of the red light.

Further experimentation revealed that optimum scattering was induced to the polyurethane, when adding an amount of about 0.030ml per gm of mixture, of this silica. Polyurethane-silica models were solely used, therefore, throughout these investigations, the material been casted according to the procedure suggested by McNicholas et al[104].

3.14 CONCLUSION

(i) Three-dimensional stress analyses, based on strain gauge data, although accurate and reliable, do, however, require a great number of gauges and associated equipment and can be, therefore, very expensive in time and money. On the other hand, photo-elastic explorations are much speedier and economical, offering in addition, the possibility of an infinite number of data points.

(ii) From the two established photo-elastic methods of three-dimensional stress analysis, the scattered light technique shows a number of attractive features. Stresses can be fully analysed on the surface or inside a model

during live loading and under any combination of applied stresses, including contact, thermal and even plastic zone stresses. This technique does not require the tedious stress freezing and physical slicing of the model and as a result is completely free from the adverse effects of the temperature on the Poisson's ratio which are the basic characteristics of the freezing method.

(iii) For a complete stress investigation, using the scattered light technique, two parameters should be known at the point of interest, the birefringence and the isoclinics. From the methods listed capable of determining these parameters, it is evident that the critical factor, in such investigations, is the presence of rotational effects. If the secondary axes do not rotate, then all these methods are applicable and any one of these can be used. If, however, the rotation is pronounced and can not be ignored, then only certain of these techniques can be used to evaluate the photo-elastic parameters.

(iv) The presence and extent of the secondary stress axes rotation can be easily established from examination of the fringe pattern. If this pattern is observed along the light beam, using the same fixed angle, equal to the

maximum intensity angle at the entrance point (i.e. 45^{o} from the secondary axes), then the fringes will be fading along the beam if rotation is present. A more scientific method capable of showing the extent of the rotation, is the one based on the fact that for observations along the secondary axes, the intensity is constant and independent of the retardation when no rotation is present. As a result, if the secondary stress axes are determined at a point inside the model, and observations along these axes at another point on the light beam, show intensity variations when the retardation is altered, then this variation is an indication of the presence and the degree of the rotation of the stress axes.

(v) The separation of stresses, in three-dimensions can be easily achieved by using the Shear Difference method. The method requires the shear stress values at neighboring points along the line of interest and the normal stress value at the starting point (usually the boundary point). However, in applying this method, care should be taken that the correct signs of the shear stresses and linear increments has been attributed, in accordance with the adopted convention.

Since the method simply consists of successive

arithmetic operations readily lends itself to computerisation. This practice is strongly recommended when an extensive investigation program is to be undertaken.

(vi) The scattered light technique has certain distinctive features when applied to two-dimensional photo-elasticity. It can either be used for direct determination of the normal stresses, under plane stress conditions, or as a means of separation of the principal stresses, obtained from conventional two-dimensional photo-elastic methods.

(vii) The scattered light polariscope, having a 2mW Helium-Neon Laser as the main optical component, showed excellent efficiency in light transmission. In addition, the photo-metric system, used for the reduction of data, was proved to be an extremely accurate and time saving one. It is felt, therefore, that any further improvement to this instrument can only be related to the type of the loading device used. Throughout the investigations the simple device, previously described, was used for loading the models. This was only capable of imposing a uniformly distributed compressive stress, with reasonable accuracy. In addition, if the nominal value of the applied stress had to be known, then a separate mechanism had to be used,

as previously mentioned. This, in effect, meant that if any investigation was to be carried out under varying loading conditions, the whole loading procedure could be inaccurate and time consuming. This problem, however, can be overcome by employing a more capable loading device as the sophisticated stress transducers.

(viii) It was estimated that the cost of building this instrument was in the region of £1,000. It is worth mentioning, at this point, that a scattered light polariscope is now commercially available in two types, from the 'Photoelastic Inc.Co.'[105]. These two, extremely sophisticated versions of the instrument were priced at about £23,000 and £14,000, respectively. It is justifiable, therefore, to claim that by comparison, the accuracy and efficiency of the built polariscope was surprisingly good.

(ix) The induced scattering effect to the otherwise non-scattering polyurethane rubber through the addition of extremely finely divided silica, was proved totally successful. Care, however, had to be taken when examining such models so that if an occasional bubble or cluster of silica particles occurred, the resulting high brightness spots would not influence the measurements of the isoclinic parameters or birefringence, when using techniques based on intensity observations.

(x) Summing up, the author's intention was to present the principles behind the scattered light method, with its advantages as well as limitations. It is not postulated here, therefore, that this method could replace conventional two- or three-dimensional stress analyses, but is merely suggested that for certain problems, scattered light photo-elasticity could be the most advantageous means of solution.

CHAPTER IV

AN IMAGE DE-ROTATION TECHNIQUE FOR GRAVITY LOADING SIMULATION IN 'REAL-TIME'

CHAPTER IV

AN IMAGE DE-ROTATION TECHNIQUE FOR GRAVITY LOADING SIMULATION IN 'REAL TIME'

4.1 INTRODUCTION

Gravitational forces constitute the primitive stress field, acting upon underground excavations. Their state of equilibrium is continually disturbed as mining progresses and, as a result, re-distribution occurs creating induced stresses.

When studying mining configurations, it is conventional to assume that they are subjected to a uniform, rather than a gravitational stress field. There are two basic reasons for this assumption. Firstly, the theoretical treatment of gravity loading is a problem of great complexity and can only be applied to rather simplified geometries. Secondly, experimental simulation of the gravitational field, using small scale similar models, is extremely difficult due to the low intensity of the body stresses and can only be attempted by using techniques of stress magnification. Uniform stress fields, on the other hand, are much more flexible to theoretical treatment, as well as being more easily achieved experimentally.

Although most underground configurations can be successfully treated, assuming uniform stress conditions, there are certain problems, as in shallow workings or multi-level excavations, in which this assumption is clearly no longer acceptable. It is important, therefore, to establish gravity

loading simulation techniques, capable of dealing with such problems.

4.2 THE MATHEMATICAL TREATMENT OF GRAVITY LOADING

Theoretical solutions of gravity loaded structures are limited to two relatively simple geometrical shapes, the circular and elliptical openings. Mindlin[106] examined the stress distribution around a horizontal circular tunnel in a semi-infinite elastic solid under gravity, and Sherman[107] that of an elliptical tunnel. Other investigators also attempted this problem with some degree of success[108]. However, from these investigations it is evident that the theoretical solutions of gravity loaded structures are very complicated even for simple geometries and become practically impossible when the shape of the structure is more complex. In the latter case, therefore, only an experimental solution is feasible.

A better approach to this problem, however, is the numerical one basedon the the previously mentioned finite element method. Barla[109] made an extensive study of various shapes of 'floating openings', (i.e. openings at depths ranging from 1.5 to 10 times the radius), under uniaxial and biaxial gravity stress fields, using this method. His conclusions were basically in agreement with the general elastic theory; for openings with aspect ratio of 1 (circle, square or arched opening), the gravitational stresses approach

those due to the uniform loading conditions, at depths more than 4 times the opening's radius; for openings with aspect ratio less than one (rectangles or ellipses), similar behaviour is expected, at depths greater than 6 times the radius.

Barla's results illustrate the differences between gravity and uniform loading for near surface openings. However, even at depths of more than 6 times the radius of the opening, some discrepancies can be observed from his results. For example, for a circular opening under uniaxial gravity stress, the stress concentrations were found to be as shown below:

DEPTH/RADIUS	S	T	B	FIELD
1.5	2.50	-1.10	-0.96	Gravitational
2.0	2.54	-0.96	-0.89	
6.0	2.44	-0.70	-0.74	
10.0	2.45	-0.70	-0.72	
Any ratio	3.00	-1.00	-1.00	Uniform

T and B are the stress concentrations at the top and bottom of the opening, along the load axis, and S a boundary point, at right angles to the applied load (tensile concentrations nregative). It is seen that tensile concentrations reduce with depth and since the gravity field is non-symmetrical with respect to the horizontal axis, the top and bottom concentrations are different. These concentrations, however, tend to

equalise, as the depth increases and uniform conditions approach. The nominal value of the concentrations, is therefore, smaller than that predicted by the uniform loading conditions and in addition, this deviation becomes progressively worst as the depth increases, instead of the opposite. A similar trend can also be seen from the concentrations of the side point S. These remarks, however, are in disagreement with Barla's conclusion, stated above, and could be the result of the basic assumptions of the finite element method, or of the actual mesh size.

This example, therefore, illustrates the need for suitable experimental procedures for gravity loading simulation. Even in the case where analytical solutions can be derived, such a procedure will be invaluable for checking the accuracy of the results.

4.3 EXPERIMENTAL SIMULATION OF GRAVITY LOADING

The study of underground excavations is carried out, experimentally, by scaling down the prototype to a small geometrically similar model. In addition, the model must also show accurate similitude to the mechanical and physical properties of the prototype in order to inter-relate their corresponding behaviour. As a result, the stresses and strains of the model are considerably smaller than those of the prototype in proportion of the linear scale. The

gravitational stress field of the model, therefore, will be of a rather low intensity and any experimental investigation under such loading conditions, is an extremely difficult task.

Gravity loading, therefore, can only be simulated in conjunction with experimental techniques capable of magnifying the very low stress level, to one which can be accurately measured. This has been accomplished in the past, with reasonable success, by using the following methods:

(a) Method of Applied Loads: Is perhaps the oldest method, firstly applied by Wilson et al[110] to study the stress distribution in a gravity dam. Rubber models were used, subdivided into small divisions, with externally fixed weights at the centre of mass of each division, in proportion of its weight. In this way, an exaggerated gravity field was achieved and measurements could be taken using strain gauges.

This method, however, is of limited practical importance due to the local abnormalities resulting from the concentrated nature of the loads. In addition, it is only suitable for large scale physical models, and is obviously unacceptable for photo-elastic investigations.

(b) Method of Immersion: Biot[111] showed an analogy between the gravity stress field of a body and that of the same body when immersed in a liquid. This analogy was further

expanded to three-dimensions, and was used by investigators[112,113] to study problems such as spheres or thick rings under gravity. For live loading conditions, conventional photo-elasticity can be used, and if a three-dimensional analysis is required, then the freezing photo-elastic technique can be employed, using a suitable immersion fluid, e.g. mercury.

(c) Centrifugal Method: The basis of this method is the substitution of the gravitational forces by centrifugal ones. However, since the latter forces are proportional to the radius of rotation for accurate results, the dimensions of the model must be small compared to the radius of rotation of the centrifuge. The method was firstly applied by Bucky[114] and Brahtz[115] and later was used by Panek[116], to study mining structures.

When the centrifugal method is used, in conjunction with photo-elasticity, the model must be stress frozen, even for two-dimensional investigations, due to the difficulty in examining a model photo-elastically while it rotates. As a result, an extremely large oven is required to house the whole centrifuging system. Dally et al[117], overcame this problem by 'locking-in' the stresses without freezing. This is accomplished in certain epoxy models by half-curing the model and thereafter completing the curing

cycle with the model loaded in the centrifuge.

In addition to the small photo-elastic models, large physical models have also been used with the centrifugal method. These studies range from rock bolting patterns in multi-layered models[116], to fracture patterns in representative plaster models[118]. However, such investigations require a rather large centrifuging system and the whole operation can be quite costly.

(d) Method of Inversion: In this method, the gravity field is magnified by observing the difference in the strain distribution between the upright and inverted positions of the model. The resulting effect, therefore, is equivalent to twice that of the gravity[119].

This method is suitable for photo-elastic studies and its sensitivity will greatly depend on the density and the Young's modulus of the model material. By increasing the density while maintaining the modulus as low as possible, the sensitivity of this method is considerably increased.

(e) Method of Construction by Stages: This method was developed by Serafim et al[120], and was applied to the study of dams. The complete model is constructed and gauged, and then sliced systematically from top to bottom, in stages. By reversing the measurements, the gradual development of the gravity stresses can be analysed.

The authors[120] claimed a major advantage in this method. Whereas the previous ones examine the complete structure, 'suddenly' placed under gravity, this method is much more realistic since the gradual development of the gravity loading of the prototype is simulated in an exactly reversed manner to the actual structural sequence.

(f) Method of Integration: This method was suggested as an improvement to the previous technique. The model is gradually sliced as before and in order to improve the low response due to the removal of one layer, a uniform load is applied on the top of the horizontal surface to exaggerate the gravity effect. By simulation[121], the results can be related to the prototype and the effect of adding a representative weight (e.g. $1m^3$ of concrete), at a particular elevation, can be deduced. The loading, therefore, of successive stages of construction, can be found by integrating.

(g) Photo-elastic Method: Attempts have also been made to study the effects of gravity loading by conventional photo-elastic techniques, and without any form of magnification. This requires a material of extreme optical sensitivity and as a result only Gelatin is capable of such examination. This material is sensitive enough to show fringes, due to its own weight, and can be

stress frozen by an actual freezing procedure. However, as mentioned previously, Gelatin is highly susceptible to optical, mechanical and biological creep.

Gelatin has been used by many investigators[122,123,124,125], to study gravity loaded structures, as dams, tunnels and shafts. In order to minimise the creeping properties of the material the photo-elastic investigations must be completed as speedily as possible with simultaneous calibration, to determine the properties of the mix.

The experimental methods for gravity loading simulation, explained above, possess certain individual merits, as well as many practical difficulties. For investigations on small photo-elastic models, the author feels that the centrifugal method offers a number of attractive features. It produces a highly magnified gravity stress field so that measurements can be carried out accurately; by varying the rotational speed of the centrifuge extreme ranges of depth can be simulated; by designing a proper model holder, plane strain conditions can be achieved; due to the stress magnification, a good range of photo-elastic materials can be used, amongst which polyurethane, so that the Young's modulus of various rocks can be simulated.

However, centrifugal testing is hindered by two basic disadvantages. Firstly, since the centrifugal stresses are

proportional to the radius of rotation, it follows that for accurate simulation, the latter must be large with respect to the size of the model. This in turn means that the whole centrifuging system must be large enough to withstand high rotational radii. This problem, however, can be considerably limited by choosing narrow models (the width of the model is assumed as the dimension at right angles to the radius of rotation). Furthermore, by placing the structure under investigation at the centre of the model (i.e. at the flat part of the rotational curve), it is reasonable to assume that the gravity forces increase along the centre line in a linear fashion, as in practice, and not in a circular form.

The second problem of the centrifugal method concerns the actual observation procedure. Stresses can only be analysed after freezing the model even for two-dimensional investigations and this means that a large size oven is required. As a result, if a number of tests have to be carried out at various stress levels, the whole process can be extremely time consuming. In addition, all the problems associated with the actual execution of the freezing method, as previously stated, are also present.

In order to achieve a live loading analysis, stroboscopic light sources have been considered. However, due to the low intensity of these sources, it is practically impossible to

obtain monochromatic light, and thus to achieve a full solution.

The author has succeeded, however, in overcoming this problem by incorporating an optical method of 'motion-freezing' to the centrifugal technique, and thus enabling an examination of photo-elastic models in 'real time'.

4.4 PRINCIPLES OF MODEL SIMULATION IN CENTRIFUGAL TESTING

The gravitational force, 'Fg', of a stationary mass 'm', is given by

$$Fg = mg \tag{4.4.1}$$

where 'g' is the acceleration due to gravity.

If the same mass rotates under a radial speed 'w', rad/sec, then the centrifugal force, 'Fc', acting on it, is given by

$$Fc = ma \tag{4.4.2}$$

where 'a' is the radial acceleration.

The ratio, 'D', of the Fc to Fg can, therefore, be expressed as

$$D = \frac{Fc}{Fg} = \frac{a}{g} = \frac{w^2 r}{g} = \frac{4\pi^2 n^2 r}{g} \tag{4.4.3}$$

where

r = radius of rotation

n = speed, in revolutions per second

Since the speed is usually expressed in revolutions per minute, then by assuming that $g = 9.81 m/sec^2$, the above equation reduces to

$$D = 1.1n^2r \times 10^{-3} \qquad (4.4.4)$$

where r is in metres.

If the suffixes 'p' and 'm' denote the prototype and model parameters, respectively, then Dp, (i.e. rock), is 1. If the specific weight of the model, however, is γm, when stationary, then the equivalent weight is $Dm\gamma m$, when it rotates, where Dm is given by equation (4.4.4). The quantity $Dm\gamma m$ is referred to, by Panek[116], as the 'effective' specific weight.

For complete similitude between model and prototype, their dimensionless terms should be equal (Buckingham's π theorem). When considering ground behaviour, therefore, the following parameters are of interest:

Depth of seam - h	(L)
Thickness of seam - t	(L)
Face length - l	(L)
Length of Advance - d	(L)
Young's Modulus of strata - E	$(ML^{-1}T^{-2})$
Poisson's ratio of strata - ν	-
Specific weight of strata - γ	$(ML^{-2}T^{-2})$
Normal stress - σ	$(ML^{-1}T^{-2})$
Normal strain - ε	-
Applied load - P	(MLT^{-2})

where M,L,T are the basic units of mass, length and time. The

following basic dimensionless terms are then possible:

$$h/t,\ h/l,\ h/d,\ \sigma/E,\ P/EL^2,\ \gamma h/E,\ \nu,\ \varepsilon\ .$$

These ratios, therefore, corresponding to model and prototype parameters, should be equal for complete similitude. It is easily seen, however, that the first three terms are purely geometrical. If the required geometrical scale of model to prototype, Lm/Lp, is denoted by 'λ', then from the next ratio it follows:

$$\frac{E_p}{E_m} = \frac{\sigma_p}{\sigma_m} = \frac{M_p}{M_m}\ \frac{L_m}{L_p}\ \left(\frac{T_m}{T_p}\right)^2 \qquad (4.4.5)$$

If the gravitational acceleration is assumed to be the same for model and prototype, then

$$\frac{L_p}{T_p^2} = \frac{L_m}{T_m^2} \quad \text{or}$$

$$\left(\frac{T_m}{T_p}\right)^2 = \frac{L_m}{L_p} = \lambda \qquad (4.4.6)$$

Substituting the last equation into (4.4.5), then

$$\frac{E_p}{E_m} = \frac{\sigma_p}{\sigma_m} = \frac{M_p}{M_m}\lambda^2 \qquad (4.4.7)$$

Consider now the ratio of the specific weights

$$\frac{\gamma_p}{\gamma_m} = \frac{M_p}{M_m}\ \left(\frac{T_m}{T_p}\right)^2\ \left(\frac{L_m}{L_p}\right)^2$$

$$= \frac{M_p}{M_m}\lambda^3 \qquad (4.4.8)$$

Equation (4.4.7), then becomes

$$\frac{E_p}{E_m} = \frac{\sigma_p}{\sigma_m} = \frac{1}{\lambda} \frac{\gamma_p}{\gamma_m} \qquad (4.4.9)$$

It is clearly seen from this analysis, therefore, the advantages of using polyurethane for photo-elastic investigations. The ability to control the material's Young's modulus, over extensive ranges, means that most rocks can be simulated and as a result, the construction and examination of multi-layered models are easily achieved.

However, as for most plastics, some problems arise due to the constant value of the Poisson's ratio of the material. This value (0.48) is non-controllable and excessively high when compared to the corresponding values of most rocks (about 0.25). Since the Poisson's ratio is of little significance in two dimensional investigations, however, it can be conveniently ignored. The effect of the Poisson's ratio in three-dimensional model simulation, is much more more important and complex, therefore, and is discussed in the following chapter.

When the prototype is stationary and the model is rotated in a centrifuge, then for dimensional similitude, the specific weight of the model must be substituted by its effective weight. Equation (4.4.9), reduces to

$$\frac{E_p}{E_m} = \frac{\sigma_p}{\sigma_m} = \frac{1}{\lambda} \frac{1}{D} \frac{\gamma_p}{\gamma_m} \qquad (4.4.10)$$

where D is given by equation (4.4.4).

The last equation, therefore, describes the conditions that must be satisfied when simulating gravity loading by means of rotating models.

4.5 FREEZING THE ROTARY MOTION BY AN IMAGE DE-ROTATION TECHNIQUE

This method is primarily based on some simple light reflection, properties of prismatic surfaces. Assume, for example, a right-angled prism. If an object is placed in front of its hypotenuse, then the reflected image is in opposition to the object. If now the prism is rotated at, say, 90^{o}, while the object is kept stationary, then it is easily seen that the reflected image has been rotated 180^{o}, i.e. twice as fast, in the same direction. It follows, therefore, that if the object is rotated, twice as fast as the rotating prism, and in the same direction, the reflected object would appear stationary. These relationships are diagramatically shown in Figure 4.5.1.

Waddell[125] utilised the above principles to establish an optical system for freezing high speed rotation. The basis of such system depends entirely on how accurately a 2:1 ratio between the speeds of the rotating object and prism can be achieved. Although mechanical drives are adequate at low speeds, Waddell suggested that better accuracy can be obtained especially at high speeds, by using an electronic synchronising system.

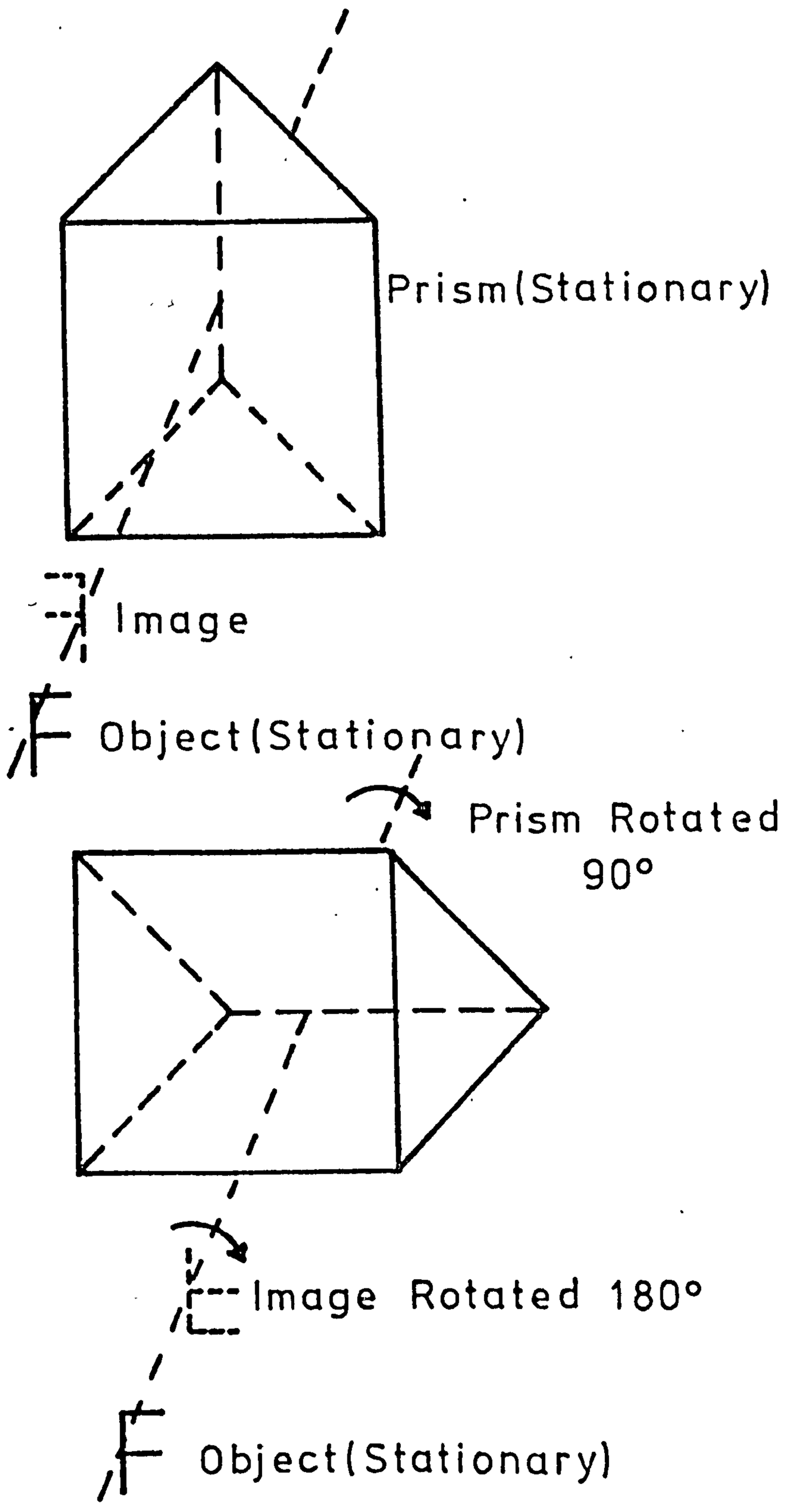

FIG. 4.5.1 STATIONARY-ROTATIONAL RELATIONSHIPS OF AN OBJECT-PRISM-IMAGE SYSTEM.

Waddell's electronic system is diagramatically shown in Figure 4.5.2. It basically consists of two parts, the electronic unit and a reflection polariscope. Circularly polarised light enters the model, in this case a disc having a number of symmetrical holes, which is placed in front of a metal encoder disc. The back surface of the model is silver painted to improve the light reflection and contrast of the fringes. The encoder disc has 48 small peripheral holes, and is rotated together with the model, by a D C motor drive. A light bulb and a photocell are placed behind and in front of the encoder disc, respectively, and are properly aligned so that the light strikes the photocell, through the encoder disc holes at all times, as the system rotates. The reflected light is then analysed and enters the prism system and observations of the image are then possible at right angles to the beam, via a beam splitter. The prism system is placed in front of a stepper motor which is connected to the photocell via a Schmitt Triger. For every revolution of the system, therefore the photocell produces 48 pulses (i.e. the 48 holes of the encoder disc), which are instantaneously transmitted to the stepper motor through the triger and power unit. Since the latter, therefore, operates at 96 pulses per revolution, it means that a whole revolution of the model induces half revolution on the prism unit, and

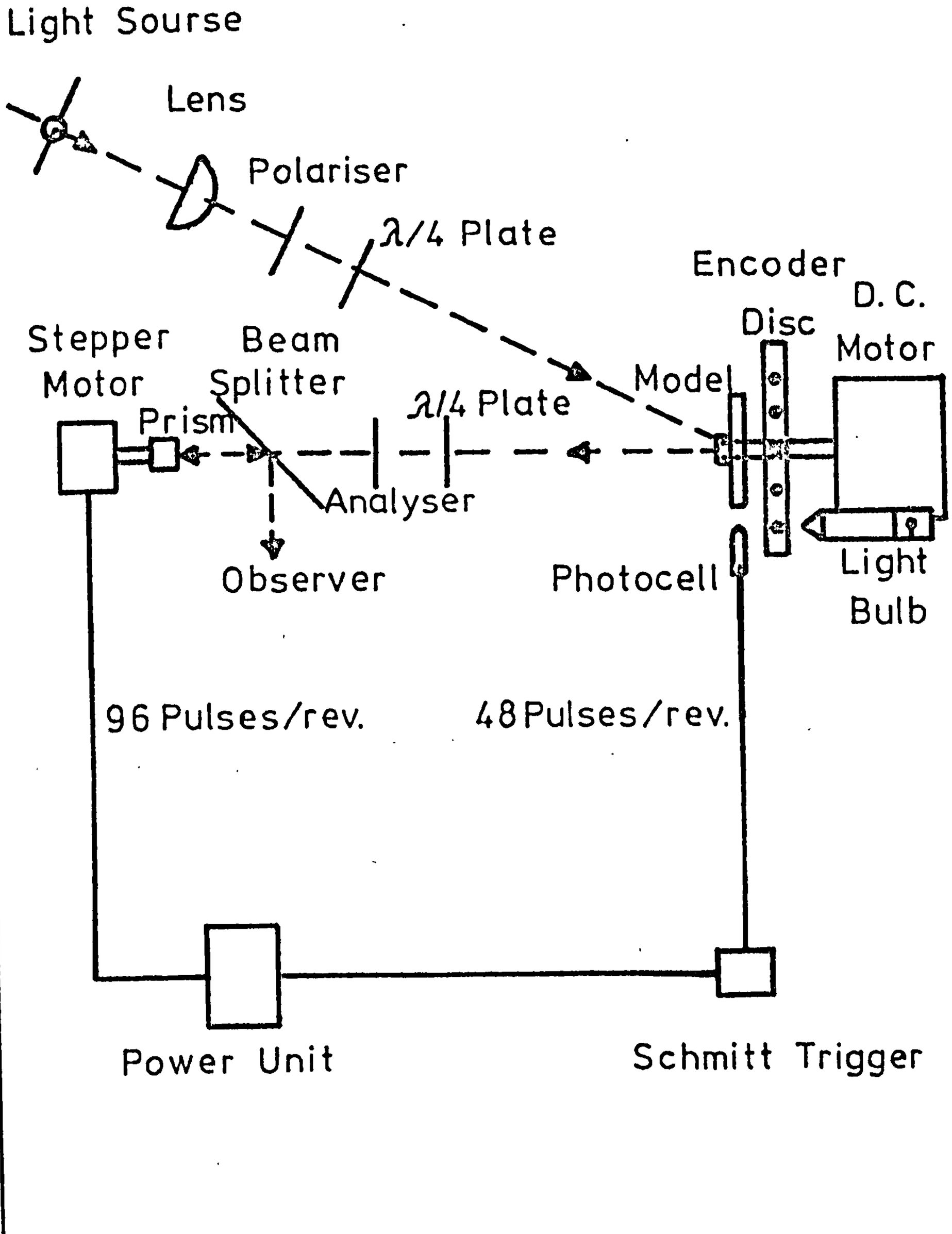

FIG. 4.5.2 PHOTO-ELASTIC SYSTEM FOR THE IMAGE DE-ROTATION TECHNIQUE.

thus the 2:1 speed ratio is established. It is important to note, however, that the rotational freezing can be accomplished either by one prism rotating at half the speed of the model, or by two prism rotating at quarter of the speed of the model, in which case the freezing is achieved in two stages.

Waddell[126] applied this method referred to as the 'Image De-rotation Technique', to study a range of vibration problems, and to examine the stress distribution in rotating objects, with and without fatigue cracks. Since this sytem can be used with any type of illuminator (e.g. laser, mercury vapour or white light sources), white, monochromatic, ultra-violet or infra-red light can be achieved, which was previously unattainable from conventional stroboscopes. As a result, this system is capable of complete examinations of photo-elastic, as well as Moire, fringe patterns.

Having realized the potentialities of the image derotation technique, for freezing the rotational motion, the author decided that the system could be introduced to the centrifugal method of gravity loading simulation, thus enabling photo-elastic observations in real time. This, therefore, was achieved by using Waddell's system with a specially designed model frame, so that the centrifugal forces were representative to the gravitational ones.

This frame consists of a 15.0 x 3.81 x 1.27cm perspex arm, having three brass sides in one end so that it forms an open rectangle. The model is then placed inside it, through the open side, and a thin perspex side is fitted on the top, so that the model is retained inside a box. As a result, plane strain conditions are achieved in every direction, except the radial one (i.e. the load axis). In order to ensure that the bottom side of the model is making proper contact with the brass side and the model is not displaced as the rotation begins, a small right-angled holder is screwed into the perspex arm, slightly pushing the model downwards.

On the other end of the perspex arm, a small weight is securely screwed into it, having a number of washers. Before each test the complete assembly is properly balanced on a knife edge, by attaching the appropriate number of washers. This is important, since excessive vibration of the motor could influence the stability and contrast of the observed image. The model frame is then placed in front of the encoder disc, through an eccentric hole. The whole assembly is illustrated, diagramatically in Figure 4.5.3. and an enlarged view is shown in Figure 4.5.4. The inside radius, 'r_1' is 7.62cm, the outside, 'r_3', is 11.43cm and the centre radius 'r_2' is about 9.52cm. The width of the model is 3.81cm and its thickness 1.27cm. The complete frame with the model in position is also shown in photograph Figure 4.5.5.

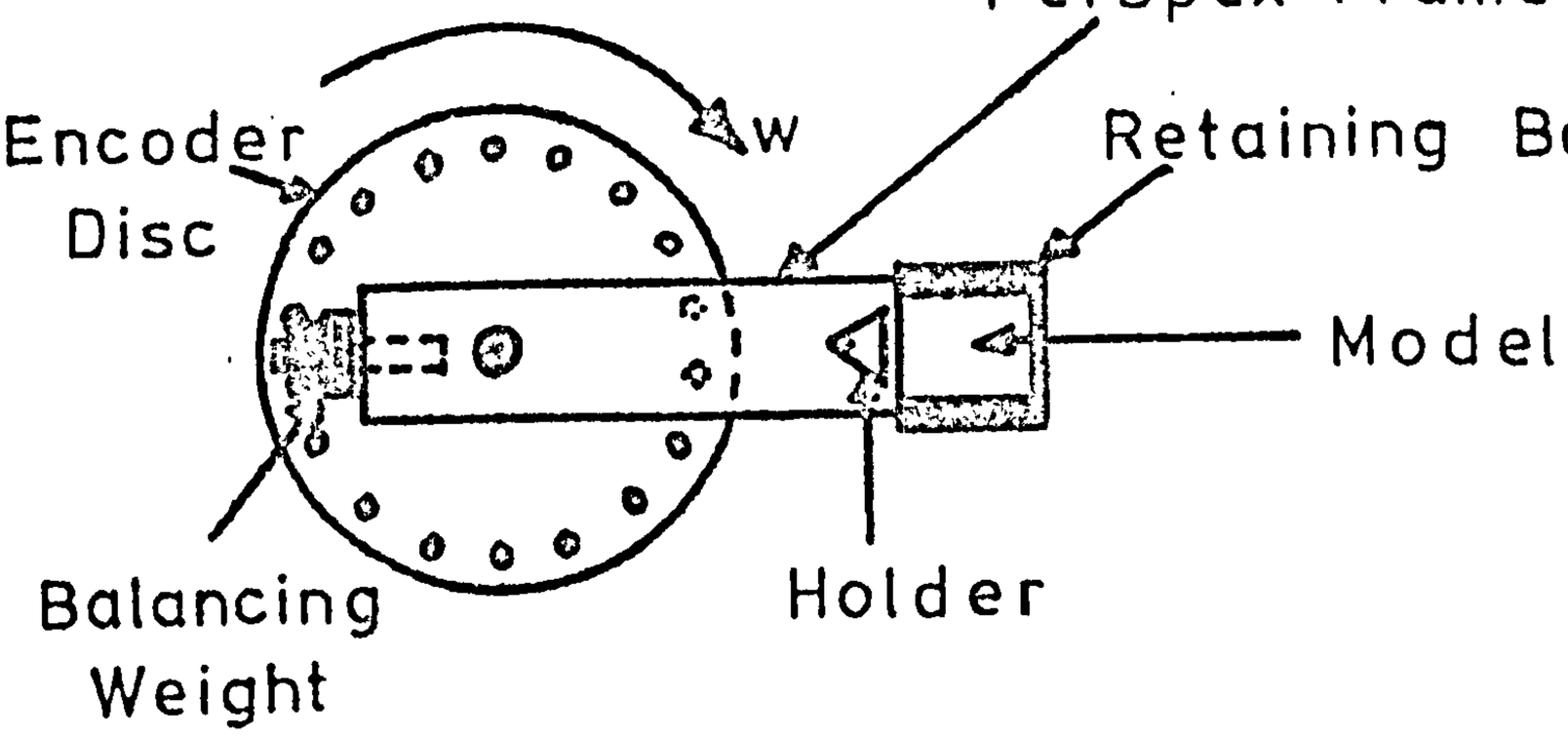

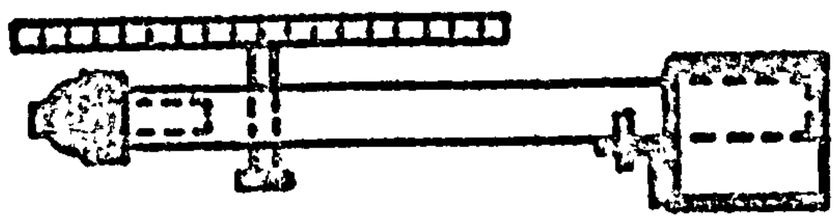

FIG. 4.5.3 CENTRIFUGAL MODEL FRAME.

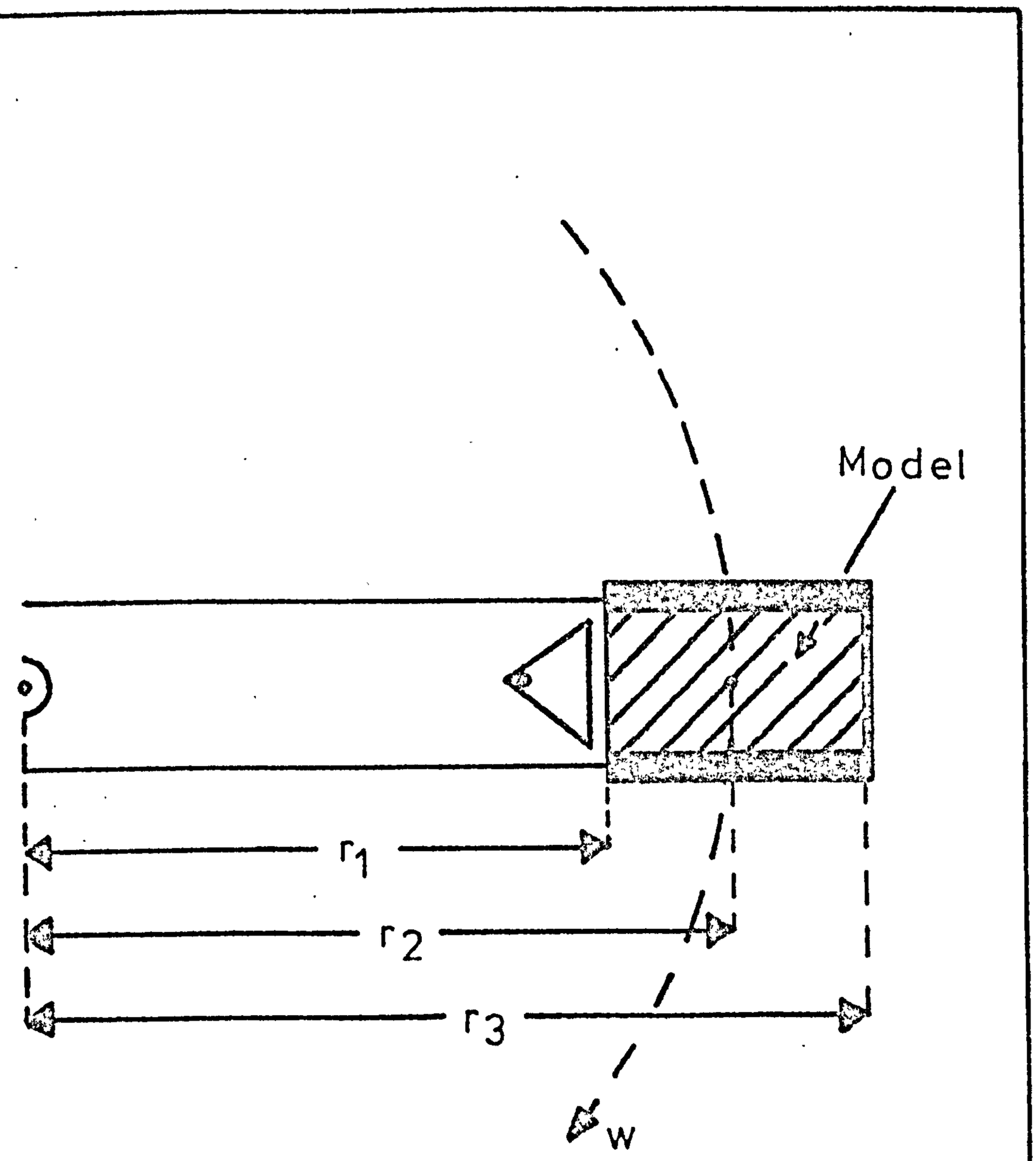

FIG.4.5.4 MODEL DIMENSIONS WITH RESPECT TO THE ROTATIONAL RADIUS.

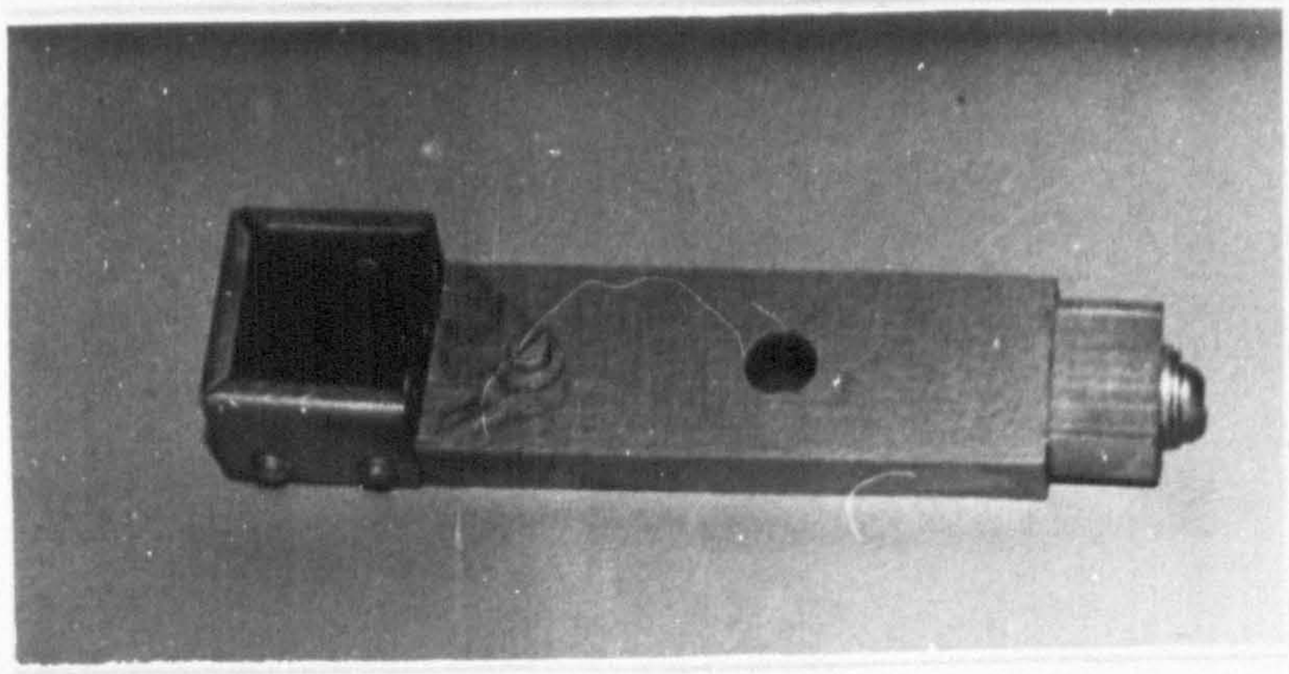

FIG.4.5.5 FRAME WITH MODEL IN POSITION.

4.6 THE ACCURACY OF THE SIMULATED GRAVITY FIELD

It was previously mentioned that, whereas the actual gravity stress field increases in a linear fashion, the simulated one is propagating radially. As a result, the larger the rotational radius is, with respect to the model width, the more accurate the simulation is going to be, (i.e. a flatter curve approximating a straight line).

The gravity stress, at a depth 'h' below the surface, is given by

$$\sigma_p = \gamma_p h \qquad (4.6.1)$$

The equivalent stress, in the model, can be expressed as follows

$$\sigma_m = \gamma_m (r - r_1) \qquad (4.6.2)$$

Since γ_p is constant, whereas γ_m (or g_m) varies with the radius of rotation, the last equation represents the idealistic stress on the model. The actual stress induced on the model, in a centrifuge, however, is given by

$$\sigma_r = \int_{r_1}^{r} \gamma_m r dr = \frac{1}{2} \gamma_m (r^2 - r_1)^2 \qquad (4.6.3)$$

where

σ_r is the actual radial stress, r the radius at some point inside the model, and r_1 the inside radius (as in Figure 4.5.4).

The error will be minimized, therefore, if the rotating speed is such that can equalise the ideal and actual stresses, at a particular radius. Since the area of interest in a mine model is usually near the geometrical centre, then by substituting r by r_2, (as in Figure 4.5.4), and equating equations (4.6.2) and (4.6.3), it follows

$$(r_2 - r_1)\,\gamma_m = \frac{1}{2}\,(r_2^2 - r_1^2)\,\gamma_m$$

$$= \frac{1}{2}\,(r_2^2 - r_1^2)D\,\gamma_p$$

where D is given by equation (4.4.3). The above equation, therefore, can be further reduced to

$$n^2 = \frac{1818\ D\ \gamma_p}{(r_2 + r_1)} \qquad (4.6.4)$$

The difference, therefore, between the ideal and actual stresses, at any radius r, when running at a speed n, as given by equation (4.6.4) (i.e. a speed that equalises the stresses at the central radius), is[118]

$$\sigma_m - \sigma_r = (r - r_1)\,\gamma_m - \frac{(r^2 - r_1^2)}{(r_2 + r_1)}\,\gamma_m$$

or

$$\left(\frac{\sigma_m - \sigma_r}{\sigma_m}\right) 100 = \left(\frac{r_2 - r}{r_2 + r_1}\right) 100 \qquad (4.6.5)$$

The last equation, therefore, shows the relative percentage error involved in the centrifugal method. For the dimensions of the models, used in this investigation, the

error in the stress is maximum at the outside radius (11%); however, steadily decreases when approaching the central area of the model (i.e. area of interest), to values below 6%.

4.7 PHOTOGRAPHING THE STRESS PATTERN

Photographing the stress pattern, through the beam splitter, presented a number of problems. Initial attempts showed that due to the extremely small size of the image, it was impossible to produce good prints of reasonable size without a considerable loss of contrast.

After trying a number of different combinations of camera lenses, it was found that the best results were obtained when using a telephoto lens on bellows, in front of the camera. This system enabled sufficient magnification of the image with the minimum loss of contrast. Since it was also difficult to focus the object accurately as it was rotating, it was proved advantageous to focus the camera precisely before movement begun and then photograph the pattern at that position.

4.8 SOME BASIC PATTERNS OF GRAVITY LOADED MODELS

The author's objective during this investigation, was to examine the potentialities of the image derotation technique when applied to gravity loading simulation by means of rotating photo-elastic models. As a result, complete stress solutions were not felt necessary since the capabilities of

the method could easily be estimated from simple observations of some typical stress patterns in real time.

The stress pattern of a 'heavy' disc, resting through a small region of its circumference (nearly a point contact) on the retaining frame, and under two different speeds, is shown in Figure 4.7.1. It is easily seen, therefore, that there is an excellent correspondence between these patterns and the well known theoretical ones. The accuracy of the method is also demonstrated in Figure 4.7.2, where a block is subjected to uniformly distributed stress. The fringes begin to generate at the corners, since the radius at these points (and therefore the stress), is greater than the one at the centre of the boundary. However, as the speed increases, and one is moving at the central part of the model, the fringes appear across the whole area of the model, and in a circular fashion. Ideally the fringes should be perfect straight bands but since the stress in this case is a function of the radius, they appear in a radial fashion and as it was previously mentioned, the bigger the radius the flatter the fringe curve, and thus a better approximation of a straight line. However, even for a relatively small radius of rotation, as in this case, the results can be very accurate if the area under investigation is at the central part of the model and the accuracy can be further increased if the speed employed is as

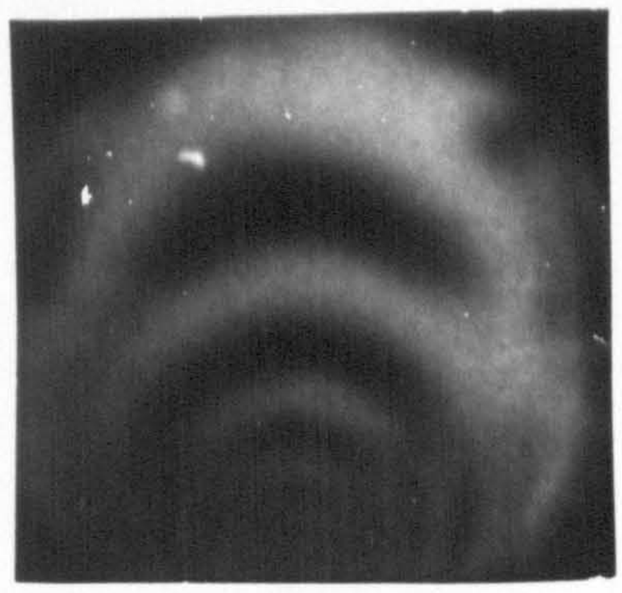

n = 770 r. p.m.

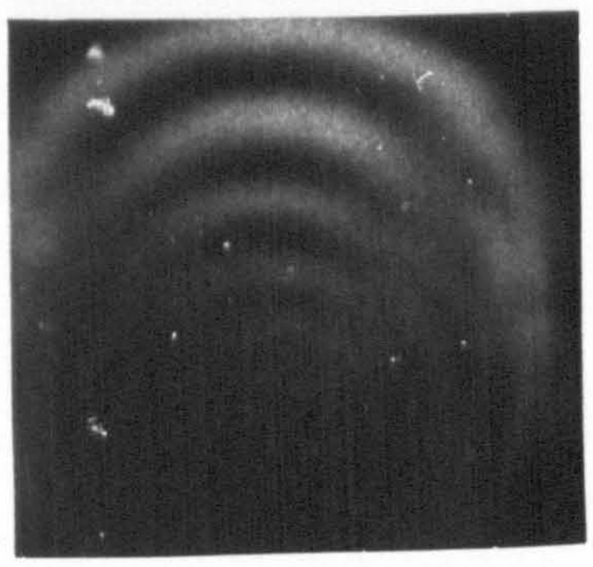

n=1160 r. p.m.

FIG. 4.7.1 HEAVY DISC UNDER GRAVITY.

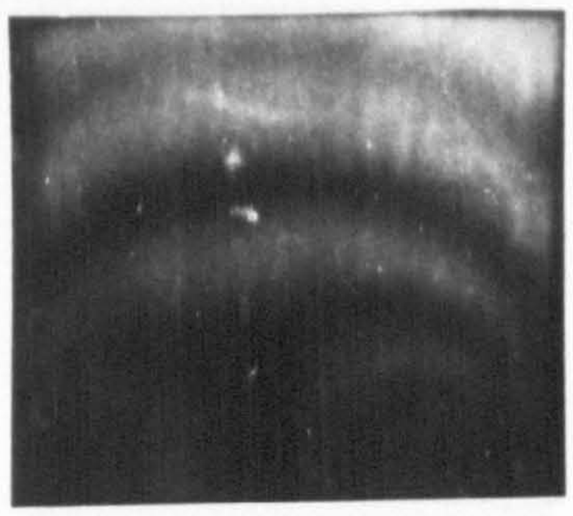

n = 650 r. p.m.

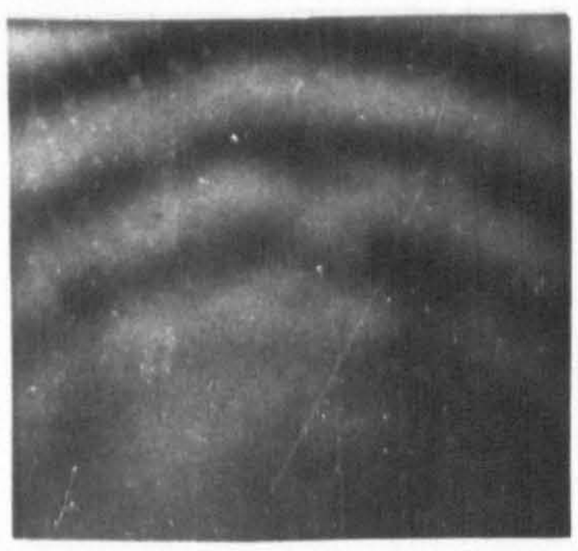

n=1160 r. p.m.

FIG. 4.7.2 BLOCK UNDER GRAVITY.

n=1160 r.p.m.

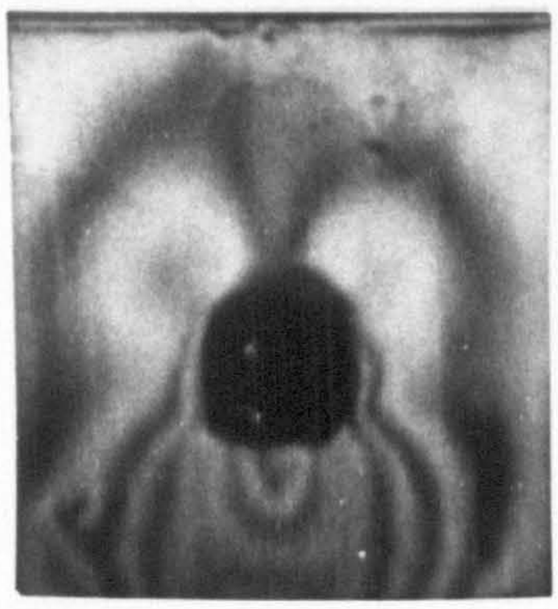

FIG. 4.7.3 SOLID BLOCK AND ARCHED OPENING UNDER SMALL STRIP GRAVITY LOAD.

suggested from equation (4.6.4). Finally, Figure 4.7.3 shows the stress pattern of a block, under a small strip loading when solid and with an arched roadway at its centre. It is worth noting, at this point, that any asymmetry of the fringe pattern, with respect to the vertical axis, is not due to the method itself but the result of non-parallelity of the two edges of the model.

4.9 CONCLUSIONS

(i) Although many underground structures have been successfully treated by assuming uniform stress conditions, there are cases (i.e. shallow workings or multi-level excavations), where this assumption is not realistic. Such problems, therefore, have to be examined inevitably, under gravity loading conditions.

(ii) The mathematical treatment of gravity loading by theoretical methods can be extremely complex and as a result, is limited to rather simplified geometries. A better approach to this problem, however, is the numerical method based on the finite element technique. It is evident, therefore, that gravity loaded structures are best analysed by experimental methods. Even in the case where results are available from finite element investigations, experimental solutions will provide the most invaluable check of the accuracy of the analytical procedure.

(iii) Experimental simulation of gravity loading can be achieved by various methods based on widely diverging principles. However, all these methods have a common feature in that their aim is to magnify the extremely low gravity stress to a level which can be accurately measured. Although the application of these methods is not always met with success, when studying underground excavations, mainly due to the large number of practical difficulties present, it is apparent that the centrifugal method offers a range of attractive features. It is capable of producing a highly magnified stress field so that accurate measurements can be taken; extreme ranges of depth can be simulated by varying the rotational speed; conditions of plane strain can be easily achieved; due to the degree of stress magnification, most photo-elastic materials can be employed including polyurethane, thus making possible the examination of multi-layered models.

(iv) The centrifugal method of gravity loading simulation is basically hindered by two defects. Since the centrifugal stresses are in proportion to the rotational radius, for accurate simulation, the latter must be as large as possible, (i.e. a flat curve approaching a straight line), with respect to the model. This, there-

fore, will necessitate a large and as a result, costly, centrifuging system. This difficulty, however, can be overcome to great extent by employing narrow models, having the area of interest at their central section. In addition, due to the extreme difficulty in examining a rotating object under live loading conditions, the model has to be stress-frozen even for two-dimensional investigations. This means that a large housing oven is needed and when a number of tests are to be carried out, the whole process will be extremely time consuming. An optical method of freezing, therefore, was suggested in this chapter, the Image De-rotation Technique, which enables the examination of photo-elastic models in 'real time'.

(v) The image de-rotation technique is simply based on the reflection properties of right-angled prisms, and has been successfully employed for freezing rotary motion, in the field of mechanical engineering. The optical bench devised by Waddell[126] was properly adjusted so that gravity loading simulation of small photo-elastic models, in plane strain, could be carried out. The model-prototype laws of similitude can be easily satisfied by considering the model's effective specific weight in the conventional dimensional analysis procedure.

(vi) Since the object of this investigation was to examine the potentialities of the image de-rotation technique, when applied to the centrifugal method of gravity loading simulation, and not to derive quantitative results, a complete stress solution of a model was not undertaken. The possibilities of the method, however, are clearly demonstrated from a number of photographs of various stress patterns. Even for a relatively small radius of rotation, as in this case, the relative percentage error of the stress was less than 6% in the central area and approached a value of about 11% at the outside radius. The accuracy of the system, therefore, can increase even further by choosing a slightly larger rotational radius.

(vii) The problem of increasing the image size, when photographing a stress pattern, was successfully overcome by employing the system mentioned. However, although the object was perfectly still when viewed through a beam splitter, an extremely small amount of light flickering was present which, although was practically undetected when observing visually, was affecting the quality of the photographs, particularly when long exposures were used. This, however, can be greatly improved by reflecting the light on to the model through

a small mirror, mounted in front of a second stepper motor, and rotating at a speed half of that of the prism. As a result, the prism system will not just freeze the rotary motion of the model, but that of the light as well, thus greatly increasing the object's illumination and practically eliminating all flickering.

(viii) In this chapter, the application of the image de-rotation technique to the centrifugal method of gravity simulation, for two-dimensional photo-elastic investigations, in 'real time', was discussed. Apart from the conventional two-dimensional photo-elastic studies, the system is also capable of Moire fringe analysis. The possibilities of the method in scattered light, three-dimensional photo-elastic studies, were also considered. Although research towards this end was not carried out in real depth, the indication from some simple preliminary experiments, using an Argon laser as the light source was very encouraging. Finally, it is worth noting that the original system, before it was modified for gravity loading studies, was used for examination of rotating components. This method, therefore, can offer a unique solution to some important mining problems which were previously outside the limits of model simulation, as in rock drilling studies.

CHAPTER V

THE APPLICATION OF THE SCATTERED LIGHT METHOD OF THREE-DIMENSIONAL PHOTO-ELASTICITY TO THE DESIGN OF MINE PILLARS

CHAPTER V

THE APPLICATION OF THE SCATTERED LIGHT METHOD OF THREE-DIMENSIONAL PHOTO-ELASTICITY TO THE DESIGN OF MINE PILLARS

5.1 INTRODUCTION

Solving stress distribution problems by reducing the prototype to a dimensionally similar small scale model, is an established technique in the field of experimental stress analysis. The application of photo-elastic models in particular has been proved extremely successful in the study of underground structures since this method can offer an inexpensive and rapidly obtained solution as well as being capable of examining any geometrical complexities of the model's shape.

Mining configurations and in particular underground pillars, are problems of three-dimensional state of stress. Their solutions, however, due to the great number of practical difficulties involved, have been limited to a large extent to two-dimensions. If representative results are to be obtained, therefore, these problems must be treated three-dimensionally and in this respect the scattered light technique offers a number of attractive features. As opposed to the freezing method, the scattered light technique is carried out under 'live loading' conditions without the need of heat treatment, and as a result the Poisson's ratio which is of extreme

importance in three-dimensional stress solutions, will remain constant throughout the investigation. In addition, stresses can be fully analysed at any point in the boundary or interior of the model, thus enabling the retrieval of the maximum possible information from a single model.

In this Chapter, two stress investigations were carried out using the scattered light technique. The stress distribution on the horizontal centre line of a small cubical pillar, typical to the room and pillar method of mining, was determined quantitatively as well as three-dimensional qualitative examination of the influence of the face advance on a pillar, left behind a longwall face. The scattered light technique as all other photo-elastic methods, necessitates a number of basic assumptions and as a result is carried out on a model simulating an idealized prototype. This means that the results obtained should not be accepted on a pure quantitative basis. It is recognised, however, that such results do give a valuable qualitative picture of the expected stress distribution which can be an excellent guide to the designer, and thus immensely increase the confidence of his predictions.

5.2 THE THREE-DIMENSIONAL DISTRIBUTION OF STRESS AROUND ROOM AND PILLAR WORKINGS

In the first part of this investigation, the scattered light technique was employed to examine the complete state of

stress on a horizontal centre line of a small cubical pillar within a room and pillar mining complex. The investigation is best described by considering the following stages:

(a) Problem's description: An imaginary case of room and pillar workings was assumed with rectangular openings and cubical pillars. It was further assumed that pillars were loaded in accordance with the tributary area theory. Investigations of other researchers in two-dimensions have shown that, for equal height pillars, the centre pillar will be under more stress than the peripheral ones[46,47]. Ideally, therefore, the model should consist of at least 25 geometrically regular pillars with the examination taking place on the centre pillar (i.e. third pillar from every side). Such a model, therefore, if complete stress separation is to be carried out, would be of an extremely large size and could not be accommodated in the polariscope's loading assembly. As a result, a single pillar was considered with a roof as suggested from the tributary area theory, and loaded uniformly externally using the perspex frame previously described.

(b) Photo-elastic model: A polyurethane model, with fine silica dust in order to induce scattering was used, and is diagramatically shown in Figure 5.2.1. The dimensions of the pillar were 4 x 4 x 4cm, and those of room and floor 8 x 8 x 4cm. This system was representative, therefore, to 75% extraction ratio. This particular ratio was chosen

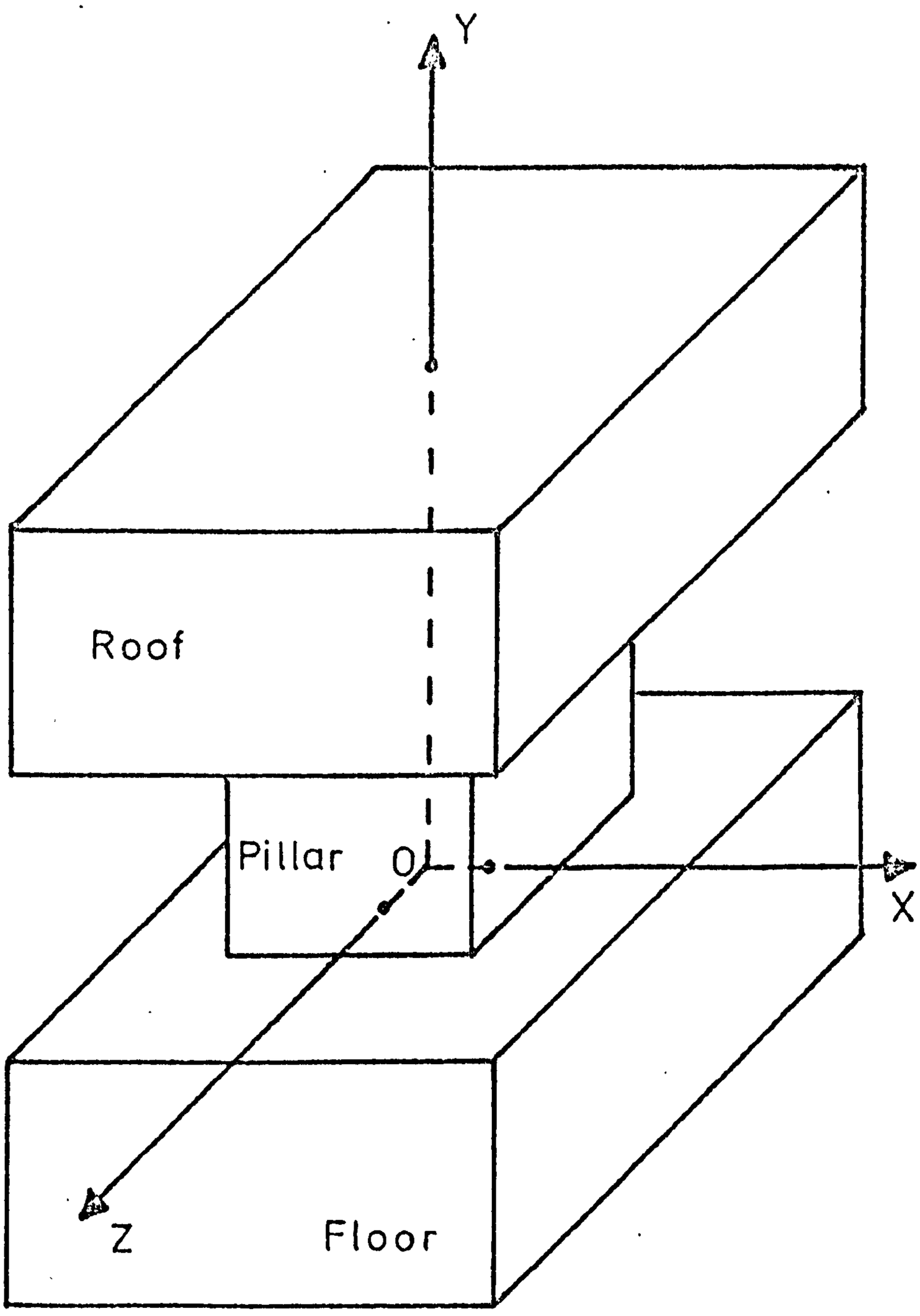

FIG. 5.2.1 MODEL OF ROOM AND PILLAR WORKINGS .

because two-dimensional investigations have revealed that above this value the stress concentrations increase rapidly. The same mixture of polyurethane was used for the whole model (50 : 50 by weight) which means that the mechanical properties of the roof, pillar and floor rock were assumed to be identical. Also, in an attempt to simulate the lateral restraint offered to the roof and floor by the adjacent material, the corresponding roof and floor of the model were restrained by four perspex sides.

(c) Experimental results: The stresses on the pillar's horizontal centre line, along OX, were to be fully analysed. The stress-optical coefficient of the material was determined as explained in Appendix A, and calibration of the compensator suggested 1 fringe being equivalent to 1.16mm. The compensator had to be used in this case since due to the symmetry of the model, the difference of the lateral stresses was extremely small. This meant that when the light was entering along the vertical (load) axis, and observations were made in the transverse (horizontal) plane, very few fringes were seen, and as a result, a fringe against distance curve could not be drawn with any degree of accuracy. The experimental procedure, see Figure 5.2.2, was carried out as follows:

(i) Light parallel to the Z-axis: By making the incident light parallel to the Z-axis, observations are made on

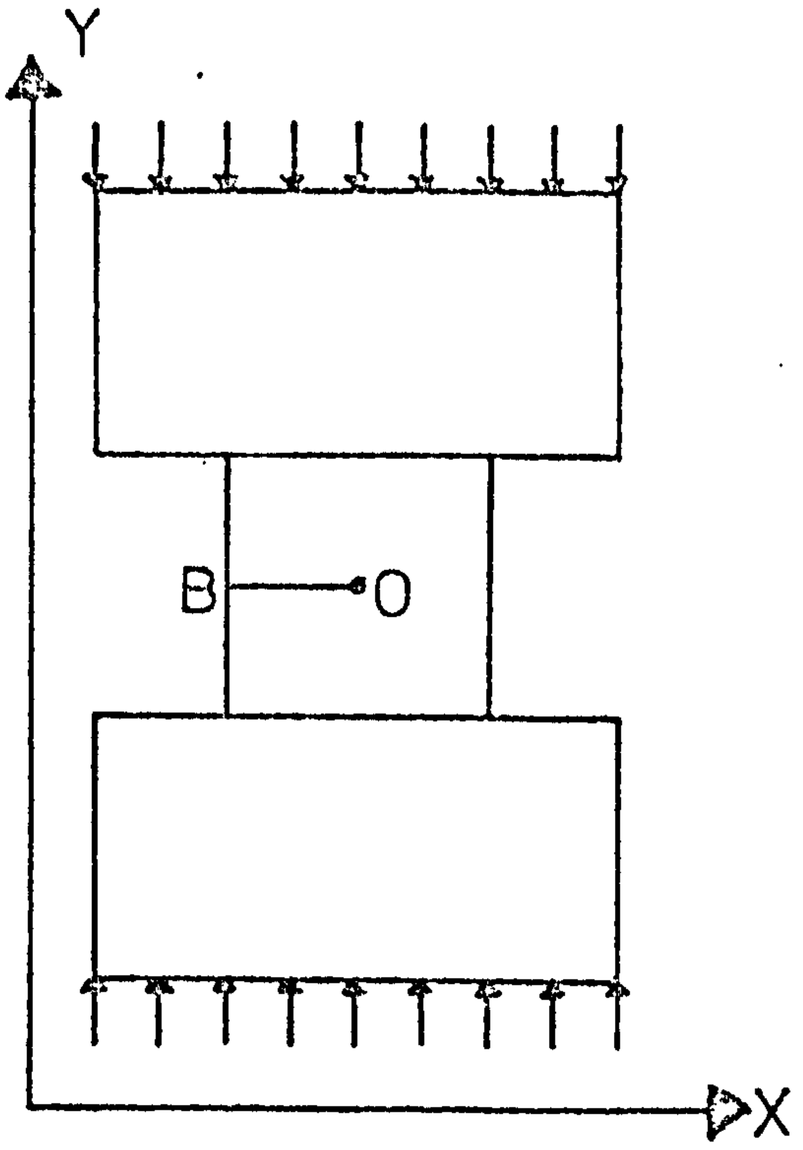

Light along Z-axis

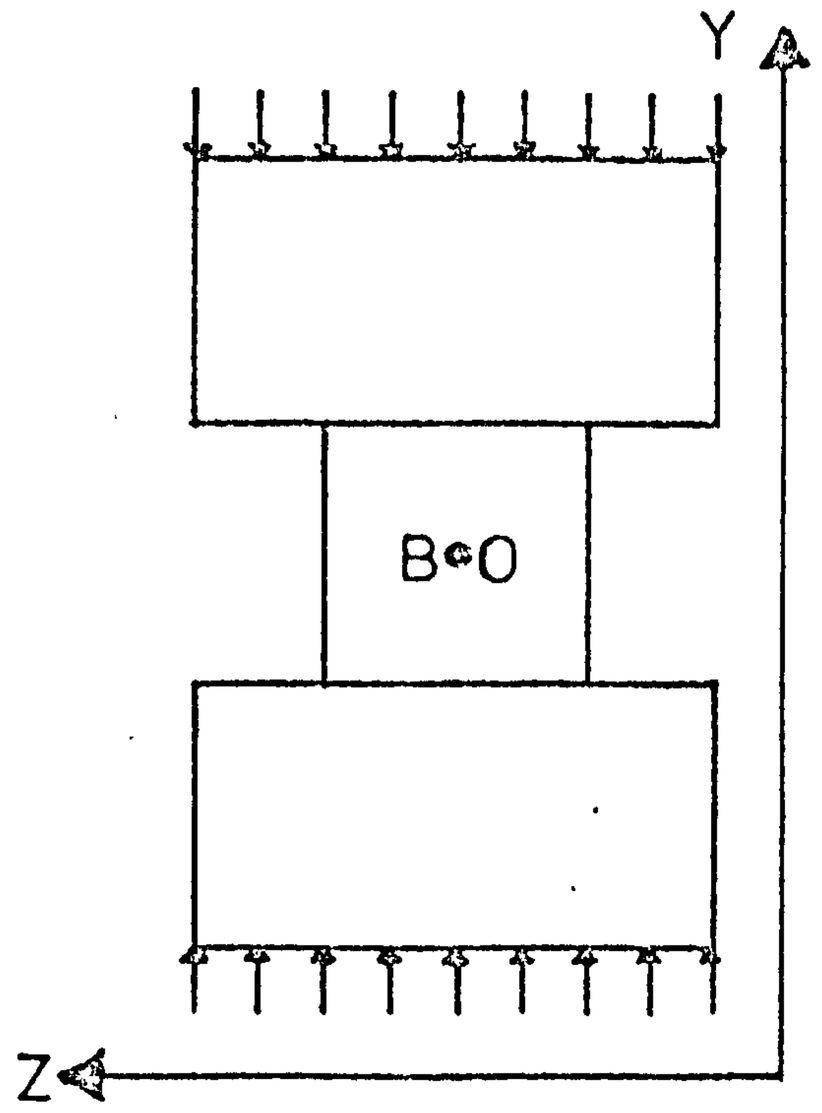

Light along X-axis

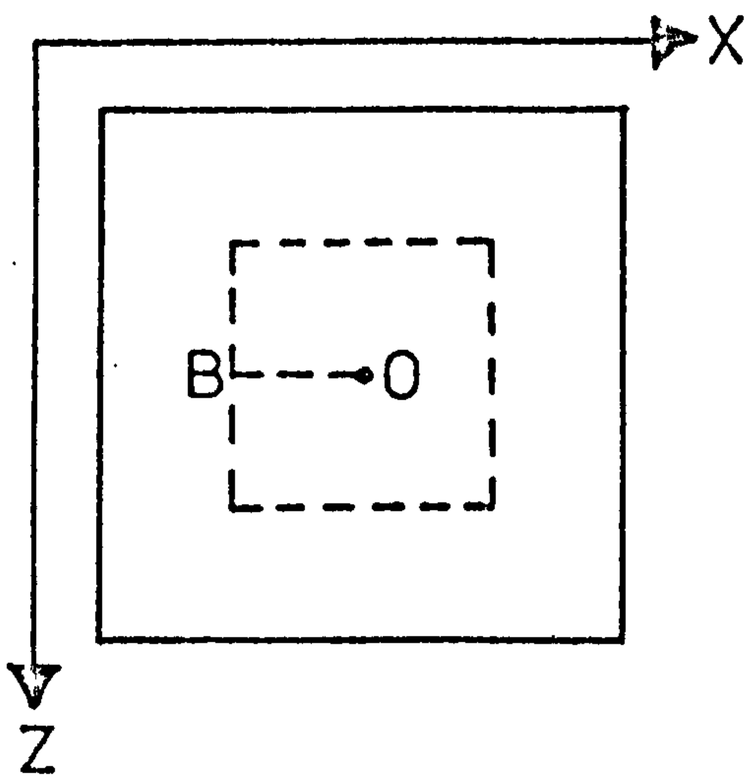

Light along Y-axis

FIG. 5.2.2 EXPERIMENTAL PROCEDURE OF PILLAR ANALYSIS.

XY plane. The isoclinics and birefringence parameters are measured along three parallel lines, the line of interest OB and two auxiliary lines OB $\pm\Delta Y/2$, were ΔY = 4mm. The stress components can then be found as explained in Chapter III, i.e.

$$(p - q)_{xy} = \frac{1}{1.16C} \frac{\Delta N}{\Delta s}$$

$$(\sigma_x - \sigma_y) = (p - q)_{xy} \cos 2h_{xy}$$

$$\tau_{xy} = \frac{1}{2} (p - q)_{xy} \sin 2h_{xy}$$

Six points were analysed along these lines, at equal distances (OB = 2cm), from the horizontal centre line of the pillar to the boundary. At the latter point, σ_x = 0, and therefore the one known normal stress, required for the execution of the shear difference method, is thus established. The analytical results, conveniently classified in tables, are as shown.

Table 1: Isoclinic Parameters along OB

OX/OB	h_{xy}	$\sin 2h_{xy}$	$\cos 2h_{xy}$
0.000	5.0°	0.1736	0.9848
0.200	2.0°	0.0698	0.9976
0.400	-1.5°	-0.0523	0.9986
0.600	-6.0°	-0.2079	0.9781
0.800	-5.5°	-0.1908	0.9816
1.000	0.0°	0.0000	1.0000

Table 2: Birefringence along OB (Δs = 1mm)

OX/OB	ΔN_1 mm	ΔN_2 mm	ΔN mm
0.000	14.625	14.275	0.350
0.200	14.675	14.320	0.355
0.400	15.000	14.615	0.385
0.600	14.260	13.820	0.440
0.800	15.025	14.500	0.525
1.000	14.405	13.765	0.640

Table 3: Stress Components along OB

OX/OB	$(p-q)_{xy}$ N/mm^2	$(\sigma_x-\sigma_y)$ N/mm^2	τ_{xy} N/mm^2
0.000	0.0520	0.0512	0.0045
0.200	0.0528	0.0527	0.0018
0.400	0.0572	0.0571	-0.0015
0.600	0.0654	0.0640	-0.0068
0.800	0.0780	0.0766	-0.0075
1.000	0.0950	0.0950	0.0000

Table 4: Isoclinic Parameters along OB $+\Delta Y/2$

OX/OB	h_{xy}	$\sin 2h_{xy}$
0.000	-3.5°	-0.1219
0.200	2.0°	0.0698
0.400	2.0°	0.0698
0.600	1.5°	0.0523
0.800	7.0°	0.2419
1.000	4.0°	0.1392

Table 5: Birefringence along OB $+\Delta Y/2$ (Δs = 1mm)

OX/OB	ΔN_1 mm	ΔN_2 mm	ΔN mm
0.000	14.625	14.250	0.375
0.200	14.580	14.270	0.310
0.400	14.675	14.320	0.355
0.600	14.240	13.850	0.390
0.800	15.155	14.600	0.555
1.000	14.505	13.850	0.655

Table 6: Stress Components along OB $+\Delta Y/2$

OX/OB	$(p-q)_{xy}$ N/mm^2	τ_{xy} N/mm^2
0.000	0.0557	-0.0034
0.200	0.0461	0.0016
0.400	0.0528	0.0019
0.600	0.0580	0.0015
0.800	0.0825	0.0100
1.000	0.0974	0.0068

Table 7: Isoclinic Parameters along OB $-\Delta Y/2$

OX/OB	h_{xy}	$\sin 2h_{xy}$
0.000	2.5°	0.0872
0.200	-1.5°	-0.0523
0.400	-2.0°	-0.0698
0.600	-1.5°	-0.0523
0.800	-7.5°	-0.2588
1.000	-4.0°	-0.1392

Table 8: Birefringence along OB -$\Delta Y/2$ (Δs = 1mm)

OX/OB	ΔN_1 mm	ΔN_2 mm	ΔN mm
0.000	14.460	14.150	0.310
0.200	14.620	14.260	0.360
0.400	14.605	14.350	0.355
0.600	14.260	13.900	0.360
0.800	15.000	14.500	0.500
1.000	14.335	13.785	0.550

Table 9: Stress Components along OB -$\Delta Y/2$

OX/OB	$(p-q)_{xy}$ N/mm^2	τ_{xy} N/mm^2
0.000	0.0461	0.0020
0.200	0.0535	-0.0014
0.400	0.0528	-0.0019
0.600	0.0535	-0.0014
0.800	0.0743	-0.0096
1.000	0.0817	-0.0057

(ii) Light parallel to the Y-axis: When the light is entering in a direction parallel to the Y-axis, then all observations are on the ZX plane. As before, the isoclinic parameters and the birefringence are determined along three lines, the line of interest OB and two auxiliary lines OB $\pm\Delta Z/2$, where ΔZ = 4mm. The results are again tabulated as shown.

Table 10: Isoclinic Parameters along OB

OX/OB	h_{zx}	$\sin 2h_{zx}$	$\cos 2h_{zx}$
0.000	86.5°	0.1219	-0.9925
0.200	85.0°	0.1736	-0.9848
0.400	83.0°	0.2419	-0.9703
0.600	80.0°	0.3420	-0.9397
0.800	83.0°	0.2419	-0.9703
1.000	90.0°	0.0000	-1.0000

Table 11: Birefringence along OB (Δs = 4mm)

OX/OB	ΔN_1 mm	ΔN_2 mm	ΔN mm
0.000	14.380	14.275	0.105
0.200	14.375	14.280	0.095
0.400	14.425	14.300	0.125
0.600	14.410	14.310	0.100
0.800	14.400	14.315	0.085
1.000	14.400	14.315	0.085

Table 12: Stress Components along OB

OX/OB	$(p-q)_{zx}$ N/mm^2	$(\sigma_z-\sigma_x)$ N/mm^2	τ_{zx} N/mm^2
0.000	0.0040	-0.0040	0.0002
0.200	0.0036	-0.0035	0.0003
0.400	0.0046	-0.0045	0.0006
0.600	0.0037	-0.0035	0.0006
0.800	0.0031	-0.0030	0.0004
1.000	0.0031	-0.0032	0.0000

Table 13: Isoclinic Parameters along OB $+\Delta Z/2$

OX/OB	h_{zx}	$\sin 2h_{zx}$
0.000	87.0°	0.1045
0.200	87.0°	0.1045
0.400	86.0°	0.1392
0.600	89.0°	0.0349
0.800	89.0°	0.0349
1.000	90.0°	0.0000

Table 14: Birefringence along OB $+\Delta Z/2$ (Δs = 4mm)

OX/OB	ΔN_1 mm	ΔN_2 mm	ΔN mm
0.000	14.405	14.300	0.105
0.200	14.415	14.310	0.105
0.400	14.475	14.350	0.125
0.600	14.460	14.355	0.105
0.800	14.480	14.365	0.115
1.000	14.480	14.365	0.115

Table 15: Stress Components along OB $+\Delta Z/2$

OX/OB	$(p-q)_{zx}$ N/mm^2	τ_{zx} N/mm^2
0.000	0.0039	0.0002
0.200	0.0039	0.0002
0.400	0.0046	0.0003
0.600	0.0039	0.0001
0.800	0.0043	0.0001
1.000	0.0043	0.0000

Table 16: Isoclinic Parameters along OB - Δ Z/2

OX/OB	h_{zx}	$\sin 2h_{zx}$
0.000	89.0°	0.0349
0.200	92.0°	-0.0698
0.400	92.0°	-0.0698
0.600	93.0°	-0.1045
0.800	92.0°	-0.0698
1.000	90.0°	0.0000

Table 17: Birefringence along OB -Δ Z/2 (Δs = 4mm)

OX/OB	ΔN_1	ΔN_2	ΔN
0.000	14.355	14.255	0.100
0.200	14.385	14.285	0.100
0.400	14.395	14.290	0.105
0.600	14.425	14.310	0.115
0.800	14.415	14.315	0.100
1.000	14.415	14.315	0.100

Table 18: Stress Components along OB -Δ Z/2

OX/OB	$(p-q)_{zx}$ N/mm^2	τ_{zx} N/mm^2
0.000	0.0037	0.0001
0.200	0.0037	-0.0001
0.400	0.0039	-0.0001
0.600	0.0043	-0.0002
0.800	0.0037	-0.0001
1.000	0.0037	0.0000

(iii) Light parallel to X-axis: Observations this time are in the YZ plane. The isoclinic parameters and birefringence on the line of interest OB are the only requirements. The results are as shown.

Table 19: Isoclinic Parameters along OB

OX/OB	h_{yz}	$\sin 2h_{yz}$	$\cos 2h_{yz}$
0.000	96.5°	-0.2259	-0.9744
0.200	93.0°	-0.1045	-0.9945
0.400	89.5°	0.0175	-0.9998
0.600	88.5°	0.0523	-0.9986
0.800	88.0°	0.0698	-0.9976
1.000	88.5°	0.0523	-0.9986

Table 20: Birefringence along OB (Δs = 1mm)

OX/OB	ΔN_1 mm	ΔN_2 mm	ΔN mm
0.000	14.635	14.300	0.335
0.200	14.355	14.015	0.340
0.400	14.995	14.640	0.355
0.600	14.780	14.370	0.410
0.800	14.790	14.290	0.500
1.000	14.500	13.880	0.620

Table 21: Stress Components along OB

OX/OB	$(p-q)_{yz}$ N/mm^2	$(\sigma_y-\sigma_z)$ N/mm^2	τ_{yz} N/mm^2
0.000	0.0498	-0.0485	-0.0052
0.200	0.0505	-0.0502	-0.0026
0.400	0.0528	-0.0528	0.0005
0.600	0.0609	-0.0608	0.0016
0.800	0.0743	-0.0741	0.0026
1.000	0.0922	-0.0921	0.0024

(iv) The shear difference method: In order to increase the accuracy of the method, the mean shear differences $M\Delta\tau_{xy}$ and $M\Delta\tau_{zx}$ are considered, where

$$\Delta\tau_{xy} = (\tau_{xy})_{OB+\Delta Y/2} - (\tau_{xy})_{OB-\Delta Y/2}$$

$$\Delta\tau_{zx} = (\tau_{zx})_{OB+\Delta Z/2} - (\tau_{zx})_{OB-\Delta Z/2}$$

It, therefore, follows

Table 22: Mean Shear Differences

OX/OB	$\Delta\tau_{xy}$ N/mm^2	$M\Delta\tau_{xy}$ N/mm^2	$\Delta\tau_{zx}$ N/mm^2	$M\Delta\tau_{zx}$ N/mm^2
0.000	-0.0054		0.0001	
		-0.0012		0.0002
0.200	0.0030		0.0003	
		0.0034		0.0003
0.400	0.0038		0.0004	
		0.0033		0.0003
0.600	0.0029		0.0003	
		0.0112		0.0003
0.800	0.0196		0.0002	
		0.0160		0.0002
1.000	0.0125		0.0000	

Table 23: Mean Shear Differences of linear Increments

OX/OB	$M\Delta\tau_{xy}\frac{\Delta X}{\Delta Y}$ N/mm^2	$M\Delta\tau_{zx}\frac{\Delta X}{\Delta Z}$ N/mm^2	S.D. N/mm^2
0.000	-0.0012	0.0002	-0.0014
0.200	0.0034	0.0003	0.0031
0.400	0.0033	0.0003	0.0031
0.600	0.0112	0.0003	0.0109
0.800	0.0160	0.0002	0.0158
1.000			

where

$$S.D. = M\Delta\tau_{xy}\frac{\Delta X}{\Delta Y} - M\Delta\tau_{zx}\frac{\Delta X}{\Delta Z}$$

The normal stress σ_x can now be calculated at any point j, on the line OB since

$$(\sigma_x)_j = (\sigma_x)_b - \sum_b^j S.D.$$

where

$(\sigma_x)_b$ is the boundary value of the σ_x, in this case zero.

Table 24: Calculation of σ_x

OX/OB	σ_x N/mm^2
0.000	-0.0315
0.200	-0.0329
0.400	-0.0298
0.600	-0.0267
0.800	-0.0158
1.000	0.0000

The other normal stresses, σ_y and σ_z, can now be calculated by substituting the σ_x values of Table 24 to the $(\sigma_x-\sigma_y)$ and $(\sigma_z-\sigma_x)$ values of Tables 3 and 12 respectively.

Table 25: Calculation of σ_y and σ_z

OX/OB	σ_y N/mm^2	σ_z N/mm^2
0.000	-0.0827	-0.0355
0.200	-0.0856	-0.0364
0.400	-0.0869	-0.0343
0.600	-0.0907	-0.0302
0.800	-0.0924	-0.0188
1.000	-0.0950	-0.0032

The last table shows the calculated σ_y and σ_z values. The difference of these stresses was found, also, experimentally in Table 21. The experimental and calculated stress differences should be ideally equal.

Table 26: Comparison of Experimental and Calculated $(\sigma_y-\sigma_z)$ values.

OX/OB	$(\sigma_y-\sigma_z)$Exp. N/mm^2	$(\sigma_y-\sigma_z)$Calc. N/mm^2
0.000	-0.0485	-0.0472
0.200	-0.0502	-0.0492
0.400	-0.0528	-0.0526
0.600	-0.0608	-0.0605
0.800	-0.0741	-0.0731
1.000	-0.0921	-0.0918

Table 26 shows that the relative percentage error between the calculated and experimentally derived (σ_y-σ_z) values, ranges from a maximum of 2.7% to a minimum of 0.3%, averaging about 1%.

(d) Discussion of results: The experimental results are shown in Figures 5.2.3 and 4. The applied stress was approximately measured using the loading mechanism explained previously and was about 0.02N/mm^2. From Figure 5.2.3 it can be seen that the normal stress σ_y reaches a maximum of 0.950N/mm^2, in compression, at the boundary. This value suggests a compressive stress concentration of about 4.75. The graph shows a small rate of decrease when moving towards the pillar's centre line at which point σ_y approaches a value of 0.084N/mm^2 or a compressive concentration of about 4.2. The average vertical pillar stress is 0.0888N/mm^2 corresponding to a compressive stress concentration of about 4.44.
The two horizontal normal stresses progress practically parallel to each other, with an average difference between them of about 0.0036/N/mm^2. Their maximum values are attained at the centre line where σ_x is 0.033N/mm^2 and σ_y 0.037N/mm^2, corresponding to compressive stress concentrations of about 1.65 and 1.85 respectively. The rate of change of the lateral stresses is higher than that of the normal stress, with the σ_x component approaching

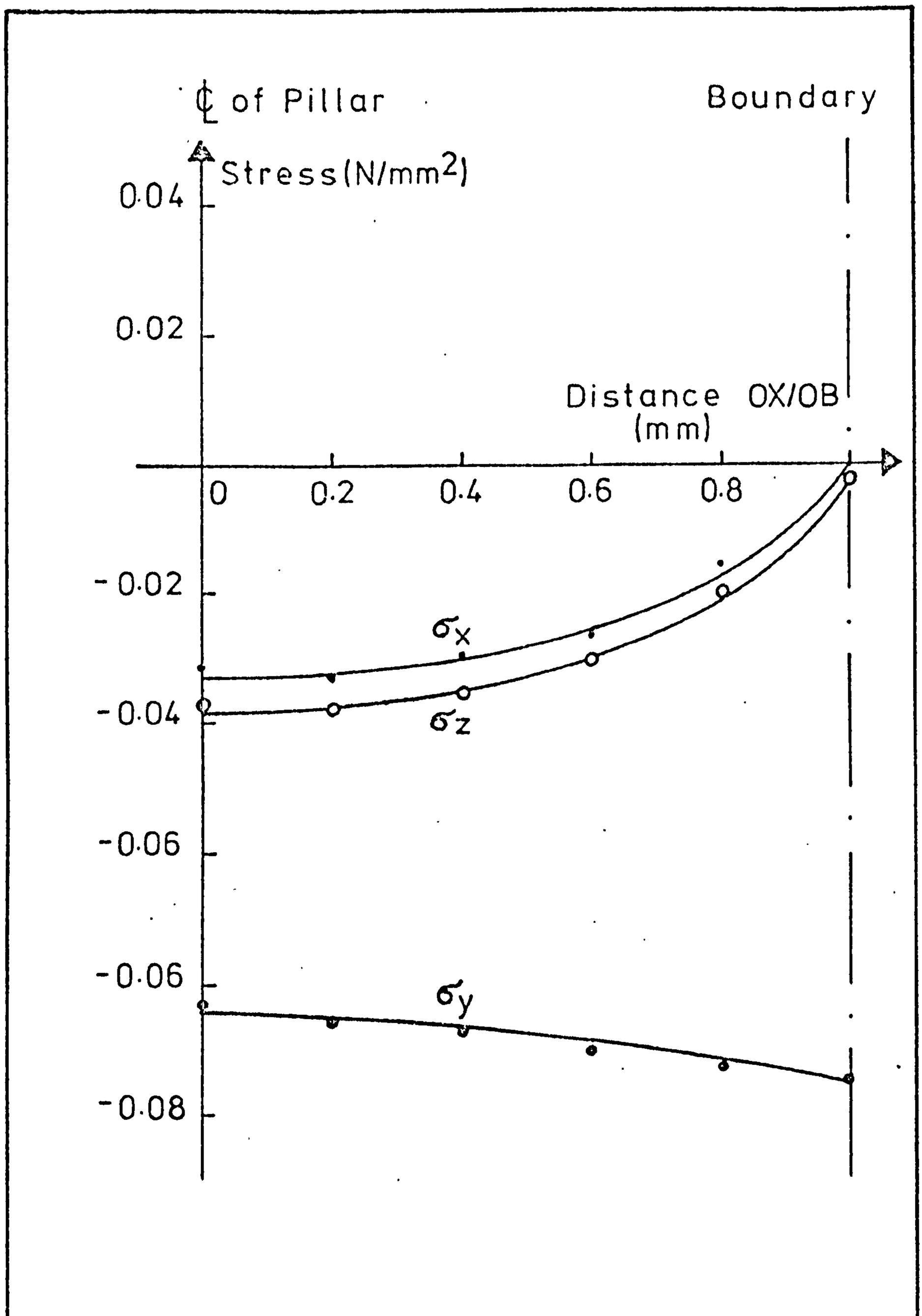

FIG. 5.2.3 NORMAL STRESSES ALONG PILLAR HORIZONTAL CENTRE-LINE.

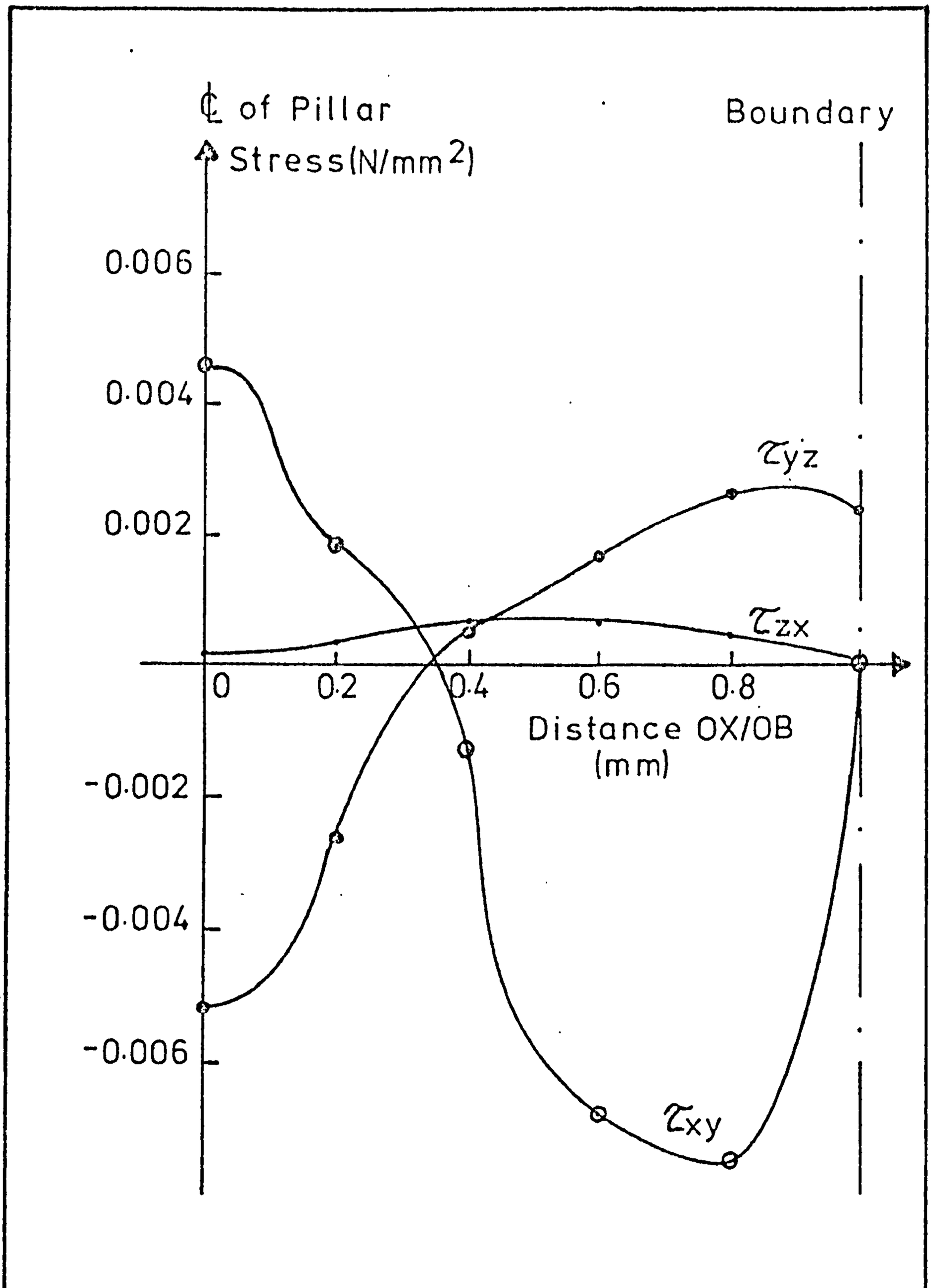

F I G. 5.2.4 SHEAR STRESSES ALONG PILLAR HORIZONTAL CENTRE-LINE .

zero at the boundary as expected, whereas a very small value ($0.0035N/mm^2$) of the σ_z is retained. Ideally, the above two curves should be identical and the deviation shown, therefore, is the result of a number of factors. Apart from the experimental errors, which as demonstrated before are very small, perfect uniformly distributed loading is extremely difficult to achieve, with the loading frame used for this investigation. In addition due to the finite size of the line of investigation, (i.e. the width of the laser), a much wider line was examined than the imaginary line of interest OB. This means that the required and examined points do not always perfectly coincide with each other and although such differences are extremely small they can, however, influence the stresses significantly in regions of sharp stress gradients.

Figure 5.2.4. shows the shear stress distribution along the horizontal centre line OB. The lateral shear stress τ_{zx} shows a small increase from zero at the boundary to $0.0006N/mm^2$ in tension at the centre of the line OB, eventually dropping to $0.0002N/mm^2$ near the point 0. The equivalent tensile stress concentrations are 0.03 and 0.01 respectively. The remaining two shear stress show a degree of symmetry, in particular near the central

area of the pillar. At this point τ_{xy} is 0.0045 N/mm^2 in tension, whereas the τ_{yz} value is 0.0052N/mm^2 in compression. This gives a tensile stress concentration of 0.225 and a compressive one of 0.26 respectively. Both shears decrease numerically towards zero and as it can be seen from Figure 5.2.4. it can be approximated that $\tau_{xy} = \tau_{yz} = 0$ at a distance OX from the pillar's centre, where OX/OB is about 0.265. At this point both curves change sign, with τ_{yz} increasing in the tensile region and τ_{xy} numerically increasing in the compressive region. The τ_{xy} reaches an overall maximum value of about 0.0075N/mm^2 or a maximum compressive stress concentration of 0.375 at a distance OX, where OX/OB = 0.8, before returning to zero at the boundary. The τ_{yz} stress approaches a maximum tensile stress of 0.0026N/mm^2, equivalent to a concentration of 0.13, at OX/OB = 0.8, which is exactly half the maximum compressive stress concentration shown by this shear stress at the centre of the pillar. Lastly, the boundary value of τ_{yz} is 0.0024N/mm^2 representing a terminal tensile concentration of 0.12.

5.3 THE INFLUENCE OF THE FACE ADVANCE ON THE THREE-DIMENSIONAL STATE OF STRESS OF A PILLAR LEFT BEHIND LONGWALL WORKINGS

In the second investigation the scattered light technique was employed to examine the three-dimensional stress changes due to the face advance, on a horizontal line, at the mid-height of a pillar, left behind a longwall face. A multi-layer model was used in this case but for reasons explained below, complete stress separation was not carried out. As before, the investigation is outlined by considering the following stages:

(a) Problems description: The case of a large rectangular pillar was considered behind a longwall face, but as opposed to the previous investigation where an imaginary situation was assumed, this time an attempt was made to simulate the conditions existing on an actual mine. Killoch Colliery in Ayrshire, was chosen as a typical example, simply because the author had investigated such pillars at this colliery by 'in-situ' techniques (see Chapter VI). The intention was to fully examine the stresses on a horizontal line parallel to the face line and at the mid-height of the pillar, using a multi-layer model simulating the strata as accurately as possible. However, it became apparent that although the mechanical similitude was reasonably achieved using a material like polyurethane, the linear one was unattainable due to the

geometrical disproportionalities of the actual prototype. If H, W and L are the representative dimensions of a pillar, (i.e. height, width and length respectively), then for the pillar under investigation the ratios W/H and L/H are 24/1 and 64/1 approximately. If the model is to satisfy the laws of similitude the above ratios must be maintained; this means that if a reasonable linear scale is selected to give sufficient pillar height in the model, and thus enable accurate calculations on the polariscope, the overall size of the model is going to be extremely large, and could not be accommodated on the instrument's base. On the other hand, if a linear scale is selected so that the whole model is within the capabilities of the polariscope, the seam thickness is going to be so small that no scattered light observations could be carried out. This problem could be negotiated, however, by using the freezing method where the model is heated under load in a large oven. Calculations can then be made by physically slicing the model, as required, and examining it in a conventional polariscope, or by isolating the particular section of interest from the model, and use the scattered light technique to perform an imaginary slicing. Although this procedure can deal with the actual linear scaling of the model, nevertheless, it is not suited for multi-layer models, since polyurethane

is not noted for any diphasic characteristics. A compromise had to be found, therefore, and it was decided to construct a model simulating a small section of the workings only, and this enabled a reasonable linear scale to be used. The model, therefore, had to be loaded in plane strain in order to compensate for the adjacent material. In addition, since a large number of layers was used, the fringe contrast was not satisfactory and as a result it was decided that observations should be limited to birefringence measurements only.

(b) Photo-elastic model: The section under investigation, with respect to the underground workings is shown in Figure 5.3.1. The geological section of the seam, in the vicinity of the N.10 panel at Killoch colliery, is as shown in Figure 5.3.2. Since it was decided to construct a multi-layer model, the laws of similitude, explained in the previous chapter, had to be satisfied. From equations (4.4.9) and (4.4.6)

$$\frac{Ep}{Em} = \frac{1}{\lambda} \quad \frac{\gamma p}{\gamma m}$$

where

$$\frac{Lm}{Lp} = \lambda$$

Taking the density of the coal measure strata as

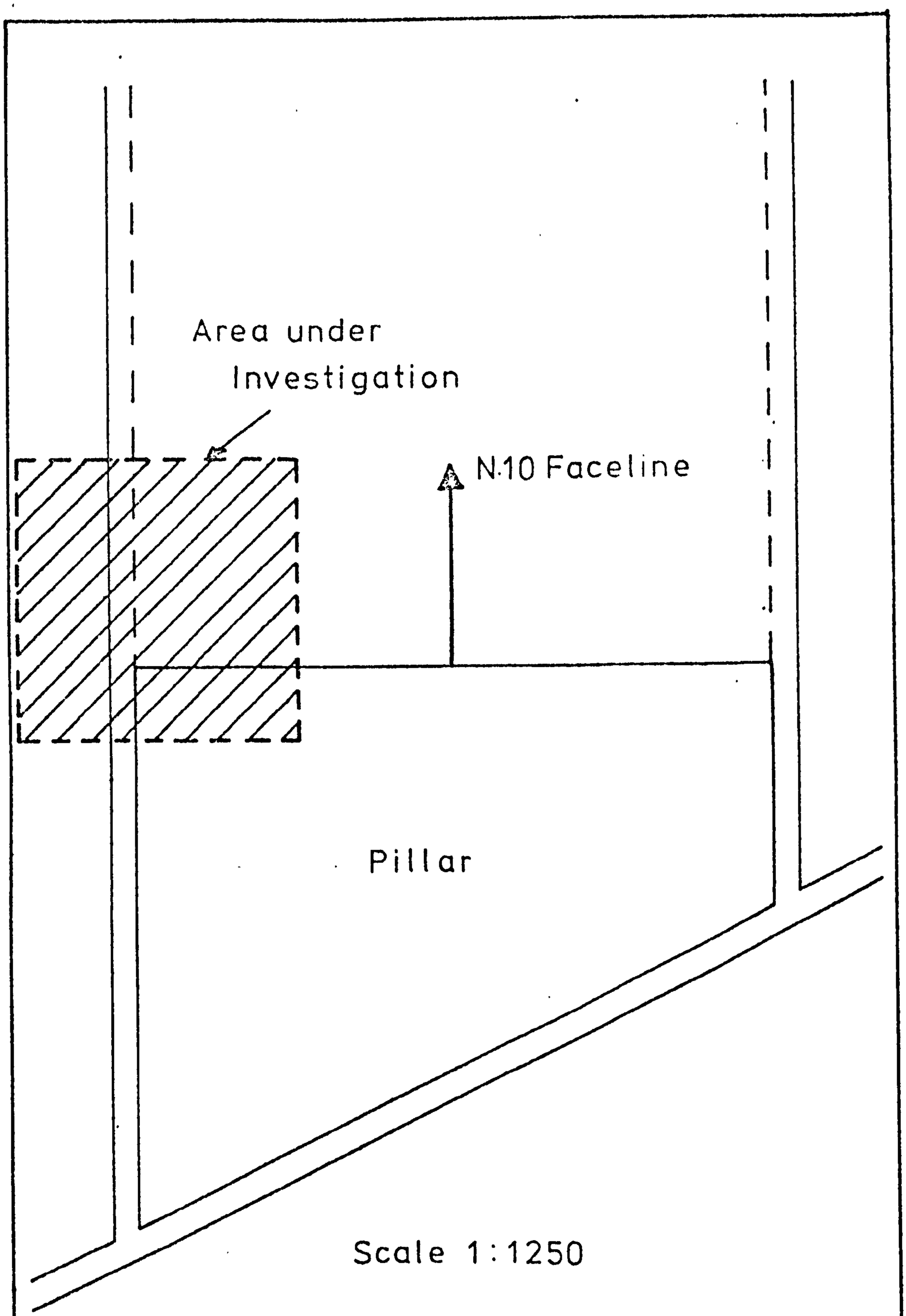

Scale 1:1250

FIG.5.3.1 AREA UNDER INVESTIGATION WITH RESPECT TO THE N.10 PANEL AT KILLOCH COLLIERY.

2.5gm/cm^3, and that of the polyurethane as 1.0gm/cm^3 then

$$\frac{Ep}{Em} = \frac{2.5}{\lambda}$$

After a careful examination of the various linear parameters involved, as previously explained, it was decided that the best linear scale is 1 : 650. The similitude equation, therefore, becomes

$$\frac{Ep}{Em} = \frac{2.5}{1/650} \doteq 1625 \qquad (5.3.1)$$

From a laboratory testing program, carried out by the author and Smart[79], the following values for the Young's modulus of the strata were found (Appendix B):

Type of Rock	Actual E ($\times 10^3$MN/m^2)	Required E (MN/m^2)
Sandstone	6.0	3.7
Shale	7.5	4.6
Coal	1.3	0.8
Mudstone	5.5	3.4

The above table shows the required Young's modulus of the various polyurethane layers, for perfect similitude. As it was previously mentioned by varying the proportions of the prepolymer and catalyst in the mixture, modular ratios of about 40/1 can be achieved.

However, in order to use the most appropriate mixtures, the

required values had to be adjusted slightly (roughly divided by 1.3), as shown below:

Type of Rock	Required E (MN/m^2)	Experimental E (MN/m^2)
Sandstone	3.7	2.8
Shale	4.6	3.5
Coal	0.8	0.6
Mudstone	3.4	2.6

The simulated geological section is shown in Figure 5.3.2. and the actual model and prototype linear relationships are illustrated in Figure 5.3.3. The various layers were casted individually in a specially designed perspex mould, having two perspex inserts, one of a rectangular cross-section and the other of an arched one, at right angles to each other. By advancing the arched insert inside the mould and increasing the width of the rectangular one any face advance could be simulated. This method was proved much more accurate than the physical slicing of the particular layer to obtain the required cross-section. By putting a liberal quantity of grease on the inserts, they could easily be withdrawn from the mould when the material was set. Grease was also used on the sides of the mould, so that the individual layers could be removed when required. The model and mould are shown in the photograph

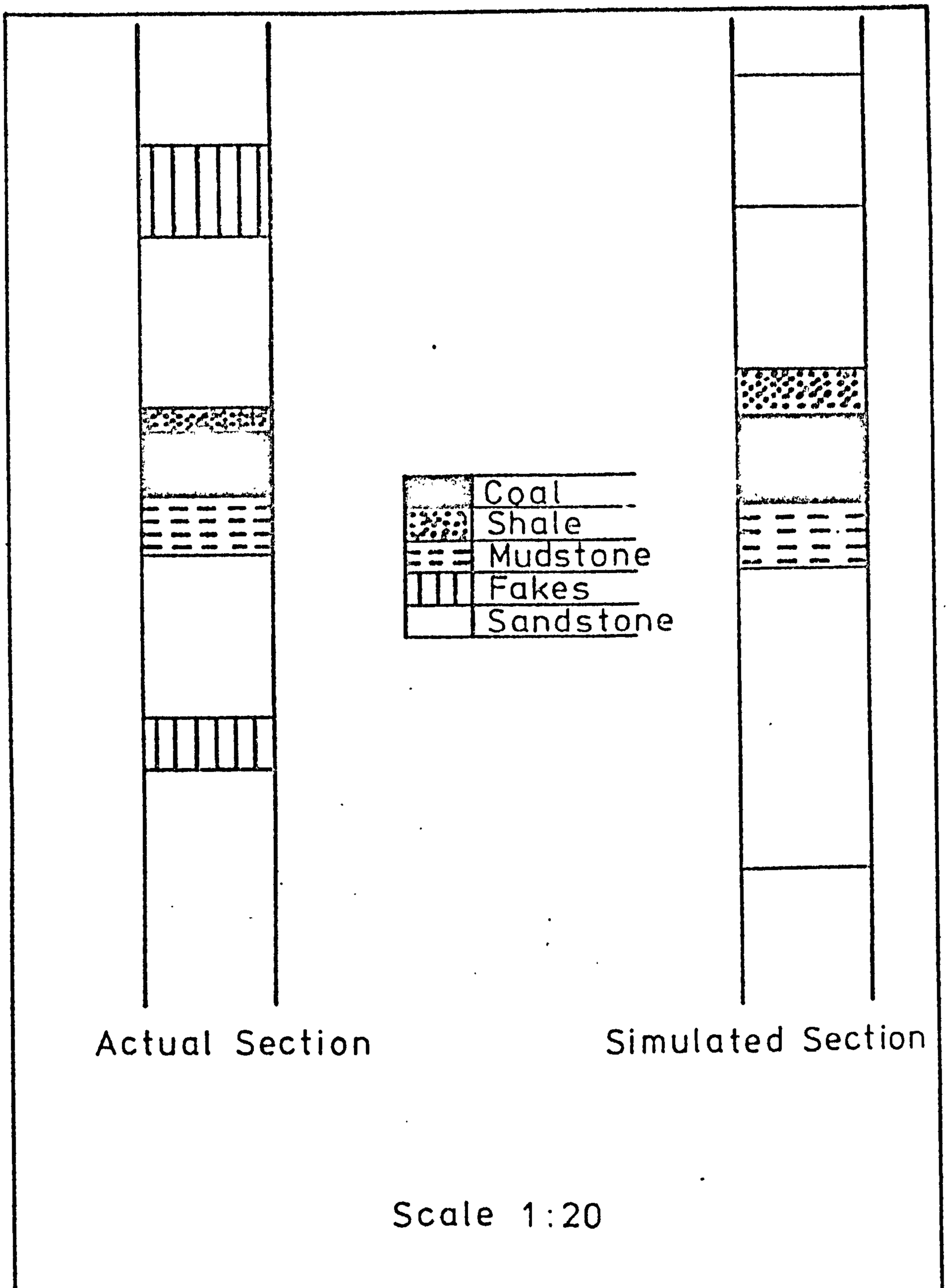

Scale 1:20

FIG. 5.3.2 ACTUAL AND SIMULATED GEOLOGICAL SECTIONS.

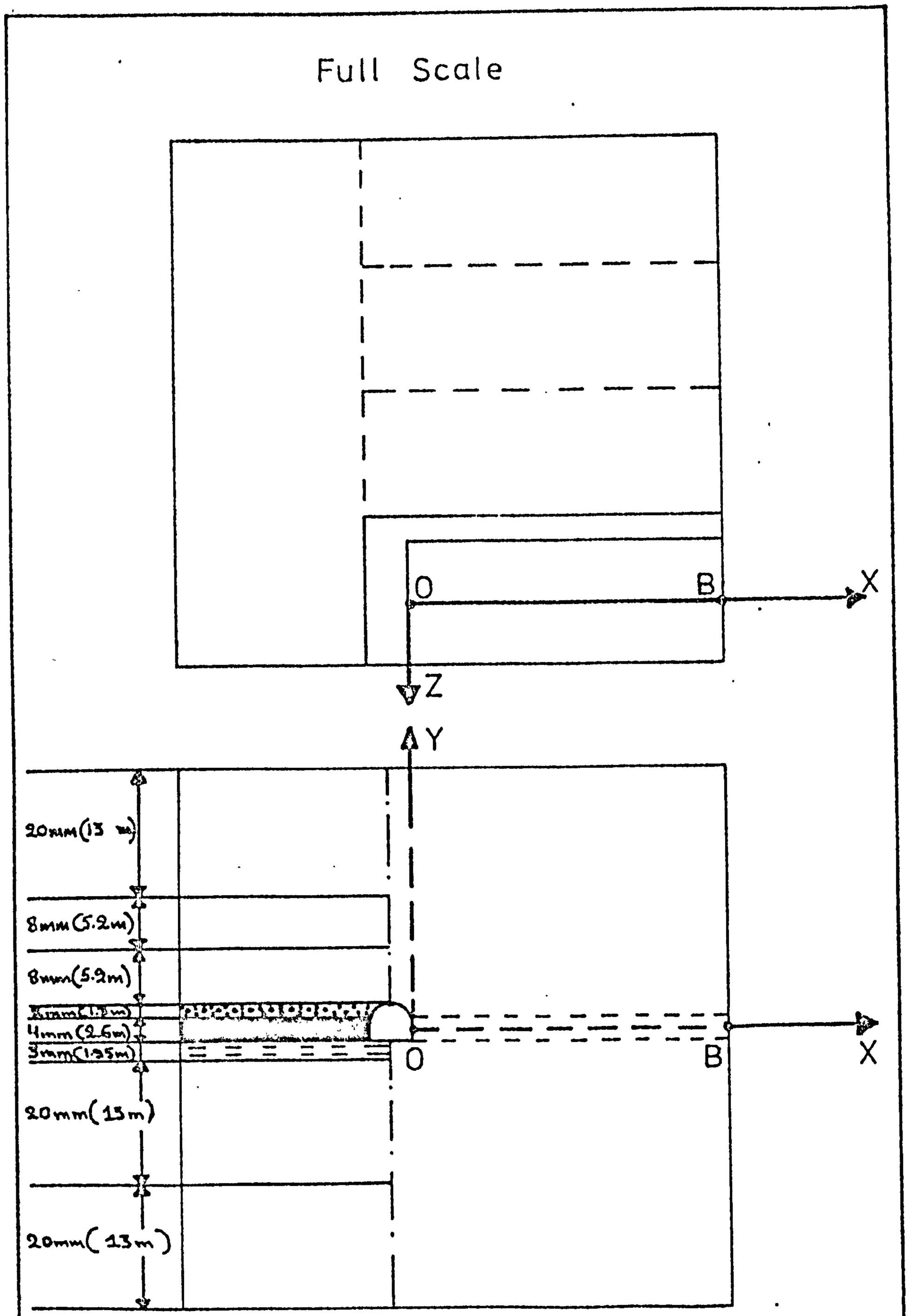

FIG. 5.3.3 MULTI-LAYER MODEL .

of Figure 5.3.4. Since the model had to be loaded in plane strain, the same loading device was used as before, but this time the model was retained inside the mould. A perspex plate, 1.27cm thick, was placed on top of the model accurately machined so that its dimensions were exactly the same to the ones of the model, and therefore could be just fitted inside the mould. The loading from the perspex platen was therefore uniformly transmitted to the model through this perspex plate. Before the investigation, all the surfaces were well lubricated, using the same grease as before (Trade name Adsil). As it can be seen from Figure 5.3.3, the line under examination was parallel to the face line, 1cm (i.e. 6.5m in terms of the prototype) inside the pillar and at mid-height. Four different face advances were chosen, 0.4cm (2.6m in prototype), 2.4cm(15.6m), 4.4cm(28.6m) and 6.4cm(41.6m). This corresponds to face advances of 1, 6, 11 and 16 times the seam thickness. The four investigations were carried out by assuming no waste simulation, however, the last face advance was also examined with the waste fully caved. In the latter case the same dimensional analysis was used, as in Prasad's work[63], in order to establish the most realistic sizes of caved material. The waste was then simulated by

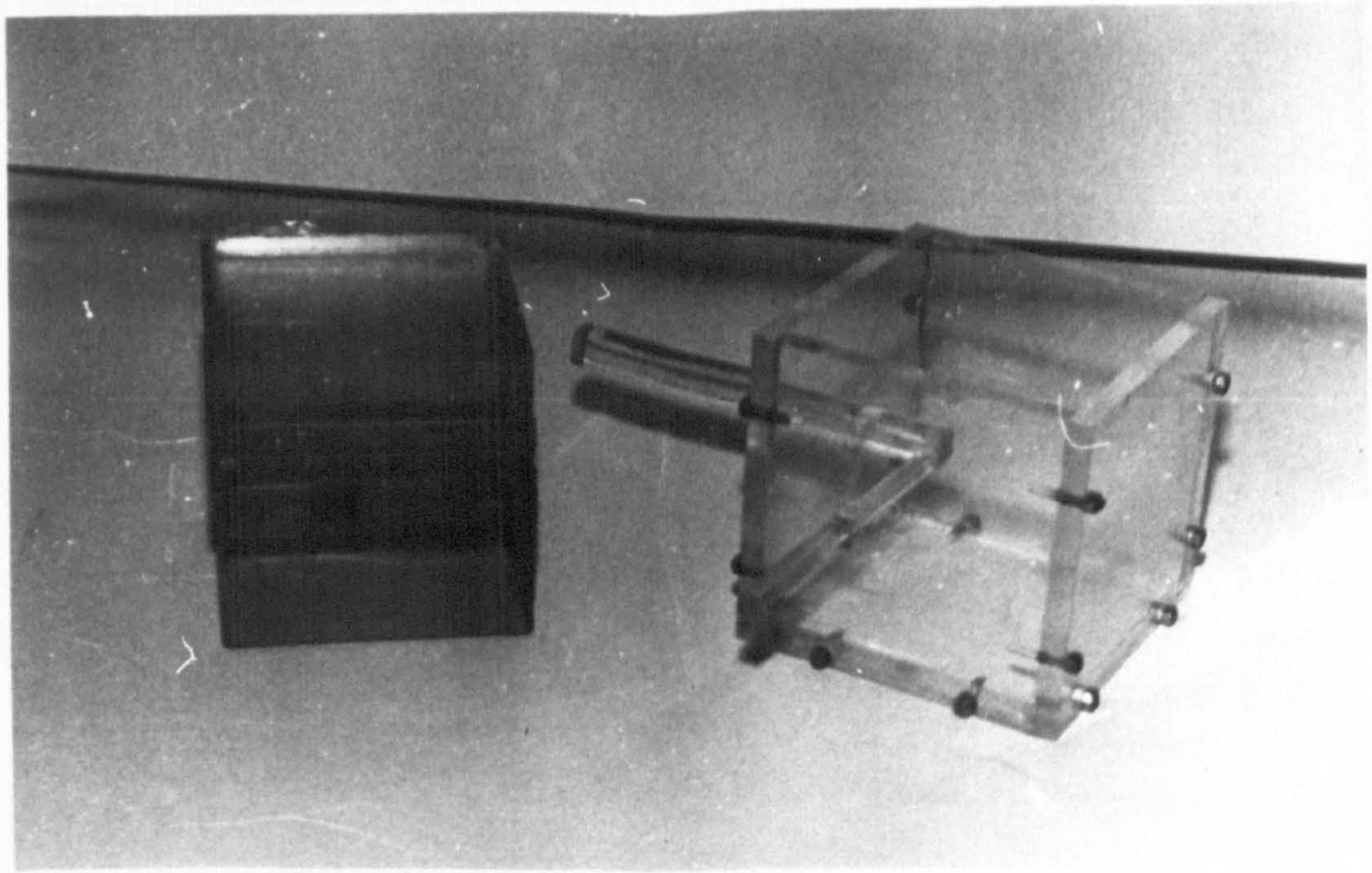

FIG. 5.3.4 MODEL AND MOULD .

slicing the roof beds to the predetermined sizes, and filling the waste area using a void ratio of about 0.28. The model for the waste simulation, for an advance of 6.4cm(41.6m), was as shown in Figure 5.3.5.

(c) Experimental results: During this investigation only birefringence measurements were taken along the line, OB, as shown in Figure 5.3.3. As previously mentioned, in the scattered light photo-elasticity, the stress difference is proportional to the birefringence gradient and not to the total birefringence. As a result, when discussing the fringe patterns, in terms of stresses, it is this gradient that is of the utmost importance and not the fringe order, as in the conventional photo-elasticity. The birefringence gradient can be determined from the compensator measurements, as in the previous case, or by differentiating the fringe order against distance along the beam curve, as in this investigation. From equation 3.5.2. it follows that

$$\frac{dn}{ds} = (p - q) = 2C\tau_{max}$$

In order to distinguish between actual fringe orders and birefringence gradients, the quantity dn/ds is referred to in this analysis as the gradient number.

The experimental procedure therefore was as follows:

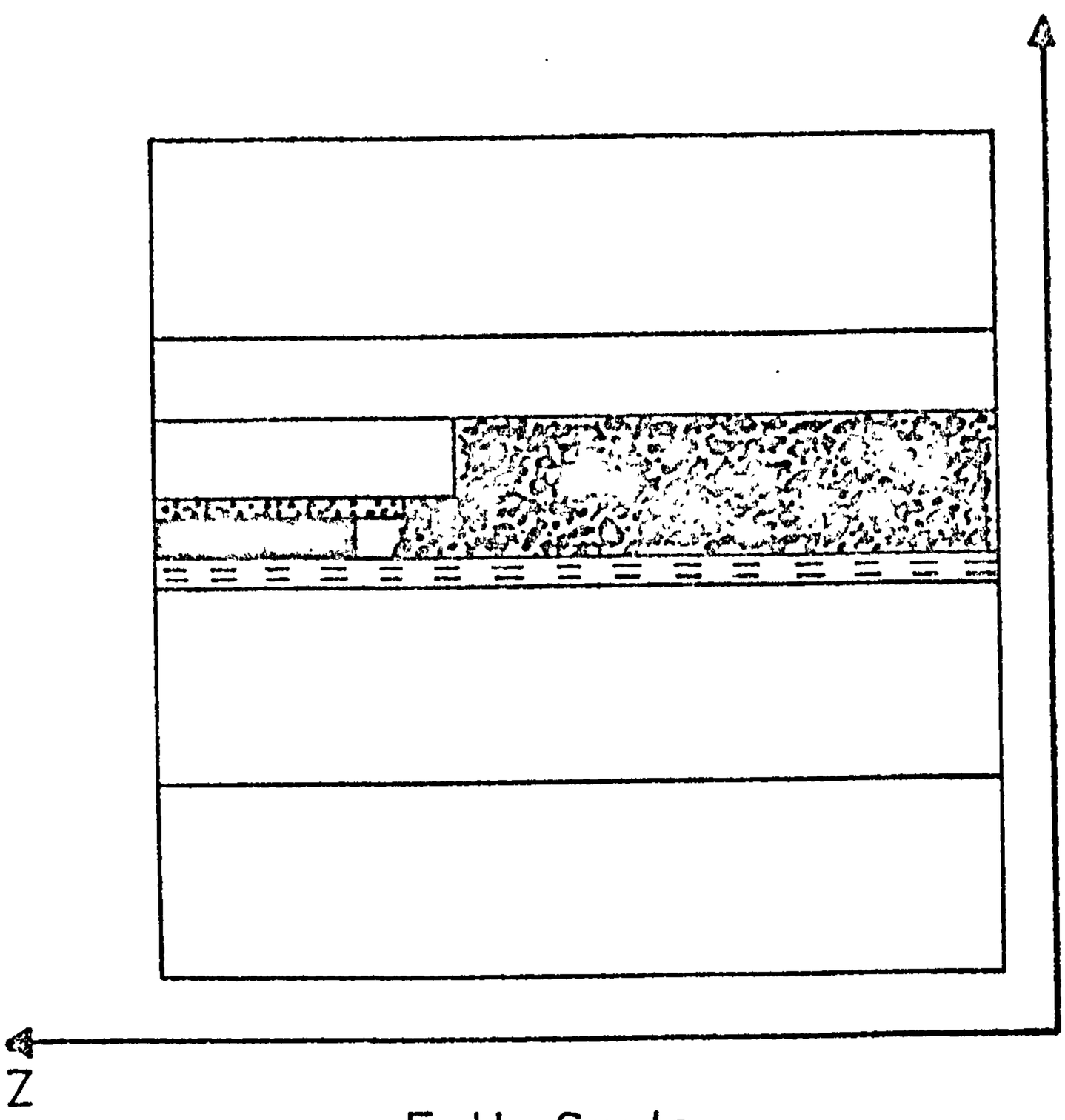

Full Scale

F I G. 5 . 3 . 5 MODEL AND SIMULATED WASTE .

(i) Face advance 2.6m: In the first model an advance of 2.6m was simulated, (0.4cm on the model), equal to the thickness of the coal. In order to eliminate any adverse effects on the birefringence due to the friction between the model and the retaining perspex mould, readings were terminated at a point on the line OB, about 1.5cm(9.75m) from B. The distance Δ_x between the points of interest was 5mm(3.25m). With the light parallel to the Z-axis, the fringe orders along this point, with respect to the distance of the entering beam, are shown in Figure 5.3.6. As expected, the maximum gradient (shear stress), occurs at the edge of the pillar, point O, and is about 0.33. The stress gradually decreases when moving inside the pillar, until an asymptotic value of 0.10 is reached at a distance of 20mm(13m) from the edge.

The fringe order and birefringence gradients with the light parallel to X-axis (i.e. along OB), are shown in Figure 5.3.7. A similar curve of gradient numbers is obtained, reaching a maximum of 0.28 at the pillar edge, with the rate of decrease becoming constant at about 25mm(16.25m) inside the pillar. The gradient number at this point is 0.14.

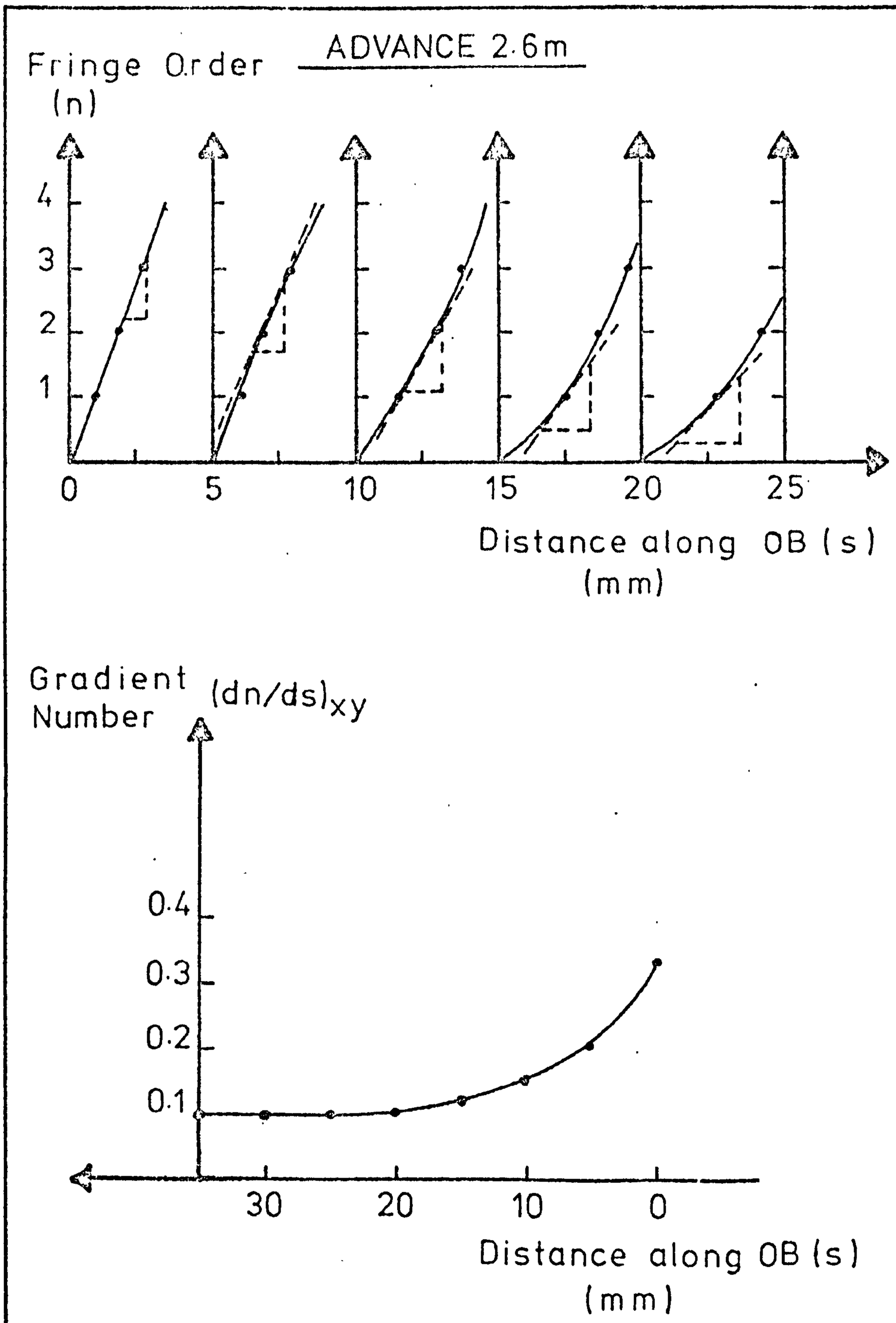

FIG. 5.3.6 BIREFRINGENCE ALONG OB IN THE XY-PLANE .

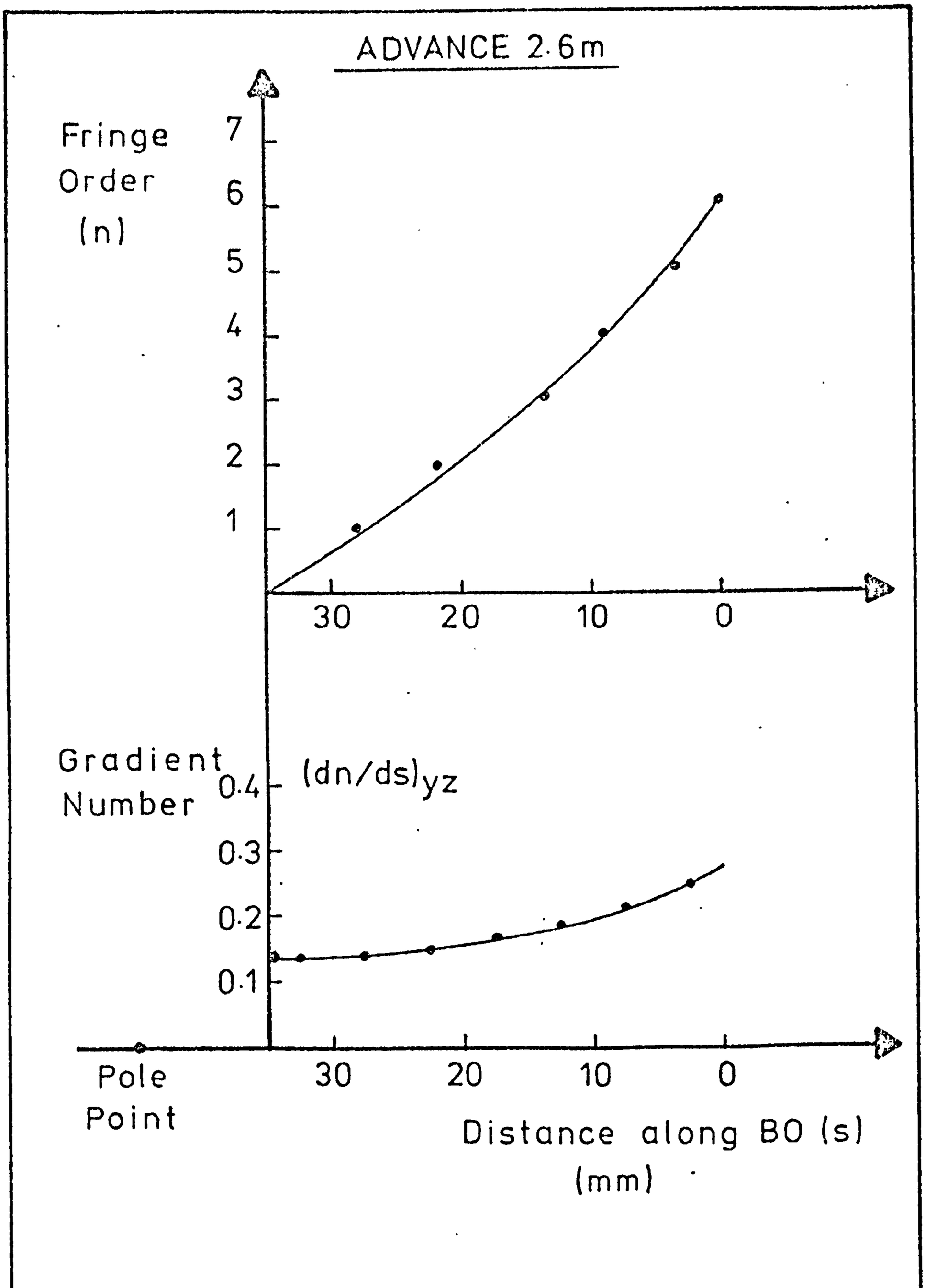

F I G. 5 . 3 . 7 BIREFRINGENCE ALONG OB IN THE YZ-PLANE .

Figure 5.3.8 shows the XY- and YZ-shear stresses along the pillar, with respect to the diameter of the opening, for this particular advance. The dotted lines represent the logical extension of the two curves towards the centre line of the pillar. Both gradient numbers are nearly parallel to each other for distances from the pillar edge more than 1.5 times the width of the opening. Between this point and the edge of the pillar both gradient numbers increase steeply, with the XY stress crossing the YZ one to reach a higher value at the latter point.

(ii) Face advance 15.6m: This advance was simulated by slicing the layer representing the coal, in the previous model, to the required length, using a well greased scalpel.

Figures 5.3.9 and 10 show the birefringence on the line OB with respect to XY- and YZ-planes respectively. A comparison of both these curves, in relation to the width of the opening is given in Figure 5.3.11. The general shape of the stresses is the same as before but higher values are this time attained at the edge of the pillar. The gradient numbers at point O are 0.4 in the XY-plane

ADVANCE 2·6 m

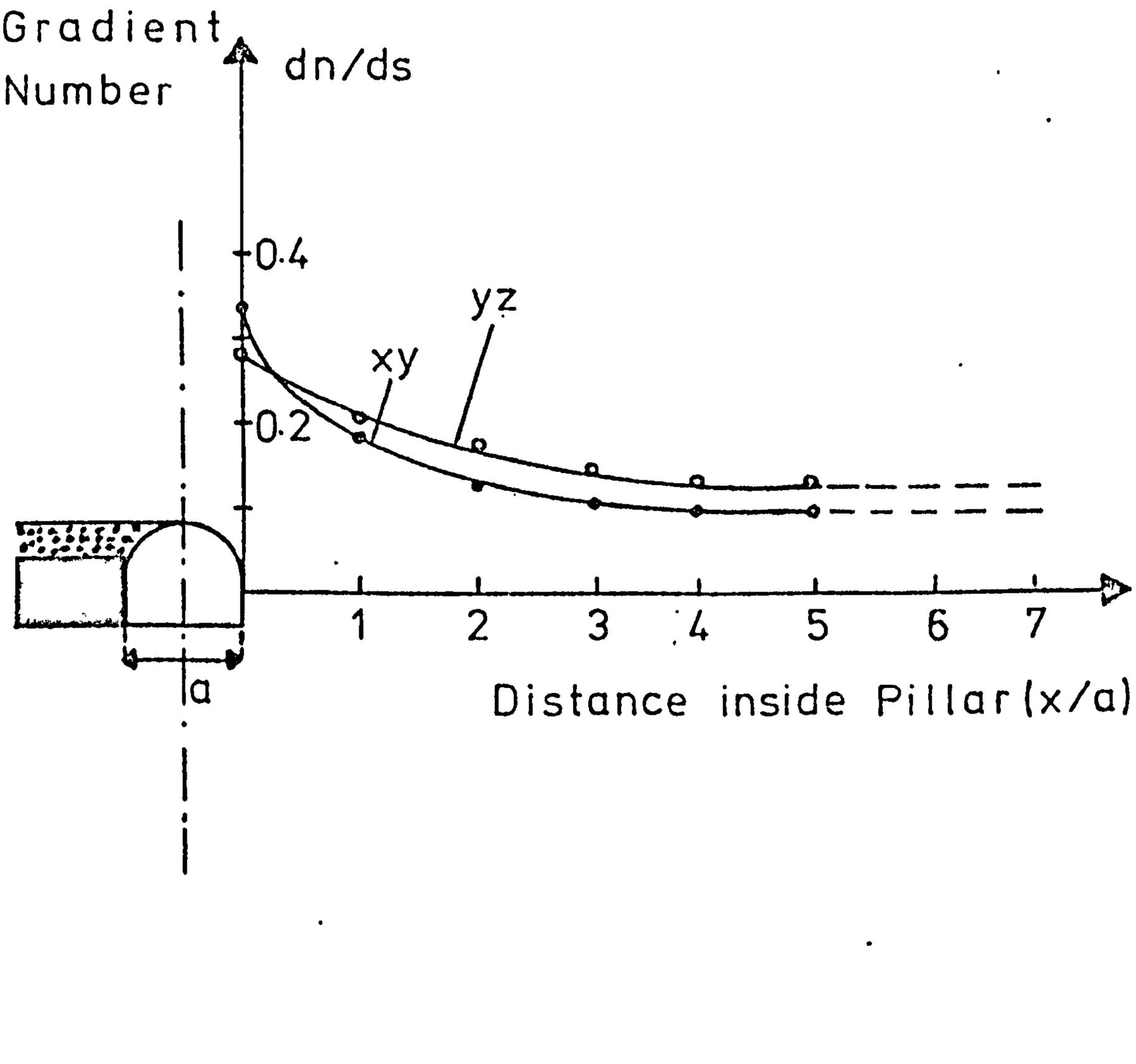

FIG. 5.3.8 GRADIENT NUMBERS ALONG OB WITH RESPECT TO THE OPENING WIDTH.

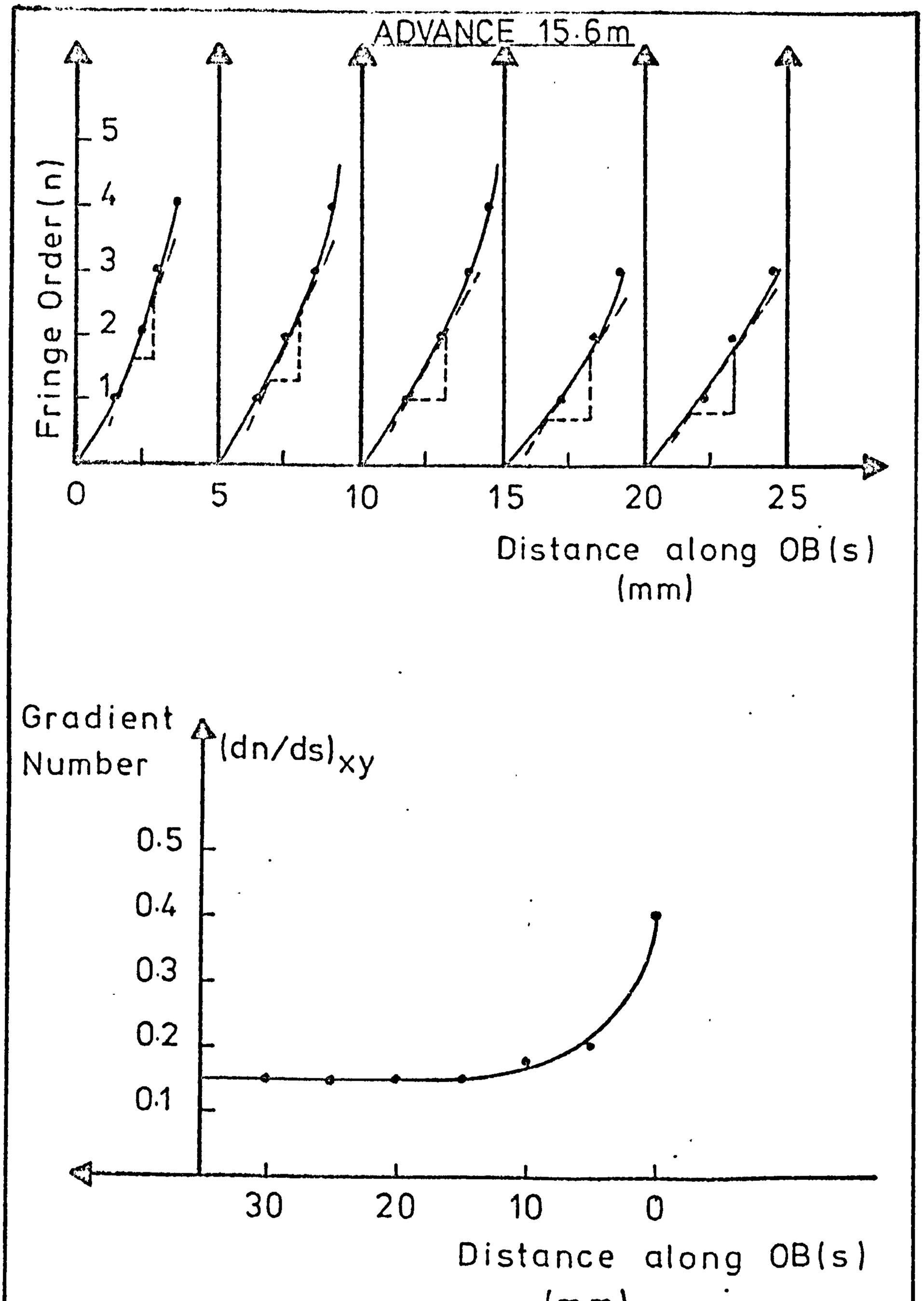

F I G. 5 . 3 . 9 BIREFRINGENCE ALONG OB IN THE XY-PLANE .

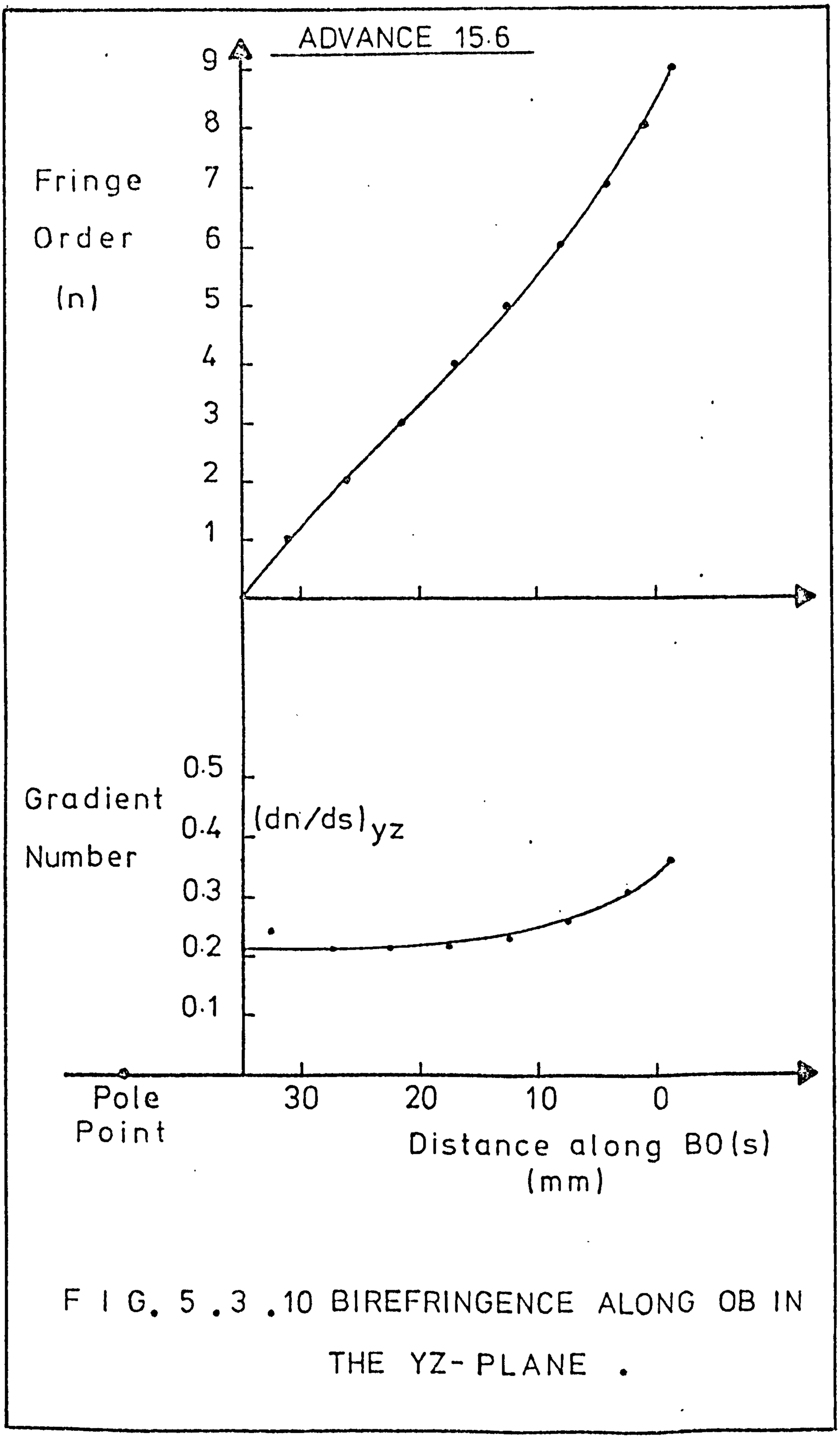

FIG. 5.3.10 BIREFRINGENCE ALONG OB IN THE YZ-PLANE.

ADVANCE 15.6m

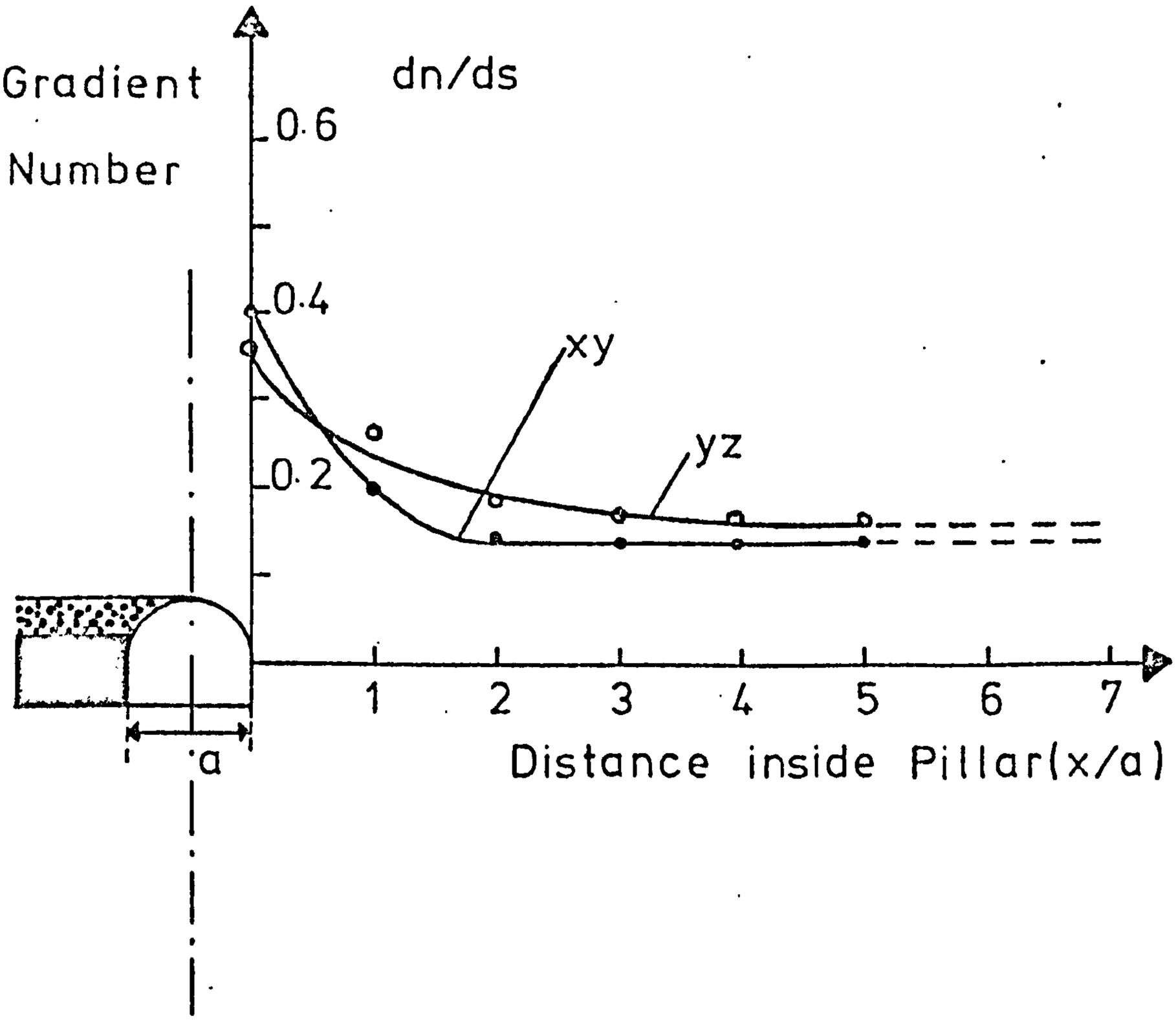

FIG. 5.3.11 GRADIENT NUMBERS ALONG OB WITH RESPECT TO THE OPENING WIDTH .

and 0.35 in the YZ-plane. The rate of decrease of the XY-stresses is much sharper but both curves approach each other at distances more than 4 times the width of the opening from the edge of the pillar.

(iii) Face advance 28.6m: The model was further sliced to simulate 4.4cm or 28.6m of face advance. The birefringence on the line OB inside the pillar, relative to the XY-and YZ-planes is shown in Figures 5.3.12 and 13. The gradient numbers have further increased near the edge of the pillar at which point the numbers are 0.5 and 0.46 in the XY- and YZ-planes respectively. Both stresses remain constant beyond a distance of 13m from the edge (x/a about 2.8), but the difference between them in this region is higher than before about 0.08 numbers, as shown in Figure 5.3.14.

(iv) Face advance 41.6m: The birefringence measurements are shown in Figures 5.3.15 and 16. The stresses at the edge of the pillar were practically unaffected due to this further increase in advance. Both curves become asymptotic for x/a equal to 2.8 as before, but as it can be seen from Figure 5.3.16, the constant stress values at the interior of the pillar are in this case greater.

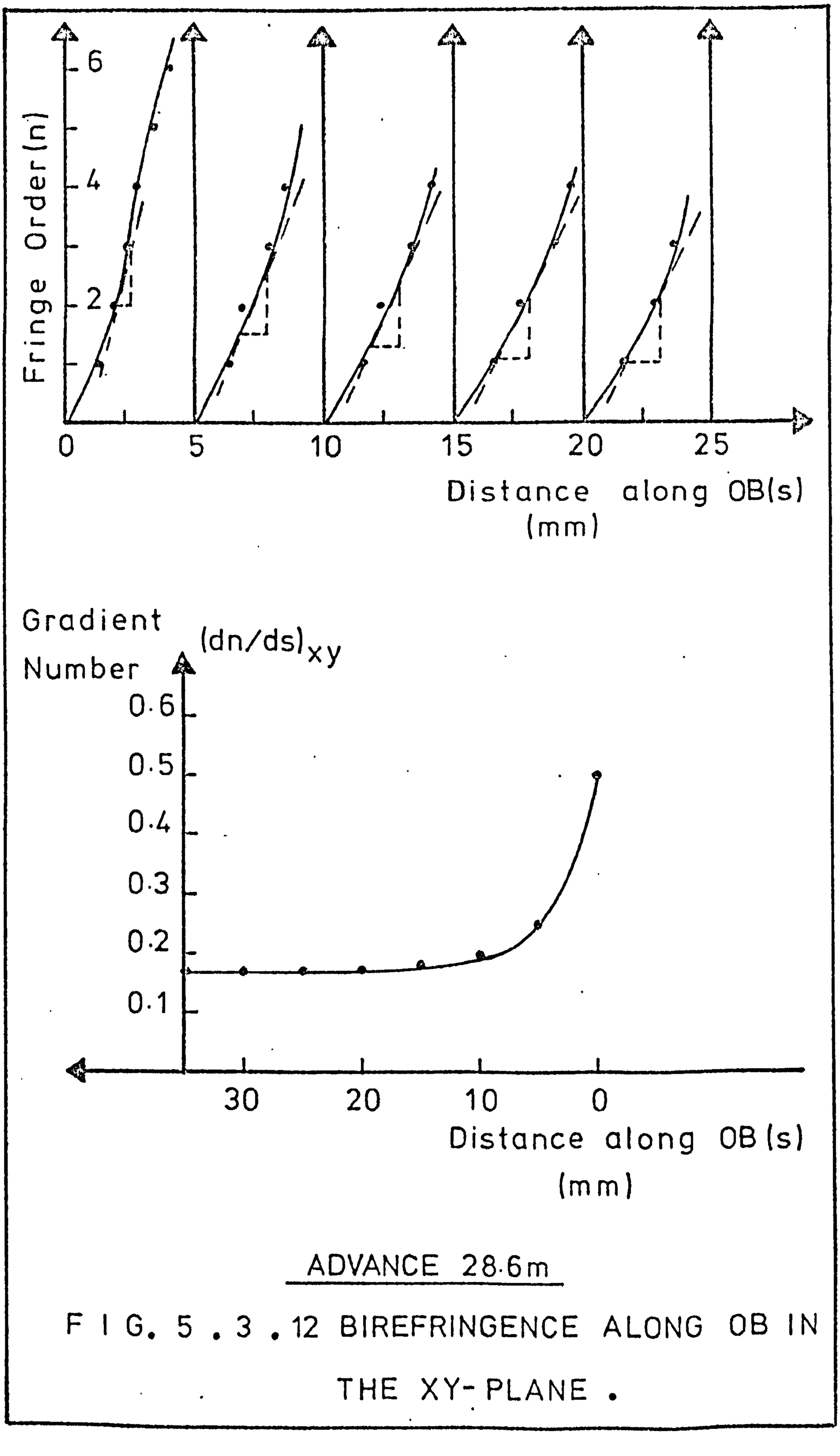

ADVANCE 28·6m

FIG. 5.3.12 BIREFRINGENCE ALONG OB IN THE XY-PLANE.

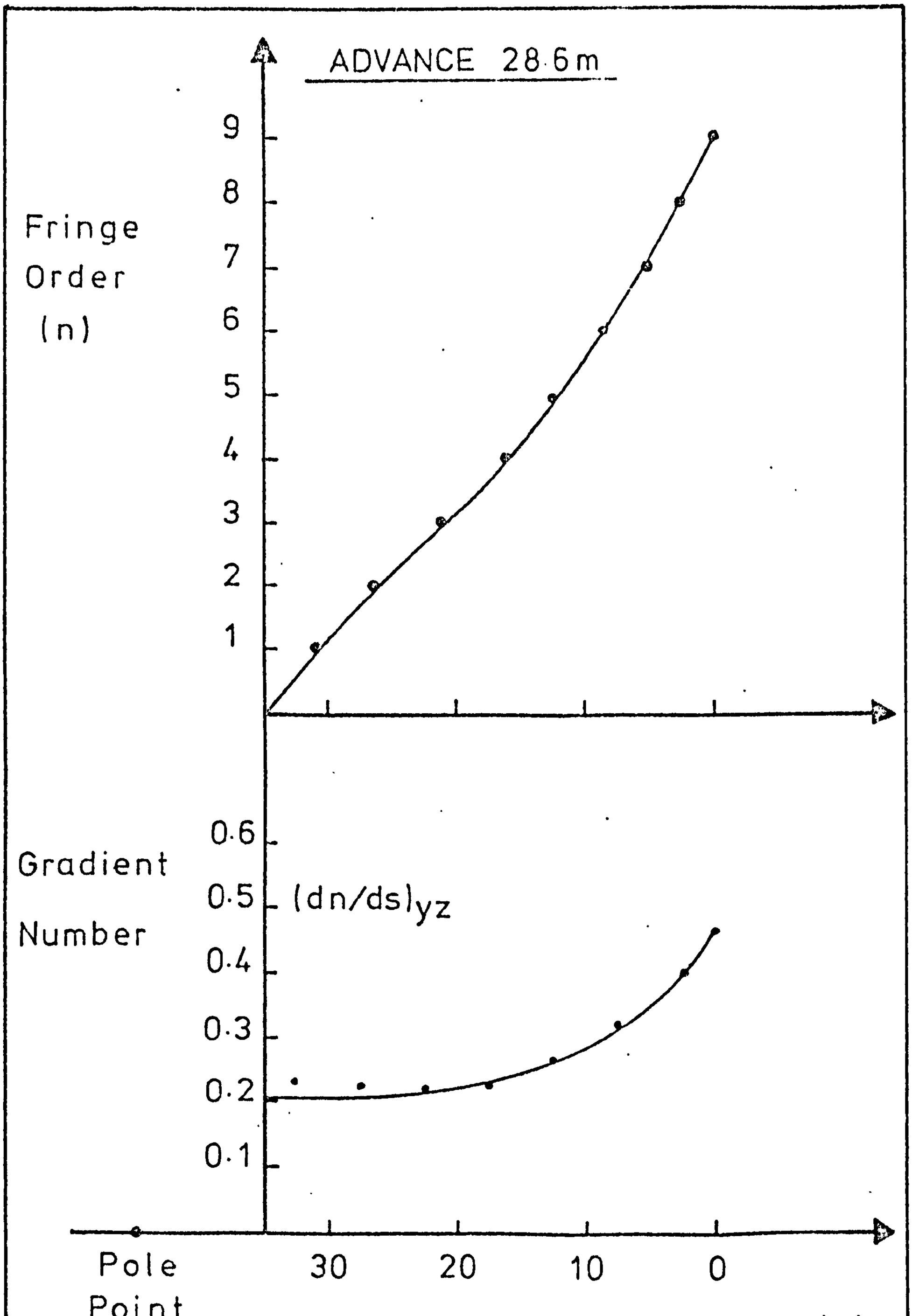

FIG. 5.3.13 BIREFRINGENCE ALONG OB IN THE YZ-PLANE.

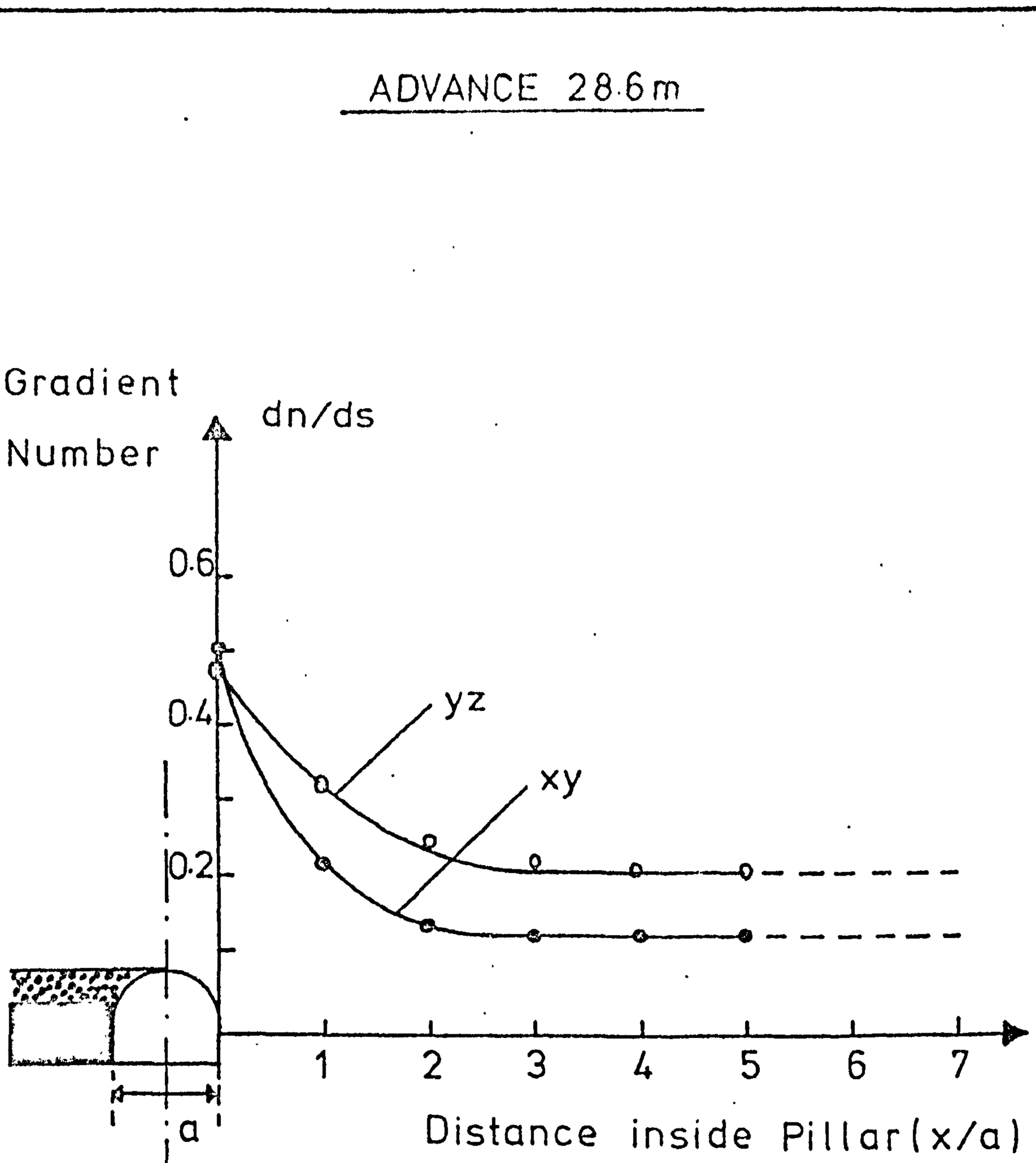

FIG. 5.3.14 GRADIENT NUMBERS ALONG OB WITH RESPECT TO THE OPENING WIDTH.

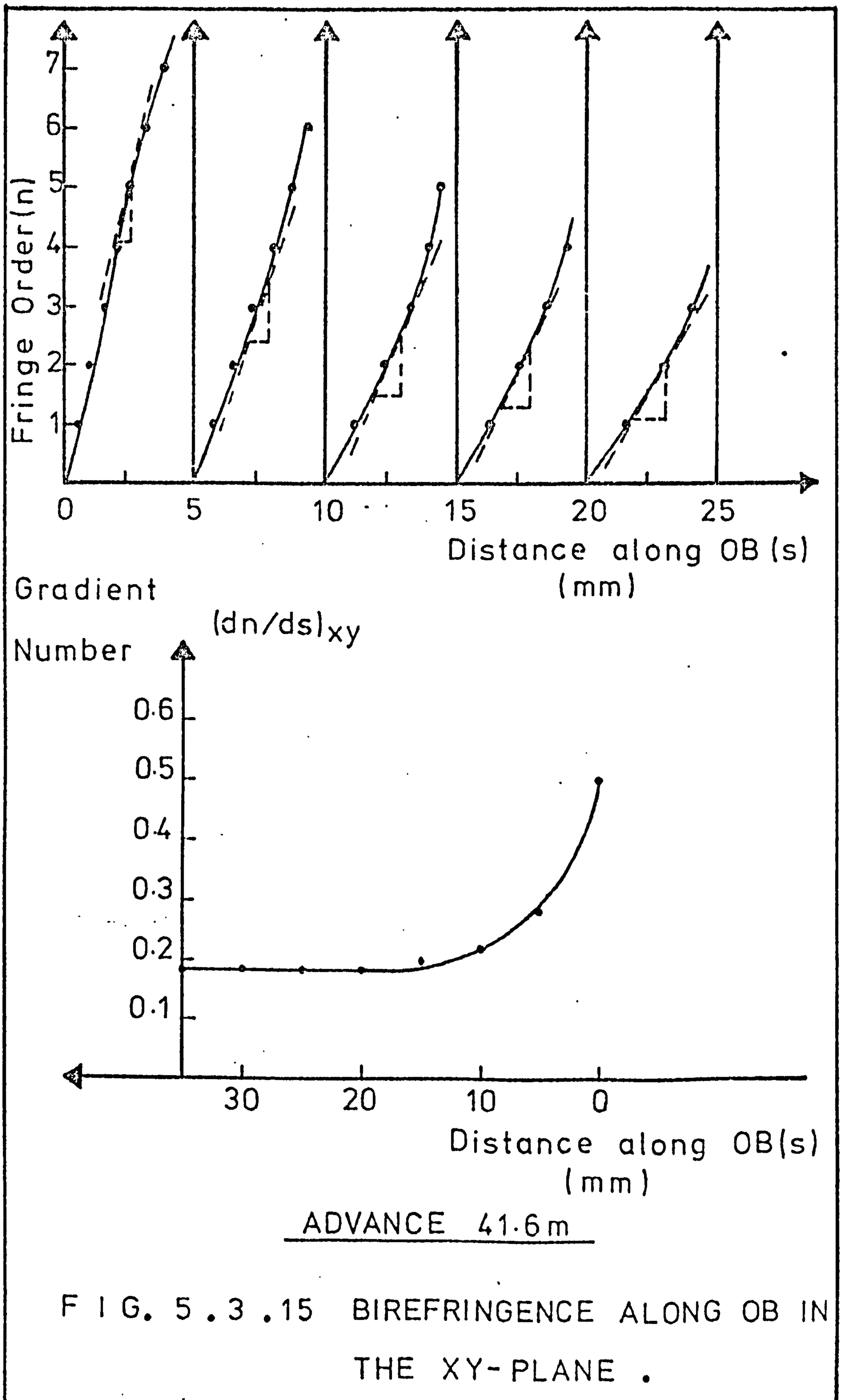

ADVANCE 41·6 m

FIG. 5.3.15 BIREFRINGENCE ALONG OB IN THE XY-PLANE .

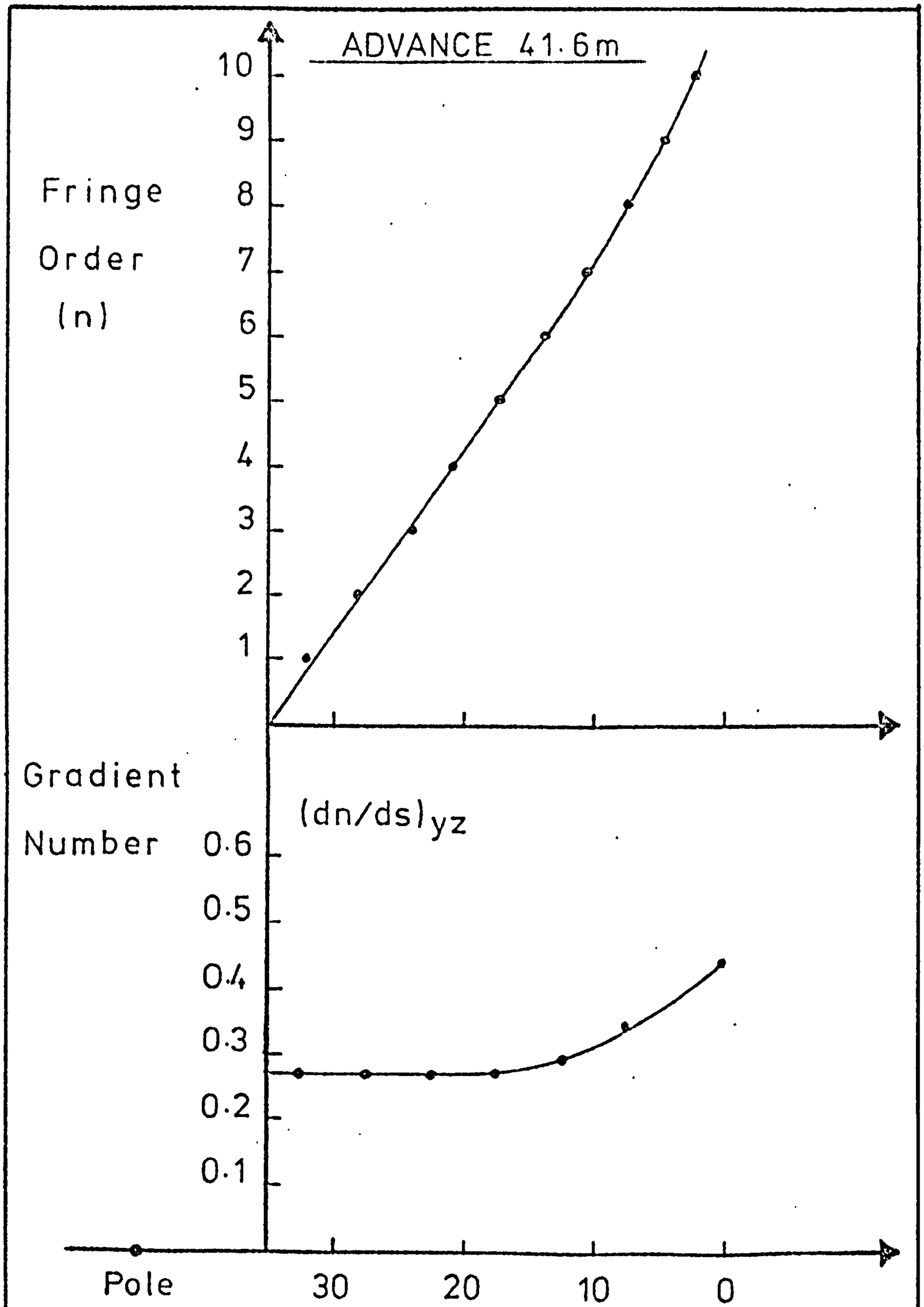

FIG. 5.3.16 BIREFRINGENCE ALONG OB IN THE YZ-PLANE.

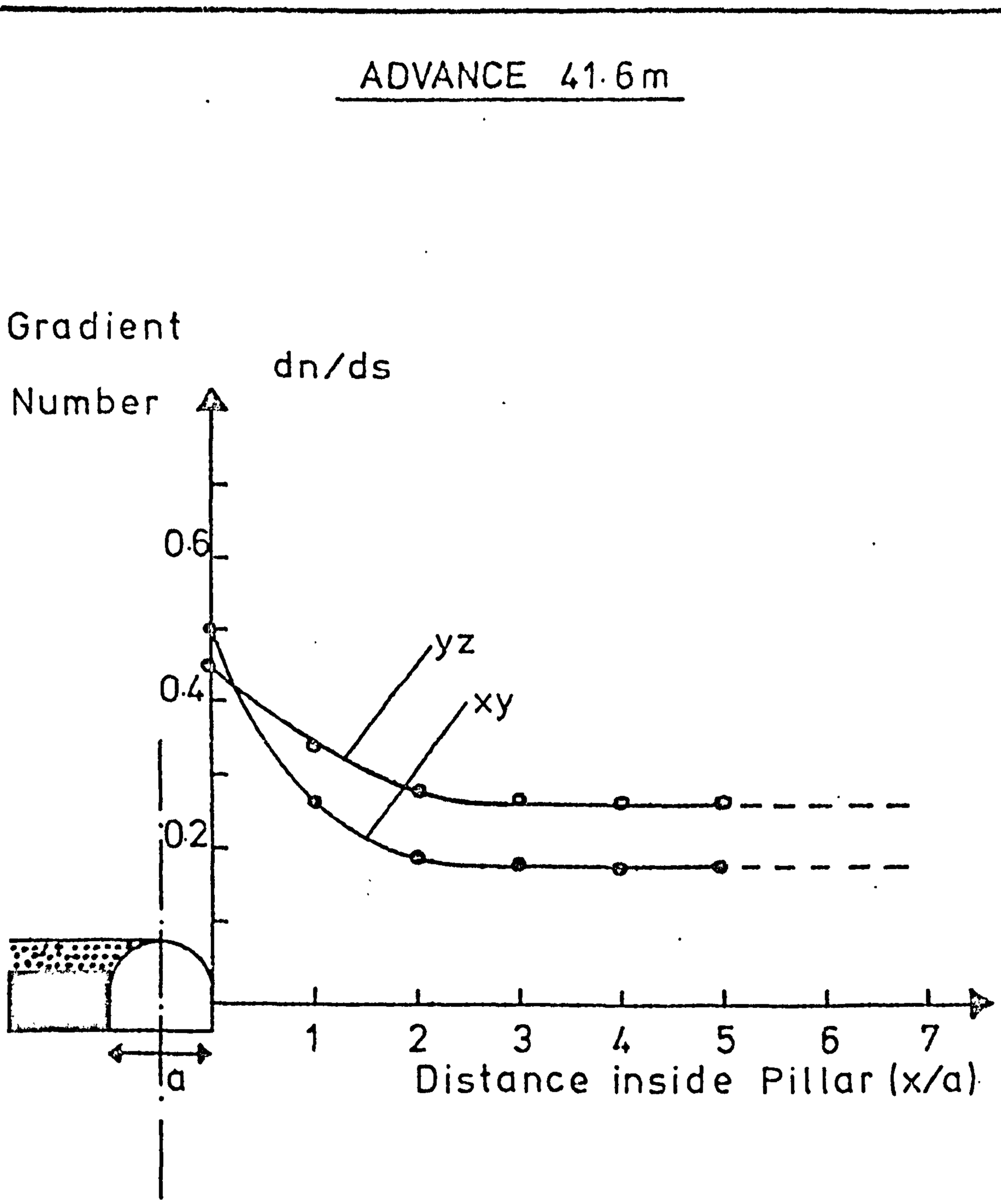

FIG. 5.3.17 GRADIENT NUMBERS ALONG OB WITH RESPECT TO THE OPENING WIDTH.

(v) Face advance 41.6m, fully caved waste: For the final analysis the model was sliced as shown in Figure 5.3.5, in order to simulate the total caving of the waste.

The birefringence in the XY- and YZ-planes is shown in Figures 5.3.18 and 19. The shear stresses at the edge of the pillar have decreased, as opposed to the previous case of no waste simulation. The gradient numbers at this point are 0.3 and 0.33 for the XY- and YZ-planes respectively. Both curves remain constant for distances beyond 15mm (9.75m) from the edge. This corresponds to x/a of just over 2 as shown in Figure 5.3.20. The difference between these stresses is slightly less than before, and at a smaller gradient level.

(d) Discussion of results: A number of common features can be seen in all the cases studied. From the fringe patterns the bending action of the roof and floor layers is evident. The maximum stress, for all advances at the mid-height of the pillar was on the pillar's edge. This was as expected since the model material is homogeneous and isotropic. From the patterns with the light parallel to the Z-axis it is also seen that as the line OB moves parallel to

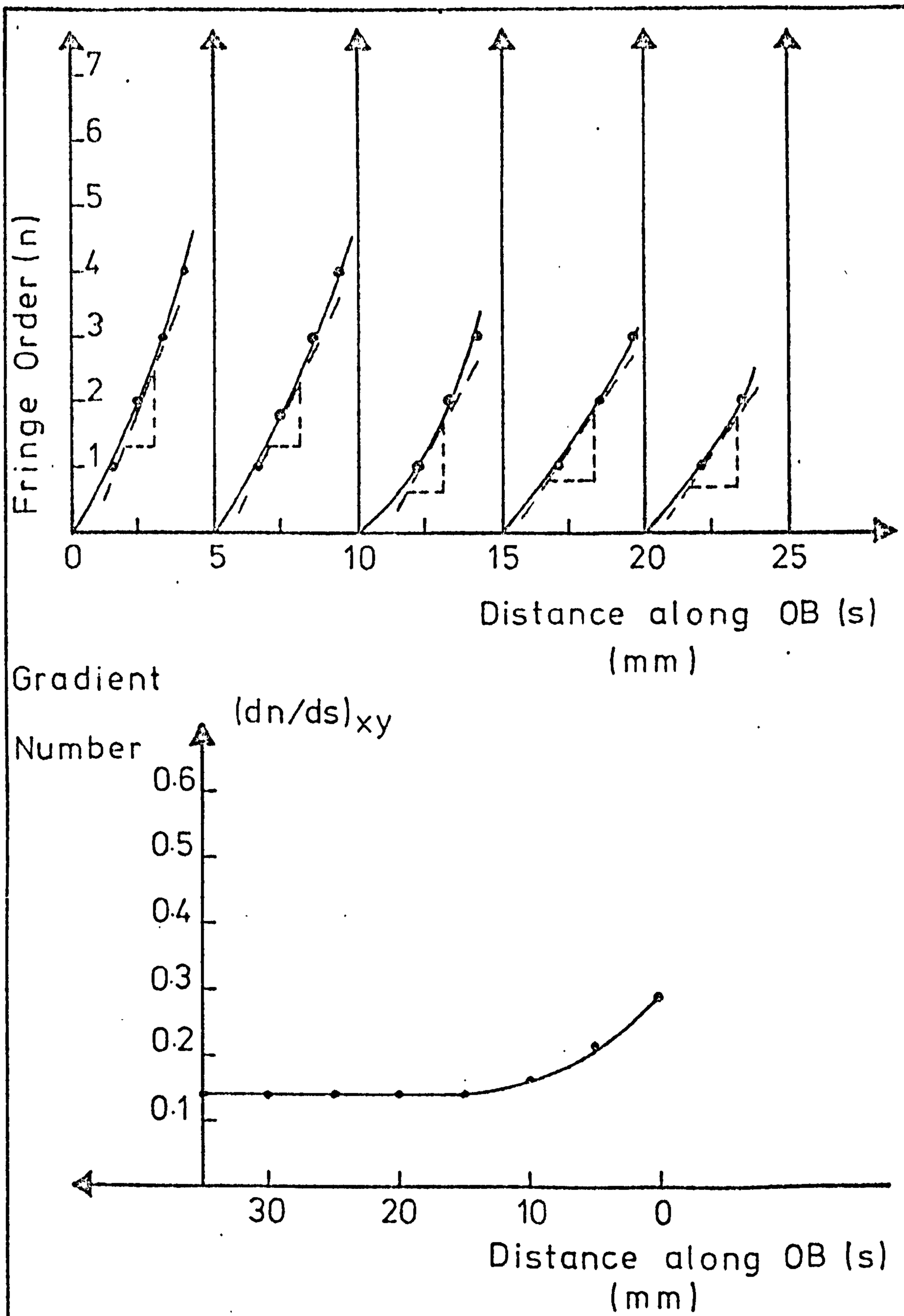

ADVANCE 41.6 m (Fully Caved Waste)

FIG. 5.3.18 BIREFRINGENCE ALONG OB IN THE XY-PLANE.

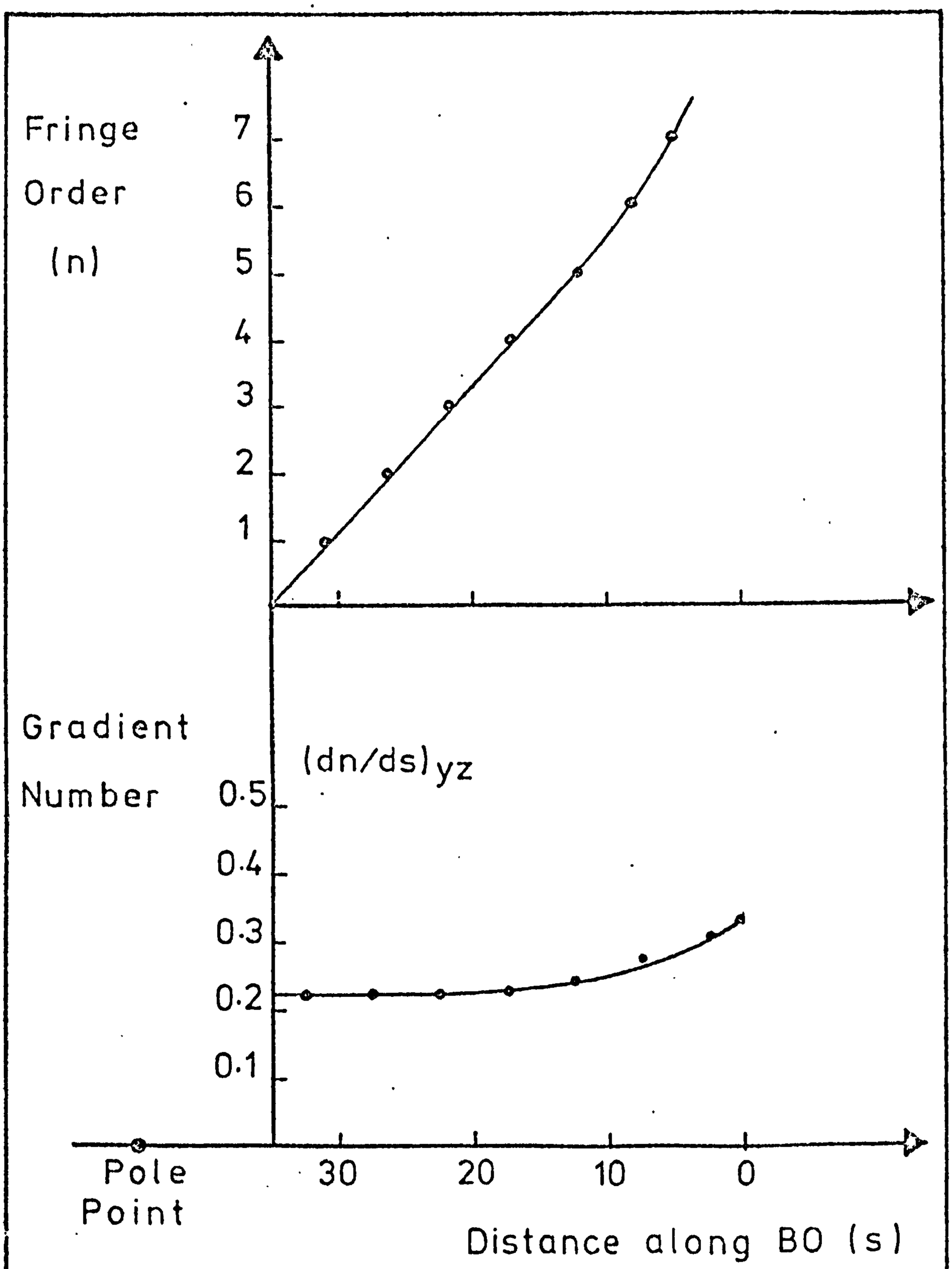

ADVANCE 41.6m (Fully Caved Waste)

FIG. 5.3.19 BIREFRINGENCE ALONG OB IN THE YZ-PLANE.

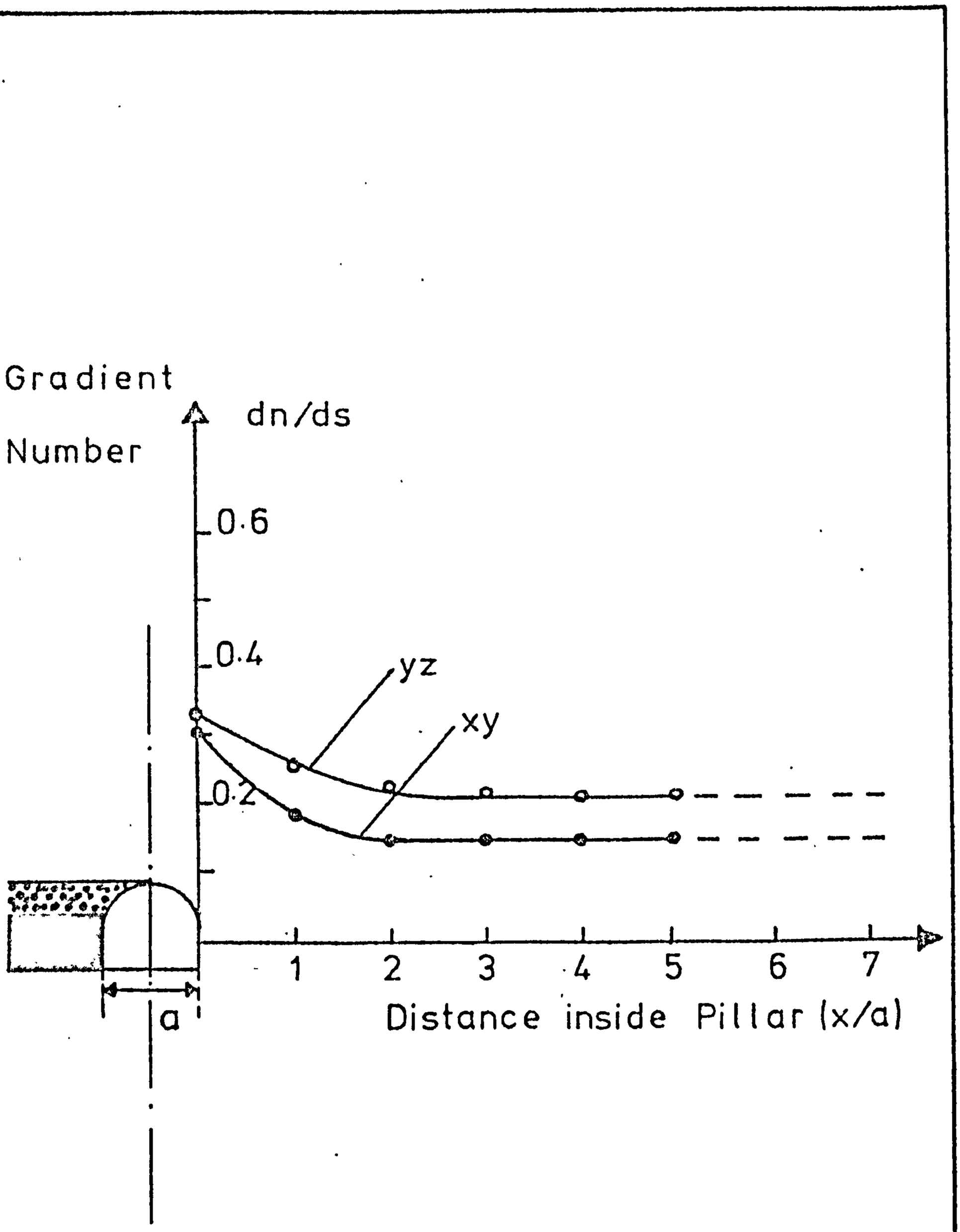

ADVANCE 41.6m (Fully Caved Waste)

FIG. 5.3.20 GRADIENT NUMBERS ALONG OB WITH RESPECT TO THE OPENING WIDTH.

itself, towards the face line, the stresses (gradients) increase considerably, whereas when moving away from it, a decrease of the stresses is shown. This is clearly demonstrated in Figure 5.3.21, where the general pattern for the whole pillar, in the XY-plane, is drawn for the various advances.

The influence of the face advance on the maximum stresses, at the edge of the pillar, is shown in Figure 5.3.22. Both stresses increase rapidly by 0.19 in the YZ-plane and 0.17 in the XY-plane until a face advance of about 32m is reached (about 12.5 times the seam thickness). Any further increase in the advance has little effect on the maximum stresses.

In all investigations both stresses show a gradual decrease when moving towards the interior of the pillar, until an asymptotic value is attained. The distance of this region, from the pillar edge, averages for both stresses about 13.5m (or $^{x}/a$ about 3). The decrease of the stresses, from the maximum at the edge to the asymptotic value at the interior of the pillar, ranges from 0.23 - 0.36 gradient numbers in the XY-plane and 0.14 - 0.28 in the YZ-plane.

At the edge of the pillar the stresses in the XY-plane appear to be higher. This is as expected since σ_x at the edge is zero and the gradient number is proportional to the difference of the two normal stresses at this plane.

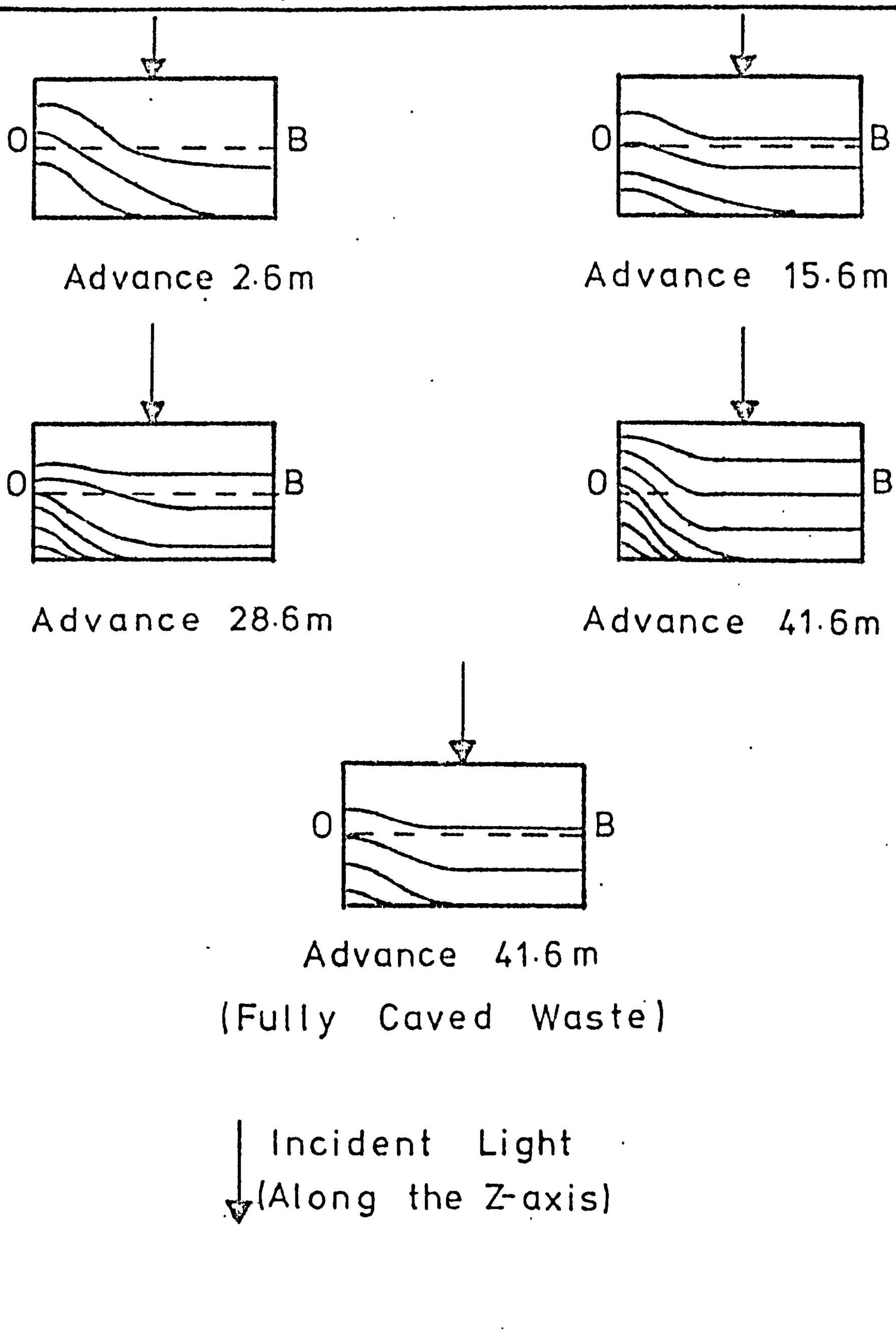

FIG. 5.3.21 FRINGE PATTERNS ALONG OB IN THE XY-PLANE.

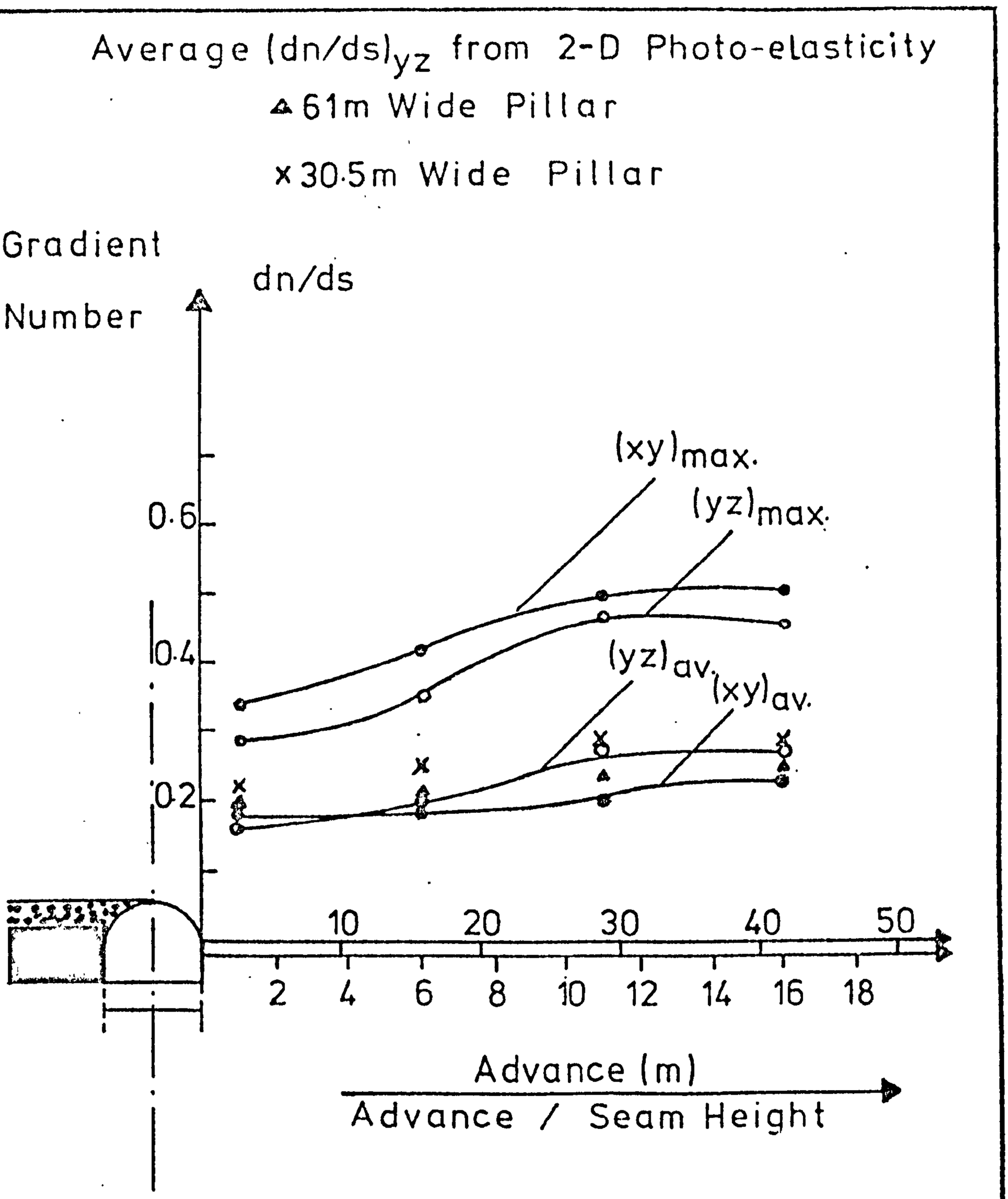

FIG. 5.3.22 INFLUENCE OF FACE ADVANCE ON THE MAXIMUM AND AVERAGE GRADIENT NUMBER ALONG OB

However, in moving inside the pillar the XY-stresses decrease much steeper than the YZ and as a result the two curves cross each other with the YZ-stress being higher in the interior of the pillar. This behaviour is also demonstrated in Figure 5.3.22, where a plot of the average gradient numbers is given, with respect to the face advance. These curves show a similar trend to the ones constructed from the maximum gradient numbers. In other words, both the maximum and average gradient numbers are practically unaffected for face advances more than 32m. In the latter figure, results obtained from two-dimensional multi-layer photo-elastic studies, for a large pillar (61m wide) and a medium size pillar (30.5m), are also shown. These results, obtained by Oram[71] for a similar mining situation on the same colliery, are representative to the YZ-plane, and are given here in terms of gradient and not fringe numbers. Although such results can not be taken as a direct comparison, due to the different simulation, they do, however, indicate a general agreement between two- and three-dimensional photo-elastic multi-layer studies.

5.4 CONCLUSIONS

(i) When solving three-dimensional stress analysis problems by means of small similar models, three basic problems are encountered. The first problem is inherent in all

three-dimensional models, and is due to the geometrical disproportionalities of the actual prototype. Whereas a a prototype having linear dimensions of similar size can be easily simulated by a model to a range of scales, in other cases where at least one of the linear dimensions of the prototype is extremely large or small, with respect to the others, three-dimensional simulation is very difficult. As a result, although the geometrical simulation of room and pillar workings was easily achieved, the simulation of a longwall panel was only possible to a manageable scale, by considering a small section within this panel.

The second problem is peculiar to photo-elastic three-dimensional simulation only. When the laws of similitude were given, it was stated that for complete similitude the Poisson's ratio of the rock should be equal to that of the model. However, since this ratio ranges for most rocks between 0.1 - 0.25, and for photo-elastic materials, the corresponding value is at least 0.4, this particular law had to be ignored. Although such differences of the Poisson's ratio are of little practical importance in two-dimensional analyses, they are significant when undertaking three-dimensional solutions, since the stress field in this case is dependent on the elastic constants. In particular, when plane strain conditions are to be simulated, any small

variations in the Poisson's ratio will have a marked effect on the induced lateral stresses. However, the Poisson's ratio problem has not been fully appreciated as yet, especially in quantitative terms, and is usually ignored in most investigations.

The third of these problems refers to the scattered light technique itself. When a model is to be investigated under uniaxial compression, the difference between the two lateral normal stresses can be extremely small. This means that when the light enters the model along the load axis, i.e. Y-axis, very few fringes will appear, as opposed to the case when the light is parallel to the X- or Z-axis. This means that when a model is loaded, it must be ensured that enough fringes appear along the Y-axis, to enable accurate calculations, without having too many fringes along the other two axes, which could hinder the measurements of the photo-meter. As a result the acceptable applied stress level is dictated by the actual fringe pattern and not the laws of similitude.

(ii) The investigation into the behaviour of small pillars, revealed a number of interesting features. From the various tables it can be seen that the angles of the secondary primcipal stresses, with respect to the three reference axes, are in general very small. This means that when assuming that the directions of the principal

stresses are in line with these axes, which is often the case when undertaking 'in-situ' measurements, the assumption is a realistic one.

As it was expected, the vertical stress was a maximum at the edge of the pillar, having a compressive stress concentration of 4.75. This stress decreased at a very small rate inside the pillar, until a value of 4.2 was obtained at the centre. The build up of the lateral stresses was a more rapid one, reaching maximum concentrations at the pillar centre of 1.65 and 1.85 in the X and Z directions, respectively. This means that even in the case of small pillars, assuming that they do possess an inner core, the state of stress at their centre is triaxial, and as a result their 'in-situ' strength must be in considerable excess of that calculated by unconfined uniaxial laboratory testing. It is worth noting, also, that since the concentration factors are with respect to the overburden stress, then the average vertical pillar stress, from the tributary theory, corresponds to a concentration of 4.

The shear stresses along the centre line resulted in a more complex distribution. The lateral shear stress τ_{zx} showed a small increase towards the centre of the pillar, whereas the other two shear components progressed, reasonably symmetrical from the centre of the pillar to the

edge, passing through a zero shear interchange point. The stress concentrations were more substantial in the latter case, and could have been exaggerated by the mode of the external loading.

(iii) The investigation of the birefringence gradient number on a line parallel to the face line, and 6.5m inside the pillar, along the XY- and YZ-planes, revealed that the maximum stresses occur at the pillar edge for all advances. The maximum as well as the average pillar stress are influenced by the face advance up to distances of 32m or 12.5 times the seam thickness. However, for face advances beyond this distance, the general state of stress of the pillar seems to be unaffected.

The stresses in both planes showed a general decrease when moving inside the pillar, until an asymptotic value was reached for distances more than 13.5m from the edge (or 3 times the width of the opening). Since the material is homogeneous and isotropic, the yielding zone at the edge of the pillar, as explained in Chapter II, is absent. In practice the maximum stress will be at some point inside the boundary, this distance depending, amongst other factors, on the seam thickness and depth of the workings, as previously explained. In the laboratory conditions, therefore, the pillar core is the whole pillar.

Looking at the gradient numbers for XY- and YZ-plane individually, it can be seen that in all investigations the XY-stress was higher to the YZ at the edge, and its rate of decrease was also steeper. The result was that the two curves crossed each other, with the YZ-stress being higher in the interior of the pillar. This means that the σ_x component builds more rapidly than the σ_z one, which is as expected, due to increase amount of confinement when moving along the X-axis.

The simulation of the waste resulted in a small relaxing of the stresses, in particular near the edge of the pillar. At the interior the YZ-stress showed a more pronounced decrease than the XY one, which was the result of the reduced bending of the roof layers.

(iv) In the last paragraph of the conclusion of Chapter III, the author stated that the scattered light method could not replace conventional two- or three-dimensional stress analyses, but that simply, for certain problems, it could provide the most advantageous means of solution. It is hoped that the investigations carried out in this chapter have fully substantiated the above statement.

CHAPTER VI

'IN-SITU' MEASUREMENTS OF THE DISTRIBUTION OF STRESS IN COAL PILLARS

CHAPTER VI

'IN-SITU' MEASUREMENTS OF THE DISTRIBUTION OF STRESS IN COAL PILLARS

6.1 INTRODUCTION

When considering the various means of solution of a rock mechanics problem, the author suggested (Chapter I, page 16), that the information retrieved from a particular method of analysis, in both qualitative and quantitative terms, is inversely proportional to the reality of the situation.

In Chapter V, a great deal of information was obtained about the behaviour of underground pillars, by employing the photo-elastic technique, and assuming an idealised prototype. However, if such information is to be of any value, at least in qualitative terms, the degree of correspondence between the behaviours of the idealised and realistic prototype should be established. This can only be achieved by 'in-situ' measurements.

This Chapter describes, therefore, the author's underground investigations on pillars, which were carried out at Killoch and Cairnhill collieries in Ayrshire. The reason that these two collieries were selected in particular, was simply the excellent co-operation of their respective mangement.

The aim of this investigation was a twofold one. It was hoped that underground measurements, on pillars serving different purposes, could greatly add to the knowledge of

their behaviour, especially since this subject has been somewhat ignored by such measurements. In addition, the analysis of 'in-situ' results could also indicate as to what extent laboratory investigations, and in particular, photo-elastic ones, are representative.

6.2 THE CHOICE OF INSTRUMENT

Underground measurements can be accomplished from a range of instruments based on widely diverging principles and with a varying degree of success, as explained in the following chapter.

For the purpose of this investigation, it was decided that stress measurements were far more important than deformation or strain recordings, and as a result the inclusion technique was chosen. When a high modulus rigid inclusion is perfectly welded on a host material, then the inclusion's measurable change of strain is directly proportional to the host's change of stress, with the mechanical properties of the host material having little influence on this relationship. As a result, an accurate knowledge of the properties of the host, in this case rock, is not required.

The instrument used to record the stain changes of the inclusion was the N.C.B/Isleworth strain gauge, high modulus plug, of the revised version 447. The instrument consists of a brass plug[127] (the inclusion part), of roughly cylindrical shape, with 1^{o} taper over its length. Four linear foil strain

gauges are embedded inside the plug, two active and two temperature compensating, and are all connected to a Wheatstone bridge, internally. This is accomplished by pre-splitting the plug along its axis and subsequently cementing the two halves together with an epoxy cement.

An orientation device is built in the instrument so that the sensitive (measuring) axis of the plug can be aligned to the desired direction. This consists of three platinum contacts, inside a perspex annulus, which are just covered with mercury with the axis being vertical. Any rotation of the plug, therefore, will result in a broken circuit, and this enables the plug to be properly orientated inside the borehole with an accuracy of $\pm$ 5°. The orientation and strain gauge leads are placed inside a six core cable and brought out together, as shown in Figure 6.2.1.

The whole assembly is protected by a shroud which is kept in position by a pin. When the instrument is installed, a borehole is drilled of adequate size to enable comfortable passage of the instrument. The inner most end of the borehole is reamed to the necessary shape so that it can form a perfect inclusion with the brass plug. The instrument is then pushed inside the hole until it reased the reamed section. The pin is at this point sheared, thus releasing the plug from the shroud. The latter is then advanced through the shroud front cover, until it is inside the reamed part, and is

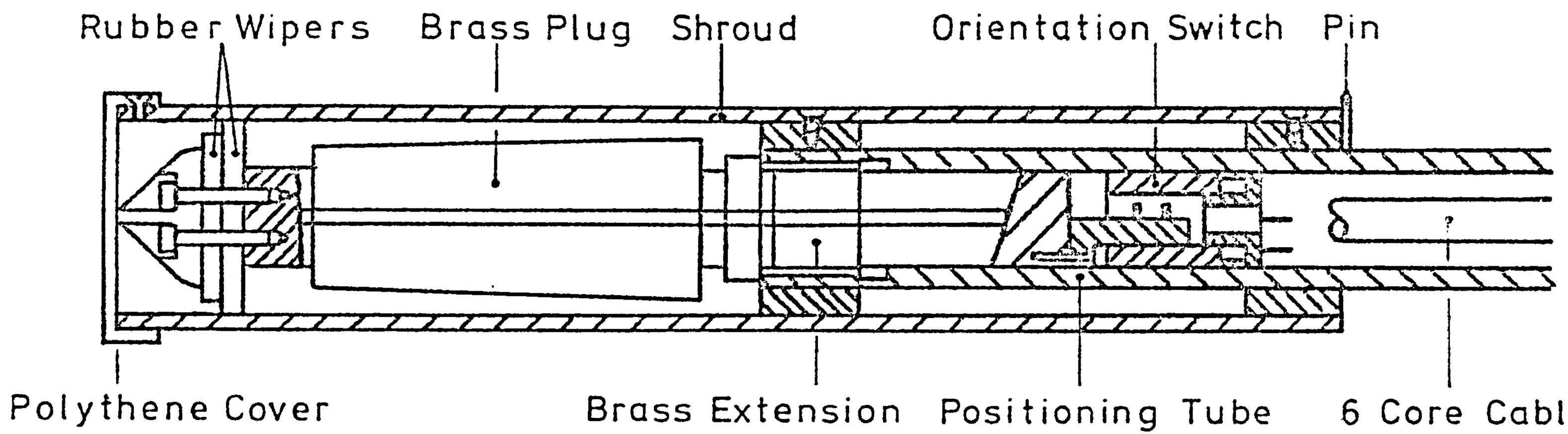

F I G. 6 . 2 . 1 DETAILS OF BOREHOLE PLUG .

subsequently prestressed by applying an external force.

Experimentation with this type of plug showed that better inclusion between the rock and the brass is achieved, by coating the plug with a thin layer of cement before installing. As a result, every plug was coated with a twin pack of Araldite cement which was cured inside the reamed section, thus encouraging better bonding.

The cable of the instrument is brought outside the borehole and connected to an N.C.B/M.R.E. Null Balance Indicator, through a six-pin socket. This balance includes the orientation indicator and three sensitivity ranges for strain measurements. The bridge can be balanced by four knobs calibrated in 1, 10, 100, 1000 microstrains. The balance was operated by four HP.2 Ever Ready batteries, reading about 84mA when new.

6.3 FIRST INVESTIGATION SITE

It was intended, originally, to measure the tri-axial changes in stress in a pillar left behind the N.5 face, Main Coal Seam, at Killoch Colliery. As explained above, the instrument is a uni-directional one and its sensitive axis can be set parallel to any line, on the plane at right angles to the direction of the installing borehole (i.e. on the secondary principal plane with respect to the borehole axis). As a result, if tri-axial measurements are to be taken at a

point, three stress meters are required, at least one of which must be installed from a plane at right angle to the one defined from the other two meters.

The investigation, however, had to be delayed for considerable time due to the 1972 miners' strike. When drilling finally begun great difficulties were experienced due to the fact that the coal was broken and badly jointed near the N.5 face. These conditions were mainly created because the development of this face was considerably delayed due to the strike. It was decided, therefore, that this particular site had to be abandoned.

An alternative site was chosen, therefore, the N.10 face, at the same colliery, as shown in Figure 6.3.1. The face line was 128m long rising 1 : 12 towards the tail gate, the main gate rising 1 : 12 towards the face line, and the support was 4.30m x 3.38m 3-piece arch girders. The face line was developed at right angles to the main gate, 102m from the junction and the face was installed with Dobson 180, 6-leg chocks, and Gullick heavy duty 240, 6-leg chocks. A ranging drum Shearer was used for cutting the coal, with total caving as the permanent system of support, and a chock-pack-chock arrangement, 3.5-4m wide, for roadway protection.

The coal was about 2m thick with a dirt band of about 5cm. The roof was a 0.6 - 017m bed of blaes immediately followed by a thick bed of sandstone, about 5.2m. The floor

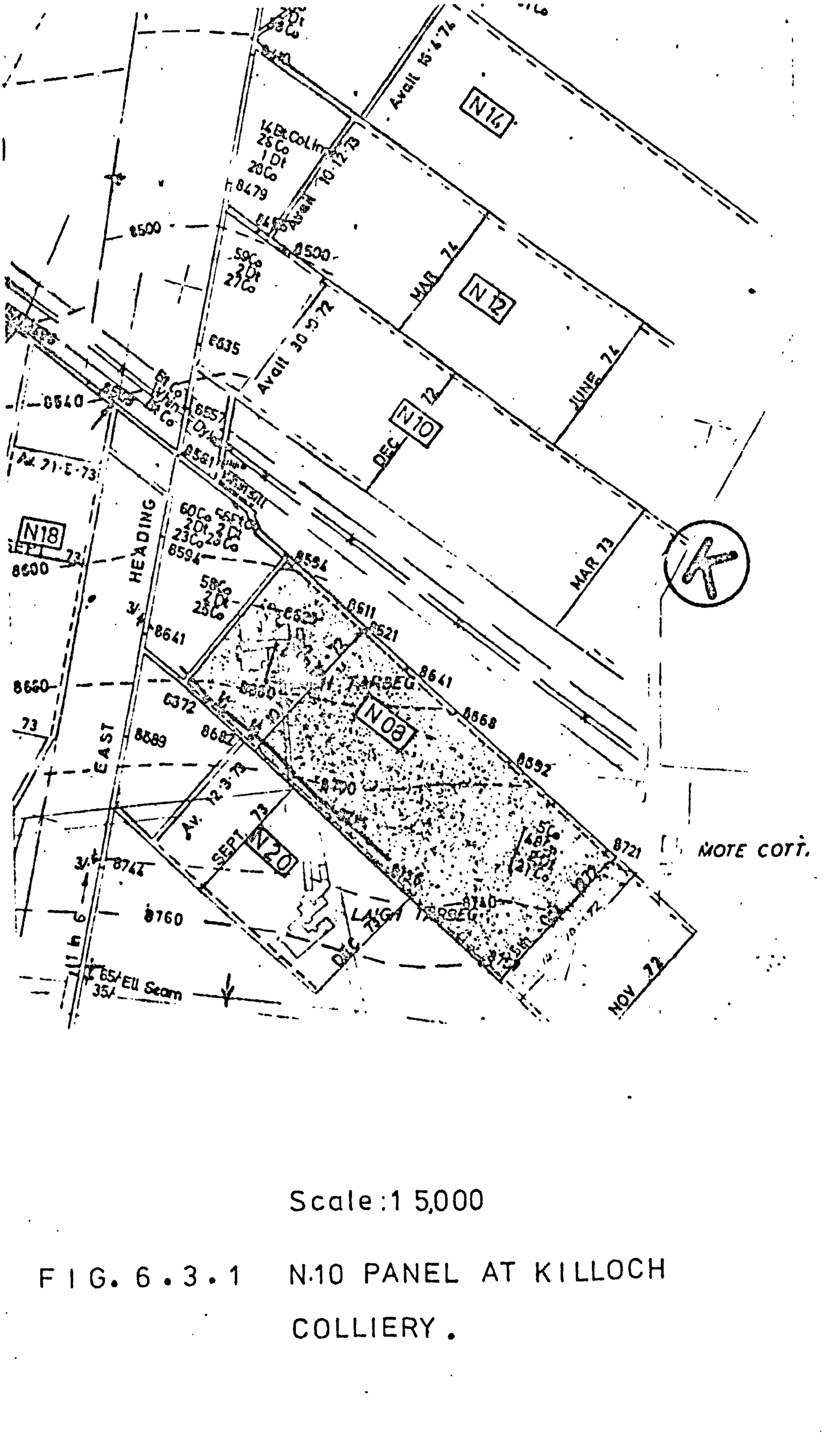
N14
N12
N10
N18
N20
N08
MAR 74
JUNE 74
DEC 72
MAR 73
NOV 72
SEPT 73
DEC 73
EAST HEADING
MAIN DIP
TAIL GATE
MOTE COTT.
8500
8540
8600
8635
8660
8680
8700
8720
8740
8760
8780
8800
8820
8840
8860
8880
8900
8920
8940
8960
8980
9000
9020
9040
9060
9080
9100
9120
9140
9160
9180
9200
9220
9240
9260
9280
9300
9320
9340
9360
9380
9400
9420
9440

was mudstone, 1.85m thick, below which was a sandstone bed varying in thickness from 0.9 - 5.2m. The geological section of the strata was as shown in Figure 5.3.2.

The depth of the strata, finally, at the pillar edge was 590m.

6.4 LAYOUT OF STRESS PLUGS

Two points A and B were to be investigated on the 'effective diagonal' of the pillar (i.e. 1m inside the pillar from all sides, was allowed for initial fracturing). As it was previously mentioned, three plugs at a point are required to determine the complete state of stress, one of which is installed from a plane at right angles to the plane of the other two. Care had to be taken, however, that the three plugs were sufficiently apart to avoid any interaction between them, and at the same time close enough so as to approximate a point. It was decided, therefore, that an 1m cube would satisfy these requirements.

The proposed layout of the plugs and the reference co-ordinate system are shown in Figure 6.4.1. The table below shows the necessary distances and orientations for each plug:

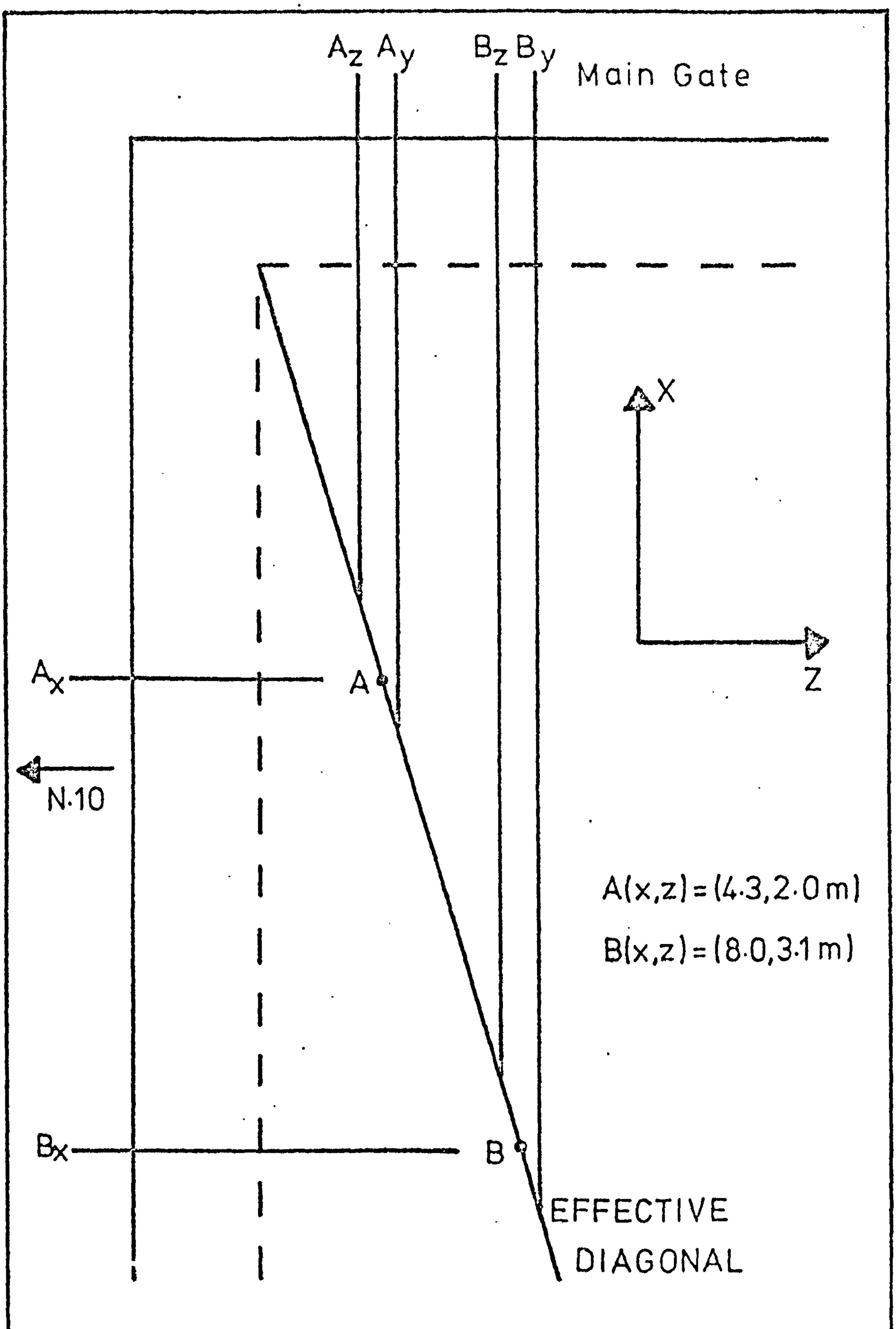

Scale 1:50.

FIG. 6.4.1 LAYOUT OF PLUGS BEHIND N.10 PANEL.

Plug	Length (m)	Installation Plane	Height from Floor (m)	Align-ment
A_x	1.5	Face	1.0	X
A_y	4.8	Road	1.4	Y
A_z	3.8	Road	0.5	Z
B_x	2.5	Face	1.0	X
B_y	8.5	Road	1.4	Y
B_z	7.5	Road	0.5	Z

6.5 INSTALLATION OF STRESS PLUGS

The installation of the stress plugs was carried out by completing the following operations:

(a) Drilling: A Victor boring machine was used, rigidly fixed near the edge of the pillar. A 7.6cm reaming bit was used and the drilling rods were of the scroll type. All the holes were drilled slightly short of the required length, since the last part of the hole had to be reamed to the brass plug shape. This was achieved by using a diamond reamer. The latter consists of a 3.72cm diameter bit, followed by a 15.5cm long hardened steel tube, to stabilise the bit before reaming begins. The reamer has three diamond rows, at 1^{o} taper, over a 15.5cm length. A Victor coupling is placed at the rear so that the reaming unit can be screwed on to the drill rods. In order to ensure that the reamer was located centrally with respect to the

borehole axis, when screwed on to the drilling rods, a small centralising unit in form of a threaded ring was used.

In reaming some of the holes it was found that the machine was not powerful enough to operate the reamer efficiently. This was overcome by drilling a small pilot hole (3.50cm) in front of the original borehole; the reamer was subsequently used, which in this case had only to ream the pilot hole with very little drilling effort.

(b) Flushing: The holes were flushed clean before and after reaming, using 2.5cm in diameter pipes, in 1.55m long sections.

(c) Plug preparation: An initial reading of the plug was taken, and the shroud was removed in order to coat the plug with Araldite cement. The shroud was subsequently returned into position and held steady by attaching the shear pin. The front of the plug was protected by a polythene cover. One end of the cable was fixed into the plug's socket, the other being connected to the Null Balance, and the instrument was then ready to be installed.

(d) Installation: A fork was screwed on to the end of the water pipes, gripping the plug tightly. The latter was then pushed inside the hole, keeping the cable tight, until it reached the reamed section. Another reading was then taken and the plug was orientated with its sensitive axis

parallel to the vertical direction. A special C-shaped protractor was designed, tightly fixed on to the pipe at the hole's entrance, which enabled an accurate turning of the plug when horizontal alignment was necessary. A hydraulic ram was then used to shear the pin and free the plug from the shroud, the former being pushed into the reamed section.

(e) Pre-stressing: With the plug in position, the same ram was used to apply an external thrust on to the plug, thus pre-stressing it.

The procedure was proved successful when installing this type of instrument. It became apparent, however, that this particular type of boring machine was only satisfactory when drilling reasonably shallow holes, since it was noticed that beyond 6m the holes started to deviate from their pre-determined direction considerably.

Plugs A_X and B_X were successfully installed from the face side, both oriented along the horizontal X-axis. At this point the face was about 3.7m from the edge of the pillar. Plug A_Y was also successfully installed from the road side, and aligned parallel to the vertical axis (i.e. Y-axis).

In preparing to drill hole A_Z it was discovered that the boring cable had been damaged. Since no other cable or machine were available at that particular time, the operations had to be stopped for the cable to be repaired.

By the time the cable was again available the face had become fully operational; as a result plug A_z was installed, with its sensitive axis parallel to the Z-axis at a face advance of 20.5m from the edge of the pillar. In drilling hole B_y the bit was gripped, very tightly, and despite prolonged efforts could not be recovered. This most probably was due to a badly broken zone at this particular point. Since no other bit of this size was readily available and to wait for a replacement meant a further delay, it was decided that by that time the face would have been too far for the oerations to continue. The investigation, therefore, came to a halt, with only four plugs successfully installed.

6.6 RESULTS OF STRESS PLUGS

The plugs were regularly read in order to evaluate stress changes in the section. They seemed to be responding reasonably except the A_x one, which showed excessively high changes (up to 2000 micro-strains) suggesting that in most probability the plug had sheared. The following tables show the results in detail, with respect to the face advance:

Plug	Face Advance (m)						
	3.7	9.5	12.2	17.5	20.5	26.8	42.7
A_x	43F	150F	380F	501F	700F	2000F	3200F
A_y	300R	270R	260R	250R	230R	200R	130R
A_z	-	-	-	-	150F	140F	115F
B_x	220R	340R	420R	525R	531R	545R	420R

Plug	Face Advance (m)						
	59	77.5	85.5	113	154.5	188.5	259
A_x			Full scale deflection				
A_y	50R	0	60R	-	-	-	-
A_z	77F	59F	50F	40F	10F	0	46R
B_x	270R	262R	240R	170R	75R	100R	110R

Readings of the plug A_y were interrupted suddenly at 85.5m of face advance, because the cable was pulled clear from the plug's socket. The letters R and F in the above tables indicate the particular arm of the strain bridge that the balance is switched to. Ignoring plug A_x, the corresponding changes in strain are as follows:

Plug	Face Advance (m)						
	3.7	9.5	12.2	17.5	20.5	26.8	42.7
A_y	0	30	40	50	70	100	170
A_z	-	-	-	-	0	10	35
B_x	0	120	200	305	311	325	200

Plug	Face Advance (m)						
	59	77.5	85.5	113	154.5	188.5	259
A_y	250	300	240	-	-	-	-
A_z	73	91	100	110	140	150	196
B_x	50	42	20	-50	-145	-120	-110

6.7 INTERPRETATION OF THE RESULTS

From the theory of elasticity it can be proved that the secondary principal stress changes P, Q, R (in this case assumed to be coincidental with the direction of the plugs) can be expressed as follows:

$$P = \frac{E}{1-\nu^2}(K_1(e_p + \nu(e_q + e_r)) + K_2(\nu e_p + (e_q + e_r)))$$

$$Q = \frac{E}{1-\nu^2}(K_1(e_q + \nu(e_p + e_r)) + K_2(\nu e_q + (e_p + e_r)))$$

$$R = \frac{E}{1-\nu^2}(K_1(e_r + \nu(e_p + e_q)) + K_2(\nu e_r + (e_p + e_q)))$$

where

E, ν = Mechanical properties of brass plug

e_p, e_q, e_r = Principal strain changes measured by the plugs

K_1, K_2 = Constants depending on the elastic properties of the host rock.

The theoretical analysis of an inclusion, in the general space axes, is explained in detail in the following chapter.

However, assuming the properties of coal as $1.3 \times 10^3 MN/m^2$ and 0.3, the corresponding values of K_1 and K_2 are 0.68 and 0.03 respectively.

If the installation had been completed successfully, then the above formula could express the measured triaxial strain changes to stress changes, at each point. However, since this was not the case, only an approximation of the stress values is possible when using the above expression.

6.8 DISCUSSION OF THE RESULTS

The strain changes A_y, A_z and B_x are diagramatically shown in Figure 6.8.1. Plug A_y shows a sharp compressive strain change rising to a peak of 300$\mu\varepsilon$ at 77.5m of face advance. This value taken in conjunction with the corresponding one of the A_z plug, suggests a vertical compressive stress change of about $22MN/m^2$. The cover load at this depth is about $13MN/m^2$, which means that the maximum vertical stress change is nearly twice the cover load. Since recordings were interrupted just beyond this point, the final shape of the curve, and as a result the final state of stress, is not shown. However, it is reasonable to assume that further face advance will result to a general decrease of strain (stress), with curve shown a similar trend to the plug B_x, thus crossing the zero change axis. Such negative (i.e. tensile) changes are in this case easily explained and are due to the zero level point established when the plug was installed. It is possible

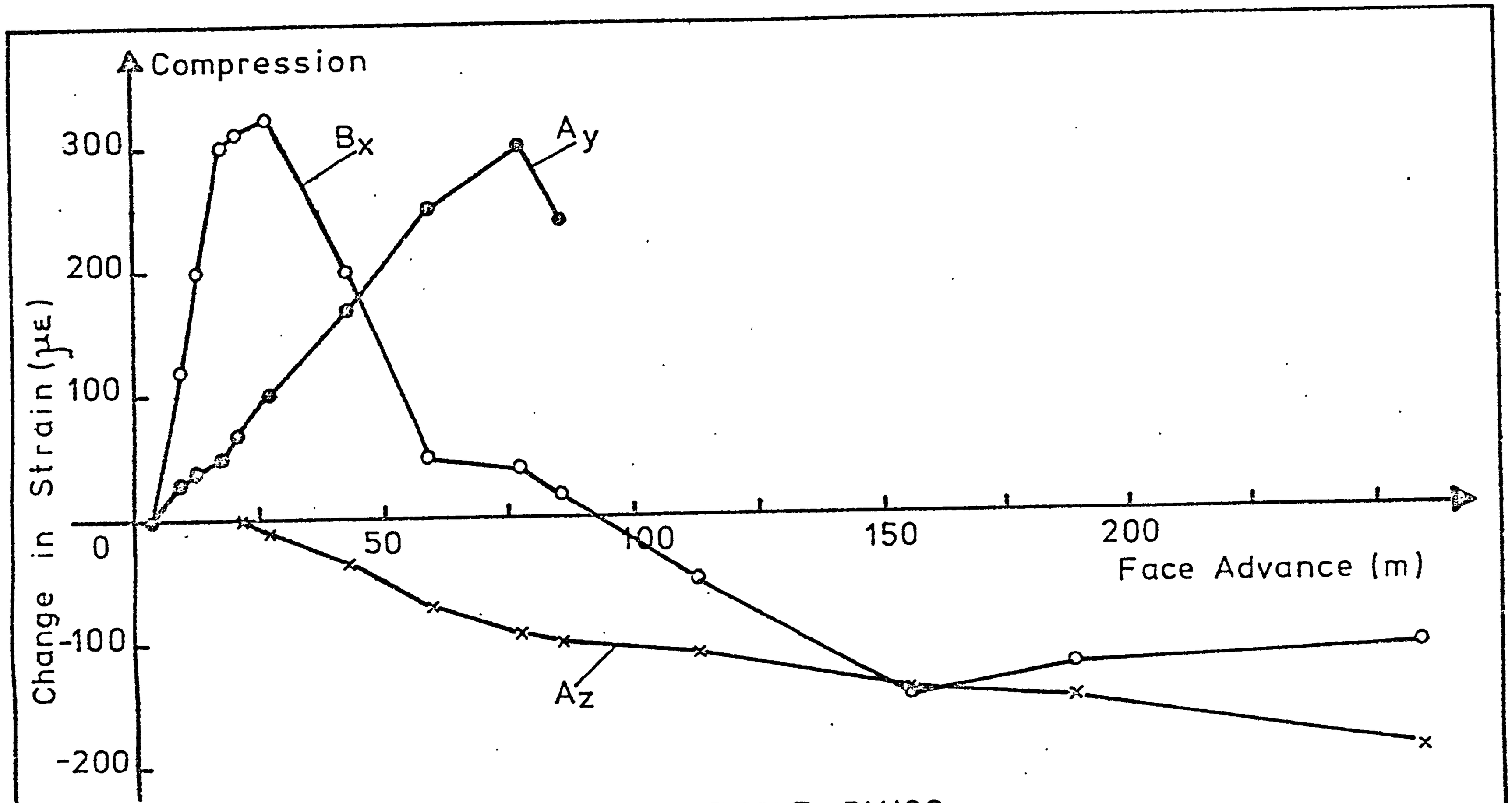

FIG. 6.8.1 RESULTS OF BOREHOLE PLUGS .

that the roadway in addition to the face opening (3.7m when the plug was installed) raised the stress concentrations considerably, around the corner of the pillar, and as a result points in this area, as point A, were under much higher stress than the cover load value. The datum, therefore, established when plug A_y was installed was considerably high. This view is also supported from the relatively low abutment shown by the plug. The value of this abutment was nearly twice the cover load, whereas values up to four were expected. It is also interesting to note, that point A is very near to the corner of the pillar, and as a result it could be within the yield zone, in accordance to the pillar core hypothesis. This could also explain any low responses of the plug at this point.

Plug A_Z, measuring in a lateral direction at right angles to the face line, showed a gradual strain change, without sensing any abutments or increased stress gradients. Whereas the sign of strain (stress) magnitudes in the vertical direction is easily determined, stress changes in the horizontal direction can be taken as either compressive or tensile. If, however, it is assumed that no tensile stresses act on the rock, then the maximum tensile strain change that a plug can experience in a lateral direction, is about half the compressive change in the vertical direction. This is the result of the

unconstrained conditions, in which case the horizontal stress change is equal to the vertical one times the Poisson's ratio of the brass plug (about 0.5). This means that significant tensile stress changes can only take place at low constraint points, as point A. The shape of the strain curve (Figure 6.8.1), and the position of the point inside the pillar suggested that plug A_z was in tension.

The results suggest that at the position of the vertical abutment, the corresponding strain change is -91$\mu\varepsilon$ in the Z-axis. This represents a stress change of 6.2MN/m^2. The degree of constraint, therefore, at this point was 0.28. It should be noted, however, that this plug was installed at a face advance of 29.5m, as compared to 3.7m of the other plugs, and as a result its datum is higher.

Plug B_x, measuring in a lateral direction parallel to the face line, and on the second point B showed a more complex distribution. The compressive strain changes rose sharply to a peak of 311$\mu\varepsilon$ at a face advance of 20.5m, thereafter increasing at a much slower rate until the maximum abutment of 325$\mu\varepsilon$ was reached at 26.8m of face advance. Since no vertical reading was taken at point B, the corresponding stress change can only be estimated by assuming a value of constraint. Since this point is inside the pillar at a distance nearly twice that of the point A, along the X-axis, and from the edge, a value of 0.5 was considered to be realistic. This

suggests a compressive stress change, in the X-axis, of about $28MN/m^2$. The above value is rather high, resulting to a compressive stress change of about $57MN/m^2$ in the vertical axis, or 4.4 times the cover load. The horizontal stress changes, therefore, is much higher at point B, as expected. In moving from point A to B, along the X-axis, the amount of the constraint offered by the adjacent material is greatly increased giving rise to much higher stresses. In addition, point B could be just outside the yield zone, and as a result capable of accepting the full load.

As the face line continued to move away from the pillar edge, the B_x strain change fell sharply with tensile changes taking place beyond 92m, as explained before. The strain change started to increase again at a face advance of 155m, thereafter showing little response to the advance.

6.9 SECOND INVESTIGATION SITE

The aim of the second investigation was to measure bi-axial stress changes across the width of a pillar, left behind a longwall face. The pillar behind N.22 face at Killoch colliery was chosen as the investigation site. Plugs were to be installed along two lines, parallel to the face line, and at 6.10m and 15.25m from the edge. The proposed layout of the plugs is shown in Figure 6.9.1.

However, this investigation, as in the case of the N.5

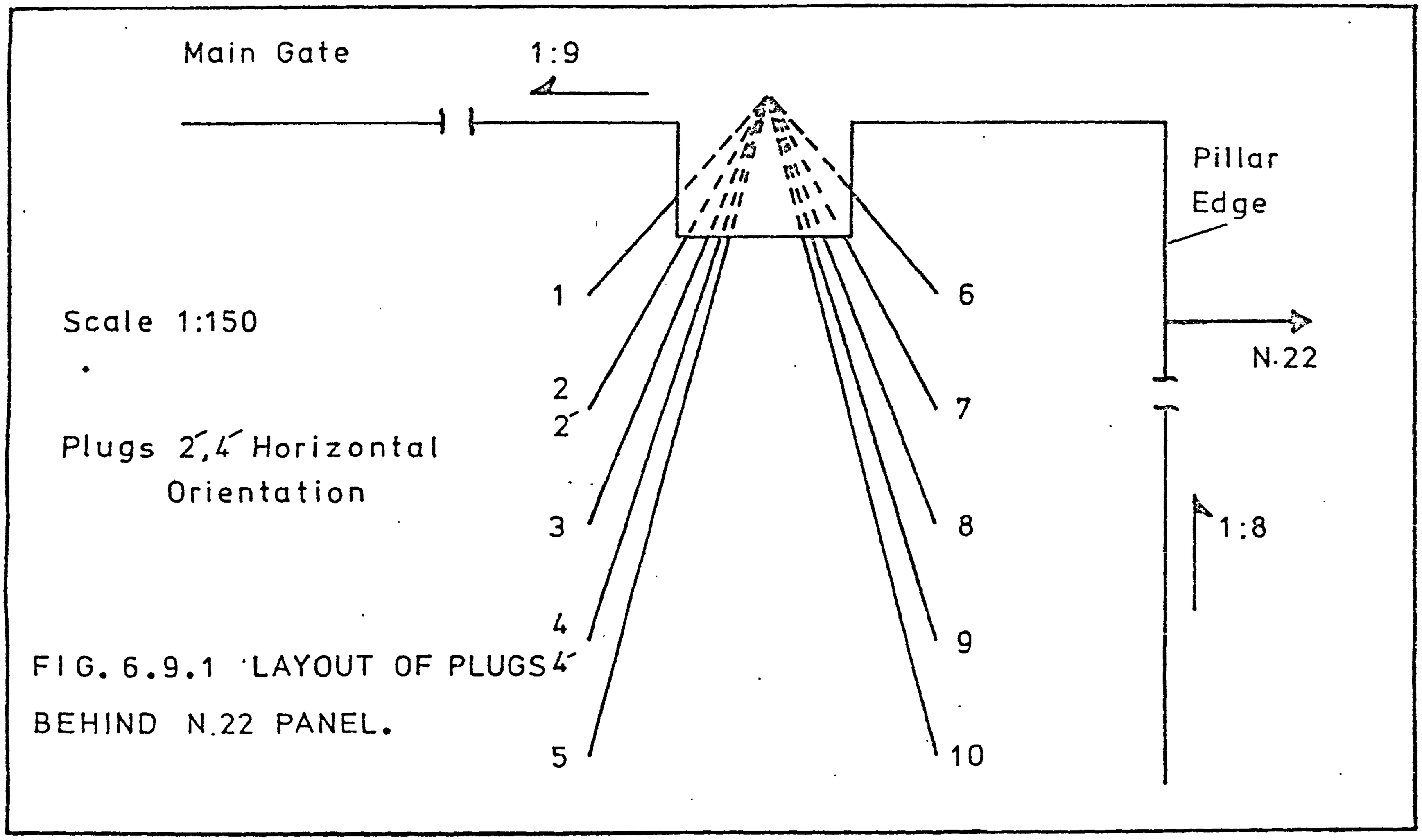

FIG. 6.9.1 LAYOUT OF PLUGS BEHIND N.22 PANEL.

panel, had to be delayed because of the 1973/4 miners' strike. After the strike had been settled, the N.22 panel was well behind schedule, and operations had to be commenced immediately. This meant that the face line would have been advancing during the installation period, the latter involving the formation of an inset, as shown in Figure 6.9.1, and the installment of twelve plugs. The installation was estimated to take at least four weeks, and as a result, it was decided that by this time the face line would have advanced too far for the results to be significant. The investigation behind N.22 panel had, therefore, to be abandoned.

Since no other panel was available at that time at Killoch colliery, the author directed his attention to alternative sites. An interesting situation was, therefore, traced at a nearby colliery, Cairnhill.

A plan of the workings in the Gaswater seam, Cairnhill colliery, is shown in Figure 6.9.2. The geological section of the strata is given in Figure 6.9.3. Panel G.27 had been completed, and panel G.32 was in progress, advancing slowly at a rate of about 6m/week. The face line was 115m dipping steeply, 1 : 2.5 towards the West, the gates being nearly level. The seam height was about 5.5m and the working height nearly 2m. The support was twin 2.5m bars on hydraulic props at about 1.05m centres, and Desford waste edge chocks at 2.1m centres.

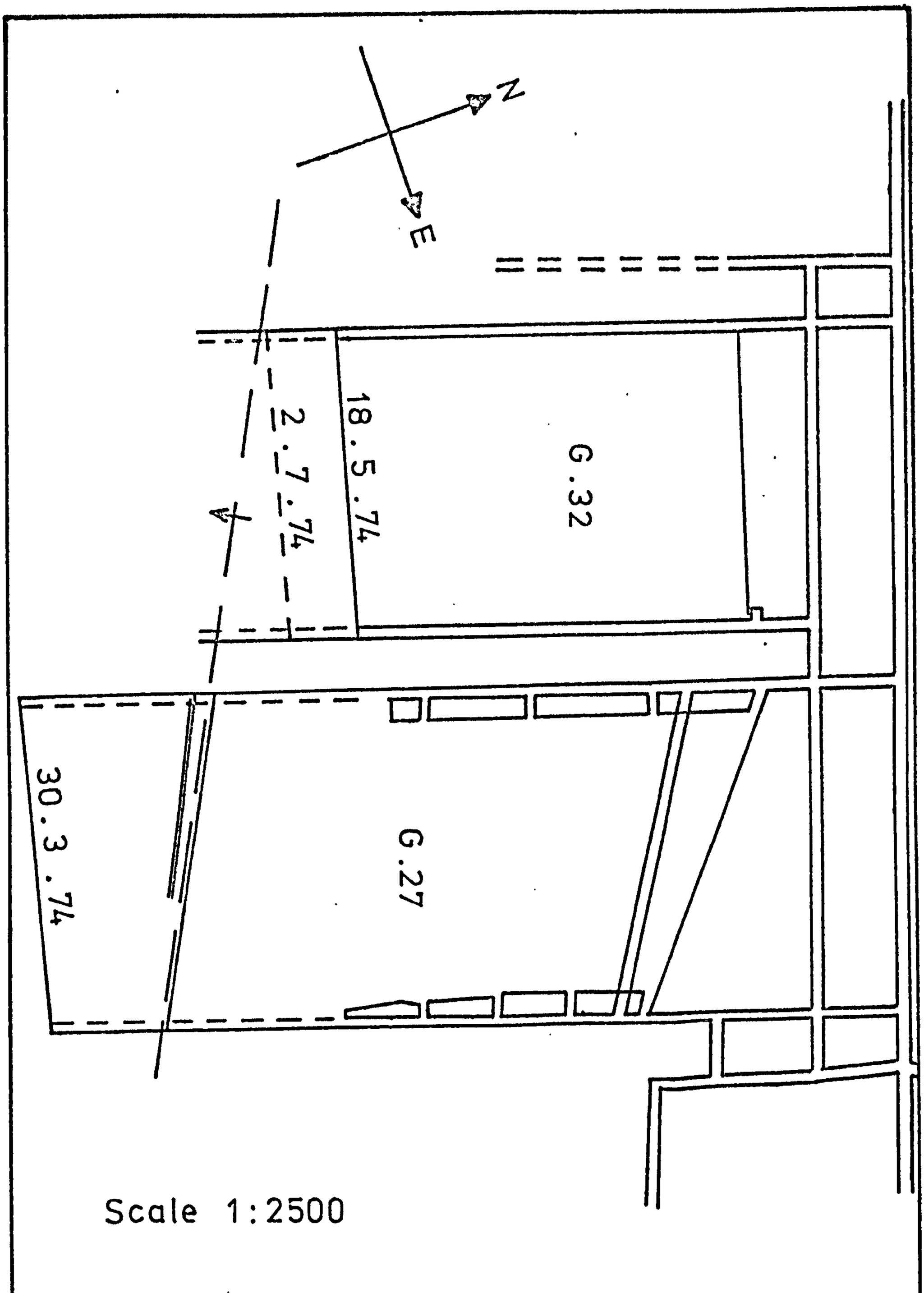

Scale 1:2500

FIG. 6.9.2 PLAN OF THE WORKINGS AT CAIRNHILL COLLIERY.

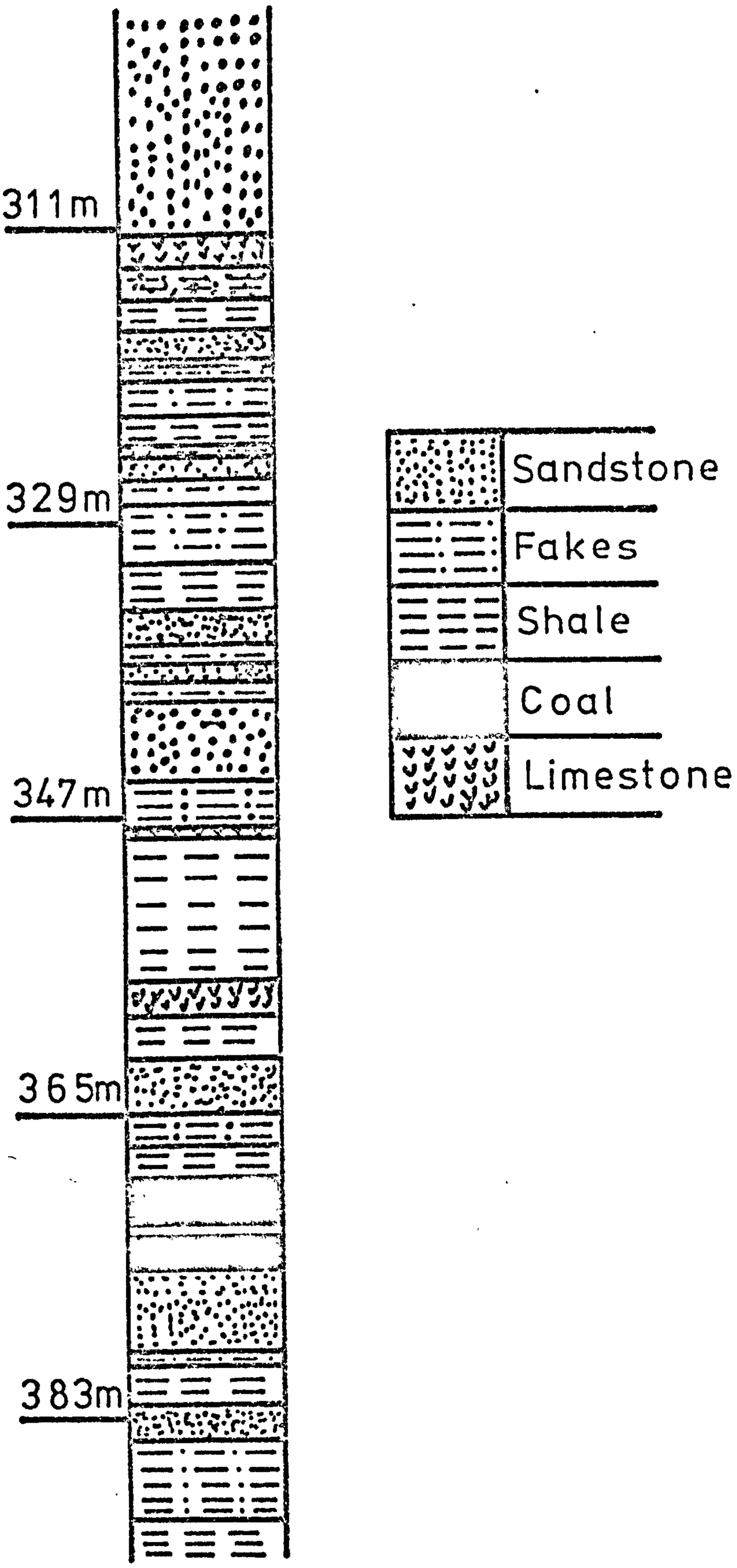

FIG. 6.9.3 GEOLOGICAL SECTION.

A pillar was left between each panel, nearly 20m wide, and the aim of the investigation was to instrument this pillar in advance, from the G.27 gate, so that the stress changes as the G.32 face line approached and passed the instrument's station, could be measured. It was thought that such an investigation on a rib pillar could be of great value, and completely different from the one carried out previously on a pillar left behind the face.

In addition, an interesting situation had developed at Cairnhill with respect to the expected subsidence. The latter was calculated as 61cm,surface measurements, however, on an established subsidence line, detected only about 6.5cm (above figures refer to date prior to the underground installation). This can be explained by considering the thick limestone beds above the seam, which are liable to bridging thus preventing the subsidence trough from reaching the surface.

In order to ensure that any sudden load, due to some of the bridging beds collapsing and extensively damaging the working area, it was decided to centre-leg the roadways. This proved to be a wise precaution, since at a face advance of about 95m a crushing occurred, which, although being felt over a great area, resulted in a very little damage due to the additional support system. Subsequent subsidence measurements, on the surface, showed practically no

difference between the values before and after the crushing, thus suggesting that a number of beds were still bridging over the working area.

Stress change measurements, therefore, across the width of the pillar, would not only show the distribution of stress as the face line approached and passed the instrument's station, but in addition it was hoped that they could also give an indication of the standing ability of the pillar in the event of further crushings taking place.

6.10 LAYOUT OF STRESS PLUGS IN THE RIB PILLAR

The plugs were to be installed from the G.27's main gate inside the barrier pillar, so that as many points as possible could be measured across its width. At the time that the installation begun, the face line was about 175.5m from the edge of the pillar left behind, and it was estimated that the face had about 45m of advance before reaching the fault, as shown in Figure 6.9.2. The layout of the plugs was as shown in Figure 6.10.1, with respect to the face advance, and the table below shows the necessary distances and orientations for each plug:

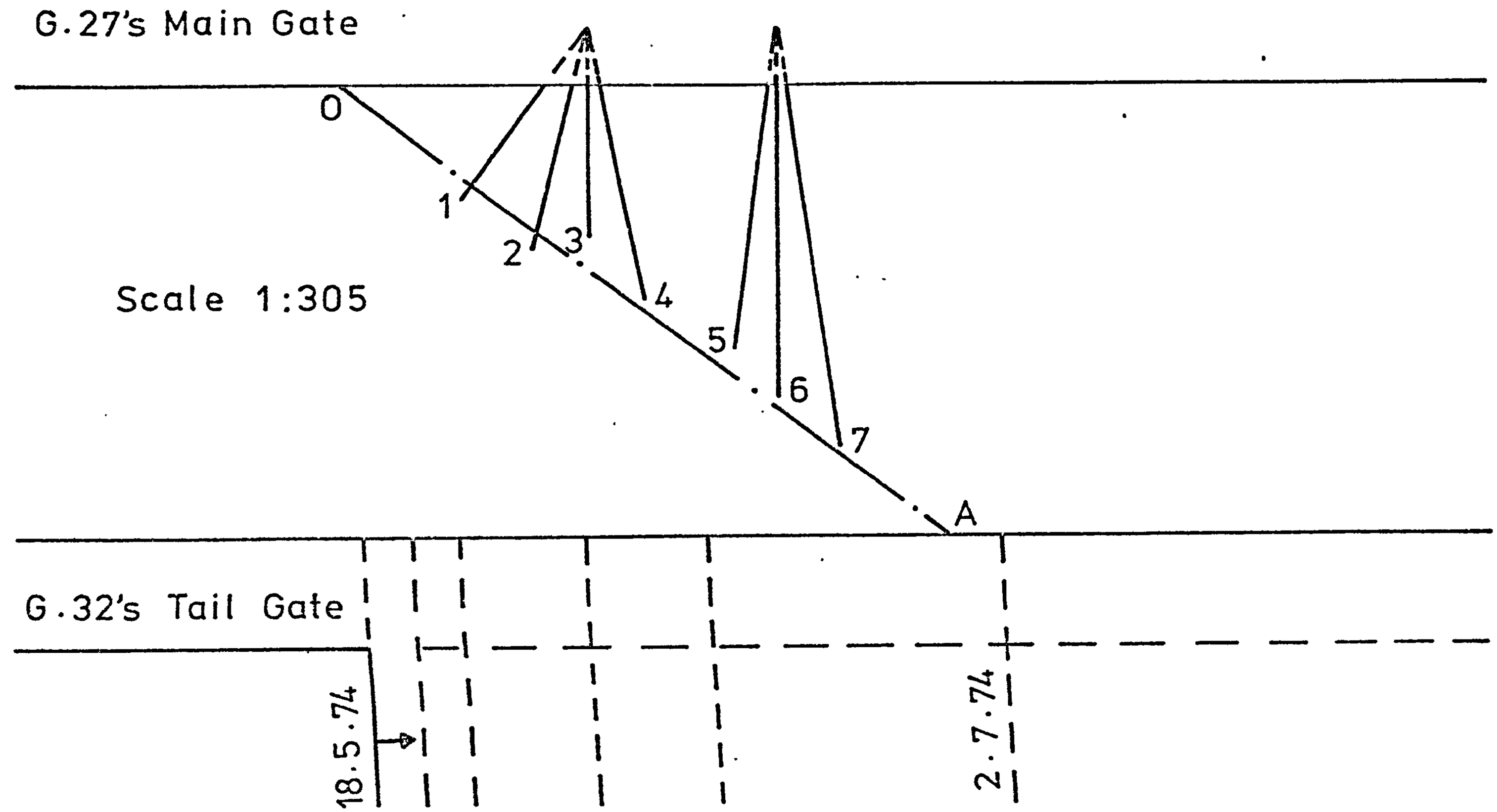

FIG. 6.10.1 LAYOUT OF PLUGS INSIDE THE RIB PILLAR.

Plug No	Length m	Height	Horizontal angle	Alignment
1	6.3	Mid-seam	42°	Vertical
2	7.2	>>	18°	>>
3	6.6	>>	0°	Horizontal
4	9.3	>>	14°	Vertical
5	11.4	>>	10°	>>
6	13.5	>>	0°	>>
7	15.3	>>	11°	>>

6.11 INSTALLATION OF PLUGS IN THE RIB PILLAR

The installation of the plugs was carried out using the same procedure as explained in section 6.5. However, since the length of the holes was far in excess of the ones used in the previous investigation, a better drilling maching had to be used. A Mini-Hydrak boring machine was made available, therefore, giving a borehole diameter of 8.7cm.

Since the face line was dipping nearly 1 : 2.5 towards the West, and water flushing had to be used to clean the boreholes due to the lack of compressed air facilities at the section, the plugs could not be installed on the working horizon. As a result, plugs 1, 2 and 3 were installed on the roof coal (locally referred to as the 'Wild' coal), whereas the rest were on the bed above, a kind of strong shale. The

geological section as established from borehole 4 is shown in Figure 6.11.1.

6.12 RESULTS OF STRESS PLUGS

The plugs were frequently read so that the changes in stress, as the face line approached and passed each measuring station, could be estimated.

Unfortunately, however, this investigation came to a sudden halt, due to a heating occurred at the G.32's tail gate.

The Gaswater seam at Cairnhill was liable to spontaneous combustion, with the colliery having a history of previous heatings. After a careful examination of the situation, the management decided that G.32 panel had to be sealed off and operations, therefore, were abandoned on 2nd July 1974.

The few results taken are shown in table below:

Plug No	Date					
	20/5/74	23/5/74	25/5/74	1/6/74	15/6/74	26/7/74
1	117F	127F	114F	110F	115F	133F
2	30R	46R	58R	81R	97R	80R
3	151R	157R	164R	179R	189R	189R
4	70F	67F	63F	40F	20F	70F
5	-	78F	108F	143F	160F	173F
6	-	-	38R	30R	28R	23R
7	-	-	40F	56F	75F	68F

Since plugs 1, 2 and 3 were in the coal and 4, 5, 6 and 7 in the shale above, both rocks having different elastic

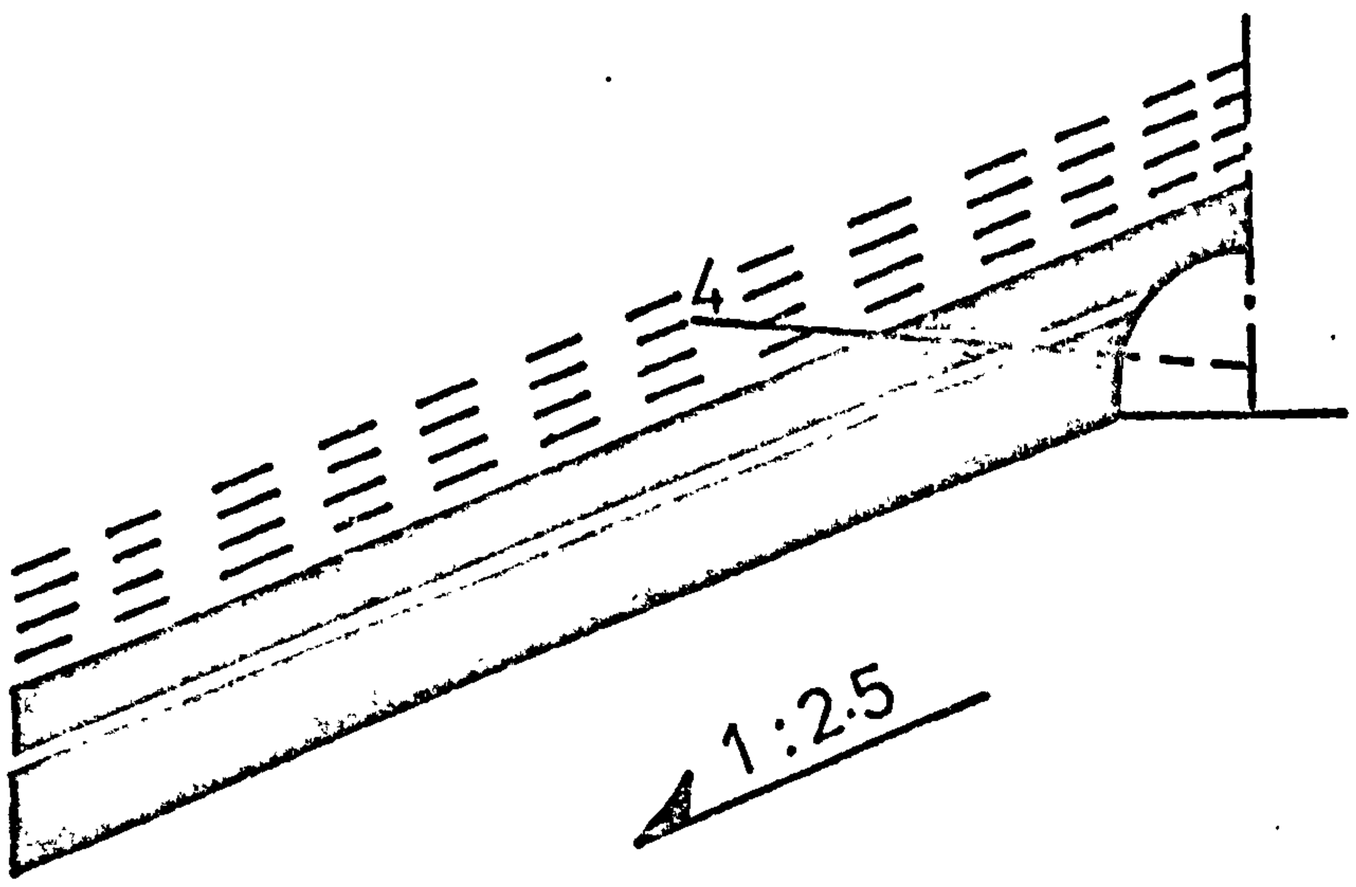

Scale 1:305

FIG. 6.11.1 SEAM SECTION FROM BOREHOLE 4.

properties, the above results cannot be compared without establishing the relationship between measured strain change and actual stress change for each rock. Assuming the Young's Modulus and Poisson's ratio of the top coal as 7 x 10^2MN/m2 and 0.4 respectively, and that of the shale as 7.5 x 10^3MN and 0.2 then

(K_1) coal = 0.71

(K_2) coal = 0.12

(K_1)shale = 0.68

(K_2)shale = -0.03

In addition, plugs 2 and 3 were both in the coal and very near to each other, 2 being aligned in the vertical axis whereas 3 in the horizontal. The results from these plugs, therefore, could give an indication of the lateral restraint, which in this case was 0.65. Substituting the above values in the inclusion equation, it follows that change of 1$\mu\varepsilon$ in the coal corresponds to 0.12MN/m^2 and in the shale to 0.09MN/m^2.

The results from the plugs are show, therefore in Figures 6.12.1 and 2. From these graphs it can be seen that face advance had little influence on plug 1. However, an abutment occurred, equal to 1.2MN/m^2 when the face was about 3.4m from the plug. Plugs 2 and 3 progressed nearly parallel to each other, after the face had passed the installation station. The difference between these plugs suggested a lateral constraint of about 0.65 as mentioned above. The

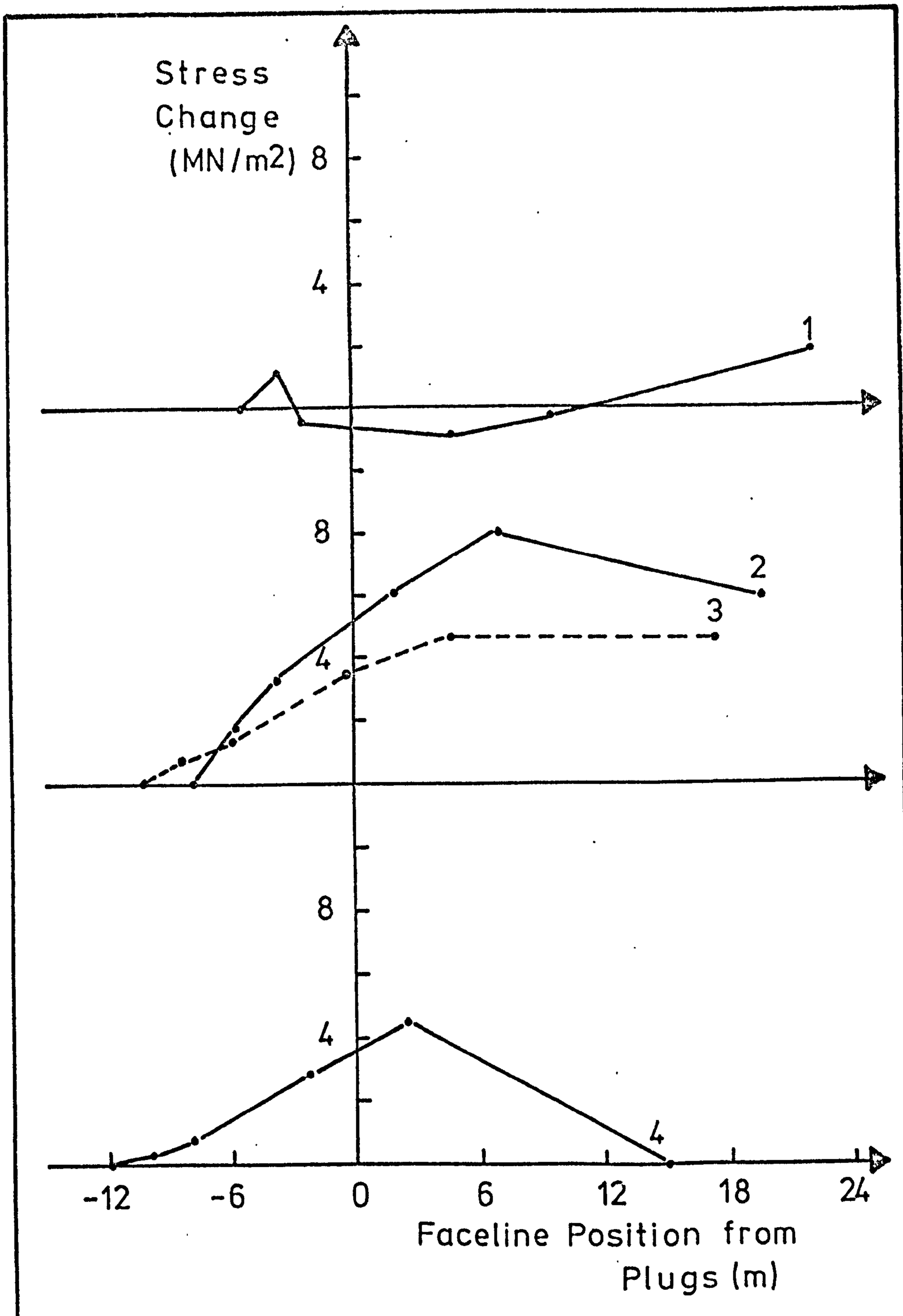

FIG. 6.12.1 RESULTS OF PLUGS 1,2,3 AND 4.

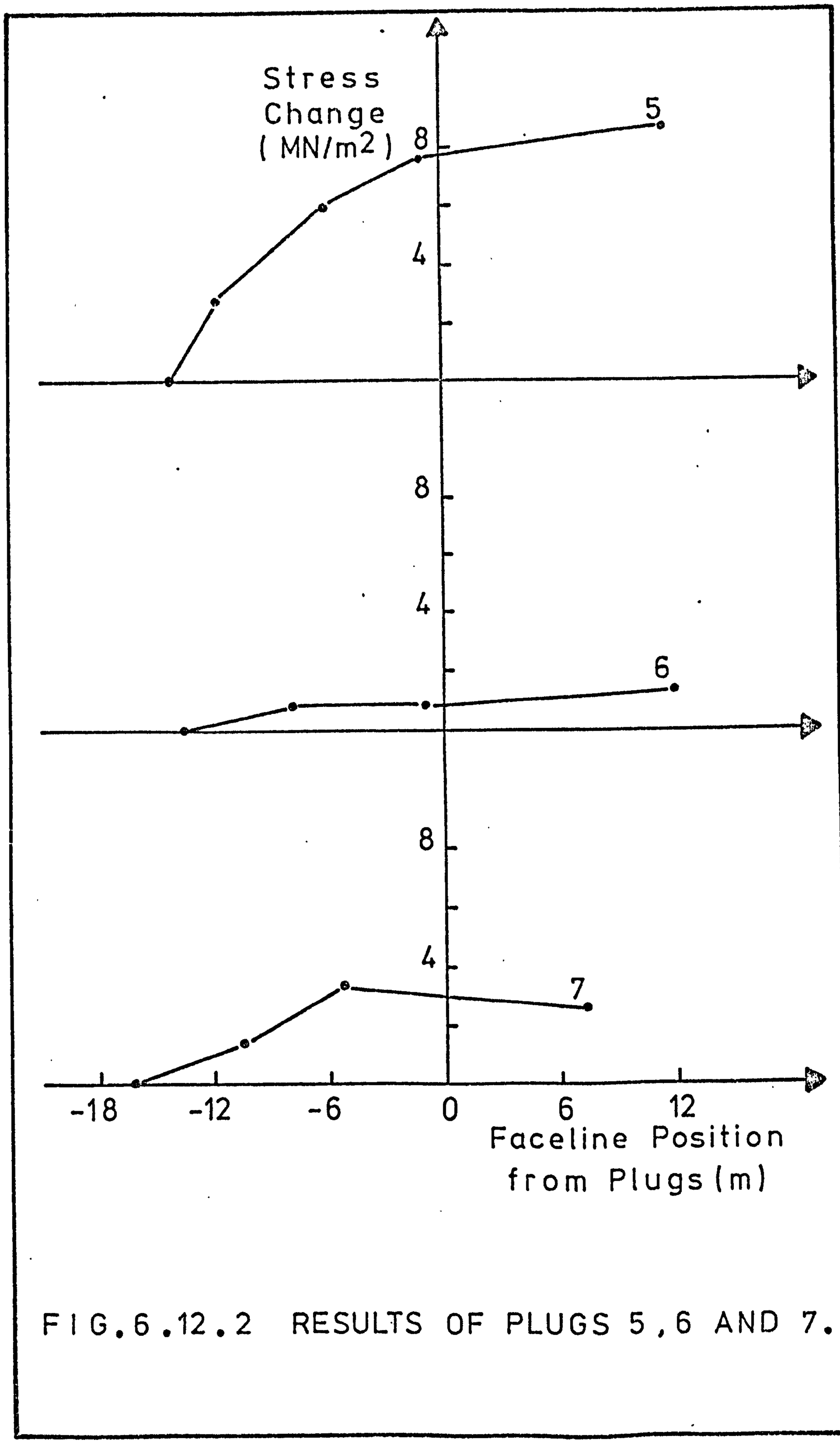

FIG.6.12.2 RESULTS OF PLUGS 5, 6 AND 7.

yield zone, from the difference of the vertical stress changes between plugs 1 and 2, can be taken between 5m to 7m whereas the value suggested by the Pillar Core hypothesis was 3m for this particular depth.

Although not enough readings were taken, to establish the position of the abutments inside the pillar, from the results of plugs 2, 4 and 5 it can be seen, however, that a reduced stress zone was present between 7 - 11m, the stress raising sharply at point 5. The stress seemed to fall again, in the vicinity of plug 6, at 13.5m inside the pillar, until point 7, 15.6 from the edge, where it begun to raise again. The last point was only 4.4m inside the pillar, from the tail gate of the advancing panel, which suggest that the yield zone in this side is much nearer to the theoretical value. This is as expected, since the G.27's main gate had been standing for much longer time, and any deterioration of the edges could have further increased the yield zone.

The results of this investigation, however, although incomplete, strongly suggest a wave-like distribution of stress across the pillar's width. If the plugs are assumed along line OA inside the pillar (see Figure 6.10.1), and the face line is taken in a parallel direction from Figures 6.12.1 and 2, then the probable stress distribution, for five particular advances, is shown in Figure 6.12.3. This is in

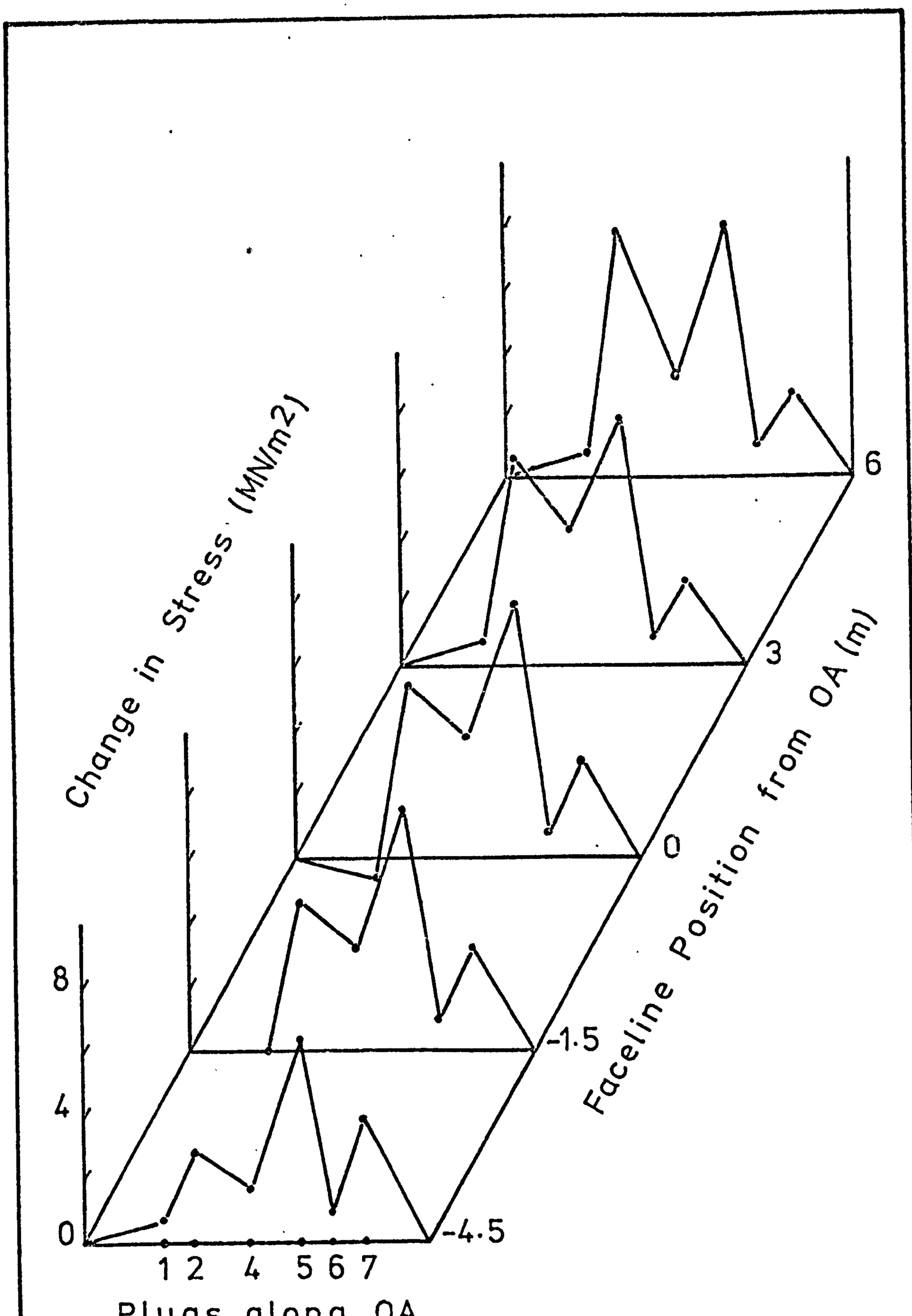

FIG. 6.12.3 STRESS DISTRIBUTION ACROSS THE PILLAR.

agreement to the distributions obtained by Ashwin[44] on a similar mining situation.

6.13 CONCLUSIONS

(i) The high modulus inclusion plug proved to be an excellent instrument when stress changes are to be measured. Although results from a single plug cannot be taken as representative, when a series of plugs is used, monitoring as many points as possible, then great faith can be attributed to the plug's performance due to the collectiveness of the retrieved information.

(ii) The installation procedure proved to be satisfactory. However, it was apparent that when long holes had to be drilled then a powerful boring machine was necessary. In this respect, the Mini-Hydrak machine proved to be ideal.

(iii) The tri-axial investigation on the corner of a pillar left behind a longwall face revealed some interesting facts. At the point nearest to the corner vertical stress changes of about two times the cover load were recorded. This point could well have been within the pillars yield zone and thus not capable of accepting the full load. In addition, the opening of the face line and the roadway could have greatly increased the stresses in the corner, prior to installation, which

explains the negative (tensile) stress changes of the vertical stress as a result of the raised datum level. The maximum load on the pillar occurred at 77.5m of face advance, which is in agreement with the results of other investigators.

The horizontal stress at right angles to the face line and on the same point, strongly suggests the possibility of a tensile zone. These tensile stress changes could be considerable due to the low degree of constraint at point A, and could greatly contribute towards the disintegration of the edges. This plug did not indicate the presence of any abutments, and at the point of the maximum vertical stress change the tensile changes in the Z-direction were about half the cover load value.

In moving from point A to B, inside the pillar's effective diagonal, the degree of lateral confinement is greatly increased, and this resulted to much higher lateral stresses. The lateral stress, parallel to the face line, showed a maximum strain change at 26.8m of face advance corresponding to a stress change of over twice the cover load. The rapid increase of the lateral stress in the X-direction, when moving into the pillar's interior was also demonstrated from the results

of the photo-elastic studies. This, therefore, justifies the claim that photo-elastic or small scale studies have a lot to offer on the understanding of the stress distribution around complex mining excavations.

The results also suggest that the vertical stress change will be around four times the cover load, at point B, which indicates that point B in most probability is just outside the yield zone. The latter in accordance to Wilson's hypothesis was about 5.5m for that particular depth. The horizontal tensile stress changes, in the Z-direction can be assumed as decreasing in moving inside the pillar, until they become compressive at some point away from the corner. At the centre of the pillar, therefore, the two lateral stresses will be approximately equal, both being between the plane strain and hydrostatic values with respect to the vertical stress.

(iv) Although the results obtained from the plugs inside the rib pillar were too few to allow a good description of the state of stress, some general comments can, however, be made. The yielding zone of the pillar was in general agreement with the Pillar Core principal, especially at the edge nearest to the tail gate as expected. Inside

the pillar, however, the results suggested a wave-like distribution of stress, with relaxed zones between 7 - 11m and 11 - 13.5m inside the pillar. Such a distribution is in agreement with the findings of other investigators, and does demonstrate the presence of three abutment zones. Although in this case a direct comparison of these abutments is not possible, due to the different datum level of the plugs, Figure 6.12.3 does, however, clearly demonstrate the wave-form of the stresses, and their increase as the face line moves towards the reference line.

During this investigation the Poisson's ratio of the coal was assumed as 0.4. It is interesting to note, therefore, that for plane strain conditions, this value corresponds to a lateral constraint of 0.667. This is practically identical to the value of 0.650, obtained from the results of plugs 2 and 3.

(v) The author's experiences during this investigation clearly demonstrated the numerous and often unpredictable practical difficulties, when undertaking 'in-situ' measurements. This in a way could explain the general lack of such information with regard to many underground configurations. In addition, the lengthy and tedious installation procedure of the instrument used in this investigation, is another factor contributing towards

this effect. In concluding, therefore, it can be said that whereas one has very little power over the unpredictability of mining, a lot can be done, however, to improve the accuracy, speed and amount of information retrieved from a particular underground instrumentation. The final chapter, therefore, is devoted towards this aim.

CHAPTER VII

THE DESIGN AND LABORATORY TESTING OF TWO INSTRUMENTS CAPABLE OF TRIAXIAL MEASUREMENTS AT A POINT 'IN-SITU' FROM A SIGNLE BOREHOLE

CHAPTER VII

THE DESIGN AND LABORATORY TESTING OF TWO INSTRUMENTS CAPABLE OF TRIAXIAL MEASUREMENTS AT A POINT 'IN-SITU' FROM A SINGLE BOREHOLE

7.1 INTRODUCTION

'In-situ' measurements are not always reliable or conclusive and they do require, in general, a great deal of effort, whereas they yield a relatively small amount of information. Nevertheless, as illustrated in Chapter VI, such measurements are necessary if the 'in-situ' behaviour of underground structures is to be established and, in addition, correlated to the one obtained from small scale simulated models.

However, since one has very little control over the many practical difficulties and unpredictable situations which characterise mining operations, any improvements on 'in-situ' experimental procedures can only come from the type of instrument itself.

In this Chapter the development and laboratory testing of two instruments, easily adaptable for underground investigations, is described in detail. It is the author's suggestion that these instruments can greatly increase the amount, accuracy and economy with which information is retrieved from underground structures.

7.2 SOME BASIC CHARACTERISTICS OF AN UNDERGROUND INSTRUMENTATION

If an instrument is to be used underground successfully then it must possess the following basic characteristics:

(a) Adaptability to the environmental conditions: Whereas most laboratory equipment requires no special precautions since it is operating in a normal (laboratory) environment, underground instrumentation is frequently subject to adverse environmental conditions. The latter may include extreme temperature ranges, high humidity or moisture contents, gassy and corrosive atmosphere, dust and dirt, and excessive vibrations or shocks. If an underground instrument is, therefore, designed it must be capable of performing satisfactory in all these conditions.

(b) Installation technique: The installation procedure, in terms of the required resources and time, is an important factor directly contributing towards the success of an instrumentation underground. If large numbers of men and machinery are required to complete an installation, in particular when the latter requires a length procedure, then the whole operation could be seriously hindered, since such resources are not always readily available especially for long periods. In addition, this type of instrumentation requires that the planning of every investigation, and as a result the mining configuration to

be examined, must be well in advance. This means that interesting mining situations which often occur unpredictably or suddenly, can not be examined with this type of instrument, since the latter may not be successfully installed at a short notice.

(c) Accuracy: In this context accuracy of an instrument includes a number of features. Initially, a measuring instrument must have a good sensitivity and range so that even extremely small quantities, such as strain, can be accurately measured, with this accuracy maintained when such quantities rise to much more significant values. Reproducibility of the measured parameter is also important and although not directly related to the accuracy of the instrument, it can, however, give an indication of the degree of reliance of the obtained results. Since underground measurements are often extended over long periods of time, the instrument must be very stable and free from any drift tendencies. The accuracy itself of the instrument, however, is much more difficult to establish. This is mainly because any tests checking the accuracy of an instrument involve a comparison between the instrument's results and some known standard. In the case of an underground instrument, the latter can only be defined within accurately controlled laboratory conditions which

in all probability, will closely satisfy the assumptions necessary for the development of the instrument. Since, however, the purpose of the instrument is underground testing, the non-controllable conditions offer, in this case, no guarantee that the assumptions will be again fulfilled as before. As a result, any accuracy calibrations must always be treated with a certain amount of caution. In general, however, when installing instruments underground, one should be extremely careful to avoid all sources of possible errors, and in particular, systematic ones.

(d) Amount of information: Every underground installation requires careful planning and considerable expense in terms of time and money. As a result, when undertaking underground installations, one should always look for an instrument which can yield as much information as possible. This is not always feasible since a great number of instruments are being designed on a uniaxial basis.

(e) Economic considerations: Ideally an underground instrument should not be difficult to construct, but on the contrary, it should be within the scope of a standard workshop. This will ensure that a number of such instruments can be completed even at short notice, which should mean a considerable saving in time and money, without the additional burden of stocking. In addition, the materials

involved in the instrument's construction must be cheaply and readily available in order to keep the cost to a minimum. This is a critical factor, especially where the instrument will be non-retrievable.

The high modulus inclusion plug, as used in this particular investigation, does not fully embrace these characteristics. Although this instrument can perform reasonably accurately in a range of extreme environments, it does, however, require a laborious and time consuming installation procedure, it can only measure in one direction, and is a rather expensive instrument particularly as it can not be retrieved. The limitations of the plug were clearly shown during the first investigation where tri-axial measurements on a corner of a pillar were undertaken. Three plugs had to be installed with their sensitive axes mutually perpendicular, and the point under consideration was a finite cube of coal of nearly 1m edge size. The results were only significant if the direction of the plugs were assumed to be coincidental to the ones of the principal stresses. For a complete solution, therefore, at least six plugs must be installed, which means the whole procedure will be extremely expensive as well as the size of the point under consideration will inevitably be large, and as a result non-realistic.

Research, therefore, towards designing an instrument in

agreement with the above five characteristics is a positive step towards increasing the amount and ease with which information is retrieved underground, and even encouraging more 'in-situ' investigations which are necessary if the behaviour of underground structures is to be fully understood.

7.3. TYPES OF UNDERGROUND INSTRUMENTS

In an extensive discussion on the measurement of stress in rock, Leeman[128] classified 'in-situ' instruments into three basic categories:

(a) Borehole deformation cells: Measure linear changes of one or more diameters in a borehole. Several types of cells have been successfully used, including surveying instruments, fluid levels, mechanical deformeters, electrical strain gauges, transformers, etc.

(b) Borehole strain gauge devices: Measure strain, usually at the flattened end of a borehole. Some typical devices are bonded and unbonded resistance strain gauges, vibrating wire strain gauges, optical strain gauges, photo-elastic strain gauges, etc.

(c) Borehole inclusion stressmeters: Measure strain of an inclusion inside the host rock. The inclusion is usually steel or brass and the meter electrical resistance strain gauges.

Apart from these basic categories, other instruments have also been used for 'in-situ' measurements, such as Hydraulic cells, Dynamometers, Seismic and Sonic equipment, and Stratoscopes or borehole Cameras for visual observations.

Of the three types, strain gauge devices are often difficult to install, and in many instances, require calibration of the gauge in the same rock, as the one to be measured underground. Deformation cells, on the other hand, are considered the most accurate and successful underground instruments, requiring simple instrument calibrations and not necessarily on the same type of rock. However, both types necessitate an accurate knowledge of the mechanical properties of the rock, if their readings are to be expressed in terms of stress. Since the mechanical properties can not be determined accurately, and in any case they will most probably vary inside the rock mass, stress values thus obtained are not always reliable. Inclusion meters, however, can overcome this problem since the strain of the inclusion is proportional to the stress of the rock, with the mechanical properties of the rock having little effect, if the inclusion is a high modulus one, (i.e. E of inclusion more than four times E rock). Only high modulus inclusion methods, therefore, can yield reliable stress values.

The following sections describe the design and testing

of two instruments, a deformation cell and an inclusion meter, both capable of tri-axial measurements at a point from a single borehole.

7.4 THE DESIGN OF A DEFORMATION CELL

In the first investigation, the design of a deformation cell fully satisfying the basic requirements set out in section 7.2 was attempted. This instrument is simply a cantilever loaded spring steel, with a strain gauge as the recording unit so that accurate measurements can be obtained. In detail, the design of the instrument was as follows:

A piece of 0.254mm thick spring steel and 11mm wide, was cut in several sections about 33mm long. Two holes were drilled at each end, and a 6BA nut was welded co-axially to the one hole, whereas a steel rod 6.35mm in diameter and 7mm long was fixed on to the other hole and in the opposite side of the nut as shown in Figure 7.4.1. The rod was then ground to a circular shape with its top remaining flat. A Showa foil strain gauge, F-5 type, was cemented, nearly, at the centre of the strip, having an actual gauge length of 5mm and width of 1.6mm, and base size of 10.4 x 3.7mm. The nominal gauge resistance was 120 Ohm, and the gauge factor 2.15 approximately.

A hollow brass tube 22mm in diameter and 180mm long was then drilled, to open four series of holes, at right angles to each other; in every series two size of holes were used in

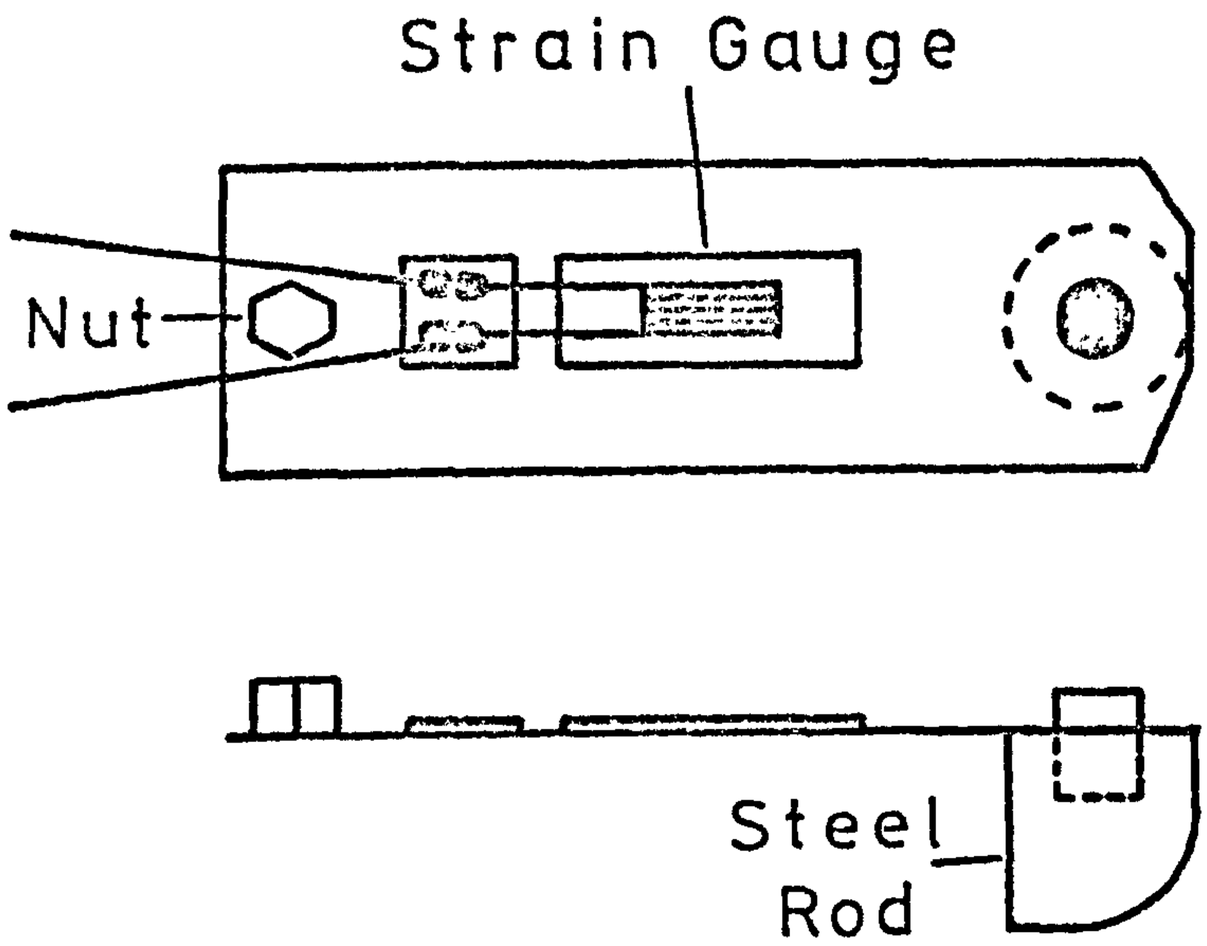

Scale 1:2

FIG. 7.4.1 MEASURING UNIT.

succession, a small one, 4mm in diameter, and a large one, 8mm.

Each gauged spring steel strip was then placed inside the brass tube, and fixed in position using a screw through the small hole of the tube, and the welded nut on the bottom of the strip. In doing so, the curved steel rod of each strip was protruding through the large hole of the brass tube.

When the whole assembly is pushed inside a hole then any displacement will cause the strip and therefore the gauge, to bend, since it is rigidly supported at one end as a cantilever. It follows that from the two diametrically opposite strips, only one really needs to be gauged, since the other could act as an anchor. However, by gauging the two strips and connecting them in series, the combined reading will be twice the particular measured displacement thus greatly increasing the instrument's sensitivity. The latter was adopted when constructing the instrument, all the leads being connected properly in series on the end plug of the tube, as shown in Figure 7.4.2.

In this preliminary investigation, therefore, the measuring heads were so positioned that the deformation of a borehole could be measured, along two perpendicular axes. It is an easy matter to increase the number of heads or axes, and change the particular orientation, so that any rosette

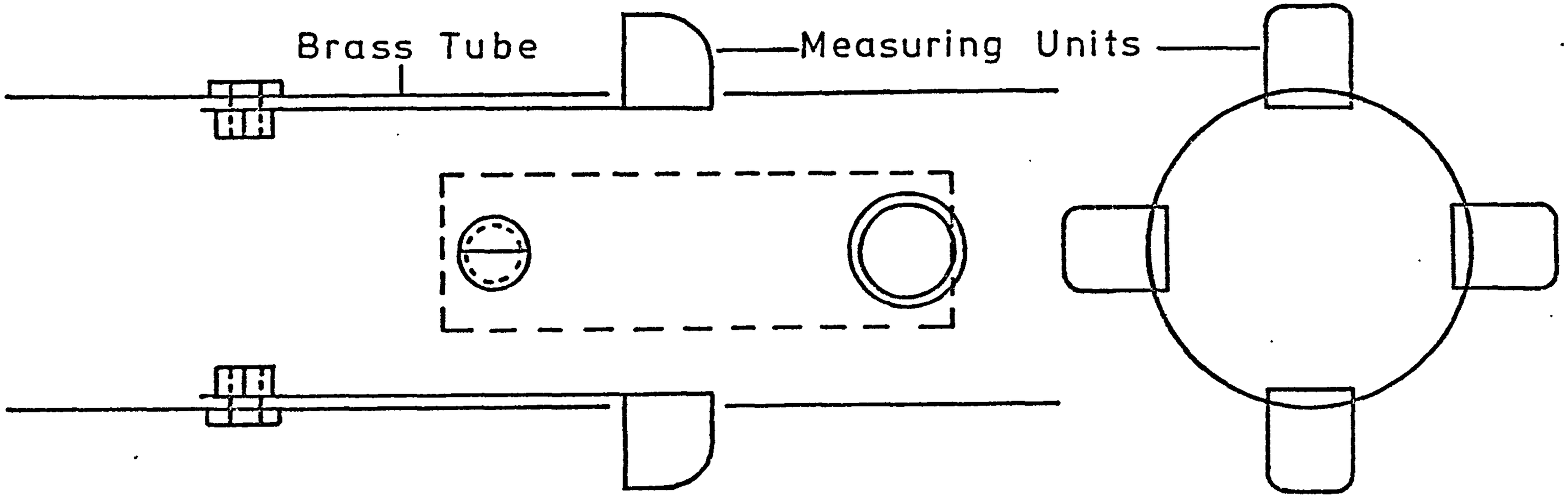

Scale 1:2

FIG. 7.4.2 BOREHOLE DEFORMATION CELL.

system can be achieved, and thus a full solution, on the secondary principal plane to the borehole axis, can be obtained.

7.5 CALIBRATION OF THE DEFORMATION CELL

Since the instrument measures the strain changes due to bending of the strip, whereas the required quantity is, in this case, the actual change in length causing the bending, the instrument must be calibrated. In addition, because no particular care was taken to ensure that the strain gauges were positioned in precisely the same place on all strips, every unit had to be calibrated individually. This was achieved by holding the brass tube on the chuck of a lathe and imposing a displacement on each head, through a rectangular block firmly held in the lathe's saddle. The latter was accurately divided into 0.0254mm increments.

Two pairs of measuring units were installed inside the brass tube for a preliminary investigation, one in the vertical and the other in the horizontal axis. The combined response of each pair (i.e. the summation of the gauges in series) is given in Figure 7.5.1. From this graph it can be seen that

$$V = 1.62\varepsilon$$
$$H = 1.78\varepsilon \qquad (7.5.1)$$

where

V,H = Vertical and horizontal displacements, respectively, in μ

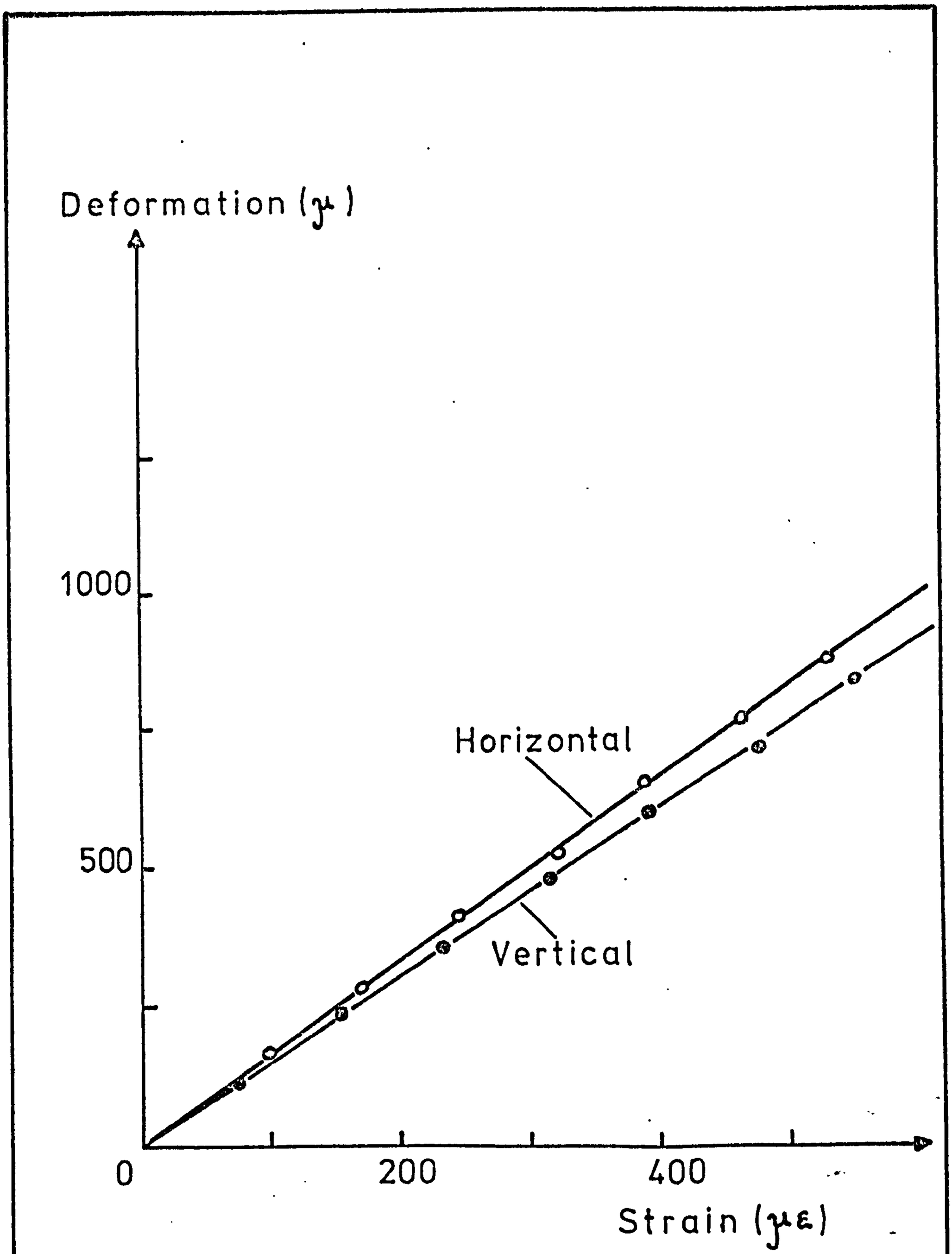

FIG. 7.5.1 CALIBRATION OF CELL.

ε = Strain reading in $\mu\varepsilon$

7.6 TESTING OF THE INSTRUMENT

The instrument was tested a number of times, always yielding satisfactory results. In each test the brass tube was placed in a borehole at the centre of an accurately cut rectangular specimen. The leads of the gauges were connected to a switch unit and strain indicator, shown in Figure 7.6.1. The block was then placed on a testing machine where the instrument's response could be measured at various loading levels. The horizontal and vertical displacements of the borehole obtained experimentally, could then be compared with the theoretical ones, to establish the accuracy of the instrument.

Using the sandstone block shown in Figure 7.6.2, as a typical example, the theoretical displacement values are as follows:

$$V = \frac{\sigma D}{E}(3 - 2\nu^2)$$

$$H = \frac{\sigma D}{E}(1 - 2\nu^2) \qquad (7.6.1)$$

where

V,H = Horisontal and vertical displacements

σ = Applied vertical stress

D = Diameter of the borehole

E = Young's Modulus of the rock

ν = Poisson's ratio of the rock

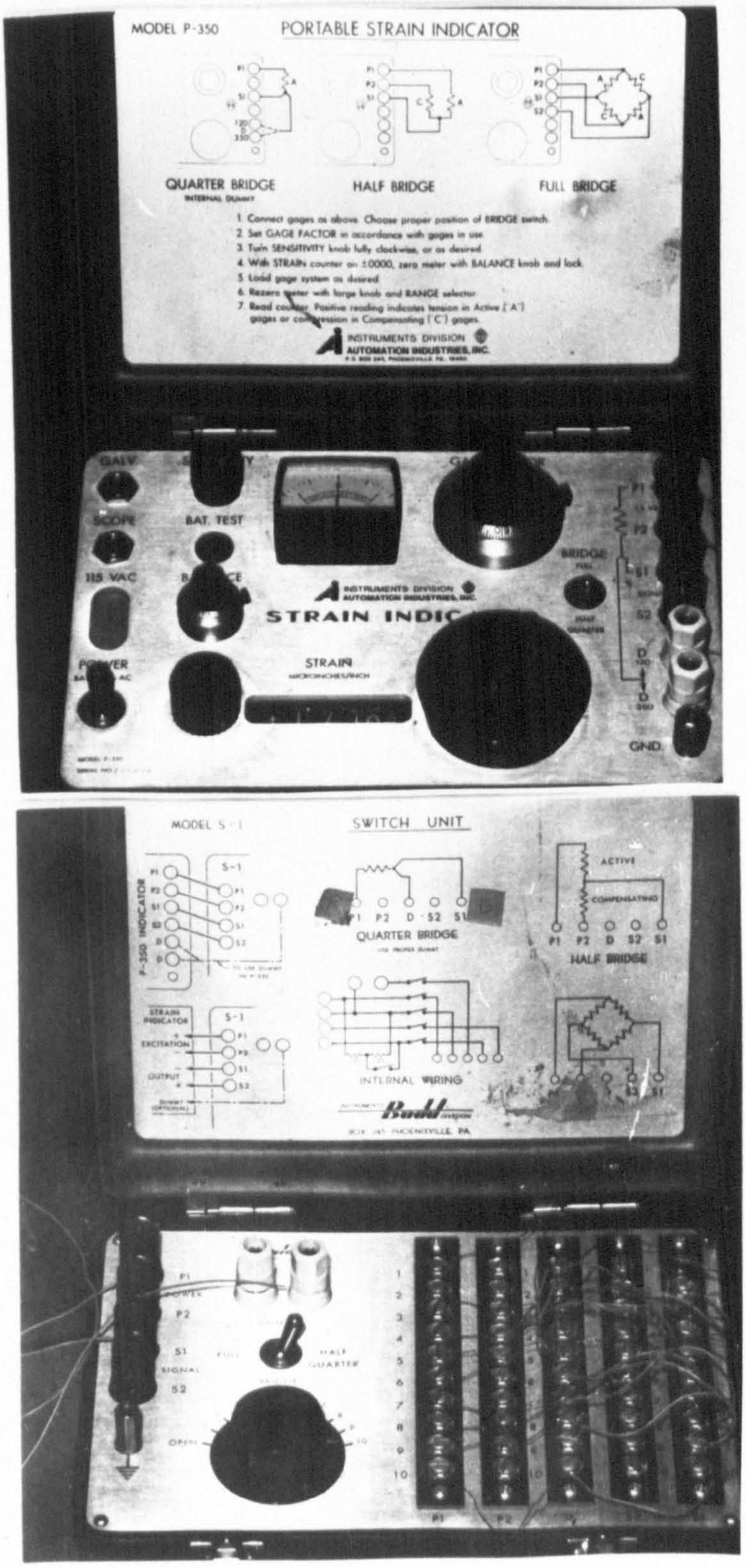

FIG. 7.6.1 STRAIN MEASURING ACCESSORIES.

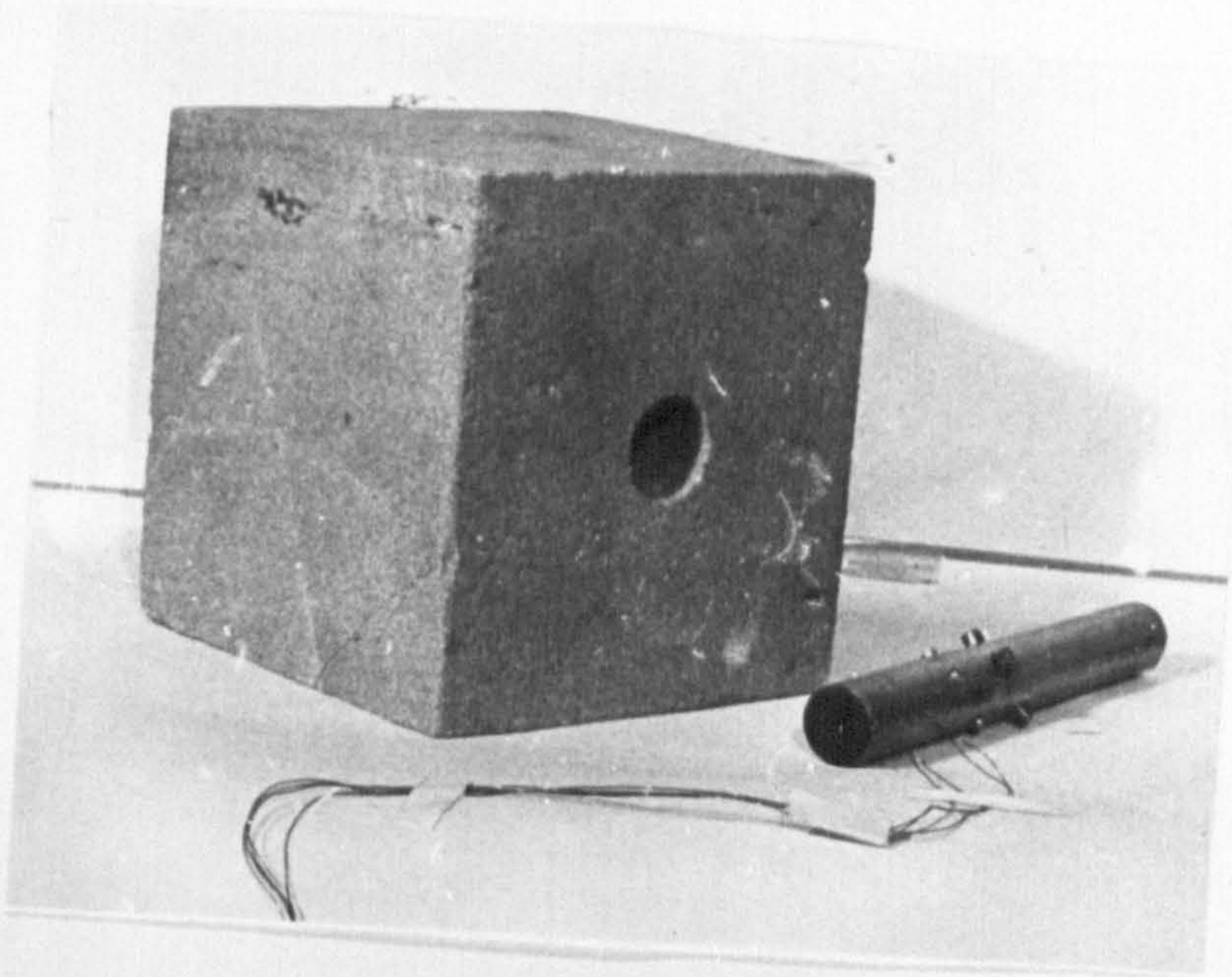

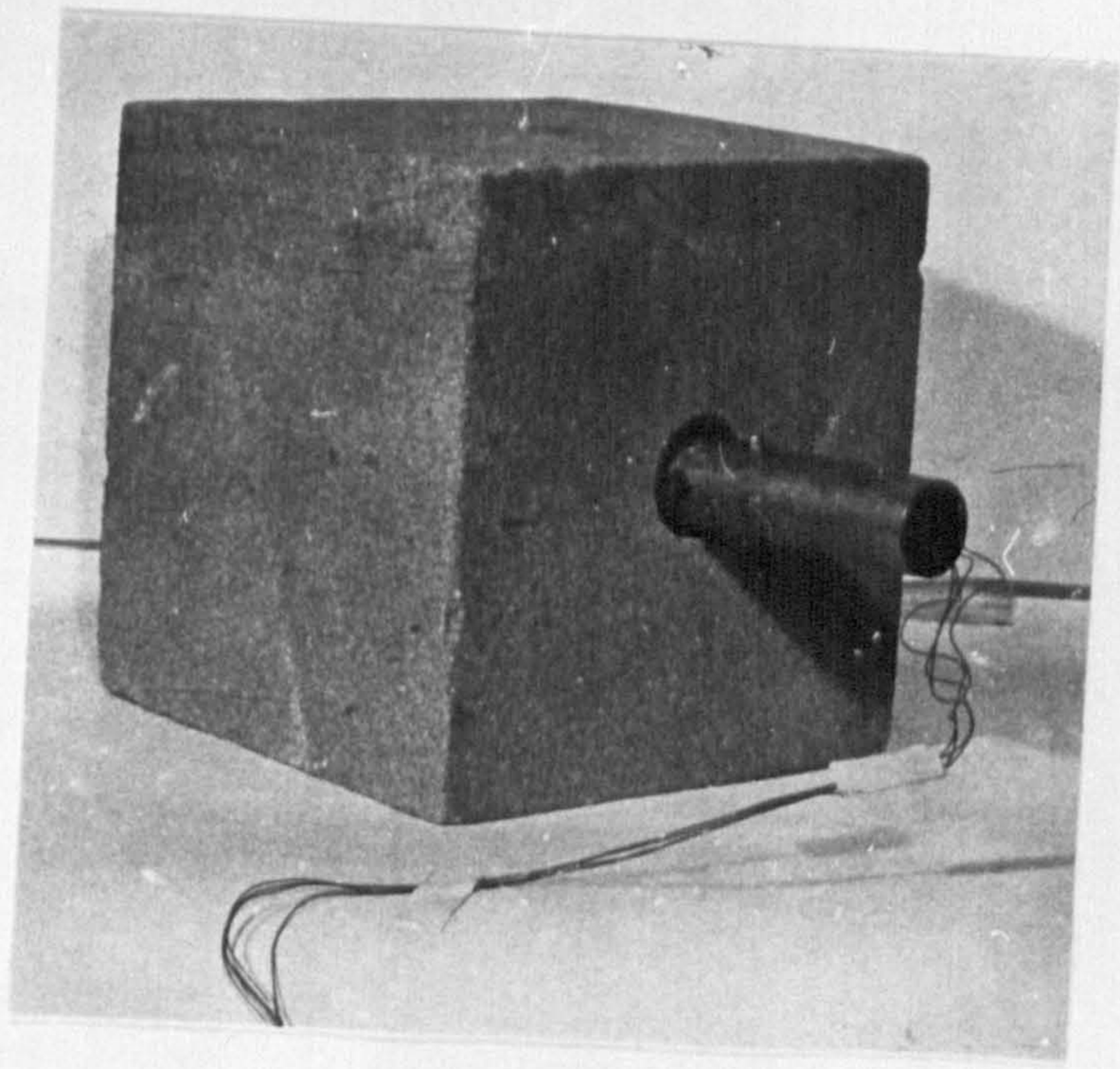

FIG. 7.6.2 SANDSTONE CUBE AND
DEFORMATION CELL.

The sandstone cube had an edge size of 15.25cm, and preliminary testing on cylinders of the same sandstone yielded the following results:

$$E = 9.1 \times 10^3 MN/m^2$$

$$\nu = 0.23$$

The diameter of the borehole was 2.7cm.

The theoretical values are shown, together with the experimental ones, in Figure 7.6.3. From these it can be seen that the experimental values, although slightly deviating from the theoretical ones, show excellent consistancy and approximate very closely straight lines. The vertical and horizontal measured displacements are less than the corresponding theoretical ones, and nearly by the same amount. Such discrepancies can not be attributed directly to the instrument, since any errors when calculating the mechanical properties of the rock can influence considerably the theoretical values of equations (7.6.1). For example, an error of 0.18% on the Young's modulus value will bring the theoretical displacement lines practically coincidental to the experimental ones.

7.7 THE POSSIBILITIES OF THE DEFORMATION CELL IN TRI-AXIAL MEASUREMENTS FROM A SINGLE BOREHOLE

The deformation cell can yield a full stress solution on the secondary principal plane to the axis of the borehole. For tri-axial measurements, readings along the borehole axis

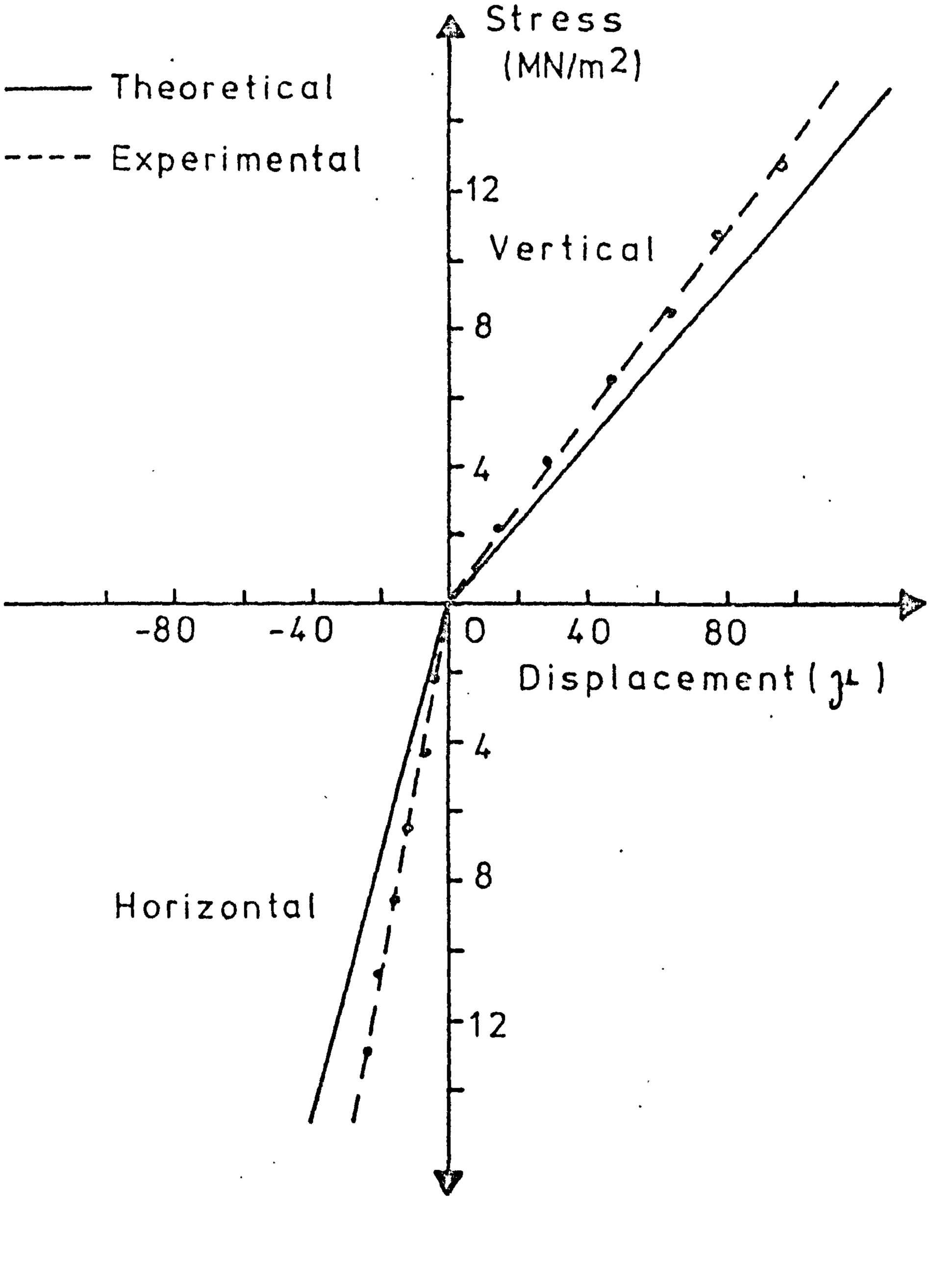

FIG. 7.6.3 THEORETICAL AND EXPERIMENTAL RESULTS OF DISPLACEMENT.

are also required, and this can be achieved by using the cell in conjunction with the displacement technique developed by Smart[79], employing point sources of radiation. The latter method was as follows: A number of radioactive isotopes (e.g. Iridium 192), were sealed in stainless steel cylinders and each one of them was fixed on a spring holder. The holders were then positioned on a residual hollow tube, so that the spring was kept peripheral to it, using a wire. The whole system could then be inserted inside a borehole and by drawing the wire, the spring holders were released at predetermined intervals, so that they gripped the sides of the hole. A film was wrapped round a second tube of smaller diameter and pushed inside the residual one. The film was then retained for sufficient time to allow the radiation from each source to expose it and was subsequently removed and developed. Using an accurate photometric arrangement, the distances between the images of the reference points on the film could be measured assuming that the darkest point of the image corresponds to the centre of the reference point. By taking a series of such measurements, any changes in the distances between the reference points (radioactive sources), and hence rock movements along the borehole's axis could be estimated. This technique was successfully tested in the laboratory and underground showing an accuracy of at least $\pm$ 25μ.

It can be seen, therefore, that the designed deformation cell can easily take the place of the residual tube. In this way a tube of an appropriate diameter can be installed inside a borehole with strain measuring units and radiation sources in a similar manner. The only improvisation required is that the internal spring containing the strain gauges must be protected so that it does not obstruct the inner tube carrying the film. This, however, can be easily negotiated by welding inside the residual tube a number of rings for each pipe length, which could then guide the inner tube between the deflected gauges. Alternatively the internal springs could be so arranged that the bottom part of the residual tube is clear for the inner tube to advance. The latter may result, due to the limited space left, in only one gauge at a point, instead of two diametrical ones connected in series. Although this will result in less sensitive recordings, it could be advantageous in this case, enabling even heavy tubes to be used, since the bottom part contains only outside anchors and not strain measuring units.

7.8 THE DESIGN OF AN INCLUSION METER, CAPABLE OF DETERMINING THREE-DIMENSIONAL STRESS CHANGES AT A POINT

The only inclusion meter capable of three-dimensional investigation, to the author's knowledge, is the one designed by Nichols et al[129]. The meter, described by its designers as a solid inclusion borehole probe, was as follows:

Three 45° strain rosettes were attached, orthogonally, on a 2.54cm in diameter steel ball. The latter shape was considered ideal, due to its uniformity in stress distribution (i.e. lack of edges or corners). A handle was then cemented on to the ball, and the whole system was subsequently encapsulated with an epoxy resin, so that it formed a cylinder 3.81cm in diameter and 4.13cm high. The probe was then grouted, using the same epoxy, in a borehole drilled into a large specimen, and tested on a loading machine.

Since the modulus of the steel is very high, it follows that if the epoxy's modulus is at least four times that of the host, then the whole unit can be considered as one high modulus solid inclusion. After testing a variety of expoxies, unfilled as well as filled (to inprove the stiffness) Nichols et al[129] concluded that the maximum Young's modulus of the epoxies was about $10.5 \times 10^3 MN/m^2$. Since this is not sufficiently high, it follows that the above system could not be taken to represent a rigid high modulus inclusion. As a result,it was suggested that in order to establish the stresses in the host from the corresponding ones measured in the inclusion, the spherical inclusion in the elastic epoxy host must be elastically approximated by a theoretical cylinder. In this case, the actual theoretical spherical approximation for a rigid sphere in a semi-infinite mass of low modulus

material produces a stress concentration factor of about 1.9 instead of the 1.5 factor for a rigid cylinder.

The author feels that the theoretical basis of the borehole probe is rather questionable. Whereas the stress meter, designed during this investigation, is structurally similar to the one above, the theoretical interpretation of the results, however, is in complete contrast. The sphere-epoxy-rock system, in the latter approach, is considered to simulate a rigid high modulus inclusion (steel ball), on a host rock, surrounded by a foreign layer (epoxy). Coutinho[130] has given a theoretical solution for a spherical inclusion and the author has incorporated the effect of such a layer to this solution (Appendix C). As a result, stress changes in the host material can be precisely determined from the equivalent measured ones in the inclusion, using in this case, however, an exact three-dimensional solution.

7.9 CONSTRUCTION OF THE STRESS METER

It was originally intended to use a brass sphere, as the high modulus inclusion element, which could greatly increase the sensitivity of the instrument. However, due to uncertain delivery schedules, this was not possible, and as a result, readily available steel spheres (ball bearings) had to be used. Each sphere was 2.54cm in diameter and was gauged using FR-2b Showa strain rosettes. The latter is a

90° -45° system, with gauge length and width of 2mm, and an overall base size of about 9 x 9mm. The nominal resistance is 120 Ohm and the gauge factor 2.09 approximately.

Before gauging, each ball was etched, and three mutually perpendicular directions at the three points of interest were accurately marked, as shown in Figure 7.9.1. This was accomplished by using a specially designed hemi-spherical cup, with two perpendicular directions clearly shown on its periphery. A handle was then cemented onto the ball with an orientation strip at its end, so that the measuring directions of the gauges were always known, with respect to the reference space axes, as shown in Figure 7.9.2. The gauges were then embedded using a standard procedure.

After consultation with CIBA-GEIGY (U K) Ltd., it was decided that the Araldite MY.778 with Hardener HY.941 epoxy resin was most suitable. This system will cure under adverse conditions, giving excellent bonding strengths. Testing of a number of cylinders of this resin, revealed that its Young's modulus and Poisson's ratio were 3.87 x $10^3 MN/m^2$ and 0.4 respectively, as shown in Figure 7.9.3.

The steel sphere was thereafter encapsulated in a cylinder of this epoxy, as shown in Figure 7.9.4, and was ready for testing.

7.10 TESTING OF THE INCLUSION METER

Preliminary tests on concrete and sandstone blocks were

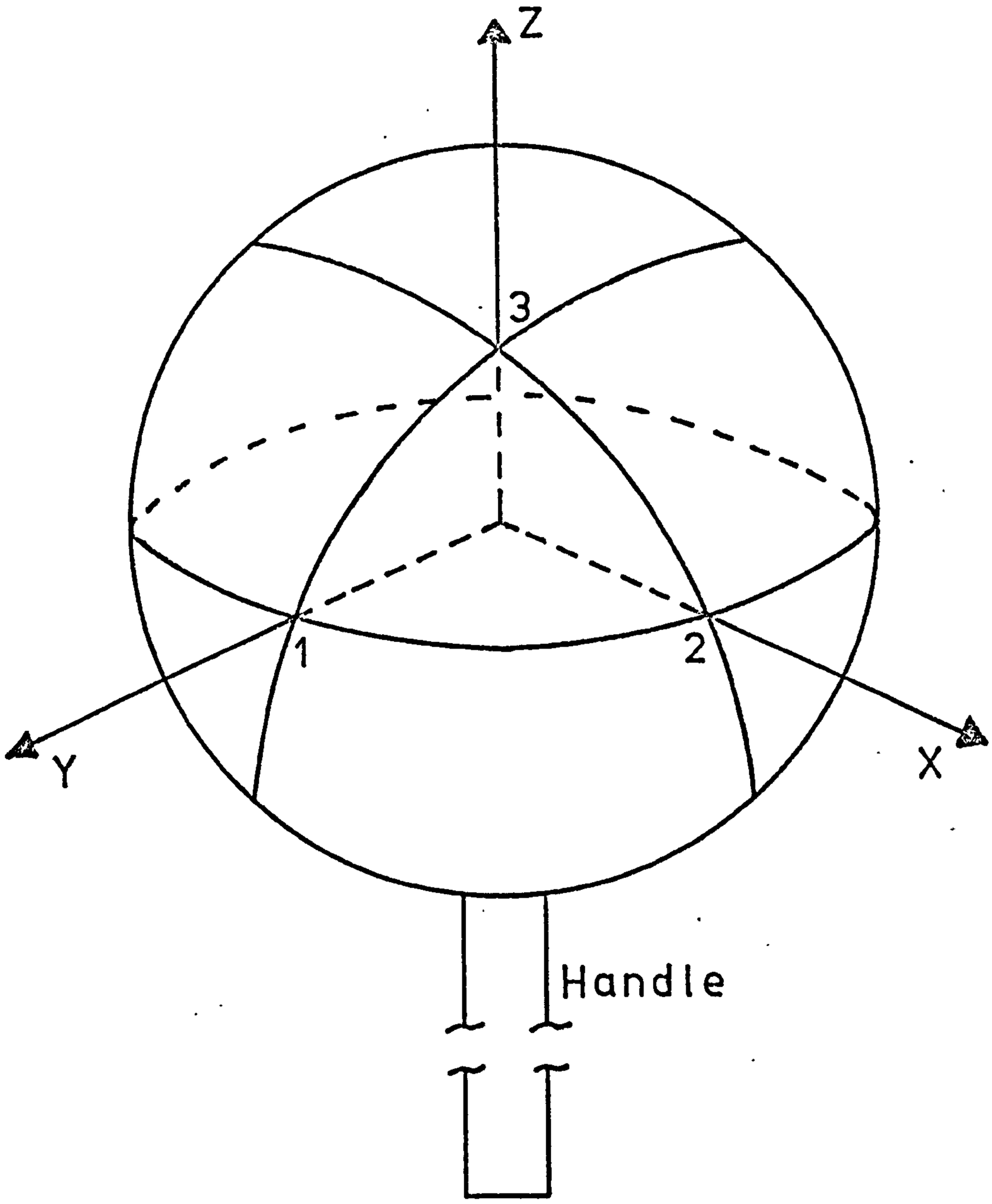

Strain Rosettes on Points
1, 2 and 3 .

FIG. 7.9.1 REFERENCE AXES OF THE SPHERE .

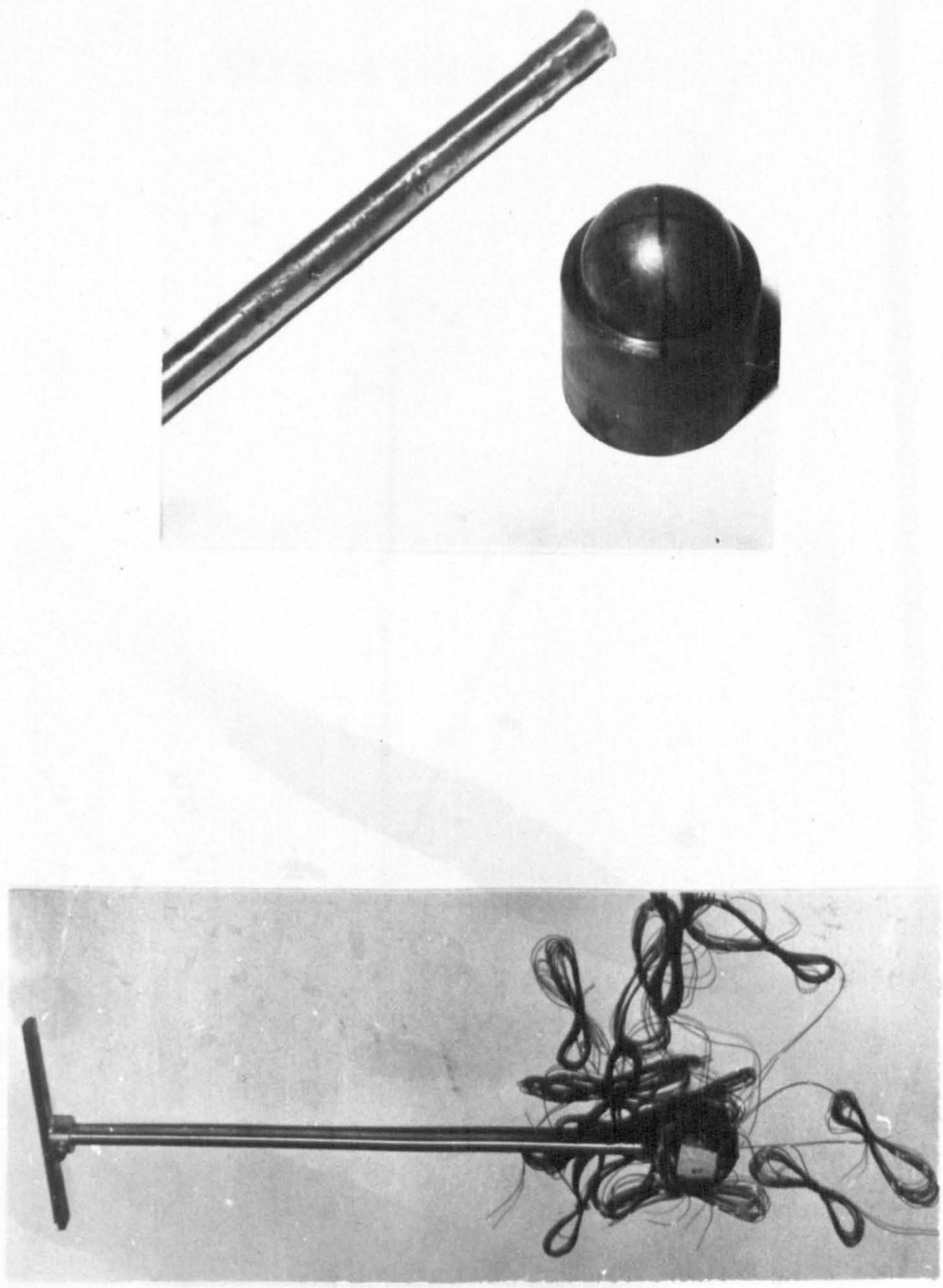

FIG. 7.9.2 STEEL BALL AND HOLDER .

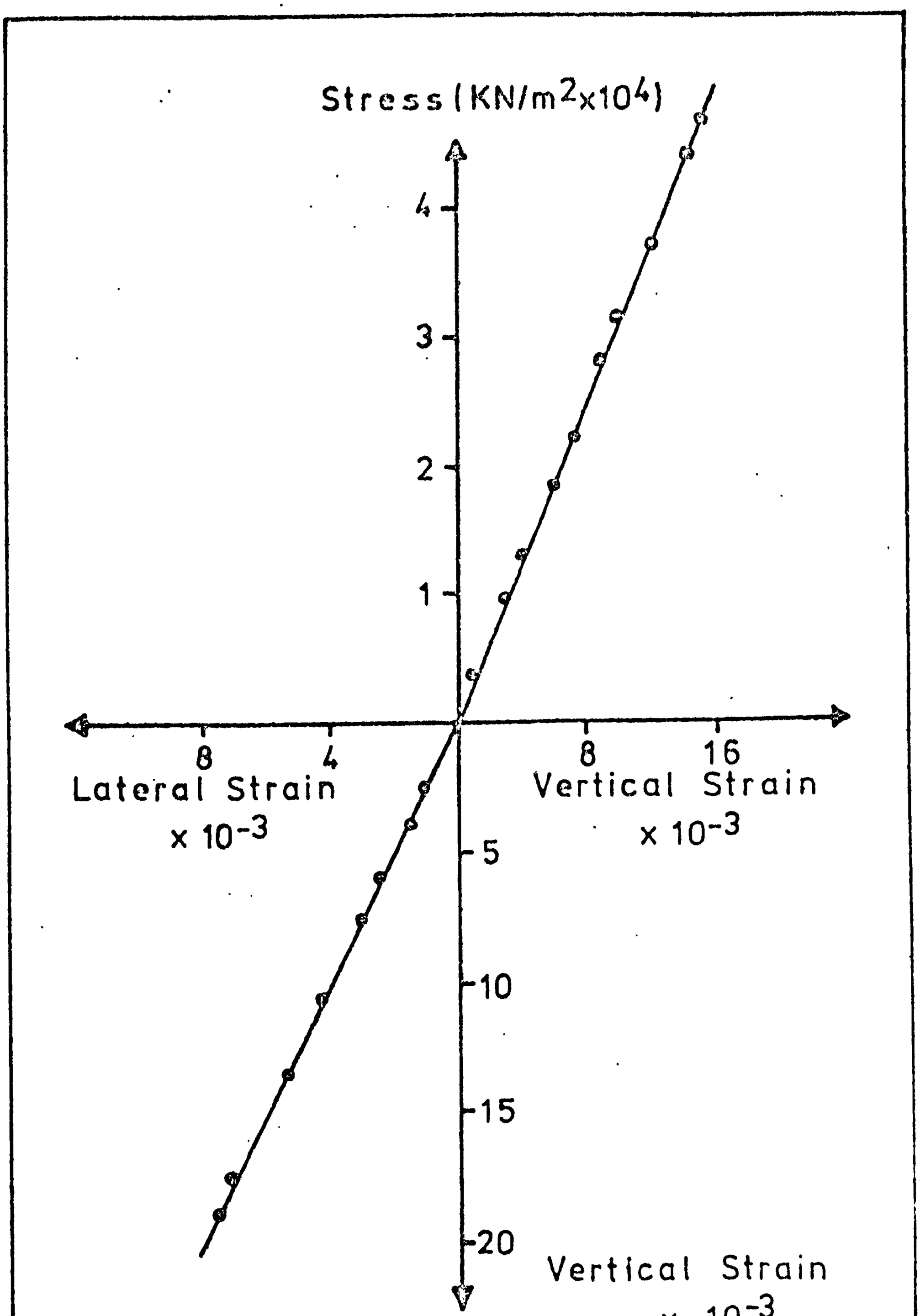

FIG. 7.9.3 MECHANICAL PROPERTIES OF THE EPOXY SYSTEM.

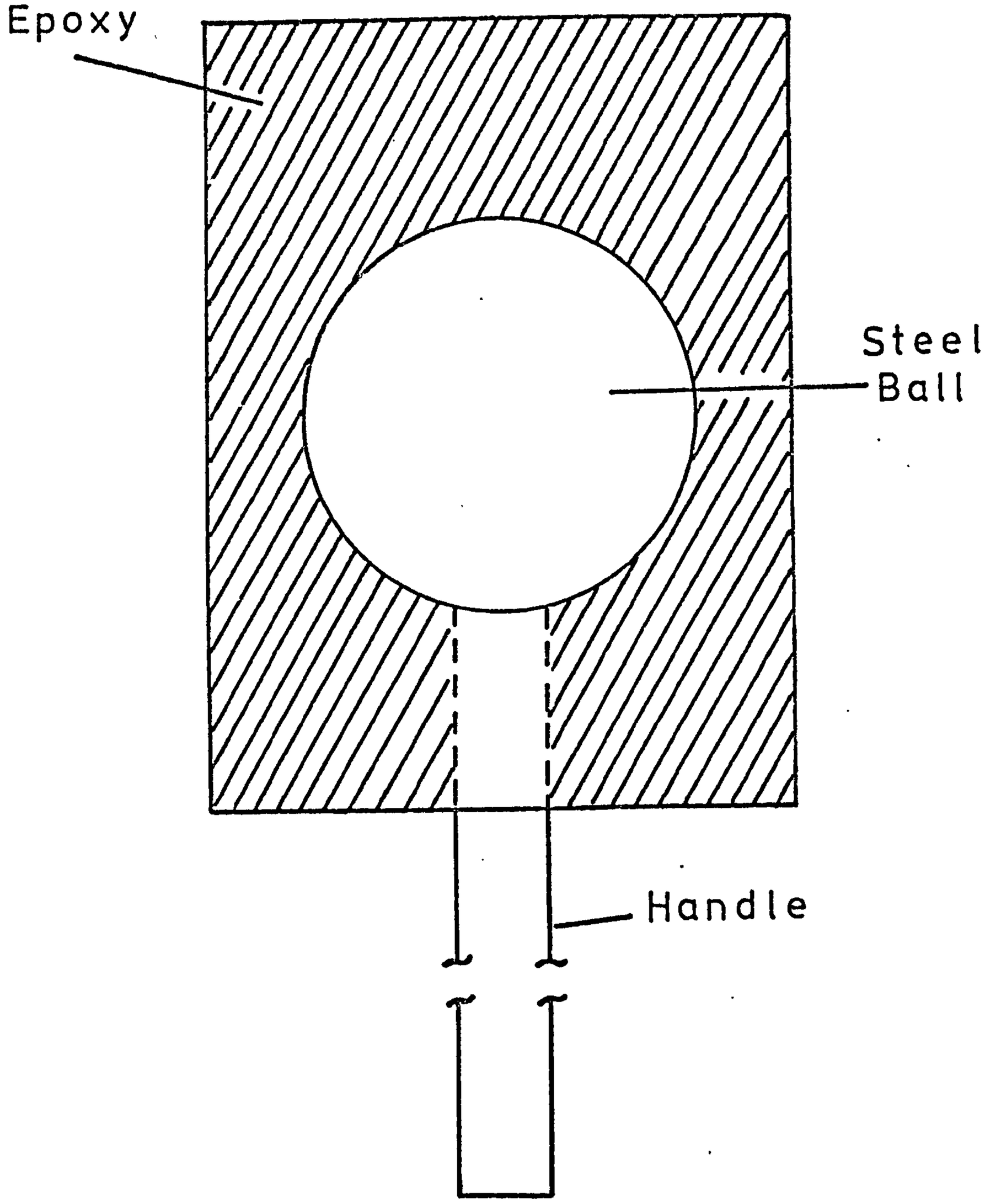

Scale 1:2

FIG. 7.9.4 DIMENSIONS OF INCLUSION METER.

most encouraging. In each test, a 5.4cm in diameter hole was drilled at the middle of a large block, using a coring bit. The meter was then placed inside and properly oriented with respect to the reference axes; the whole unit was subsequently grouted inside the hole by filling the latter with the same epoxy resin as the one used for encapsulating the steel sphere. After the resin was cured (Figure 7.10.1), the block was placed on a testing machine. Since the machine's platens were only about 33cm in diameter, whereas the average size of the blocks was 30.5 x 30.5 x 33cm, a set of additional platens was positioned between the corresponding ones of the machine and the block. These platens were of steel, and their size was sufficient to ensure that bending could not take place (35.5 x 45.7 x 3.8cm). This is shown in Figure 7.10.2.

Before testing began, the leads of the strain gauges were connected to the switch unit and strain indicator as before (Figure 7.6.1). In this way the gauges could be read in succession by selecting the appropriate channel on the unit. This is demonstrated in Figure 7.10.3.

Tests on a sandstone block, 30.5 x 35.6 x 35.6cm, under a stress of 19.2MN/m^2 resulted to the following values on the inclusion, using the convention shown in Figure 7.10.4.

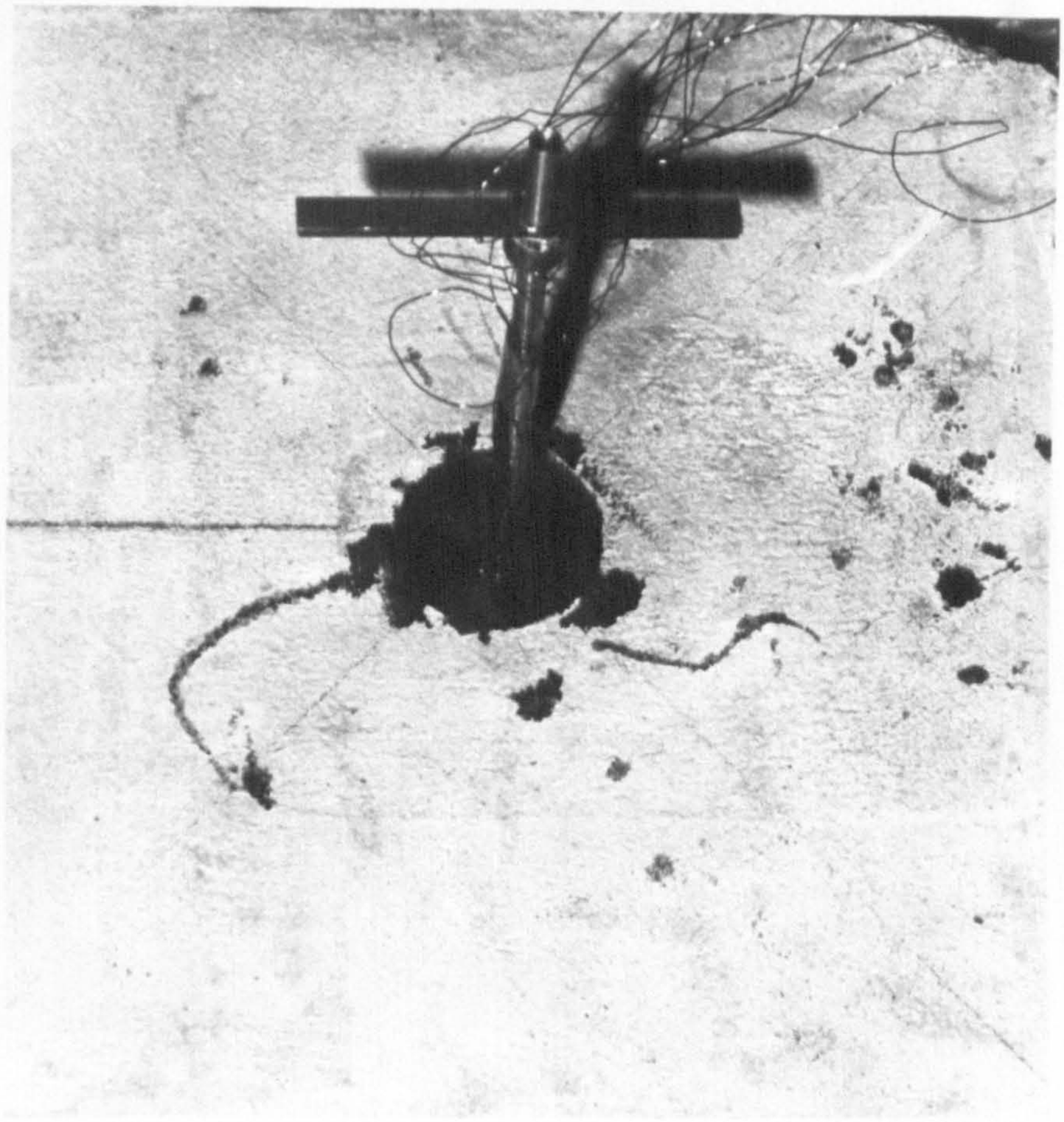

FIG. 7 . 10 . 1 INCLUSION METER CEMENTED IN CONCRETE BLOCK .

FIG.7.10.2 TEST BLOCK AND LOADING PLATENS.

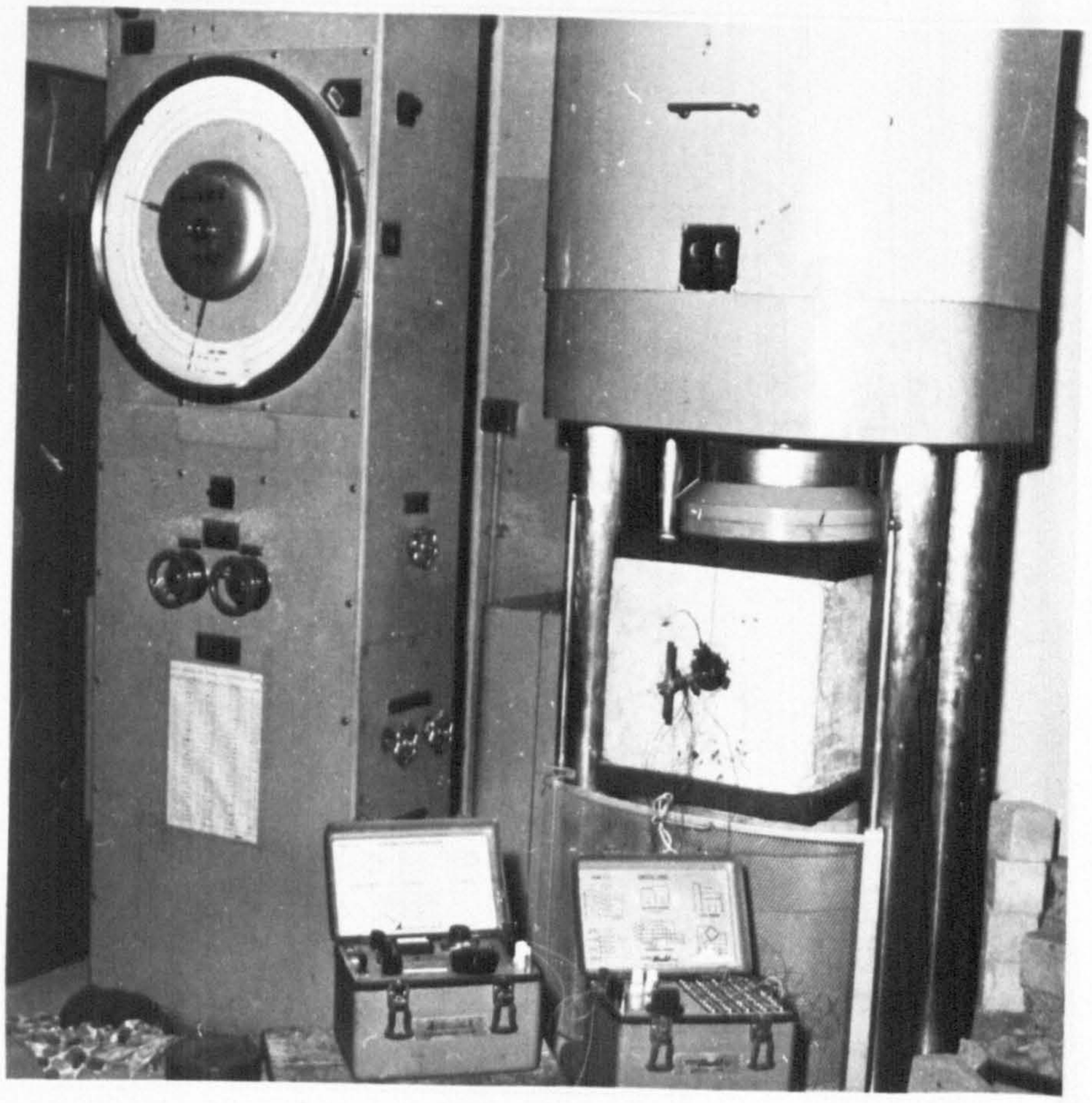

FIG. 7.10.3 TESTING INCLUSION METER .

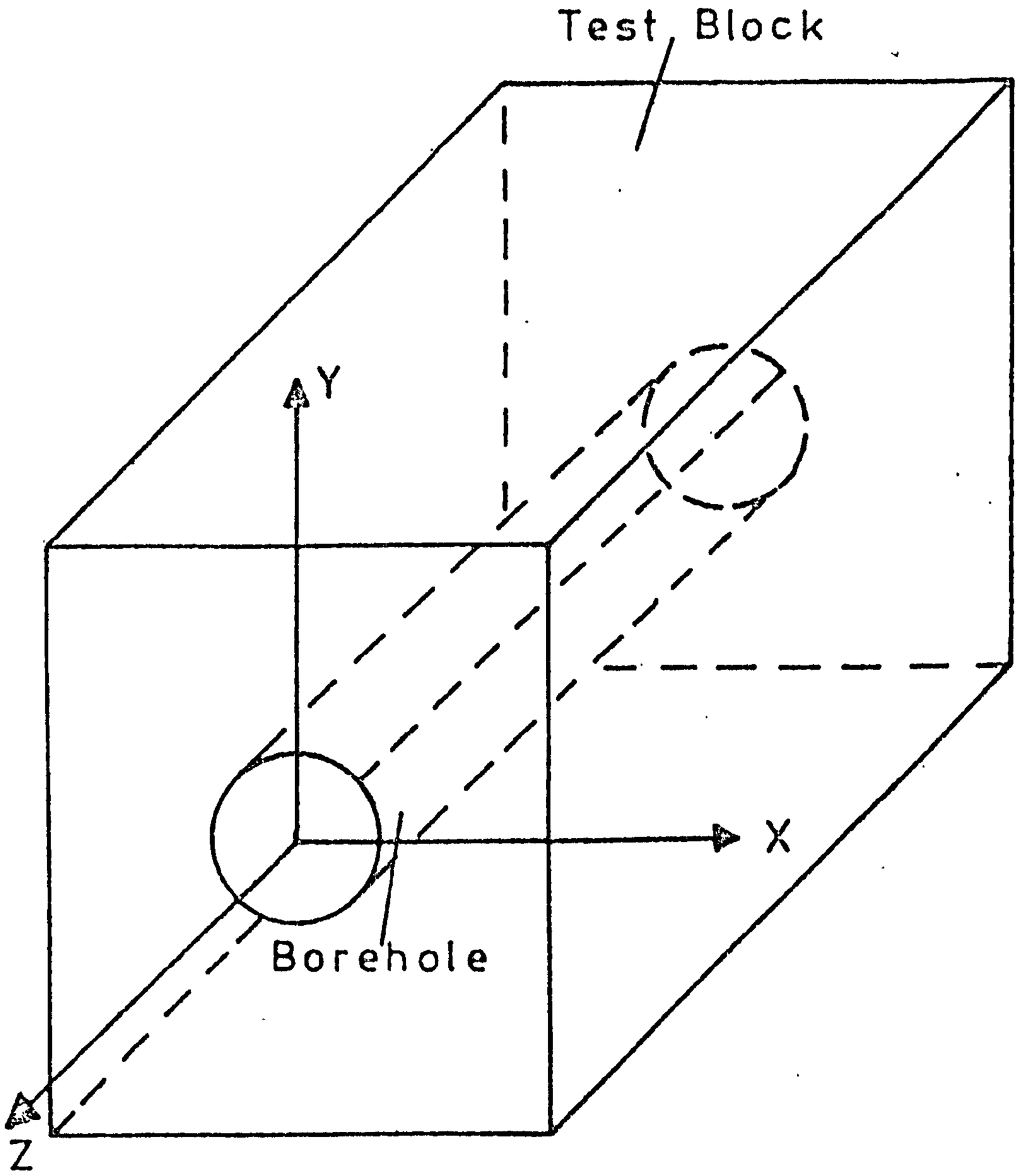

FIG. 7.10.4 REFERENCE AXES.

$$\sigma_x = -4.6 MN/m^2$$

$$\sigma_y = 21.0 \text{ >>}$$

$$\sigma_z = -6.2 \text{ >>}$$

$$\tau_{xy} = 3.6 \text{ >>}$$

$$\tau_{yz} = -1.8 \text{ >>}$$

$$\tau_{zx} = 0.7 \text{ >>}$$

where the negative value denotes tensile stresses.

The principal stresses of the inclusion can then be calculated, using equation C.2.2, i.e.

$$\sigma_1 = 21.3 MN/m^2$$

$$\sigma_2 = -4.7 \text{ >>}$$

$$\sigma_3 = -6.6 \text{ >>}$$

where the orientations of the principal stresses, with respect to the reference axes (equation C.2.4), are shown in Figure 7.10.5.

Having calculated the principal stresses of the inclusion, the corresponding ones of the rock must be determined, assuming that they act in the same direction. The mechanical properties of the rock were $9.1 \times 10^3 MN/m^2$ and 0.23, and from Figure C.4.1, the equivalent stress factors are

$$(K_1)_{r/c/i} = 0.8549$$

$$(K_2)_{r/c/i} = -0.0591$$

The principal stresses, therefore, using equations C.4.4 are

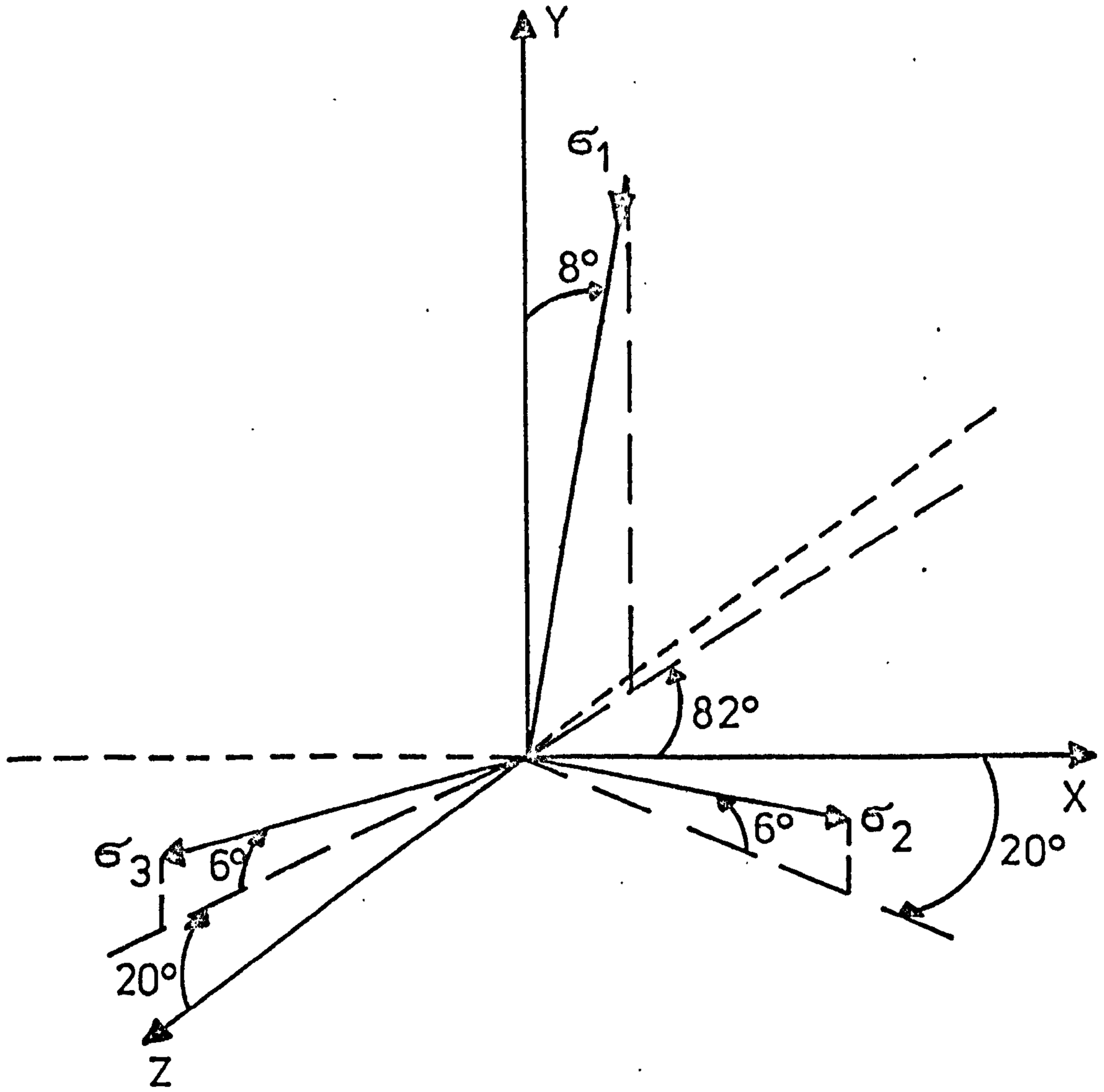

F I G. 7 . 10 . 5 RESULTS OF FIRST TEST .

$$(\sigma_r)_1 = 18.9 MN/m^2$$

$$(\sigma_r)_2 = -5.0 \gg$$

$$(\sigma_r)_3 = -6.6 \gg$$

A second test, carried out on a concrete block, 30.4 x 30.5 x 33cm under an applied stress of $14MN/m^2$, resulted in the following principal stress values for the inclusion:

$$\sigma_1 = 9.7 MN/m^2$$

$$\sigma_2 \gtrless -1.5 \gg$$

$$\sigma_3 = 3.3 \gg$$

Taking the mechanical properties as $17 \times 10^3 MN/m^2$ and 0.16, the corresponding stress factors are 1.2864 and -0.1884.

The principal stresses on the rock, therefore, from equations C.4.4, are

$$(\sigma_r)_1 = 13.3 MN/m^2$$

$$(\sigma_r)_2 = -3.1 \gg$$

$$(\sigma_r)_3 = -5.8 \gg$$

acting in the direction given in Figure 7.10.6.

From these two tests some common features can be noted. In both cases, the lateral stresses are tensile; this is because the size of each block is not large enough to allow the host to be considered as a semi-infinite medium, with

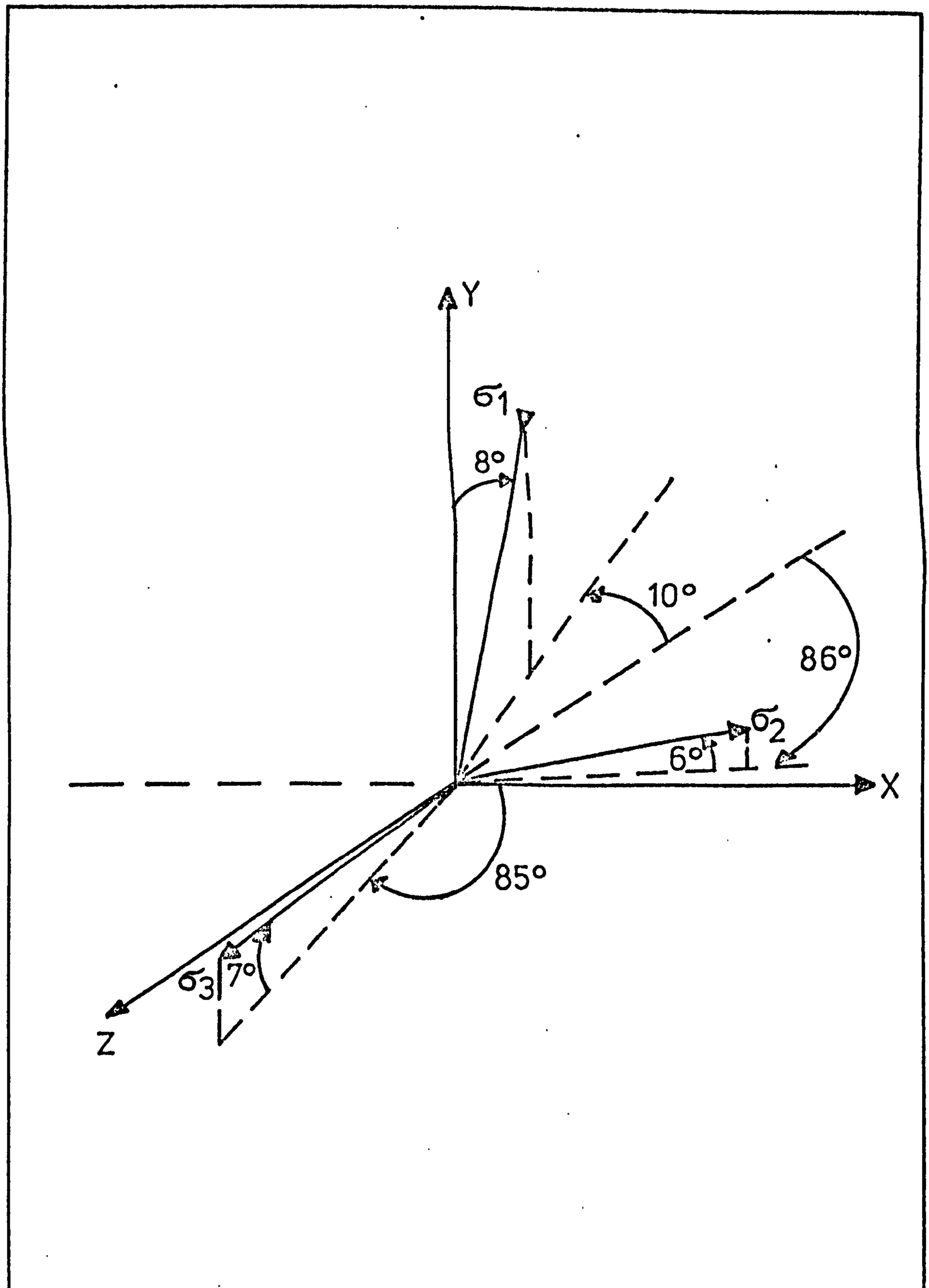

FIG. 7.10.6 RESULTS OF SECOND TEST.

respect to the inclusion. The unavoidable lack, therefore, of any lateral restraint will give rise to tensile stresses. However, the actual value of these stresses was higher than expected.

The orientation of the principal stresses, in both tests, shows that the stresses have remained close to the reference axes. In addition, the near vertical compressive principal stress σ_1 is, in both cases, practically identical to the applied stress, which is an excellent indication of the accuracy of this method.

7.11 CONCLUSIONS

(i) In this Chapter a list of some basic characteristics was given, to which an 'in-situ' instrument must conform if it is to be successful. It was suggested that apart from the obvious requirements of the accuracy and adaptability to the underground environment, the installation technique, amount of retrieved information, and the economic considerations of an 'in-situ' instrumentation, are also of equal importance. The high modulus inclusion plug, therefore, does not fully meet these specifications, and the object of this investigation was to attempt alternative methods of underground examinations.

(ii) Two types of instruments were developed, a deformation cell and an inclusion meter, both capable of triaxial

measurements from a single borehole, and in close agreement with the requirements set out above. Preliminary testing of these instruments, in the laboratory, was encouraging enough to suggest that both could be successfully used for underground instrumentations.

(iii) The deformation cell can be quickly and easily manufactured and installed with very little expense. Laboratory testing of the instrument showed excellent sensitivity, which can be further improved by connecting the two diametrically opposite, cantilever loaded, measuring units, in series. In addition, the curved shape of the protruding part of the unit, enabled the instrument to withdraw with no difficulty even from soft rocks. The deformation cell can yield a full stress solution, on the secondary principal plane to the axis of the borehole. For triaxial measurements, the instrument must be used in conjunction with a technique monitoring the displacement along this axis. In this respect, it appears that the method developed by Smart[79], using point sources of radiation, is ideally suited and could be easily adapted to the deformation cell, with very little improvisation. The accuracy of the deformation cell results, finally, was within 0.2%

of the theoretical values.

(iv) The inclusion meter, designed in this investigation, is capable of a complete stress solution, without the need of additional instrumentation. Although this instrument is structurally similar to the one used by other investigators, the theoretical interpretation of the results is based on a different principle. The author considered the sphere-epoxy-rock system to simulate a high modulus inclusion (sphere) inside a rock, surrounded by foreign layer (epoxy). The theoretical solution of this system, developed in Appendix C, can directly and precisely determine the principal stresses of the rock, from the measured principal stresses of the inclusion, assuming that both act in the same directions. Further, since the mechanical properties of the inclusion and epoxy can be determined accurately, the former being of high modulus with respect to the rock, any variations of the mechanical properties of the latter will have a very small impact on the calculated principal stresses. It is also worth noting that although the data reduction is to a certain degree laborious, the numerical operations easily lend themselves to computerisation which could greatly increase the

accuracy of the results, saving considerable time. The testing of this meter, on sandstone and concrete blocks, yielded encouraging results. Although some of the theoretical assumptions are not fully met using such specimens, (e.g. the semi-infinite size of the host with respect to the inclusion), nevertheless the obtained information was in agreement with the theoretical considerations. The potentiality of this technique, therefore, for 'in-situ' measurements was clearly demonstrated from these preliminary trials.

(v) 'In-situ' investigations are the only means by which the underground behaviour of mining configurations can be studied. At present there is a great lack of such examinations and the limitations of most 'in-situ' instruments can be partly responsible for it. The author feels that this is why research directed to the design of new techniques is so important. The two instruments developed in the course of this investigation, although only tested in the laboratory, have shown great potential. It is the author's hope, therefore, that their application to underground measurement will be the subject of further research.

GENERAL CONCLUSIONS

GENERAL CONCLUSION

(i) The design of underground pillars, and in particular those encountered in longwall workings, is a problem of considerable complexity due to the number and nature of the parameters involved. As a result, pillar sizes are approximated from empirical knowledge rather than calculated from a scientific analysis. In Britain, for example, pillars have been successfully designed using the empirical equation (2.4.11), which, although it has no theoretical background, is in agreement with the results obtained from recent scientific methods (equation (2.4.8.)). Nevertheless, however successful the empirical design of the pillars may be, it is an inferior engineering practice, often associated with expensive overdesign tendencies and even a lack of a complete understanding of the problem. Scientific analyses, on the other hand, although not capable of producing a singular design criterion for a problem of such complexity are, however, the only means of really appreciating the influence of the individual parameters on the behaviour of pillars. Empirical knowledge and intuition, therefore, should not be the only design considerations, but important aids towards consolidating the scientific findings.

(ii) The solution of a complex rock mechanics problem, such as pillar design, can be approached by a variety of methods, based on widely diverging principles. A number of assumptions, however, is necessary before a particular scientific method can be applied, which will transform the actual problem to either a realistic or an idealised prototype. Furthermore, as the amount and accuracy of the information retrieved from the various methods of solution is increased, the degree of realism of the situation becomes progressively worse. The best suited methods of analysis of a rock mechanics problem, therefore, are directly determined by the problem's particular nature and characteristics. As a result, after a careful study of the various parameters influencing the behaviour of pillars, it was decided that three-dimensional photo-elastic techniques, and 'in-situ' measurements on pillars, could greatly increase our present knowledge.

(iii) Photo-elastic solutions are established techniques in the science of rock mechanics, and are usually carried out by assuming an idealised prototype situation. As a result, such solutions can not be accepted on a pure quantitative basis; they do, however, give an excellent picture of the stress distribution and can be an

important guide to the designer, immensely increasing the confidence of his predictions. The behaviour of pillars has been studied photo-elastically by many investigators using conventional two-dimensional techniques on small scale single- and multi-layer models. This problem, however, is a three-dimensional one and for representative results, it should be treated as such whenever possible. During this investigation the Scattered Light photo-elastic technique was introduced for three-dimensional stress investigations on pillars. This method shows a number of attractive features when compared to the other three-dimensional technique of Stress Freezing, and in addition, is suitable for multi-layer studies. The examination of the behaviour of small and large pillars, using the scattered light technique, suggested that although the method could not replace conventional two- or three-dimensional photo-elastic techniques, it can, however, provide the most advantageous means of solution for many problems such as that of the design of pillars. It is hoped, therefore, that this investigation will encourage other researchers to undertake similar investigations so that mining configurations can be extensively studied, in their proper three-dimensional context.

A second photo-elastic technique was also described in the course of this work, known as the Image De-rotation technique, capable of freezing completely the rotary motion. This method was specially adapted to enable gravity loading simulation of centrifuging photo-elastic models, in 'real time'.

The simulation of the gravity field has been proved a very difficult task in experimental stress analysis, and a nearly impossible one in theoretical procedures. As a result, it is usually substituted by uniform stress conditions. The latter treatment, although successful for many problems, is unacceptable in others such as shallow workings, multi-level excavations or steeply inclined seams. In these cases, therefore, gravity field must be considered and the Image De-rotation technique, introduced here, is best suited for an experimental simulation.

The full potential of the method, however, has not been yet fully realised. Recent research has shown that by rotating the incident light as well as the model, and subsequently freezing both motions, the object's contrast and illumination is greatly increased, and as a result, the photographic problems experienced during the investigation are totally removed. Furthermore,

the application of the scattered light technique to this method and the possibilities of examining rock drilling problems (previously outside the scope of most model simulation techniques), are some topics that could be investigated in the future.

(iv) The underground behaviour of mining configurations can only be studied by 'in-situ' investigations, most of which necessitate a number of reasonable assumptions, thus producing a realistic prototype situation. In addition, 'in-situ' results can also indicate the degree of correspondence, at least in qualitative terms, between the realistic prototype and the idealised one, as assumed in the photo-elastic studies.

The 'in-situ' strength of pillars is considerable, and the possibility of pillar failure, even when narrow, is remote. As a result, pillar design based on empirical or strength criteria is not sufficient. What is more important is the general distribution of stress on such pillars, and how it is affected by the various parameters and, in particular, pillar width. The purpose of the two underground investigations carried out during the course of this work, was to retrieve as much information as possible regarding pillar behaviour. The effect of the increased constraint conditions, on the stress when moving from corner to the pillar's interior, is clearly

demonstrated by the first investigation, as is the influence of the face advance on the corner's stresses. The wave-like distribution of stress across the width of a rib pillar, as determined from the second investigation, is also of interest, and should be the subject of future research.

Finally, the author's experiences, during the 'in-situ' investigations, demonstrated clearly the numerous and often unpredictable practical difficulties when undertaking such measurements. This explains the general lack of 'in-situ' results, regarding many underground configurations, including pillars. In addition, the lengthy and tedious installation procedure of the inclusion borehole plug, used in this investigation, and the limited information retrieved from each instrument, is another discouraging factor. An attempt was, therefore, made by the author to investigate improved methods of 'in-situ' measurements. Two instruments, a deformation cell and an inclusion stress meter, both capable of tri-axial measurements at a point from a signle borehole, were designed. These embraced a set of requirements that the author feels are necessary for the success of an underground instrument. Preliminary testing of these instruments

in the laboratory, yielded encouraging results, and it is the author's hope that their application to underground measurements will be the subject of further research.

APPENDICES

APPENDIX A

DETERMINATION OF THE STRESS-OPTICAL COEFFICIENT

A.1 INTRODUCTION

When complete solutions are to be obtained, either in two- or three-dimensional photo-elasticity, the value of the stress-optical coefficient of the particular model material must be determined. In addition, when using a material such as polyurethane, great care must be taken since its coefficient is dependent on the Young's Modulus, and therefore, on the amounts of the prepolymer and catalyst in the mixture. In the case of polyurethane, therefore, the stress-optical coefficient should be always stated with respect to the mixture used.

A.2 THEORY

The most convenient method of calibrating photo-elastic materials is the disc under diametrical compression. For such conditions, from the theory of elasticity, the difference of the principal stresses at the centre of the disc is given by

$$(p - q) = \frac{8P}{\pi dt} \qquad (A.2.1)$$

where

P = Applied load

d = Diameter of the disc

t = Thickness of the disc

The same difference can also be estimated from the photo-elastic technique, using the stress-optic law, i.e.

$$(p - q) = \frac{1}{C}\frac{R}{t} \qquad (A.2.2)$$

where

R = Retardation

C = Stress-optical coefficient

The last equation is customarily written as

$$(p - q) = f\frac{n}{t} \qquad (A.2.3)$$

where

f = Material fringe value

n = Fringe order

Equating expressions A.2.1 and 3, it follows

$$f = \frac{8}{\pi d}\frac{P}{n} \qquad (A.2.4)$$

By counting the fringe order at the centre of the disc, under a particular load P, the value of f can be found. However, it is more accurate to take a series of such readings, in which case P/n will be the slope of the straight line, and thus estimate the average material fringe value.

A.3 EXPERIMENTAL PROCEDURE

The accuracy of the method depends entirely on the precision of the loading device. In this case the disc was loaded diametrically with extreme accuracy, using a lever

system and weights, as described in reference 71. Since the loading frame was too large to be accommodated within the base of the scattered light polariscope, the material was calibrated in an ordinary transmission polariscope, using green light from a filtered mercury vapour lamp.

A number of polyurethane discs were cast, 4.76cm in diameter and 1.2cm thick, and subsequently tested in the polariscope. The mixture used, for all tests, was 50/50 by weight. A typical fringe order against load curve is shown in Figure A.3.1.

A.4 RESULTS

From equation (A.2.4), it follows:

$$f = \frac{8}{\pi \times 4.76} \times 2.90$$

$$= 1.55 \quad \text{N/cm.fr.}$$

The above value corresponds to green light ($\lambda = 5460\,\text{Å}$) whereas the scattered light polariscope operates under red light or $\lambda = 6328\,\text{Å}$. Therefore,

$$f_r = \frac{\lambda_r}{\lambda_g} \, f_g$$

$$= \frac{6328}{5460} \, 1.55$$

$$= 1.80 \text{N/cm.fr.}$$

$$= 0.18 \text{N/mm.fr.}$$

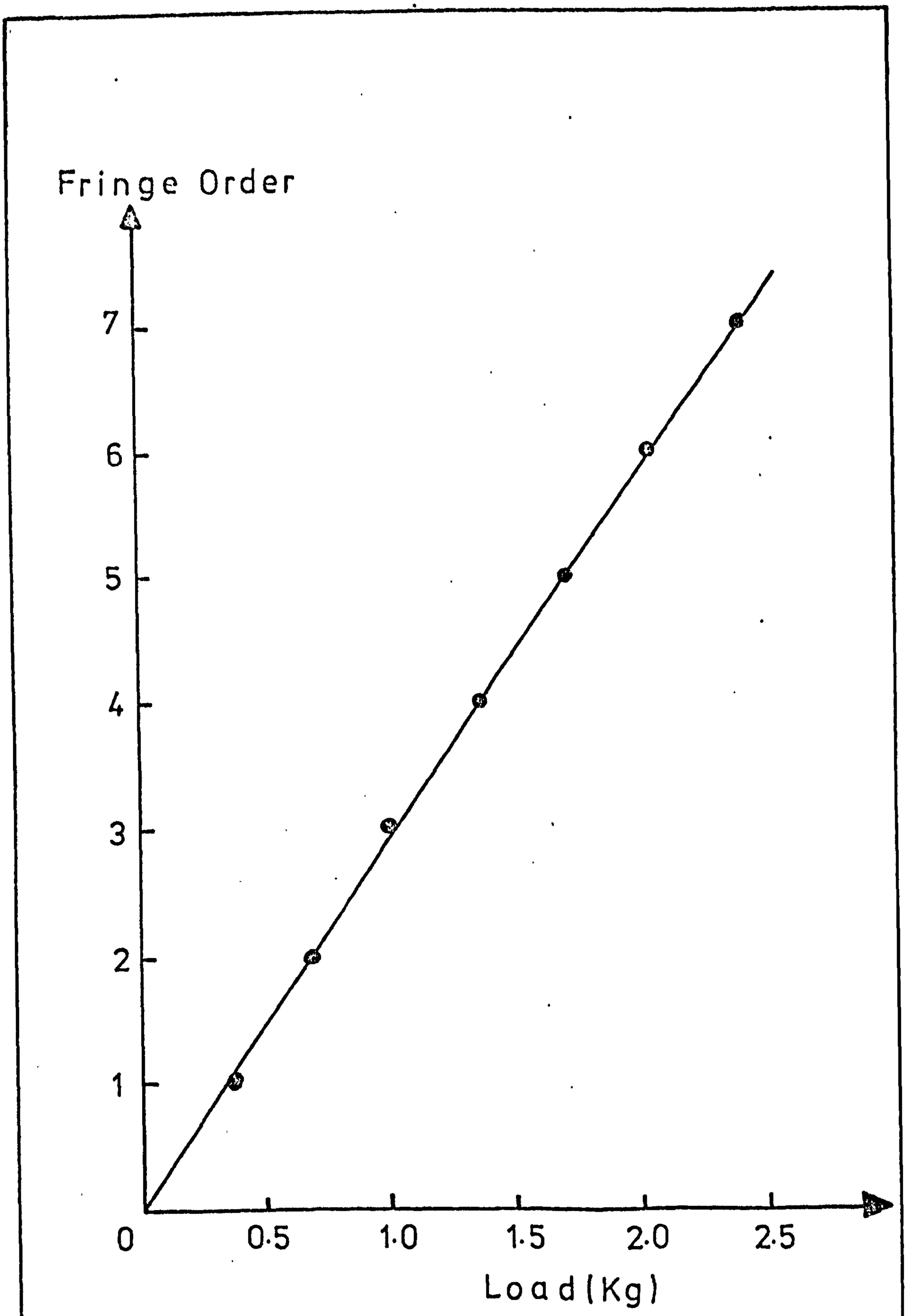

F I G. A . 3 . 1 THE LOAD-FRINGE ORDER RELATIONSHIP .

APPENDIX B

DETERMINATION OF THE MECHANICAL PROPERTIES OF THE MAIN SEAM STRATA

B.1 INTRODUCTION

An accurate knowledge of the mechanical properties of rocks was essential during this investigation, since both the multi-layer photo-elastic studies and the calibration of the borehole plugs results, were based on such knowledge.

It was originally intended to carry out a laboratory testing program involving the strata of the Main and Gaswater seams in the vicinity of the N.10 and G.32 panels at Killoch and Cairnhill collieries, respectively. However, due to lack of time, only the first part of this investigation was completed. A detailed examination of the mechanical properties (static and dynamic) of a range of Scottish Coal Measures, is currently the subject of an extensive research program at the Mining Engineering Department, University of Strathclyde, and results will be published soon.

B.2 SPECIMEN PREPARATION

Specimen rocks were taken from N.10 panel, Killoch colliery, of the Main Seam coal, the immediate roof (shale and sandstone), and floor. The rocks were subsequently cored by the author and Smart, using the technique described in reference 79. A number of cores was taken, therefore, from each rock, having 2.54cm diameter. The ends were

accurately flattened using a grinding machine, in the case of the sandstone, shale and mudstone, and a lapping plate in the case of the much more friable coal.

B.3 TESTING FOR COMPRESSIVE STRENGTH

A number of specimens, from each rock, were tested to destruction in an Avery testing machine. Since all specimens had the same diameter (2.54cm) but varying lengths, the strength values thus obtained had to be corrected to a standard specimen of D/L = 1/2 using the following empirical formula:

$$S_{1/2} = \frac{S_{D/L}}{0.304D/L + 0.848}$$

where

$S_{1/2}$ = Strength of a specimen with D/L = 1/2

$S_{D/L}$ = Strength of a specimen with D/L $\neq$ 1/2

D/L = Diameter to length ratio

The corrected strength results are shown in table below:

ROCK TYPE	$S_{1/2}$ x $10^4 KN/m^2$
Sandstone	3.73
	5.83
	2.19
	3.35
	6.99
Mudstone	6.86
	6.71
	5.85
	7.61
Shale	4.72
	6.04
	4.15
	7.27
	3.60
Coal	5.90
	3.95
	3.88
	4.34
	3.60

The average values are shown below, together with the compressive and tensile strengths of sandstone and coal found from the cone indenter test.

ROCK TYPE	Average $S_{1/2}$(Testing) x 10^4KN/m^2	Average $S_{1/2}$(Indenter) x 10^4KN/m^2	Average T(Indenter x 10^4KN/m^2
Sandstone	4.42	6.43	1.18
Mudstone	6.76	-	-
Shale	5.16	-	-
Coal	4.33	4.24	0.76

B.4 TESTING FOR THE MECHANICAL PROPERTIES

Only one specimen was used for each rock during this program, and as a result the values obtained must be treated with a certain degree of caution.

Since small loading increments were required in this case, a much more sensitive loading machine was necessary. An Instron Universal machine proved to be ideal, enabling accurate reading in both loading and unloading cycles. Huggenberger extensiometers were used, reading in microns, to measure changes of linear dimensions. Whereas the vertical strain was read accurately, using this instrument, the lateral strain measurements were extremely small. This was attributed to the square brass frame, surrounding the specimen which was used to determine the diametrical length changes. As a result the lateral strain measurements[79] were of little value and therefore are omitted.

Figures B.4.1 to 4 show the stress against strain

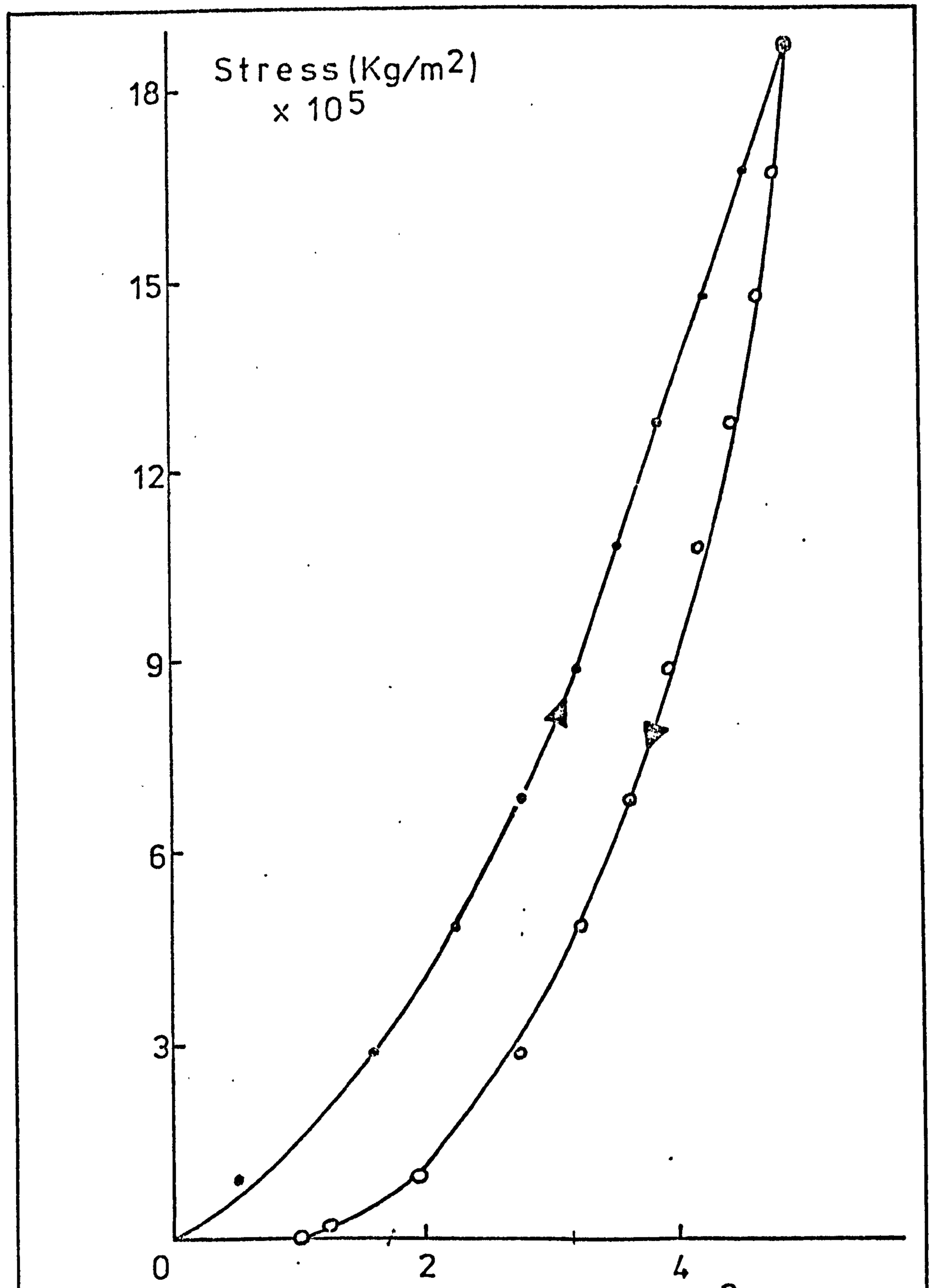

FIG. B.4.1 STRESS-STRAIN RELATIONSHIP FOR SANDSTONE .

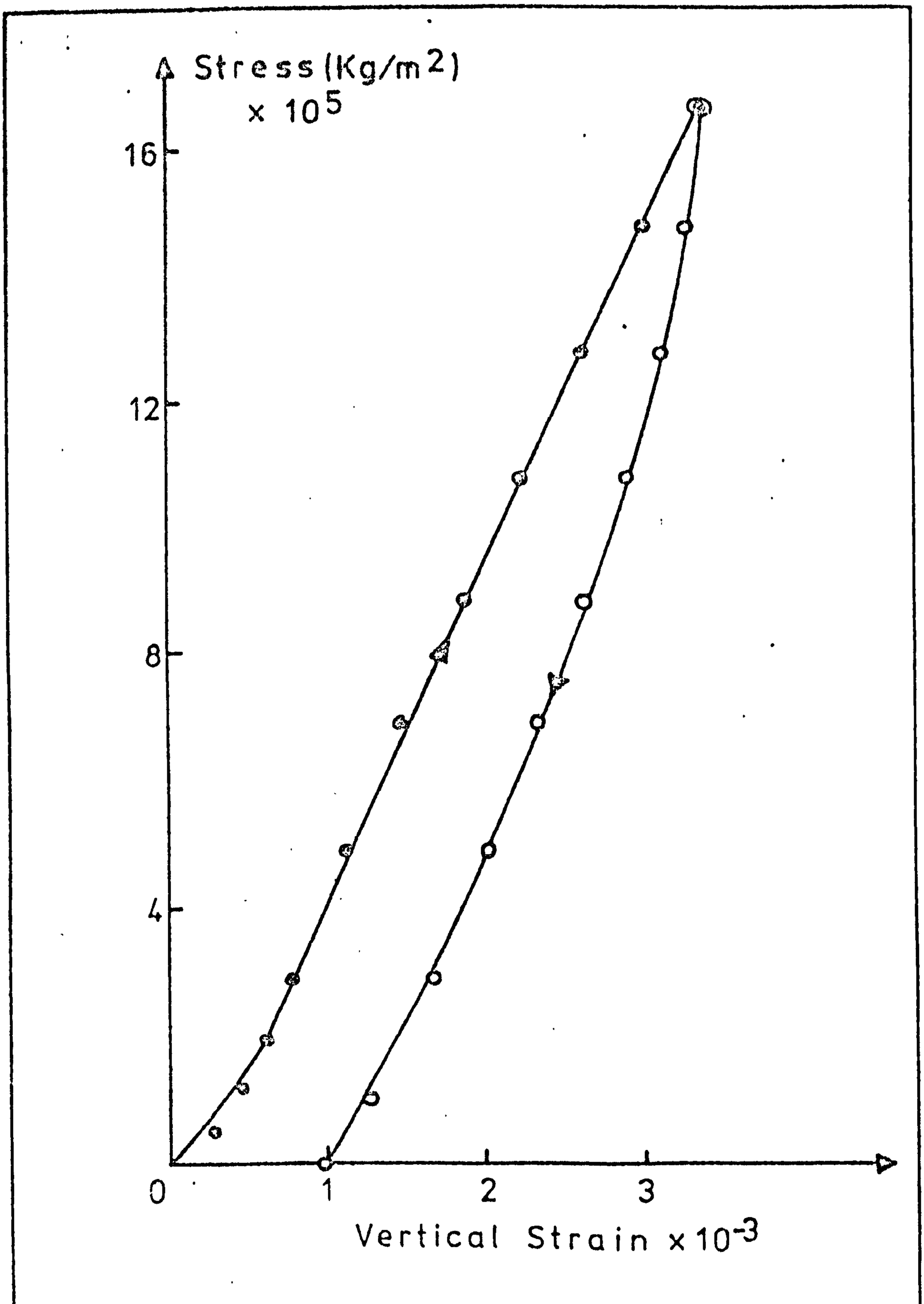

FIG.B.4.2 STRESS-STRAIN RELATIONSHIP FOR MUDSTONE.

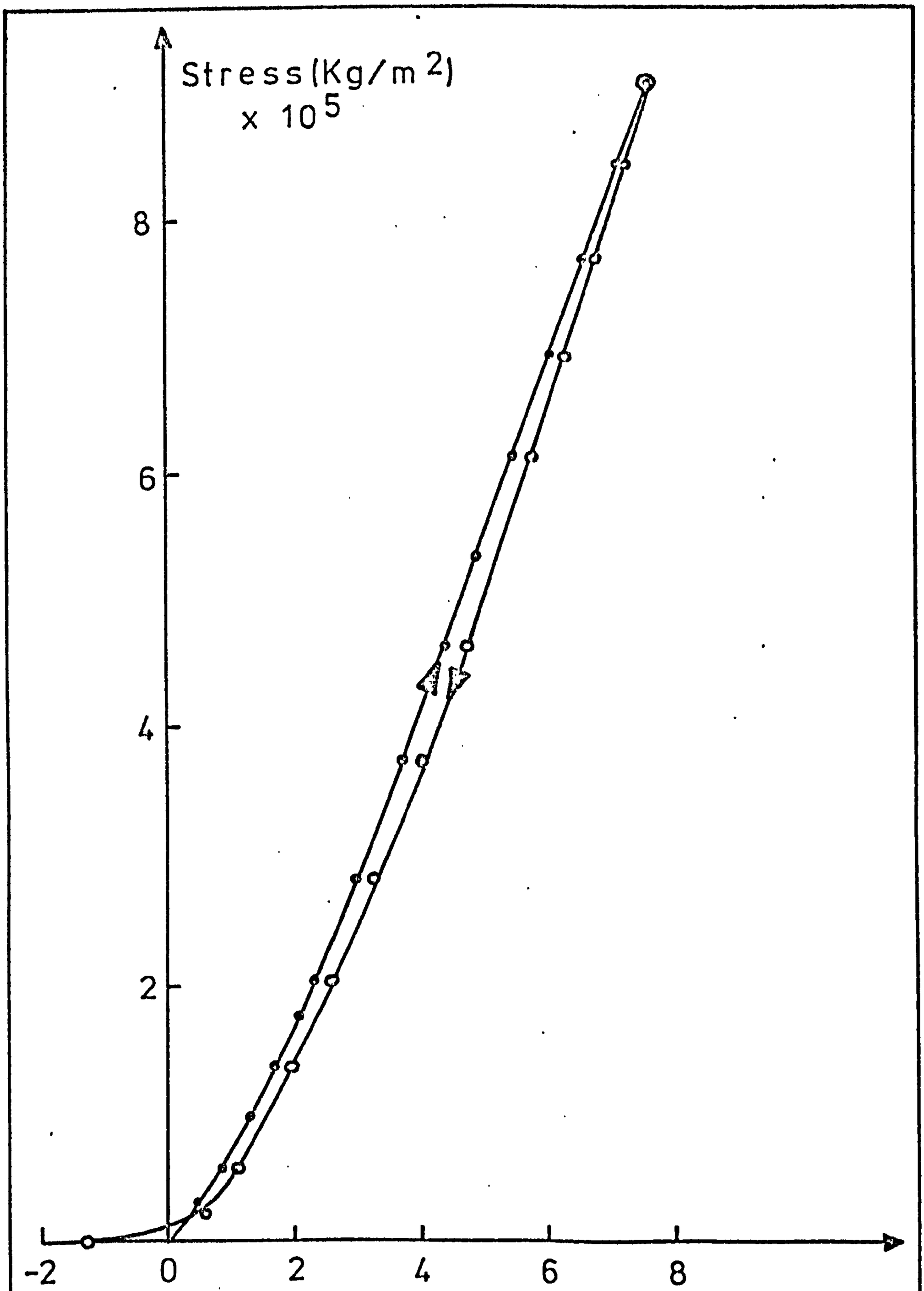

FIG. B.4.3 STRESS-STRAIN RELATIONSHIP FOR COAL.

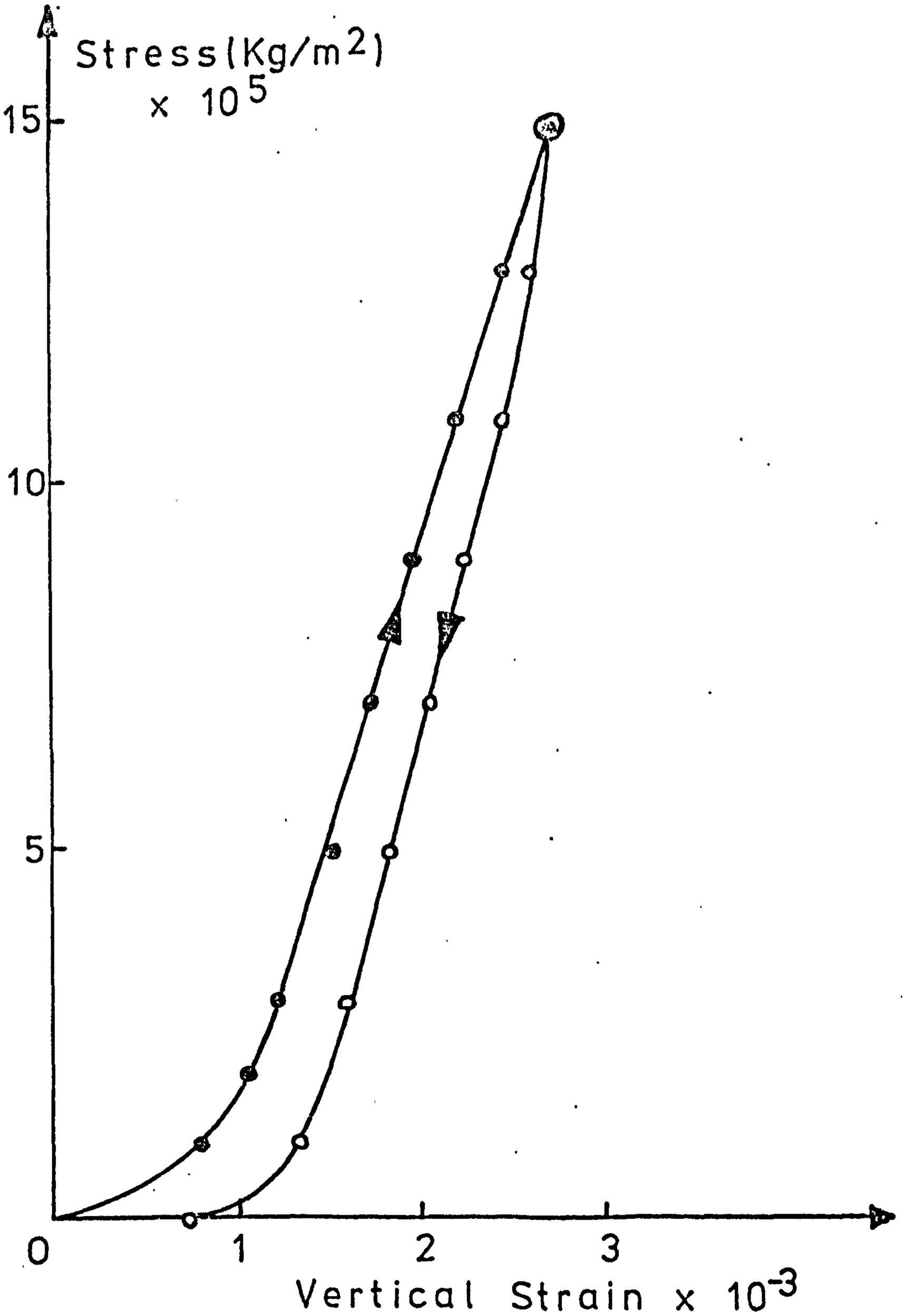

FIG. B.4.4 STRESS-STRAIN RELATIONSHIP FOR SHALE.

relationships, of the four rock types, in both loading and unloading cycles.

The vertical strain was the average of two readings. The corresponding values of the Young's modulus are given below:

ROCK TYPE	E x $10^3 MN/m^2$
Sandstone	6.0
Mudstone	5.5
Shale	7.5
Coal	1.3

APPENDIX C

THE THEORETICAL THREE-DIMENSIONAL SOLUTION OF A SPHERICAL INCLUSION IN ROCK, SURROUNDED BY A FOREIGN LAYER

C.1 INTRODUCTION

In this section the theoretical three-dimensional solution of a spherical inclusion in rock is described in detail. A further expansion of this solution, covering the case where the inclusion is surrounded by a thick foreign layer is also given. The latter closely represents the steel sphere - epoxy cement - rock system, which was the basis of the developed inclusion meter.

C.2 THREE-DIMENSIONAL ANALYSIS OF STRESS

Assume that the nine Cartesian components of stress are known at a point. From the theory of elasticity it is known that the corresponding principal stresses σ_i, where i = 1,2,3, can be found by solving the following determinant:

$$\begin{vmatrix} (\sigma_i - \sigma_x) & -\tau_{xy} & -\tau_{zx} \\ -\tau_{xy} & (\sigma_i - \sigma_y) & -\tau_{yz} \\ -\tau_{zx} & -\tau_{yz} & (\sigma_i - \sigma_z) \end{vmatrix} = 0 \qquad \text{C.2.1}$$

or by developing the above determinant

$$\sigma_i^3 - I_1 \sigma_i^2 - I_2 \sigma_i - I_3 = 0 \qquad \text{C.2.2}$$

where I_1, I_2, I_3 are the three stress invarients given by the following expressions:

$$I_1 = \sigma_x + \sigma_y + \sigma_z$$

$$I_2 = -(\sigma_x\sigma_y + \sigma_y\sigma_z + \sigma_z\sigma_x - \tau_{xy}^2 - \tau_{yz}^2 - \tau_{zx}^2) \qquad \text{C.2.3.}$$

$$I_3 = \sigma_x\sigma_y\sigma_z + 2\tau_{xy}\tau_{yz}\tau_{zx} - \sigma_x\tau_{yz}^2 - \sigma_y\tau_{zx}^2 - \sigma_z\tau_{xy}^2$$

Equation C.2.2 is a cubic one with respect to σ_i, and its three real roots are the principal stresses σ_1, σ_2 and σ_3 ($\sigma_1 > \sigma_2 > \sigma_3$ algebraically).

The orientations of the principal stresses, with respect to the Cartesian reference axes are given by

$$(\sigma_i - \sigma_x)l - \tau_{xy}m - \tau_{zx}n = 0$$

$$-\tau_{xy}l + (\sigma_i - \sigma_y)m - \tau_{yz}n = 0 \qquad \text{C.2.4}$$

$$-\tau_{zx}l - \tau_{yz}m + (\sigma_i - \sigma_z)n = 0$$

$$l^2 + m^2 + n^2 = 1$$

where l, m, n are the direction cosines with respect to the X, T and Z axes.

If, therefore, measurements are taken on a system consisting of three strain rosettes at a point, then the nine components of stress along the Cartesian (or any other) axes can be evaluated from the theory of elasticity, and using equations C.2.2 and C.2.4 the principal stresses and their directions with respect to the reference axes can be found, at the point of interest.

C.3 THEORY OF AN INCLUSION

Let us assume that σ_i are the principal stresses of an inclusion, acting along the directions (l,m,n) with respect to the reference axes, as explained above. If σ_r are the corresponding principal stresses in the host material, in this case rock, acting along the same directions, then for a spherical inclusion, Coutinho[130] showed that

$$
\begin{aligned}
(\sigma_r)_1 &= K_1\sigma_1 + K_2(\sigma_2 + \sigma_3) \\
(\sigma_r)_2 &= K_1\sigma_2 + K_2(\sigma_1 + \sigma_3) \\
(\sigma_r)_3 &= K_1\sigma_3 + K_2(\sigma_1 + \sigma_2)
\end{aligned}
\qquad \text{C.3.1}
$$

where the stress factors K_1 and K_2 are given by

$$K_1 = \frac{T + 2F}{T(T + 3F)}$$

$$K_2 = -\frac{F}{T(T + 3F)} \qquad \text{C.3.2}$$

with T and F determined from the following system of equations:

$$
\begin{aligned}
&\frac{2(1+\nu_r)}{5\ E_r}\frac{A}{R^3} - \frac{(1+\nu_r)}{2\ E_r}\frac{B}{R^3} + \frac{\nu_i}{E_i}\ T - \frac{(1-2\nu_i)}{E_i}\ F = \frac{\nu_r}{E_r} \\
&\frac{4(1+\nu_r)}{E_r}\left(\frac{4}{5} - \nu_r\right)\frac{A}{R^3} - \frac{(1+\nu_i)}{E_i}\ T = -\frac{(1+\nu_r)}{E_r} \\
&\left(-\frac{2}{5} + 2\nu_r\right)\frac{A}{R^3} + \frac{B}{R^3} - F = 0 \\
&\left(\frac{14}{5} - 2\nu_r\right)\frac{A}{R^3} + T = 1 \\
&A - \frac{5C}{R^2} = 0
\end{aligned}
\qquad \text{C.3.3}
$$

where

R = Radius of the inclusion

E_r, ν_r = Mechanical properties of rock (host) material

E_i, ν_i = Mechanical properties of the inclusion

A, B, C, T, F = Constants

Equations C.3.3 and C.3.1 show that the presence of a rigid inclusion of radius R in a material will alter its stress distribution within a radius equal to the inclusion's diameter 2R. As a result, σ_r represent the principal stresses on a volume element which is large enough, at least three times the inclusion's diameter, so that σ_r is not affected by the presence of the inclusion.

Figures C.3.1 and 2 show the variation of K_1 and K_2 with E_i/E_r for a spherical inclusion. Points for the same parameters for a circular inclusion are also shown. From the first graph it can be seen that the K_1 values are nearly the same for the two geometries, although slightly lower for the spherical inclusion along the asymptotic part of the curves. A greater variation can, however, be observed in the K_2 values, especially in the case of ($\nu_r = 0$, $\nu_i = 0.25$) and ($\nu_r = 0.25$, $\nu_i = 0$) where the spherical inclusion factor is higher. In the case of ($\nu_r = \nu_i = 0.25$) variations are only present for low values of E_i/E_r (less than 1).

If the inclusion material is steel, with mechanical properties $E_i = 210 \times 10^3 MN/m^2$ and $\nu_i = 0.30$, then by

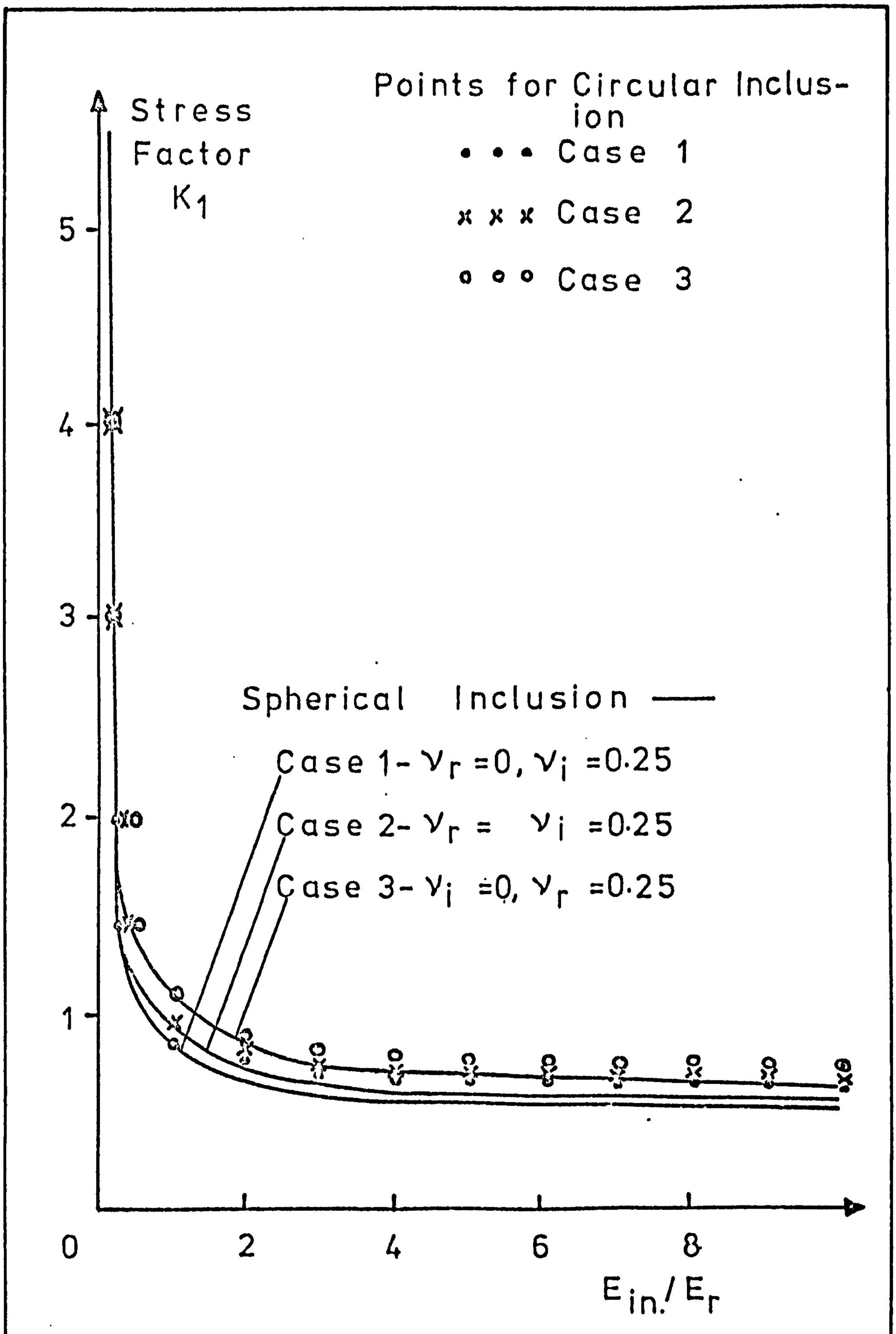

FIG.C.3.1 STRESS FACTOR K_1 FOR A SPHERICAL INCLUSION.

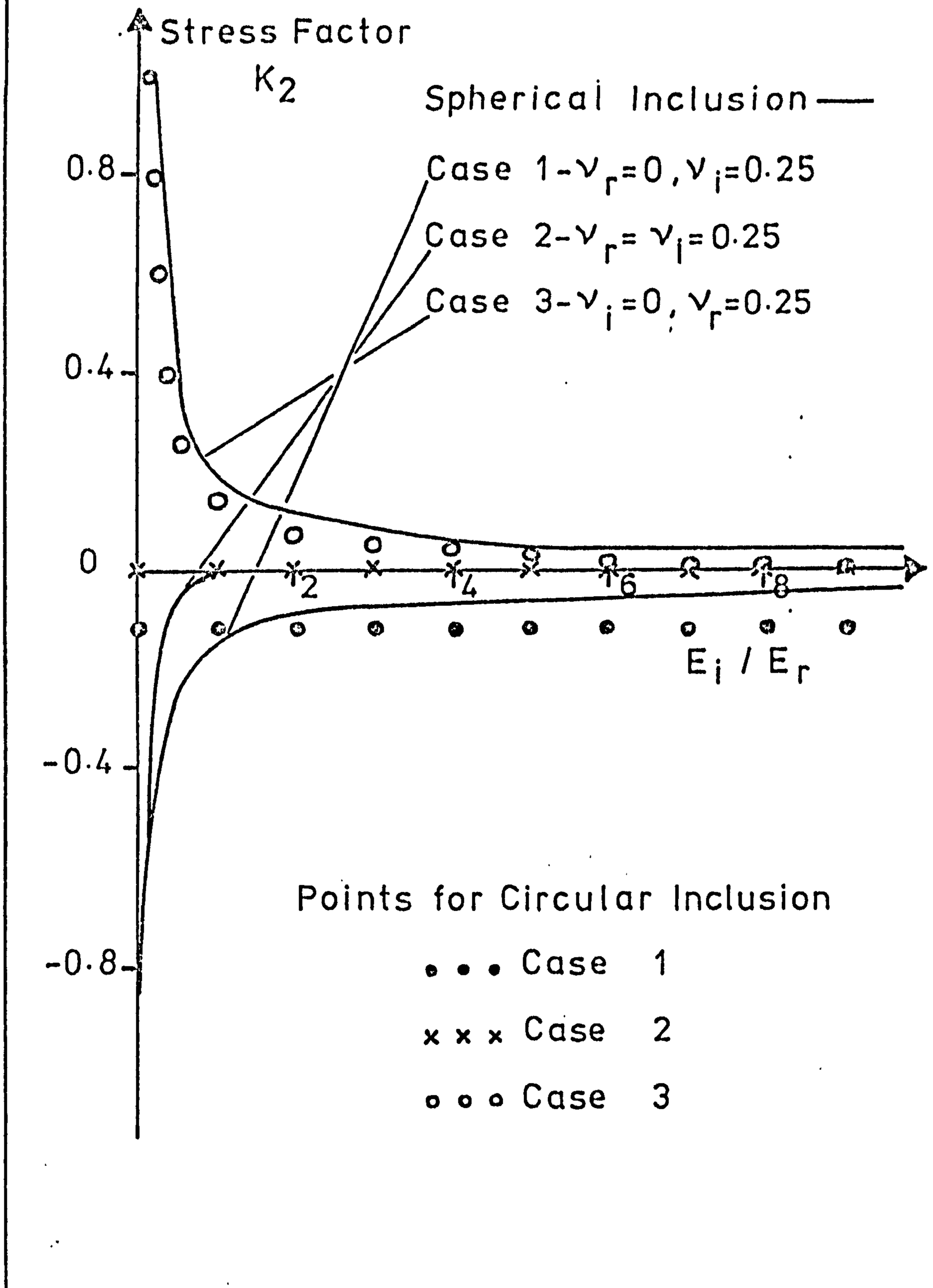

FIG. C.3.2 STRESS FACTOR K_2 FOR A SPHERICAL INCLUSION .

substituting these values into the inclusion equations, the graph shown in Figure C.3.3 is obtained. The latter can easily determine the stress factors K_1 and K_2, for this type of inclusion, if the Young's modulus and Poisson's ratio of the rock are known.

The graphs shown in Figures C.3.1, 2 and 3 were determined from points which were accurately calcubated, by using computer techniques to evaluate numerically equations C.3.2 and 3. The graphs suggest little variation of the stress factors K_1 and K_2, with respect to the properties of the rock, if E_i/E_r is greater than 4. In fact Coutinho[130] calculated that even when E_r greatly varies, for a given E_i, the changes in the stress factors are minimal. For example, a variation of 50% on the E_r values will cause an error of about 10% in the stresses calculated from equation C.3.1. This error will become a maximum of 15% in the limited case where ν_i is zero. As a result, the accuracy of the inclusion technique is increased considerably, if the Poisson's ratio of the inclusion is high compared to that of the host.

Having, therefore, determined the principal stresses and directions of an inclusion, by using the strain rosette system, as explained in section C.2, the corresponding principal stresses of the rock can be found, (directions are assumed the same) using the inclusion theory. Furthermore, the

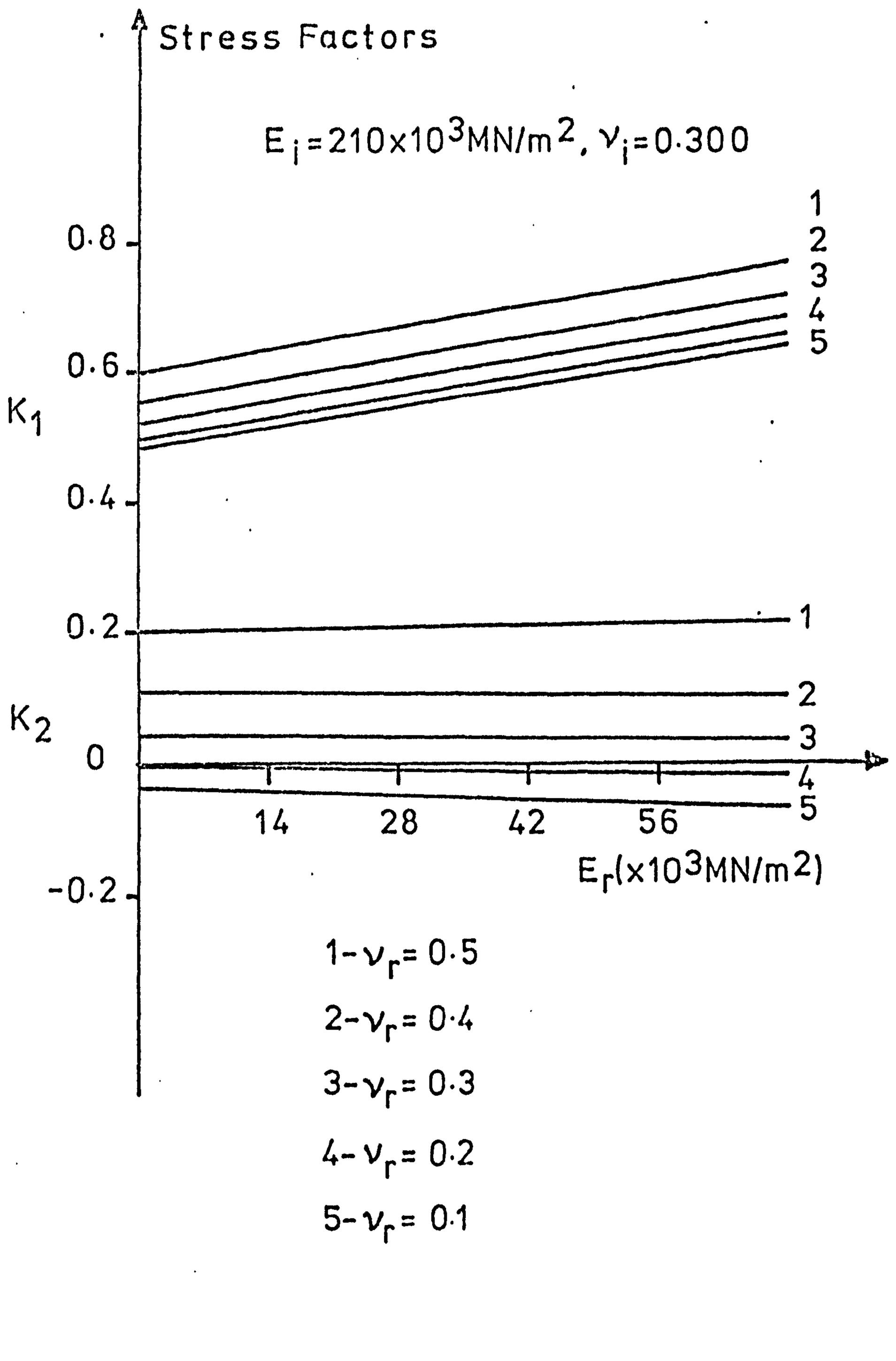

FIG. C.3.3 STRESS FACTORS FOR A STEEL SPHERICAL INCLUSION .

inevitable variations of the mechanical properties of the rock, will have little impact on the stress values if the rigid inclusion is a high modulus one, i.e. E_i/E_r at least 4.

C.4 THE EFFECT OF A FOREIGN LAYER ON THE INCLUSION SYSTEM

So far, the problem of a high modulus spherical inclusion was solved by assuming that the inclusion and the host material are perfectly welded with each other. Consider now the case where a thick foreign layer is between the inclusion and the host, and assume, as before, that all layers are perfectly and uniformly welded.

The latter case can be divided into two systems, the host-foreign layers (r/c); and the foreign-inclusion layers (c/i). From equation C.3.1, therefore, it follows:

$$(\sigma_r)_1 = (K_1)_{r/c}(\sigma_c)_1 + (K_2)_{r/c}((\sigma_c)_2 + (\sigma_c)_3)$$

$$(\sigma_r)_2 = (K_1)_{r/c}(\sigma_c)_2 + (K_2)_{r/c}((\sigma_c)_1 + (\sigma_c)_3) \qquad \text{C.4.1}$$

$$(\sigma_r)_3 = (K_1)_{r/c}(\sigma_c)_3 + (K_2)_{r/c}((\sigma_c)_1 + (\sigma_c)_2)$$

and

$$(\sigma_c)_1 = (K_1)_{c/i}\,\sigma_1 + (K_2)_{c/i}\,(\sigma_2 + \sigma_3)$$

$$(\sigma_c)_2 = (K_1)_{c/i}\,\sigma_2 + (K_2)_{c/i}\,(\sigma_1 + \sigma_3) \qquad \text{C.4.2}$$

$$(\sigma_c)_3 = (K_1)_{c/i}\,\sigma_3 + (K_2)_{c/i}\,(\sigma_1 + \sigma_2)$$

where

$(\sigma_r)_i$, $(\sigma_c)_i$, σ_i, (i = 1,2,3) are the principal stresses acting on the host rock, foreign layer (cement), and inclusion

respectively.

$(K_1)_{r/c}$, $(K_2)_{r/c}$ are the stress factors with respect to the host-cement system, given by equations C.3.2 and 3.

$(K_1)_{c/i}$, $(K_2)_{c/i}$ are the stress factors with respect to the cement-inclusion system, given from the same equation as above.

By substituting equations C.4.2 into C.4.1 it follows

$$(\sigma_r)_1 = (K_1)_{r/c}((K_1)_{c/i}\,\sigma_1 + (K_2)_{c/i}\,(\sigma_2 + \sigma_3))$$

$$+ (K_2)_{r/c}((K_1)_{c/i}\,\sigma_2 + (K_2)_{c/i}\,(\sigma_1 + \sigma_3)$$

$$+ (K_1)_{c/i}\,\sigma_3 + (K_2)_{c/i}\,(\sigma_1 + \sigma_2))$$

$$= \sigma_1((K_1)_{c/i}\,(K_1)_{r/c} + 2(K_2)_{r/c}\,(K_2)_{c/i})$$

$$+ (\sigma_2 + \sigma_3)\,((K_1)_{c/i}\,(K_1)_{r/c} + (K_2)_{r/c}\,(K_1)_{c/i}$$

$$+ (K_2)_{r/c}\,(K_2)_{c/i})$$

Similar expressions can also be derived for $(\sigma_r)_2$ and $(\sigma_r)_3$. Let us now define the following quantities

$$(K_1)_{r/c/i} = (K_1)_{r/c}(K_1)_{c/i} + 2(K_2)_{r/c}(K_2)_{c/i}$$

$$(K_2)_{r/c/i} = (K_1)_{r/c}(K_2)_{c/i} + (K_2)_{r/c}\,(K_1)_{c/i}$$

$$+ (K_2)_{r/c}\,(K_2)_{c/i} \qquad \text{C.4.3}$$

where $(K_1)_{r/c/i}$ and $(K_2)_{r/c/i}$ are the equivalent stress factors of a rock-cement-inclusion system.

The principal stresses of the rock, therefore, can now be expressed in the familiar form with respect to the inclusion stresses, with the influence of the foreign cement layer being included, as shows:

$$(\sigma_r)_1 = (K_1)_{r/c/i}\,\sigma_1 + (K_2)_{r/c/i}\,(\sigma_2 + \sigma_3)$$

$$(\sigma_r)_2 = (K_1)_{r/c/i}\,\sigma_2 + (K_2)_{r/c/i}\,(\sigma_1 + \sigma_3) \qquad \text{C.4.4}$$

$$(\sigma_r)_3 = (K_1)_{r/c/i}\,\sigma_3 + (K_2)_{r/c/i}\,(\sigma_1 + \sigma_2)$$

Wilson[127] found similar expressions for a circular inclusion. By plotting graphs corresponding to the two systems, i.e. rock-inclusion and rock-cement-inclusion, and assuming E_c and ν_c as $10.5 \times 10^3 MN/m^2$ and 0.170 respectively, he concluded that a cement layer had very little influence on the stress factors, if the Young's modulus of the rock was below $21 \times 10^3 MN/m^2$. In the latter case, therefore, even a thick layer of cement can be neglected. However, for E_r values above $21 \times 10^3 MN/m^2$, the divergence of the stress factors between the two systems is considerable, and as a result the cement layer can not longer be ignored.

The stress factors for a rock-inclusion and a rock-cement-inclusion system, for a spherical inclusion, are compared in Figure C.4.1. These graphs were accurately plotted, with the aid of a computer, assuming that the Young's modulus and

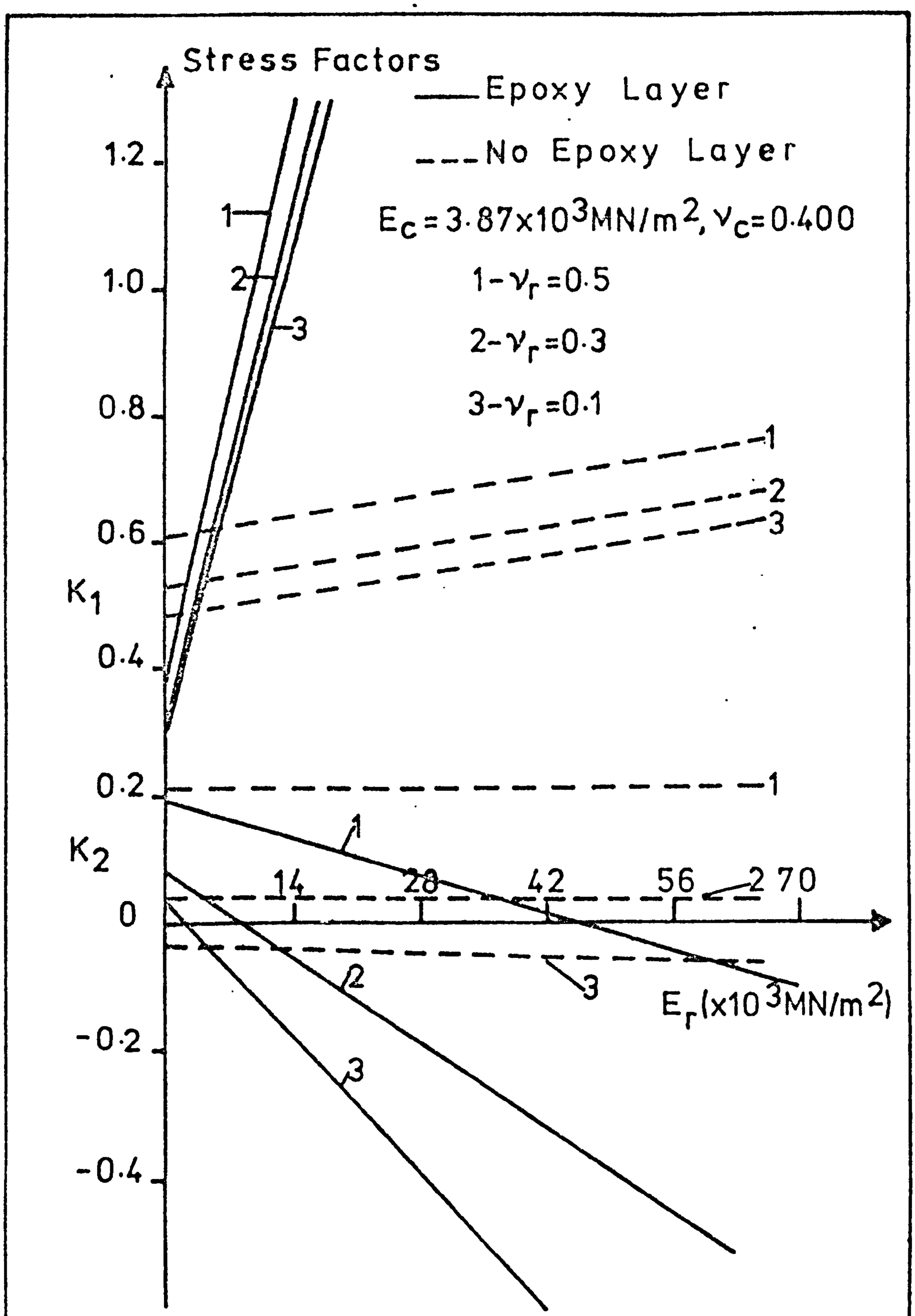

FIG. C.4.1 STRESS FACTORS FOR A STEEL SPHERICAL INCLUSION SURROUNDED BY AN EPOXY LAYER .

Poisson's ratio of the cement layer are $3.87 \times 10^3 MN/m^2$ and 0.400 respectively. It is clearly seen from Figure C.4.1, that the cement layer has a pronounced effect on the stress factors and in particular the K_1. Although its effect is considerably less for E_r values below $7 \times 10^3 MN/m^2$, nevertheless the graphs strongly indicate that for a spherical inclusion in rock, surrounded by a cement layer, the stress factors can only be estimated using equation C.4.3.

For a high modulus inclusion (steel sphere) cemented inside a rock, therefore, the principal stresses of the rock can be found if the corresponding ones of the inclusion are known, using equations C.4.4.

BIBLIOGRAPHY AND REFERENCES

BIBLIOGRAPHY

(A) ROCK MECHANICS TEXTS

A.1/. COATES, D., Rock Mechanics Principles, Dept.Mines Tech. Surveys, Ottawa, 1970.

A.2/. DREYER, D W, The Science of Rock Mechanics, Vol 1, Trans. Tech. Publications, Germany, 1972.

A.3/. EVANS, I, POMEROY, C D, Strength, Fracture and Workability of Coal, Pergamon Press, Oxford, 1966.

A.4/. FARMER, I W, Engineering Properties of Rocks, E and F N Spon Limited, London, 1968.

A.5/. ISAACSON, E ST.Q, Rock Pressures in Mines, Mining Publications, London, 1962.

A.6/. JAEGER, J C, Elasticity, Fracture and Flow, Methuen, London, 1962.

A.7/. JAEGER, J C, COOK, N G W, Fundamentals of Rock Mechanics, Methuen, London, 1968.

A.8/. OBERT, L, DUVAL, W I, Rock Mechanics and the Design of Structures in Rock, J Wiley & Sons, New York, 1967.

A.9/. REYNOLDS, H R, Rock Mechanics, Crosby Lockwood, London, 1961.

A.10/. SPRUTH, F, Face supports in Steel and Light Metals, Colliery Guardian Limited, London, 1955.

A.11/. STAGG, K G, ZIENKIEWICZ, O C, (Ed.) Rock Mechanics in Engineering Practice, J Wiley & Sons, London, 1968.

A.12/. WAHLSTROM, E E, Tunneling in Rock, Elsevier, New York, 1973.

A.13/. WOODRUFF, S, Methods of Working Coal and Metal Mines, Vol.I, Pergamon, Oxford, 1966.

(B) STRESS ANALYSIS TEXTS

B.1/. COKER, E G, FILON, L N G, A Treatise on Photo-Elasticity, (Rev.JESSOP, H T), Cambridge University Press, 1957.

B.2/. JESSOP, H T, HARRIS, F C, Photo-elasticity, Cleaver-Hume Press, London, 1949.

B.3/. FROCHT, M M, Photo-elasticity Vol I, II, J Wiley & Sons, New York, 1941-8.

B.4/. HENDRY, A W, Photo-elastic Analysis, Pergamon Press, Oxford, 1966.

B.5/. HEYWOOD, R B, Designing by Photo-elasticity, Chapman & Hall, London, 1952.

B.6/. HETENYI, M (Ed.), Handbook of Experimental Stress Analysis, J Wiley & Sons, New York, 1950.

B.7/. JAEGER, H C, Elasticity, Fracture and Flow, Methuen, London, 1962.

B.8/. MUSKHELISHVILI, N.I., Some Basic Problems of the Mathematical Theory of Elasticity, E P Noordhoff, Groningen, Netherlands, 1963.

B.9/. SAVIN, G N, Stress Concentration around Holes, Pergamon Press, New York, 1961.

B.10/. TIMOSHENKO, S P, GOODIER, J N, Theory of Elasticity, McGraw-Hill, New York, 1970.

B.11/. ZIENKIEWICZ, O C, CHEUNG, Y K, The Finite Element Methods in Structural and Continuum Mechanics, McGraw-Hill, London, 1967.

REFERENCES

1/. JUDD, W R, Rock stress, Rock mechanics and Research, The state of stress in the earth's crust (Ed.JUDD, W R), Elsevier, New York, 1964, pp.5-53.

2/. HABIB, M P, Measurement of Modulus of Elasticity of 'in-situ' rocks, Ann.hist.Tech.Bat.Trav.Publ.Sols et Foundations, No 3, September 1950, 27-35.

3/. ALEXANDER, L G, Field and Laboratory tests in Rock mechanics, 3rd Austr.-N Z Conf. on Soil Mech., 1960, pp.161-8.

4/. NOSE, M, Rock test 'in-situ' conventional tests on rock properties and design of Kurobegawa No 4 dam based thereon, 8th Inter. Cong. on Large Dams, Trans., No 1, Edinburgh, 1964, pp.219-52.

5/. BIENIAWSKI, Z T, The effect of specimen size on the Compressive strength of Coal, Inter.Jour.Rock Mech.Min.Scin., (5), 1968, 325-35.

6/. OBERT, L, WINDES, S L and DUVALL, W I, Standardized tests for determining the physical properties of Mine Rock, U S Bur.Mines, Rep.Inv.3891, 1946.

7/. AMERICAN SOCIETY FOR TESTING AND MATERIALS, Testing techniques for rock mechanics, 1966.

8/. DONATH, F A, Strength variation and deformational behaviour in Anisotropic rock, The state of stress in the earth's crust, (Ed.JUDD, W R), Elsevier, New York, 1964, pp.281-97.

9/. EVANS, I, POMEROY, C D and BERENBAUM, R., The compressive strength of Coal, Coll.Eng, (58), 1961, 75,123,172.

10/. HOAGLAND, R G, HAHN, G T and ROSENFELD, A R, The influence of microstructure on fracture propagation of rock, Journ. Int.Soc.Rock Mech. (5), No 2, August 1973, 77-106.

11/. TERZAGHI, K, Introduction to Tunnel Geology, Rock Tunnelling with Steel Supports, by PROCTOR, R and WHITE, T, Youngstown Printing, Ohio, 1946.

12/. U S BUR.MINES, A study of Mining Examination Techniques, for Detecting and Identifying Underground Nuclean Explosions, IC 8091, 1962.

13/. *COATES, D F, Classification of rocks, for Rock mechanics,* Inter.Jour.Rock Mech.Min.Scin. (1), 1964, 421-29.

14/. COATES, D F and PARSONS, R C, Experimental Criteria for Classification of Rock substances, Inter.Jour.Rock Mech. Min.Scin. (3), 1966,.181-9.

15/. SEAGER, J S, Pri-mining Lateral Pressures, Inter.Jour. Rock Mech.Min.Scin., (1), 1964, 413-9.

16/. TERZAGHI, K, and RICHART, F.E.Jr. Stresses in rock about cavities, Geotechnique, (3), June 1952, 57-90.

17/. OLESON, O J, Measurements of residual stresses by the strain-relief method, Quart.Color.Sch.Mines, 52(3), July 1957, 183-204.

18/. HAST, N., The measurement of Rock Pressure in Mines, 52 No 3, Series C, P A Norstedt and Sons, Stockholm, 1958.

19/. PANEK, L A, Measurement of Rock Pressure with a Hydraulic Cell, Tran.Am.Inst.Min.Eng., (220), 1961, 287-90.

20/. MERIL, R H, The 'in-situ' determination of stresses by relief techniques, The state of stress in the earth's crust, (Ed. JUDD, W R), Elsevier, New York, 1964, pp.343-78.

21/. HOOKER, V E, and DUVAL, W F, Stresses in rock outcrops near Atlanta, U S Bur.Mines, Rep.Inv.6860, 1966.

22/. COATES, D F, Some cases of residual stress effects in Engineering work, The state of stress in the earth's crust, (Ed.JUDD, W R), Elsevier, New York, 1964, pp.679-88.

23/. EVERLING, G, Discussion in reference 20.

24/. DENKHAUS, H G, The application of the mathematical theory of elasticity to problems of stress in hard rock at great depth, Pap.Ass.Min.Mugrs.S.Africa, September 1958, 271-310.

25/. DENKHAUS, H G, Critical review of strata movement theories and their application to practical problems, Jour.S.African Inst.Min.Metal, (64), 1963-4, 310-32.

26/. SALAMON, M G D, Elastic analysis of displacements and stresses induced by the mining of seam or reff deposits, Part I, II, III, Jour.S.African Inst.Min.Metal, (64), 1963-4, 128-49, 197-218, 468-500.

27/. RYDER, J A, and OFFICER, N C, An elastic analysis of strata movement observed in the vicinity of inclined excavations, *Jour.S.African Inst.Min.Metal, (64), 1963-4* 219-244.

28/. HACKETT, P, An elastic analysis of rock movements caused by mining, Trans.Inst.Min.Eng. (118), 1959, 421-35.

29/. BERRY, D S, An elastic treatment of ground movement due to mining, Part I, Isotropic ground, Jour.Mech.Phys.Solids, (8), 1960, 280-92.

30/. CLUTTERBUCK, M, The dependence of Stress Distribution on Elastic Constants, Brit.Jour.Appl.Phys. (9), 1958, 323-9.

31/. BERRY, D S and SALES, T W, An elastic treatment of ground movement due to mining, Part II, Transversely Isotropic ground, Jour.Mech.Phys.Solids, (9), 1961, 52-62.

32/. BERRY, D S, The ground considered as transversely isotropic material, Inter.Jour.Rock Mech.Min.Scin., (1), 1964, 159-69.

33/. MARSHALL, G J, and BERRY, D S, Calculation of the stress around an advancing longwall face in viscoelastic ground, Proc.1st Cong.Inter.Soc.Sock Mech., Lisbon 1966, Vol II, pp.379-84.

34/. HOFFER, K H, The principles of creep in rock salts and their general significance to mining engineering, Inter. Strata Control Cong., Leipzig, October 1958, pp.19-63.

35/. ROBERTSON, E C, Viscoelasticity of rocks, The state of stress in the earth's crust, (Ed.JUDD, W R), Elsevier, New York, 1964, pp.181-234.

36/. OBERT, L, and DUVAL, W I, Microseismic methods of determining the stability of underground openings, U S Bur.Mines, Bull.573,1957.

37/. COOK, N G W, The seismic location of rock bursts, Proc. 5th Rock Mech.Symp., Oxford, Pergamon Press, 1963, pp.493-516.

38/. STIMPSON, B, Modelling materials for engineering rock mechanics, Inter.Jour.Rock Mech.Min.Scin.(7), 1970, 77-122.

39/. WILSON, J W, Private communication.

40/. HOBBS, D W, A study of the behaviour of a broken rock under triaxial compression and its application to mine roadways, Inter.Jour.Rock Mech.Min.Scin., (3), 1966, 11-43.

41/. HOBBS, D W, The behaviour of broken rock under triaxial compression, Inter.Jour.Rock Mech.Min.Scin., (7), 1970, 125-48.

42/. HOBBS, D W, Strata movements around mine workings, results of scale model studies, Min.Engr., (128), 1969, 450-66.

43/. WILSON, A H, Research into the determination of Pillar Size, Part I, An Hypothesis concerning Pillar Stability, Min Engr., (131), 1972, 409-17.

44/. ASHWIN, D P, Research into the determination of Pillar Size, Part II, Measurements of stress in two Pillars, at Lea Hall Colliery, Min.Engr., (131), 1972, 417-27.

45/. BRYAN, A, Planning permission and the place of the Public Inquiry in the development of mineral resources in Birtain: problems of potash extraction in Yorkshire, Trans.Inst.Min. Metal., (80), 1971, A63-70.

46/. DUVALL, W I, Stress Analysis Applied to Underground Mining Problems, Part II, Multiple Openings and Pillars, U S Bur. Mines, Rep.Inv.4387, November 1948.

47/. DUVAL, W I, Stress Analysis Applied to Underground Mining Problems, Part I, Single openings, U S Bur.Mines, Rep. Inv.4192, March 1948.

48/. HOLLAND, C T, Some aspects of Pillar Stresses and their control in Coal Mines, Trans.Can.Inst.Min., (LVII) 1954, 248.

49/. STEART, F H, Strength and Stability of Pillars in Coal Mines, Jour.Chem.Metal.Min.Soc.S.Africa, (54), 1953-54, 309-25.

50/. COATES, D F, Pillar Loading, Part I, Literature Survey and a New Hypothesis, Mines Branch, Res.Rep.R168, Dept.Mines Tech.Surv.Ottawa, Canada, October 1965.

51/. COATES, D F, Pillar Loading, Part II, Model Studies, Mines Branch, Res.Rep.R.170, Dept. Mines Tech.Surv. Ottawa, Calada, November 1965.

52/. COATES, D F, Pillar Loading, Part III, Field Measurements, Mines Branch, Res.Rep.R.180, Dept.Mines Tech.Surv., Ottawa, Canada, February 1966.

53/. COATES, D F, Pillar Loading, Part IV, Inclined Workings, Mines Branch, Res.Rep.R.193, Dept.Energy Mines & Resources, Ottawa, Canada, December 1966.

54/. DHAR, B B, and COATES, D F, A Three-Dimensional Study of Pillar Stresses in Mines with Irregular Mining Boundaries, Proc. 6th Rock Mechanics Symposium, Mines Branch, Canada, 1970.

55/. DHAR, B B, and COATES, D F, A Three-Dimensional method of predicting Pillar Stresses, Inter.Jour.Rock Mech.Min.Scin., (9), 1972, 789-802.

56/. SALAMON, M D G, and ORAVECZ, K I, Displacement and strains induced by bored and pillar mining in South African Collieries, Proc. 1st Cong.Inter.Soc.Rock Mech., Vol II, Lisbon 1966, pp.227-31.

57/. STACEY, T R, Three-dimensional finite element stress analysis applied to two problems in rock mechanics, Jour.S.African Inst.Min.Metal, May 1972, 251-6.

58/. VAN HEERDEN, W L, Stress measurements in Coal Pillars, Proc. 2nd Cong.Inter.Soc.Rock Mech., Vol II, Belgrade 1970, pp.497-501.

59/. LOGIE, C V, Photo-elastic model study into the ground stress in bord and pillar coal mining, discussed in Ref.57.

60/. PHILLIPS, D W and JONES, T J, Strata movement ahead and behind long wall faces, Trans.Inst.Min.Engr., (101), July 1942, 346-62.

61/. JACOBI, O, The pressure on seam and goaf, Inter.Strata Control Congr., Essen 1956.

62/. SHEPHERD, R, Current Work on Strata displacements around Roadways, Symp. of Strata Control in Roadways, Univ. Nottingham, April 1970, pp.91-102.

63/. PRASAD, A S, A study of some of the factors influencing the movement of rock around longwall roadways, PhD Thesis, Univ. Strathclyde, July 1970.

64/. VAN ITERSON, F K T H, The Marvel of Mining, Inter.Conf. Rock Press.Supp.Workings, Liege 1951, pp-67-78.

65/. EVANS, W H, and HENSHAW, H, An investigation of the loads on Packs at Shallow Depths, Trans.Inst.Min.Engr.(96), 1938-9, 368-89.

66/. JENKINS, J D, and STOREY, I, Support Loads at Coal face, Tran.Inst.Min.Engr. (119), 1959-60, 699-712.

67/. WORKING PARTY REPORT, Design of Mine Layouts with reference to geological and geometrical factors, National Coal Board, Mining Dept., 1972.

68/. DIVISIONAL STRATA CONTROL RESEARCH COMMITTEE, Report on the Effects of Workings in Adjacent Seams upon New Developments, Tran.Inst.Min.Engr. Vol 113, Jan.1954, pp.389-403.

69/. ALDER, H, POTTS, E L, and WALKER, A, Research on strata control in the Northern coalfields of Great Britain, Inter.Conf.Rock Press.Supp.Workings, Liege 1951, pp.106-20.

70/. PHILLIPS, D W, Research problems on fall of ground, Trans.Inst.Min.Engr., (102), 1942-3, 122-40.

71/. ORAM, J S, A study of the behaviour and design of Coal Pillars for Underground Support, PhD Thesis, Univ.Strathclyde, 1971.

72/. JENKINS, J D, Pillars in longwall mining, Presented to the Scot.Inst.Min.Engr., Univ.Strathclyde, 1971.

73/. KING, H J, and WHITTAKER, B N, A Review of current knowledge on Roadway Behaviour, Especially the Problems on which Further Information is required, Symp.Strata Control Roadways, Univ.Nottingham, 1970,pp.73-87.

74/. GREENWALD, H P, HOWARTH, H C, and HARTMANN, I, Experiments on strength of small pillars of coal in the Pittsburgh Bed, U S Bur.Mines, Rep.Inv.3575, 1941.

75/. GROBBELAAR, G., The theoretical strength of mine pillars, Part I, Jour.S.African Inst.Min.Metal, (69), 1968-9, 173-84.

76/. SALAMON, M D S, and MUNRO, A H, A study of the strength of Coal Pillars, Jour.S.African Inst.Min.Metal, (68), 1967-68, 55-67.

77/. BRYAN, A, BRYAN, J G, and FOUCHE, J, Some problems of strata control and support in pillar workings, Min.Engr. (123), 1963-4, 238-66.

78/. PRICE, N J, A study of the time-strain behaviour of coal measure rocks, M R E Report No 2232, 1963.

79/. SMART, B G D, The development and application of techniques for conducting model and 'in-situ' observations of the interaction between elastically dissimilar strata, PhD Thesis, University of Strathclyde, 1973.

80/. WHITTAKER, B N, Design and Planning of Mine Layouts, Univ.Nottingham, Min.Magazin, (XXIV), 1972, 57-68.

81/. JACOBI, O, The Increase of roof flanking in longwall faces as a result of working under Pillar edges, and of abutment pressure of adjacent workings, Inter.Jour.Rock Mech.Min.Scin. (3), 1966, 221-30.

82/. WHITTAKER, B N, and HODGKINSON, D R, Design and Layout of longwall Workings, Min.Engr. (134), 1971, 79-92.

83/. DENKHAUS, H G, A critical review of the present state of scientific knowledge related to the strength of mine pillars, Jour.S.African Inst.Min.Meta., (63), 1962-3, 59-75.

84/. SINGH, R D, An Enquiry into the Stability and Failures of Coal Pillars, Proc. 2nd Congr.Inter.Soc.Rock Mech. Beograd, 1970, Vol II, pp-605-15.

85/. STRATA CONTROL RESEARCH SUB-COMMITTEE, N.ENGLAND INSTIT., Control of the strata in mining, Investigations in the Durham and Northumberland Coalfields, Tran.Inst.Min.Engr. (113), October 1953, 83-95.

86/. BREWSTER, D, On the communication of the structure of double refracting crystals to glass, by mechanical compression and dilation, Phil.Trans.Royal Soc., 1816, 156-78.

87/. MAXWELL, J C, On the equilibrium of elastic solids, Trans. Royal Soc.Edinb., 20, 1853, 87-120.

88/. COKER, E G, and FILON, L N G, A treatise on Photo-Elasticity, Camb.Univ.Press, 1931.

89/. FILON, L N G, and HARRIS, F C, On the diphasic nature of glass as shown by photo-elastic observations, Proc.Roy. Soc.London, A.103, 1923, 561-71.

90/. OPPEL, G, Photo-elastic investigations of three-dimensional stress and strain conditions, N A C A, T M.824, 1937.

91/. HETENYI, M, Photo-elastic studies of three-dimensional stress problems, 5th Inter.Cong.App.Mech.,1938, pp.208-12.

92/. RICHTER, J B, See PARTINGTON, J R., An advance Treatise on Physical Chemistry, (IV), 242.

93/. TYNDALL, J, Phil.Mag.1869, 37-384.

94/. RAYLEIGH, LORD, Phil.Mag.1881, 12-81.

95/. STACEY, K A, Light Scattering in Physical Chemistry, Butterworths Scien.Pub., London, 1956.

96/. WELLER, R, A new method for photo-elasticity in three-dimensions, Jour.App.Phys., (10), 1939, 266.

97/. JESSOP, H T, The scattered light method of exploration of stresses in two- and three-dimensional models, Brit.Jour. App.Phys., (2), 1951, 249-60.

98/. FROCHT, M M, and SRINATH, L S, A non-destructive method for three-dimensional photo-elasticity, Proc. 3rd U S Nat.Cong. App.Mech., 1958, pp.329-37.

99/. SRINATH, L S, and FROCHT, M M, The potentialities of the scattered light method, 1st P.S.P.1961, pp.277-92.

100/. FROCHT, M M, and GUERNSEY, R, Application of the Shear Difference method to the general space problem, Proc.1st U S Nat.Congr.App.Mech., 1952, pp.301-7.

101/. TAYLOR, W F, BOWMAN, C E, NORTH, W P, and SWINSON, W F, Application of Lasers to photo-elasticity, Proc.Soc.Exp. Str.Anal. (1), 1966, 289-96.

102/. DAVIES, D O, PhD Thesis to be published, Univ.Strathclyde.

103/. KARMIS, M, An investigation of the Scattered Light Technique as applied to Three-Dimensional Photo-Elasticity, BSc (Hons) Thesis, Univ.Strathclyde, 1971.

104/. McNICHOLAS, J B, and RANKILOR, P R, The preparation and use of a Stress-Sensitive Material in Multi-layer Photo-Elastic Models, Inter.Jour.Rock Mech.Min.Scin., (5), 1968, 465-74.

105/. PHOTOELASTIC INC. Technical Bulletins No 1-4100 and TDG-3.

106/. MINDLIN, R D, Stress Distribution around a tunnel, Trans.Am.Soc.Civ.Engr., (105), 1940, 1117-53.

107/. SHERMAN, D I, The Elastic Heavy Half-Plane weakened by holes with Elliptical shapes, laying sufficiently close to its Boundary, Probl.Cont.Mech., Soc.Ind.App.Maths., 1961, pp.440-72.

108/. YU, YI-YUAN, Gravitational Stresses in Deep Tunnels, Jour.App.Mech., Trans.Am.Soc.Mech.Engr., (74), 1952, 537-42.

109/. BARLA, G, Part I, Stresses around a single underground opening near a traction-free surface, Part II, The distribution of stress around a single underground opening in a layer medium under gravity loading, Inter.Jour.Rock Mech.Min.Scin.(9), 1972, 103-26 and 127-54.

110/. WILSON, J S, and GORE, W, Stresses in dams, An experimental investigation by means of India rubber models, Proc.Inst. Civ.Engr., 172, 2, 1908, 3705.

111/. BIOT, M A, Distributed gravity and temperature loading in two-dimensional elasticity, replaced by boundary pressures and dislocations, Jour.App.Mech.(2), 1953, 41-5.

112/. PARKS, V J, DURELLI, A J, and FERRER, L, Gravitational stresses determined using immersion Techniques, Jour.App. Mech.(34), 1967, 583-90.

113/. DURELLI, A J, PARKS, V J, and FERRER, L, Gravity and surface load stresses in spheres, Jour.Engr.Mech.Div. Proc.Am.Soc.Civ.Engr., 1970, 407-20.

114/. BUCKY, P B, The use of models for the study of mining problems, Am.Inst.Min.Metal.Engr., Tech.Pub.No 425,1931.

115/. BRAHTZ, J H A, The stress function and photo-elasticity applied to dams, Trans.Am.Soc.Civ.Engr.No 101, 1936.

116/. PANEK, L A, Centrifugal testing apparatus for mine structure stress analysis, U S Bur.Mines, Rep.Inv. 4833, 1952.

117/. DALLY, J W, DURELLI, A J, and RILEY, W F, A new method of 'Lock-in' Elastic effects for experimental stress Analysis, Jour.App.Mech. (25), 1958, 189-95.

118/. HOEK, E, The design of a centrifuge for the simulation of gravitational force fields in mine models, Jour.S.African Inst.Min.Metal, (65), 1964-5, 455-87.

119/. ROCHA, M, Structural model techniques, some recent developments, Stress Analysis (Ed. ZIENKIEWICZ, O C, and HOLISTER, G S), J Wiley, 1965, pp.385-461.

120/. SERAFIM, J L, and DA COSTA, J P, Methods and materials for the study of the weight stresses in dams by means of models, R I L E M Int.Colloq.of Models and Structures, Madrid 1959.

121/. RAPHAEL, M J, Dead load stress in model dams by methods of integration, Proc.Am.Soc.Civil.Engr., 87, Struct.Div., No SI.6, 31-46.

122/. FARQUHARSON, F B, and HENNES, R G, Gelatin models for photo-elastic analysis of stress in earth masses, Civ. Engr. 10, No 4, 1940, 211-4.

123/. CRISP, J D C, The use of gelatin models in structural analysis, Proc.Brit.Inst.Mech.Engr. 18(12), 1952, 580-604.

124/. RICHARDS, R,Jr., and MARK, R, Gelatin models for photo-elastic analysis of gravity structures, Exp.Mech., 3(2), 1966, 30-8.

125/. RICHARDS, R Jr., Photo-elastic Analysis for gravity stresses with stress-frozen Gelatin, Proc.Soc.Exp.Str. Anal. (1), 1972, 100-3.

126/. WADDELL, P, Stopping rotary motion with a prism, Mach. Desn., May 1973, 151-2.

127/. WILSON, A H, A laboratory investigation of a High Modulus Borehole Plug Gauge, for the measurement of Rock Stress, M R E Report No 2181, 1960.

128/. LEEMAN, E R, The Measurement of Stress in Rock, Jour. S.African Inst.Min.Metal, Vol 65, 1964-5, 45-114.

129/. NICHOLS, T C, ABEL, J F, Jr, and FITZHUGH, T L Jr, A Solid-Inclusion Borehole Probe to Determine Three-Dimensional Stress Changes at a Point in a Rock Mass, Geol.Surv.Bul.1258-C, 1968.

130/. COUTINHO, A, A Theory of an Experimental Method for determining Stresses, Not Requiring an Accurate Knowledge of the Elasticity Modulus, N C B Trans.A.632/A.B.